^{6}Li-based suspended foil microstrip neutron detectors

by

Nathaniel Scott Edwards

B.S., Kansas State University, 2009

AN ABSTRACT OF A DISSERTATION

submitted in partial fulfillment of the requirements for the degree

DOCTOR OF PHILOSOPHY

Department of Mechanical and Nuclear Engineering
College of Engineering

KANSAS STATE UNIVERSITY
Manhattan, Kansas

2018

ABSTRACT

The low natural abundance and supply shortage of ^{3}He has resulted in an increase in the cost of ^{3}He. The increase in cost of ^{3}He proportional counters has motived the development of low cost, high efficiency, low gamma-ray sensitivity alternative technologies. A recently developed alternative technology is the ^{6}Li-based suspended foil microstrip neutron detector (SFMND) that combines the neutron-conversion and gamma-ray discrimination capabilities of ^{6}Li foils with the mechanical robustness and electrical capabilities of microstrip electrodes. SFMNDs differ from Li-foil multi-wire proportional counters because the anode wires are replaced by a single microstrip electrode that improves the mechanical robustness, reduces the microphonic sensitivity, and allows for more ^{6}Li foils to be incorporated within a smaller form factor.

The first-ever SFMNDs containing one and five 96%-enriched, 75-μm thick ^{6}Li foils were fabricated using a silicon microstrip electrode. Neutron-sensitivity testing was performed yielding measured intrinsic thermal-neutron detection efficiencies, ε_{th}, of 4.02 ± 0.04% and 14.58 ± 0.11%, respectively. High electrode capacitance and gain instability were exhibited by the silicon microstrip electrode during neutron-sensitivity testing that led to the search for an electrically-stable microstrip-electrode substrate. Schott Borofloat® 33 glass was identified as an electrically-stable substrate and microstrip electrodes were fabricated and characterized. The Schott Borofloat® 33 microstrip electrodes were electrically-stable for a minimum duration of time of approximately 23 hours and had capacitances over an order of magnitude less than the identically sized silicon microstrip electrodes. One- and five-foil SFMNDs were fabricated with a Schott Borofloat® 33 microstrip electrode. Using 96%-enriched, 75-μm thick ^{6}Li foils, the one- and five-foil devices had maximum measured ε_{th} of 12.58 ± 0.15% and 29.75 ± 0.26%, respectively, with measured gamma-ray rejection ratios of $6.46 \times 10^{-5} \pm 4.32 \times 10^{-7}$ and $7.96 \times 10^{-5} \pm 4.65 \times 10^{-7}$ for a ^{137}Cs exposure rate of 50 mR hr^{-1}. Devices containing one, five, ten, and twenty 96%-enriched, 75-μm thick ^{6}Li foils were simulated using *MCNP6* and are theoretically capable of having ε_{th} of 18.36%, 54.08%, 65.43%, and 68.36%, respectively. The deviation between measured and simulated ε_{th} is suspected to occur due to the electric field strength distribution, electron attachment, microstrip-electrode capacitance, or any combination thereof and solutions for each of these suspected concerns are described.

^{6}Li-based suspended foil microstrip neutron detectors

by

Nathaniel Scott Edwards

B.S., Kansas State University, 2009

A DISSERTATION

submitted in partial fulfillment of the requirements for the degree

DOCTOR OF PHILOSOPHY

Department of Mechanical and Nuclear Engineering
College of Engineering

KANSAS STATE UNIVERSITY
Manhattan, Kansas

2018

Approved by:

Major Professor
Douglas S. McGregor

COPYRIGHT

ABSTRACT

The low natural abundance and supply shortage of ^{3}He has resulted in an increase in the cost of ^{3}He. The increase in cost of ^{3}He proportional counters has motived the development of low cost, high efficiency, low gamma-ray sensitivity alternative technologies. A recently developed alternative technology is the ^{6}Li-based suspended foil microstrip neutron detector (SFMND) that combines the neutron-conversion and gamma-ray discrimination capabilities of ^{6}Li foils with the mechanical robustness and electrical capabilities of microstrip electrodes. SFMNDs differ from Li-foil multi-wire proportional counters because the anode wires are replaced by a single microstrip electrode that improves the mechanical robustness, reduces the microphonic sensitivity, and allows for more ^{6}Li foils to be incorporated within a smaller form factor.

The first-ever SFMNDs containing one and five 96%-enriched, 75-μm thick ^{6}Li foils were fabricated using a silicon microstrip electrode. Neutron-sensitivity testing was performed yielding measured intrinsic thermal-neutron detection efficiencies, ε_{th}, of 4.02 ± 0.04% and 14.58 ± 0.11%, respectively. High electrode capacitance and gain instability were exhibited by the silicon microstrip electrode during neutron-sensitivity testing that led to the search for an electrically-stable microstrip-electrode substrate. Schott Borofloat® 33 glass was identified as an electrically-stable substrate and microstrip electrodes were fabricated and characterized. The Schott Borofloat® 33 microstrip electrodes were electrically-stable for a minimum duration of time of approximately 23 hours and had capacitances over an order of magnitude less than the identically sized silicon microstrip electrodes. One- and five-foil SFMNDs were fabricated with a Schott Borofloat® 33 microstrip electrode. Using 96%-enriched, 75-μm thick ^{6}Li foils, the one- and five-foil devices had maximum measured ε_{th} of 12.58 ± 0.15% and 29.75 ± 0.26%, respectively, with measured gamma-ray rejection ratios of $6.46 \times 10^{-5} \pm 4.32 \times 10^{-7}$ and $7.96 \times 10^{-5} \pm 4.65 \times 10^{-7}$ for a ^{137}Cs exposure rate of 50 mR hr^{-1}. Devices containing one, five, ten, and twenty 96%-enriched, 75-μm thick ^{6}Li foils were simulated using *MCNP6* and are theoretically capable of having ε_{th} of 18.36%, 54.08%, 65.43%, and 68.36%, respectively. The deviation between measured and simulated ε_{th} is suspected to occur due to the electric field strength distribution, electron attachment, microstrip-electrode capacitance, or any combination thereof and solutions for each of these suspected concerns are described.

TABLE OF CONTENTS

LIST OF FIGURES

LIST OF TABLES

LIST OF ACRONYMS

ε_{th}	Intrinsic Thermal-Neutron Detection Efficiency
BCS	Boron-Coated Straws
BOE	Buffered Oxide Etch
CLYC	Cs_2LiYCl_6:Ce
CLLB	$Cs_2LiLaBr_6$:Ce^{3+}
D.I.	Deionized
E-Beam	Electron Beam
GRR	Gamma-ray Rejection Ratio
HDPE	High-Density Polyethylene
HMDS	Hexamethyldisilazane
KSU	Kansas State University
LCR	Impedance – L, Capacitance – C, Resistance – R
LLD	Lower Level Discriminator
MCNP6	Monte Carlo N-Particle, Version 6
MIF	Metal Ion Free
MPFD	Micro-Pocket Fission Detector
MSGC	Microstrip Gas Chamber
MSND	Microstructured Semiconductor Neutron Detector
MWPC	Multi-Wire Proportional Counter
NIM	Nuclear Instrument Module
PEB	Post-Exposure Baking
PEEK	Polyether Ether Ketone
PMT	Photomultiplier Tube
PPI	Pores Per Linear Inch
PSD	Pulse-Shape Discrimination
PTFE	Polytetrafluoroethylene (Teflon™)
PVD	Physical Vapor Deposition
RVC	Reticulated Vitreous Carbon
SB33	Schott Borofloat® 33

SFMND	Suspended Foil Microstrip Neutron Detector
SiPM	Silicon Photomultiplier
S.M.A.R.T.	Semiconductor Materials And Radiological Technologies
SRIM	Stopping and Range of Ions in Matter
TGEM	Thick Gaseous Electron Multiplier
TLD	Thermoluminescent Dosimeter
TMAH	Tetramethylammonium Hydroxide
TRIGA Mk II	Training, Research, Isotopes, General Atomics Mark II
TRIM	Transport of Ions in Matter
UV	Ultraviolet

ACKNOWLEDGEMENTS

The research described in this dissertation would not have been possible without the extensive use of the many design, fabrication, characterization, and testing facilities and capabilities at the Kansas State University (KSU) Semiconductor Materials And Radiological Technologies (S.M.A.R.T.) Laboratory, Manhattan, KS 66502. The use of the KSU Training, Research, Isotopes, General Atomics (TRIGA) Mark (Mk) II research reactor made conducting several of the neutron-sensitivity measurements possible. Finally, the support, in part, of this research was provided by the Defense Threat Reduction Agency (DTRA), under contract HDTRA1-12-c-0002.

The author wishes to express the utmost gratitude to Dr. Douglas McGregor for the unending support and immense amount of invaluable knowledge, wisdom, guidance, and expertise that he imparted throughout the years. The author would also like to thank the KSU S.M.A.R.T. Laboratory members, past and present, as well as employees of Radiation Detection Technologies, Inc. (RDT), for providing their insight, expertise, assistance, and contributions to this work - each of whom has influenced me, both personally and intellectually, along my journey to develop as a scholar. Most notably, and in no particular order, the author would like to specifically thank Dr. Elsa Ariesanti, Dr. Steven Bellinger, Dr. Ryan Fronk, Dr. Alireza Kargar, Dr. Benjamin Montag, Dr. Kyle Nelson, Dr. Michael Reichenberger, Dr. Philip Ugorowski, Jerrod Conley, Brian Cooper, Priyarshini Ghosh, Luke Henson, Niklas Hinson, Daniel Nichols, Taylor Ochs, Sam Shelley, Christopher Tiner, and Logan Whitmore. The author would like to extend his gratitude to Steve DiPietro and Exothermics, Inc. for their generosity in applying $^{10}B_4C$ coatings using magnetron sputtering. The KSU TRIGA Mk II research reactor faculty and staff were always immensely helpful while conducting many of the neutron-sensitivity measurements and the author would like to specifically thank Dr. Amir Bahadori, Dr. Jeffrey Geuther, and Max Nager. Likewise, the author would like to thank the KSU Mechanical and Nuclear Engineering (MNE) department and machine shop for providing support both in and out of the laboratory. Throughout this academic journey, Dr. William Dunn, Dr. Andrew Rys, and Dr. J. Kenneth Shultis provided influence, guidance, wisdom, and support and the author wishes to thank each of them.

Lastly, the author wishes to thank his wife, family, and friends for the constant support and encouragement throughout this journey.

DEDICATION

This work is dedicated to my amazing wife and incredible parents. To my wife, Meredith, for never wavering in her support and for always being a constant source of strength. And to my parents, Brenda and Randy, for providing me with all of the opportunities and experiences throughout my life and the tools necessary to be a successful man. I cannot express my gratitude enough for the unending support, words of encouragement, and invaluable insight.

CHAPTER 1
INTRODUCTION

Somewhere, something incredible is waiting to be known.

Carl Sagan

Provided in this chapter is a brief discussion regarding the history of the development of neutron detectors (Section 1.1). Descriptions of modern neutron-detector technologies follow (Section 1.1). The motivation for the design and development of the ^{6}Li-based suspended foil microstrip neutron detector (SFMND) is discussed and the advantages of SFMNDs over current commercially-available neutron-detection technologies are also explained (Section 1.1). A list of contributions to the gas-filled neutron detection science and technology follows (Section 1.2). Description of the organization of the thesis concludes the chapter (Section 1.3).

1.1 Motivation for Research

The first gas-filled radiation detector capable of detecting individual particles was introduced in 1908 by Rutherford and Geiger and consisted of an axially-oriented anode wire positioned within a cylinder containing ionizing gas [1-3]. Their detector measured the motion of charge carriers[1] within the gas and was developed as an improvement over spinthariscopes [1]. Throughout the next several decades, numerous studies were conducted to understand and improve the functionality of gas-filled radiation detectors [2, 3].

As gas-filled radiation detectors were being developed, the concept of a neutrally-charged particle, initially called *beryllium radiation* and eventually defined as *neutrons*, was first hypothesized in 1920 by Ernest Rutherford [4] and later experimentally-quantified in 1932 by James Chadwick [5]. Chadwick positioned an ionization chamber containing N_2 gas, and later H_2

[1] The term *charge carrier* is used when referring to a particle that operates as a mobile platform to move charge.

gas, in front of a chamber containing a polonium alpha-particle source. The alpha-particle source was positioned near a beryllium target to produce neutrons using the (α, n) reaction. He studied neutron-interaction properties by measuring the response of the ionization chamber with and without several materials, namely paraffin film, positioned between the source and detector. An immediate measurable detector response was observed without any material present and the response was significantly more pronounced when paraffin film was present. He attributed the detector responses to recoil atoms, specifically protons, within the N_2 gas. Through the measurement of the recoil protons, Chadwick was able to calculate the mass of the neutron [5].

The development of nuclear power, physics, and weaponry followed soon after the discovery of the neutron, which necessitated the development of a variety of neutron detectors. The first neutron detectors emerged in the mid-to-late 1930s that contained BF_3 gas [6], were boron-lined [7], or were cloud chambers [8], depending on the application [9]. ^{3}He gas-filled radiation detectors were introduced in 1949 [10], and both boron- and helium-based gas-filled devices were widely used by the mid-1950s [11-14]. Solid-state neutron detectors were first introduced in 1949 [15] and the first solid-state device coated with a neutron-conversion material emerged in 1959 [16]. The first neutron-sensitive scintillator was introduced in 1960 [17]. The complexity and variety of neutron detectors and detection systems expanded throughout the decades following the discovery of the neutron as particle physics experiments became more diverse.

A variety of neutron detectors exist today [18-21] including modernized versions of the ^{3}He and $^{10}BF_3$ gas-filled proportional counters [22-24], boron-lined proportional counters [22, 23] (e.g. boron-coated straws (BCS) [25]), foil detectors (e.g. lithium-foil multi-wire proportional counters (Li-foil MWPCs) [26]), multi-layered thin-film-coated semiconductor devices (e.g. microstructured semiconductor neutron detectors (MSNDs) [27]), fission chambers (e.g. micro-pocket fission detectors (MPFDs) [28]), and scintillators containing neutron-conversion material(s) (e.g. Cs_2LiYCl_6:Ce (CLYC) [29] and $Cs_2LiLaBr_6:Ce^{3+}$ (CLLB) [30]). Each of these devices rely on neutron-sensitive materials to convert neutrons into ionizing reaction products. The neutron-sensitive material, and, therefore, the neutron-interaction method, typically corresponds to the neutron-energy range.

Thermal-neutron detectors are routinely used for nuclear non-proliferation, homeland security, oil-well logging, particle physics, and neutron scattering science, along with numerous

other applications [20]. Currently, ^{3}He proportional counters are considered the "gold standard" for thermal-neutron detection. ^{3}He proportional counters are used in several industries requiring thermal-neutron detectors and, therefore, are manufactured for a variety of effective areas and pressures ranging from approximately 1.6 to 1000 cm^{2} and 2 to 40 atm, respectively [31-37]. However, the natural abundance of ^{3}He of approximately 0.000137% [38] is quite low. The only production method currently being employed is the collection of ^{3}He as a byproduct from the radioactive decay of tritium, and the tritium is sourced from the dismantlement and refurbishment of the U.S. nuclear stockpile [20]. A supply shortage over the past decade has resulted in an increase in the cost of ^{3}He, with an estimated increase from \$40 – \$85 per liter between 2003 – 2008 to \$765 and \$2500 per liter in 2012 for federal and commercial use, respectively [20]. Therefore, the increase in ^{3}He cost has motivated the development of several ^{3}He alternative technologies. ^{3}He alternative technologies are developed with the goal of producing a rugged device that has high intrinsic thermal-neutron detection efficiency, ε_{th}, (> 80%), and low sensitivity to gamma rays (gamma-ray rejection ratio (GRR) $\leq 10^{-6}$). Additionally, the ability to manufacture alternative technologies for a variety of sizes while remaining cost effective is also advantageous.

All commercially-available ^{3}He alternative technologies have advantages and disadvantages. Crystalline and doped scintillators offer high ε_{th} but suffer from poor gamma-ray discrimination capabilities due to the abundance of high atomic-number materials composing typical crystals [20, 39-41] (although pulse-shape discrimination (PSD) techniques can be used to improve the gamma-ray discrimination capabilities [19]). Multi-layered thin-film-coated devices such as the MSND are capable of high ε_{th} and low gamma-ray sensitivity [42, 43]. However, due to the compact size of MSNDs, a large quantity of devices are required when producing large effective-area instruments [27]. $^{10}BF_3$ and boron-lined proportional counters suffer from low ε_{th} and sensitivity to microphonics. Additionally, $^{10}BF_3$ is a toxic gas [20]. An alternative to individual boron-lined proportional counters are BCSs [25, 44, 45]. BCSs contain bundles of boron-lined proportional counters that, as a detection system, are capable of high ε_{th}. However, BCSs are inherently susceptible to microphonics and require PSD in order to discriminate gamma rays [44]. Li-foil MWPCs are capable of meeting the ε_{th} and low gamma-ray sensitivity performance of ^{3}He proportional counters for a sufficient number of lithium foils [46, 47]. However, Li-foil MWPCs are also inherently susceptible to microphonics and are size limited due to the spacing required to accommodate anode wires.

A new type of gas-filled neutron detector, the ^{6}Li-based SFMND, has recently been developed at the Kansas State University (KSU) Semiconductor Materials And Radiological Technologies (S.M.A.R.T.) Laboratory. The ^{6}Li-based SFMND combines the neutron-conversion and gamma-ray discrimination capabilities of ^{6}Li foils with the mechanical robustness and electrical capabilities of microstrip electrodes. SFMNDs are capable of having a variety of ε_{th}, depending on the quantity and thickness of foils, while still maintaining low gamma-ray sensitivity. Neighboring foils can be positioned closer in proximity to one another due to the elimination of anode wires, thus allowing for smaller individual devices to be fabricated while still maintaining ε_{th} performance. The replacement of anode wires with a single microstrip electrode inherently improves the robustness and reduces microphonic sensitivity. The small form factor of the SFMND allows for modular devices to eventually be fabricated and arrayed together to form a variety of instrument sizes. Cost analysis has not yet been conducted because SFMNDs are under prototypical investigation. However, given the materials and labor required to fabricate prototype devices, the cost of SFMNDs is expected to be lower relative to ^{3}He proportional counters and other alternatives of similar size.

1.2 Contributions to Gas-Filled Neutron Detection Science and Technology

A summary of the novel contributions to the science of gas-filled neutron-detection technologies is listed below.

- Determined that electrons could not traverse the bulk of reticulated vitreous carbon (RVC) foam using a parallel-plate ionization chamber with and without a Frisch grid.
- Measured the neutron sensitivity of $^{10}B_4C$-coated RVC foam using a single-anode wire, P-10 continuous gas-flow proportional counter. The neutron-sensitivity measurement yielded an intrinsic thermal-neutron detection efficiency, ε_{th}, of 3.40 ± 0.09%, which verified that the sample functioned essentially as a thin-film-coated substrate.

- Measured the neutron sensitivity of $^{10}B_4C$-coated aluminum honeycomb using a single-anode wire, P-10 continuous-gas-flow proportional counter resulting in the highest measured ε_{th} to date for coated honeycomb media of 21.45 ± 0.26%.
- Conducted Monte-Carlo N-Particle, Version 6 (*MCNP6*) simulations to define the optimal coating thickness of $^{10}B/^{10}BN/^{10}B_4C/^{6}LiF$-coated aluminum honeycomb for various honeycomb cell sizes.
- Characterized the theoretical angular neutron sensitivity of $^{10}B/^{10}BN/^{10}B_4C/^{6}LiF$-coated aluminum honeycomb for various cell sizes using *MCNP6*.
- Simulated the effects of gas pressure on the theoretical neutron-detection performance of $^{10}B/^{10}BN/^{10}B_4C/^{6}LiF$-coated aluminum honeycomb for various cell sizes using *MCNP6*.
- Designed and developed the SFMND, which is a novel, parallel-plate-oriented proportional counter neutron detector that is a compact and robust improvement over Li-based MWPCs. The SFMND design eliminates the need for anode wires by using a single microstrip electrode as the collection electrode.
- Conducted *MCNP6* simulations to define the SFMND neutron-detection capabilities as a function of foil thickness and quantity.
- Simulated the effects of gas pressure on the theoretical neutron-detection performance of SFMNDs containing one- and five-^{6}Li foils using *MCNP6*.
- Optimized the geometry of the SFMNDs as a function of foil width and sensitive volume size using *MCNP6*.
- Fabricated Schott Borofloat® 33 microstrip electrodes and characterized the counting and gas multiplication curves, as well as the gain stability, in reference to silicon microstrip electrodes.
- Characterized the electric field strength distribution within a SFMND using a Schott Borofloat® 33 microstrip electrode and compared to *COULOMB* simulations.
- Adapted foil-lamination techniques for smaller-sized ^{6}Li foils in order to fabricate the first-ever ^{6}Li-based SFMNDs.
- Conducted the first-ever SFMND neutron-sensitivity measurements using one- and five-foil devices, which were compared to *MCNP6* simulations.

- Measured the distribution of ε_{th} within the SFMND and compared the results to the results of the electric field strength distribution study.

1.3 Organization of Thesis

Although the ^{6}Li-based SFMND was the eventual development of the described research, the consistent research intent was to design a compact and robust device featuring a neutron-conversion medium positioned between two parallel-plate electrodes. $^{10}B_4C$-coated RVC foams and $^{10}B_4C$-coated aluminum honeycomb were each initially studied as potential neutron-conversion media. Unfortunately, both of these conversion media have detrimental characteristics preventing the development of a high ε_{th} and low gamma-ray sensitivity device, as will be described in Chapter 4. Therefore, lithium foils were selected as the neutron-conversion medium given the success of Li-foil MWPCs [26, 46-48]. Microstrip electrodes were selected as the collecting electrode with the intent of allowing the device to function as a single charge-carrier device while also being operated in proportional mode and, therefore, being capable of producing large amplitude pulses.

Provided in Chapter 2 is a discussion of the general properties and interaction types of neutrons. The neutron-detection processes for common commercially-available thermal-neutron detectors are also described. Chapter 3 provides a discussion of the general theoretical considerations surrounding gas-filled radiation detectors. Because the development of the ^{6}Li-based SFMND involved several preliminary experiments, Chapter 4 details the experimental and computational efforts and results regarding the study of $^{10}B_4C$-coated RVC foams and aluminum honeycomb. Chapter 5 follows with a description of the design methodology and theoretical considerations of the ^{6}Li-based SFMND. Provided in Chapter 6 are descriptions of the design, fabrication, and characterization of the microstrip electrodes. Chapter 6 also discusses the ^{6}Li-based SFMND fabrication process before describing the neutron-sensitivity testing and results. Finally, Chapter 7 provides concluding remarks as well as discussion of future efforts to further study and refine the performance of ^{6}Li-based SFMNDs.

CHAPTER 2
NEUTRON DETECTION BACKGROUND

Nothing in life is to be feared, it is only to be understood.
Now is the time to understand more, so that we may fear less.

Marie Curie

The origin, characteristics, and nuclear interactions of neutrons are discussed first in the following chapter (Section 2.1). Description of common neutron-absorber materials follows (Section 2.2). Important characteristics and functional qualities of several types of commercially-available neutron detectors are then described (Section 2.3). Finally, accepted characterization methods and associated terms are explained (Sections 2.4 and 2.5).

2.1 The Neutron

Neutrons and protons are subatomic particles categorized as baryons because both particles are composed of a combination of three quarks [49]. Neutrons have a mass of 939.566 MeV c^{-2} and consist of one up quark, with charge of $+2q/3$, and two down quarks, with charge of $-q/3$, resulting in a net neutral charge [49]. In comparison, protons have a slightly smaller mass of 938.272 MeV c^{-2} and are composed of two up quarks and one down quark, resulting in a net charge of $+q$ [49]. The mean lifetime of free neutrons, the duration of time from birth to decay, is 885.7 ± 0.8 s [50]. Neutron decay occurs as depicted by the Feynman diagram of Figure 2.1 [49]. A virtual W^- boson is emitted resulting in the emission of an electron, e^-, and an antineutrino, $\bar{\nu}_e$. Neutrons are created with energies ranging from a few meV up to several MeV, depending on the source. Neutron production typically occurs by one of the following methods: cosmic rays, spontaneous fission, nuclear fission, nuclear fusion, (n, $2n$) or (n, $3n$) reactions, particle-accelerator-based methods like the spallation neutron source or *D-D* and *D-T* generators, photoneutrons produced from the (γ, n) reaction, and radioisotope sources typically relying on the

(α, *n*) reaction. Descriptions of various neutron sources are provided in the literature [9, 19, 51-53].

$$n \rightarrow p + e^{-} + \bar{\nu}_e$$

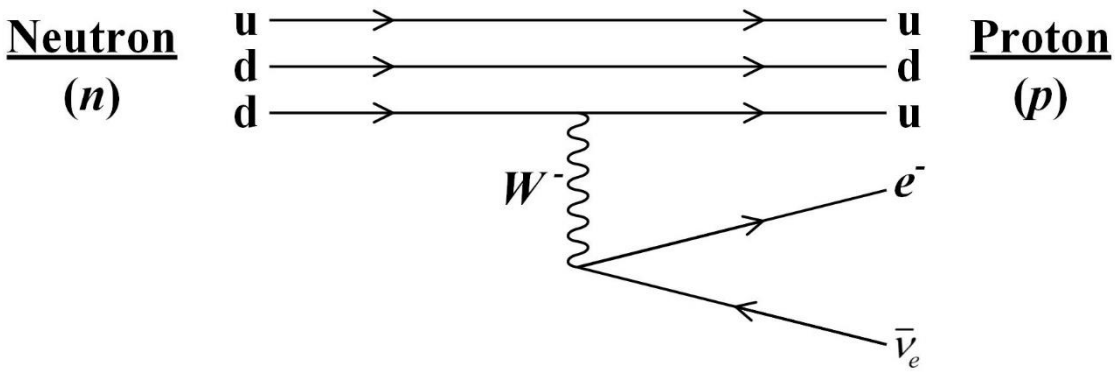

Figure 2.1. Feynman diagram depicting the β-decay of a neutron (n) to a proton (p) [49]. Because neutrons have slightly higher mass than protons, a down quark (d) is converted to an up quark (u) resulting in the emission of a heavy, virtual W^- boson. The virtual W^- boson then decays resulting in the emission of an electron (e^-) and an antineutrino ($\bar{\nu}_e$).

2.2 Neutron Interactions

Direct detection of neutrons can be difficult because neutrons are highly penetrating and, being neutrally-charged, do not undergo Coulombic interactions with the surrounding medium. Thus, indirect detection methods are employed that rely on the creation of ionizing reaction products emitted from either neutron scattering or absorption interactions. The interaction method depends on the energy of the incident neutrons and the isotope and density of the surrounding medium. For neutron energies above 0.1 MeV, referred to as *fast neutrons*, elastic and inelastic scattering interactions are the predominant interaction methods [54, 55]. Elastic scattering (*n*, *n*) occurs when a portion of the incident neutron energy is imparted to the target nucleus, resulting in a recoil nucleus [52, 56]. For sufficiently high-energy neutrons, inelastic scattering (*n*, *n*') occurs when the target nucleus is elevated to an excited state following the neutron scattering event, resulting in a reduction of the neutron kinetic energy [52, 56]. Gamma-ray emission immediately follows as the elevated target nucleus de-excites and returns to the ground state [56]. The reduction in neutron kinetic energy due to scattering interactions is known as *moderation* and the most

common isotope for moderation is hydrogen [52]. Thus, materials containing large abundances of hydrogen are often used as neutron moderators [57].

As neutrons travel through a moderator, kinetic energy is lost due to scattering interactions and the neutrons are called *slow neutrons* once the kinetic energy is below 1 eV [56]. Neutron kinetic energies between 1 eV and 0.1 MeV are called *epithermal neutrons* [56]. Neutrons that lose enough kinetic energy to reach thermal equilibrium with the surrounding medium are called *thermal neutrons*. The most probable kinetic energy of thermal neutrons is 0.025 eV, which corresponds to a velocity of approximately 2200 m s^{-1} [58]. As the neutron kinetic energy decreases, neutron absorption typically becomes the predominant interaction method [52]. Neutron absorption interactions that result in the emission of charged-particle reaction products are of particular interest for thermal-neutron detection applications.

The probability that a neutron undergoes an interaction of type *j* per unit path length [51] (where *j* may refer to elastic scatter (*s*), inelastic scatter (*i*), absorption (*a*), capture (*c*), fission (*f*), etc.) in a given material is defined by the macroscopic cross section of the material for the *j*th interaction type, Σ_j. The Σ_j, typically reported in units of cm^{-1}, is a function of the microscopic cross section of the j^{th} interaction, σ_j (b or cm^2), and atomic density N (atoms cm^{-3}) of the material as described by [58]

$$\Sigma_j = \sigma_j N . \tag{2.1}$$

σ_j is the probability that an interaction of type *j* will occur within a target nucleus per neutron per unit area. The unit of *barns* (b) is often used when reporting σ_j and is approximately equal to the cross-sectional area of a nucleus (1 b = 10^{-24} cm^2) [58]. The atomic density is dependent on the density of the material, ρ (g cm^{-3}), Avogadro's number, N_a (6.022 x 10^{23} atoms mol^{-1}), and the molar mass of the material, M (g mol^{-1}), as defined by [55]

$$N = \frac{\rho N_a}{M} . \tag{2.2}$$

For a compound mixture of density ρ, Σ_j is defined by the summed products of the atomic density, N_k, and microscopic cross section, $\sigma_{j,k}$, of the j^{th} interaction for the specific isotope, *k*, as [51]

$$\Sigma_j = \sum_k N_k \, \sigma_{j,k} = \sum_k w_k \, \frac{\rho N_a}{M_k} \sigma_{j,k} \,, \tag{2.3}$$

where N_k is dependent on the atomic fraction, w_k, and molar mass, M_k, of the k^{th} isotope. The total macroscopic cross section, Σ_{tot}, the probability that any type of interaction will occur, is defined by the sum of the separate interaction cross sections, (elastic scattering (Σ_s), inelastic scattering (Σ_i), absorption (Σ_a), capture (Σ_c), fission (Σ_f), etc.), as [52]

$$\Sigma_{tot} = \Sigma_s + \Sigma_i + \Sigma_a + \Sigma_c + \Sigma_f + \ldots. \tag{2.4}$$

Consider the scenario illustrated in Figure 2.2 in which a beam of neutrons, with intensity I_0, is incident on a slab of neutron absorber, with thickness l. The beam intensity, I, decreases exponentially as a function of distance, x, due to the absorption of neutrons within the absorber slab, as defined by [52]

$$I(x) = I_0 \, e^{-\Sigma_{a,th} x}, \tag{2.5}$$

where $I(x)$ is the beam intensity at position x. Thus, the amount of neutron absorption occurring within the absorber slab is dependent on the macroscopic thermal-neutron absorption cross section, $\Sigma_{a,th}$, of the slab material. By substituting the absorber slab thickness, l, into the distance term, x, the neutron-beam intensity emerging from the absorber slab, $I(l)$, is calculated as

$$I(l) = I_0 \, e^{-\Sigma_{a,th} l}. \tag{2.6}$$

Finally, the neutron absorption fraction, I_F, within the absorber is described by [59],

$$I_F = 1 - \frac{I(l)}{I_0} = 1 - e^{-\Sigma_x l}. \tag{2.7}$$

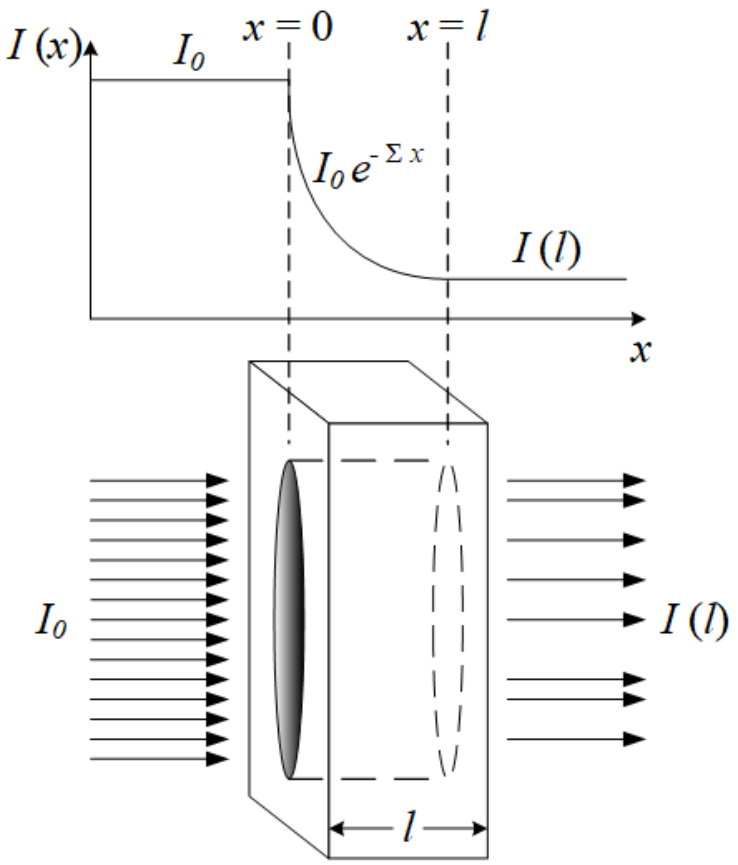

Figure 2.2. Exponential decay of a neutron beam with intensity I_0 through a slab of absorber with thickness l. The beam intensity decreases as a function of the macroscopic thermal-neutron absorption cross section, $\Sigma_{a,th}$, of the absorber material and absorber thickness.

The microscopic neutron absorption cross sections, σ_a, as a function of neutron energy for ^{3}He, ^{6}Li, ^{10}B, ^{113}Cd, and ^{157}Gd (commonly-used neutron-absorption isotopes) are shown in Figure 2.3 [60]. The σ_a of ^{3}He, ^{6}Li, and ^{10}B follow a 1/*v* dependence for neutron energies from thermal up to 100 keV. ^{3}He, ^{6}Li, and ^{10}B are referred to as 1/*v* absorbers due to the inversely-proportional relationship between σ_a and neutron velocity, *v* [59]. However, ^{113}Cd and ^{157}Gd are not considered 1/*v* absorbers due to the resonances that occur over the range of neutron kinetic energies of 3 eV – 6 keV.

As shown in Figure 2.3, ^{157}Gd, with a natural abundance of 15.65% [38], has the highest microscopic thermal-neutron absorption cross section, $\sigma_{a,th}$, of approximately 253,553 b [60]. A second gadolinium isotope, ^{155}Gd, with a natural abundance of 14.80% [38], has a $\sigma_{a,th}$ of approximately 60,794 b [60]. The combined $\sigma_{a,th}$ for all Gd isotopes results in a total $\sigma_{a,th}$ of approximately 48,770 b for natural Gd [38]. Both ^{155}Gd and ^{157}Gd rely on neutron-capture

interactions that produce internal conversion electrons within the energy range of 29 – 246 keV for approximately 60% of interactions [61]. Thus, natural Gd has an effective $\sigma_{a,th}$ of approximately 29,260 b. The most intense electron-emission energy from the neutron-capture interactions occurs at 71 keV [61]. Although gadolinium has a large $\sigma_{a,th}$, discrimination of neutron-induced pulses from gamma-ray events and electronic noise is difficult due the high probability of low-energy conversion-electron emissions [42]. However, neutron detectors incorporating gadolinium as the neutron-conversion medium have been explored and developed, and examples are described in [62-66].

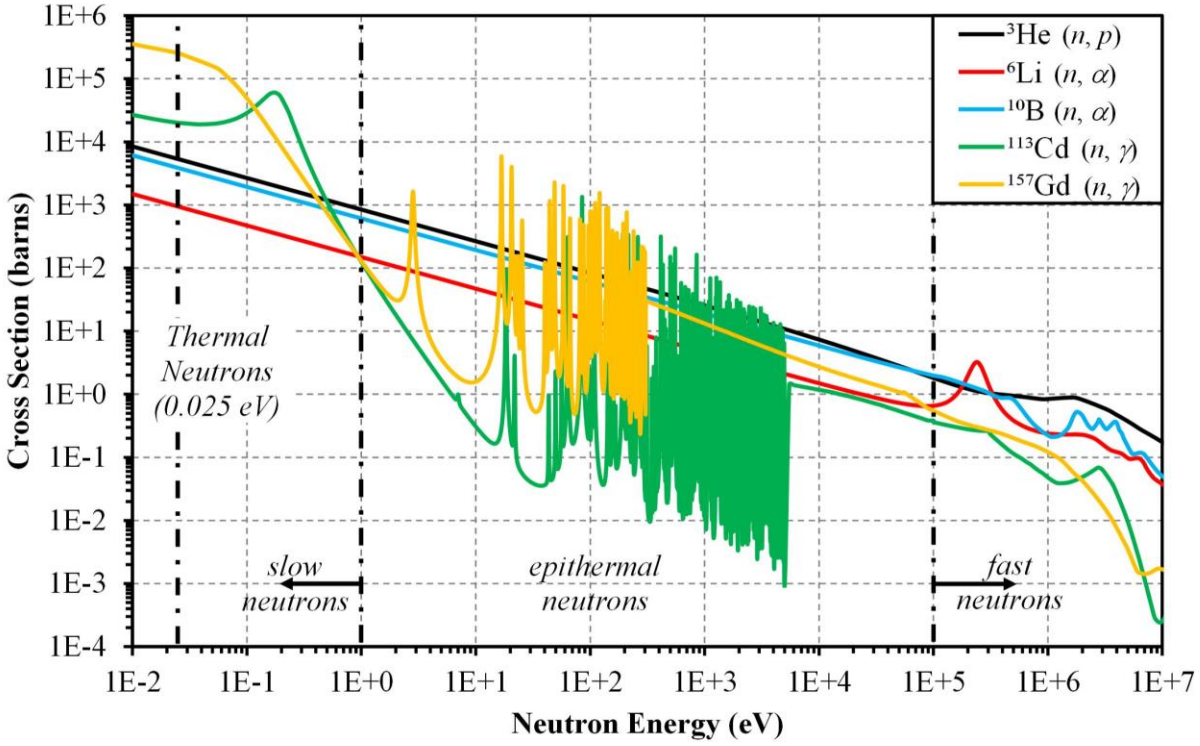

Figure 2.3. Microscopic absorption cross section as a function of neutron energy for ^{3}He, ^{6}Li, ^{10}B, ^{113}Cd, and ^{157}Gd [60].

From the isotopes shown in Figure 2.3, the $^{113}Cd(n, \gamma)^{114}Cd$ reaction has the next highest $\sigma_{a,th}$ of approximately 20,014 b [60]. The natural abundance of ^{113}Cd is 12.22% [38] and, therefore, the $\sigma_{a,th}$ of natural cadmium is approximately 2,446 b. The $^{113}Cd(n, \gamma)^{114}Cd$ reaction results in the emission of several gamma-rays over an energy range spanning 95.88 – 5934.39 keV [38]. However, only the two highest-probability gamma-ray emission energies are used for thermal-neutron detection applications, as described by

$$ {}^{1}_{0}n + {}^{113}_{48}\mathrm{Cd} \rightarrow \gamma_1\left(0.558\ \mathrm{MeV}\right) + \gamma_2\left(0.651\ \mathrm{MeV}\right) + \gamma\text{'s}. \tag{2.8} $$

Due to the emission of a broad continuum of gamma-ray energies from the ^{113}Cd(n, γ)^{114}Cd reaction, discrimination of neutron-induced events from background gamma-ray events as well as electronic noise is difficult using ^{113}Cd-based neutron-conversion media. However, efforts have been made to develop thermal-neutron detectors relying on the ^{113}Cd(n, γ)^{114}Cd reaction, which are described in [67, 68]. More common, however, is the use of cadmium for radiation shielding purposes [9, 14, 69-71].

^{3}He is one of the most widely-used isotopes for thermal-neutron detection with a $\sigma_{a,th}$ of approximately 5318 b [60]. Charged-particles are emitted in opposite directions following the absorption of a thermal neutron by ^{3}He, with energies described by the ^{3}He(n, p)^{3}H reaction as

$$ {}^{1}_{0}n + {}^{3}_{2}\mathrm{He} \rightarrow {}^{3}_{1}\mathrm{H}\left(0.191\ \mathrm{MeV}\right) + {}^{1}_{1}\mathrm{H}\left(0.573\ \mathrm{MeV}\right). \tag{2.9} $$

The reaction Q-value, the amount of kinetic energy gained from the reaction [51], is 0.764 MeV. The boiling point of helium is 4.16 K [72] and, therefore, ^{3}He is used in the gaseous state as a neutron-conversion material. The performance of ^{3}He-based neutron detectors will be discussed later in Section 2.3.3.

^{10}B is often used as a neutron-conversion isotope with a $\sigma_{a,th}$ of approximately 3843 b [60] and a natural abundance of 19.9% [38]. The absorption of a slow neutron by ^{10}B produces charged-particles that are emitted in opposite directions, with energies defined by

$$ {}^{1}_{0}n + {}^{10}_{5}\mathrm{B} \rightarrow \begin{cases} {}^{7}_{3}\mathrm{Li}\left(1.015\ \mathrm{MeV}\right) + {}^{4}_{2}\mathrm{He}\left(1.777\ \mathrm{MeV}\right), & 6\% \\ {}^{7}_{3}\mathrm{Li}^{*}\left(0.840\ \mathrm{MeV}\right) + {}^{4}_{2}\mathrm{He}\left(1.470\ \mathrm{MeV}\right), & 94\% \end{cases}. \tag{2.10} $$

The Q-values of the 6% and 94% ^{10}B(n, α)^{7}Li reaction branches are 2.792 and 2.310 MeV, respectively. The discrepancy between the reaction Q-values occurs because the 94% reaction branch results in the emission of the ^{7}Li atom in its first excited state, which rapidly de-excites by releasing a 0.480 MeV gamma ray. ^{10}B can be used in both gaseous ($^{10}BF_3$) and solid forms (^{10}B, $^{10}B_4C$, ^{10}BN, $^{10}B_2O_3$, enriched boric acid (H_3BO_3)) depending on the application (although $^{10}BF_3$

is a highly-toxic gas [73]). Enriched boron (and boron-based compounds) can be purchased from a variety of vendors such as Ceradyne, Inc. [74], American Elements [75], and Sigma-Aldrich, Inc. [76]. The advantages, disadvantages, and performance of ^{10}B-based gas-filled, thin-film coated, and solid-state neutron detectors will be discussed in Section 2.3.

Lastly, ^{6}Li is often used as a neutron-conversion isotope, with a $\sigma_{a,th}$ of approximately 939 b [60] and a natural abundance of 7.59% [38]. Similar to the ^{3}He(n, p)^{3}H and ^{10}B(n, α)^{7}Li reactions, the ^{6}Li(n, α)^{3}H reaction also results in the emission of charged particles in opposite directions, with energies defined by

$$ {}^{1}_{0}n + {}^{6}_{3}\mathrm{Li} \rightarrow {}^{4}_{2}\mathrm{He}(2.050\ \mathrm{MeV}) + {}^{3}_{1}\mathrm{H}(2.730\ \mathrm{MeV}). \tag{2.11} $$

The Q-value of the ^{6}Li(n, α)^{3}H reaction is 4.78 MeV [59], which allows for sufficient discrimination of background and gamma-rays from neutron-induced events. Enriched ^{6}Li can be acquired from the Y-12 National Security Complex [46, 77] and Sigma-Aldrich [78]. The lithium-battery industry provides the infrastructure for ^{6}Li to be manufactured into foils of a specific thickness. Specifically, Albemarle (formerly Rockwood Lithium) [46, 79] can manufacture lithium foils of varying thicknesses. Given the chemical reactivity of lithium metal, resulting in a gradual degradation of the material, the chemically-stable compound ^{6}LiF is often used instead. Additionally, the mass density of ^{6}LiF is higher than that of ^{6}Li at 2.54 g cm^{-3} and 0.463 g cm^{-3}, respectively [59]. However, due to the increase in mass density, thinner layers of ^{6}LiF are often required, which are prone to flaking [46].

2.3 Common Thermal-Neutron Detectors

A variety of thermal-neutron detectors presently available to the commercial consumer and scientific-research community are discussed in the following section. The process of detecting thermal neutrons using commercially-available scintillators and thermoluminescent dosimeters (Section 2.3.1), thin-film-coated and solid-state semiconductors (Section 2.3.2), and gas-filled devices (Section 2.3.3) are also described.

2.3.1 Scintillator Neutron Detectors & Thermoluminescent Dosimeters

A variety of scintillator neutron detectors exist for thermal-neutron detection applications and are typically one of the following [18-20, 30, 80]: crystalline (LiI:Eu, CLYC, and CLLB), B- or Li-doped (plastic, glass, or liquid scintillators), or Li- and LiF-coated. The combination of ZnS(Ag) with a lithium compound is also a common scintillation-based thermal-neutron detection method. Charged-particle reaction products are emitted within the scintillating medium following the absorption of a neutron by either B or Li contained within the scintillator. Charge carriers are liberated as reaction products ionize the scintillating medium and the ensuing detection process follows the typical detection process of a scintillator. Consequently, separation of neutron-induced events from gamma-ray interactions can be a weakness among scintillator neutron detectors and often requires PSD techniques [19]. As with most scintillator radiation detectors, a photomultiplier tube (PMT) is commonly coupled to several of the aforementioned scintillator neutron detectors. PMTs are prone to being sensitive to magnetic fields and gain fluctuations, fragile, require high power, and are susceptible to dark current produced from thermionic emissions [19, 81]. Photodiodes are a rugged, low-power alternative to PMTs that are virtually insensitive to magnetic fields. However, photodiodes are sensitive to direct ionization and the capacitance is problematic, making them size limited while also having poor signal-to-noise ratio from leakage current and low-amplitude output signals [19]. Another alternative to PMTs are silicon photomultipliers (SiPMs) that are compact, require low operating voltage, and are significantly less sensitive to magnetic fields [82]. However, SiPMs are susceptible to fluctuation in performance due to changes in temperature and voltage [83]. SiPMs are also prone to crosstalk between individual cells as well as dark current [82, 83].

Thermoluminescent dosimeters (TLDs) are commonly used as integrating, passive neutron detectors [19]. As neutrons interact within a TLD, reaction products excite charge carriers in the form of electrons and holes to the conduction and valence bands, respectively. The charge carriers migrate randomly within their respective energy bands before being captured in trapping centers that are intentionally incorporated into the crystal structure using dopants. The charge carriers remain trapped until thermally liberated. The amount of energy deposited by the incident radiation integrated over the exposure period can be determined by thermally-liberating charge carriers from their trap sites through annealing methods. Measurable thermoluminescent photons are released as the charge carriers are captured at luminescent centers [84]. Although TLDs are primarily used for

gamma-ray measurements, a variety of TLDs exist for neutron detection as well. The most common are LiF-based TLDs that contain natural lithium (TLD-100), 95.6%-enriched ^{6}Li (TLD-600), or 99.93%-depleted ^{7}Li (TLD-700). LiF-based TLDs are frequently used for personnel dosimetry due to the tissue equivalence of LiF [19, 84]. The neutron and gamma-ray doses can be simultaneously determined by exposing a combination of a TLD-100 and a TLD-700, or a TLD-600 and a TLD-700, and calculating the difference in measured dose between the two [84]. Although power efficient and compact, the dose received from TLDs cannot be determined in real time. Additionally, TLDs suffer from gradual fading over time and the charge carriers can be inadvertently released from the trap centers if the ambient temperature of the environment surrounding the TLDs increases [18, 84]. The range of exposures is quite broad for LiF-based TLDs, however supralinearity occurs at high exposures [84].

2.3.2 Semiconductor Neutron Detectors

Two types of semiconductor neutron detectors exist in the form of solid-state devices and thin-film-coated devices. Solid-state semiconductor neutron detectors rely on the ionization of reaction products within the semiconductor bulk, which results in the liberation of charge carriers. The charge carriers then drift toward their respectively-charged electrodes under the influence of an electric field formed from the potential difference between the electrodes. Solid-state semiconductor neutron detectors are theoretically capable of high ε_{th} because the neutron-absorption medium is also the detection medium. However, fabrication of solid-state semiconductor neutron detectors has proven quite difficult [85]. Additionally, significant charge-carrier trapping also tends to occur resulting in low measured ε_{th} [85].

Thin-film-coated semiconductor neutron detectors consist of a thin layer of neutron-converting material deposited onto the surface of a semiconductor diode, as shown in Figure 2.4 [59, 86]. Reaction products are emitted in opposite directions following the absorption of a thermal or slow neutron within the converting layer. Due to the geometric limitations of thin-film-coated devices, only one reaction product can enter into the semiconductor diode (detection region of the device), thus limiting ^{10}B- and ^{6}LiF-based devices to a maximum ε_{th} of approximately 4.5% [59]. The neutron-absorption location combined with the reaction-product trajectories within the thin-film-coating layer results in a distribution of energies that are deposited within the detection region

(e.g. scenarios *a* and *c* of Figure 2.4). The converting-layer thickness is crucial; too thick of a layer results in reaction-product self-absorption (e.g. scenarios *b* and *d* of Figure 2.4) and insufficient neutron absorption occurs for too thin of a layer. Thin-film-coated semiconductor neutron detectors are compact, low cost, and require low power to operate [43, 77, 86]. However, due to their compact form-factor, several thin-film-coated semiconductor neutron detectors must be interconnected into an array in order to fabricate a device having a large effective area [27].

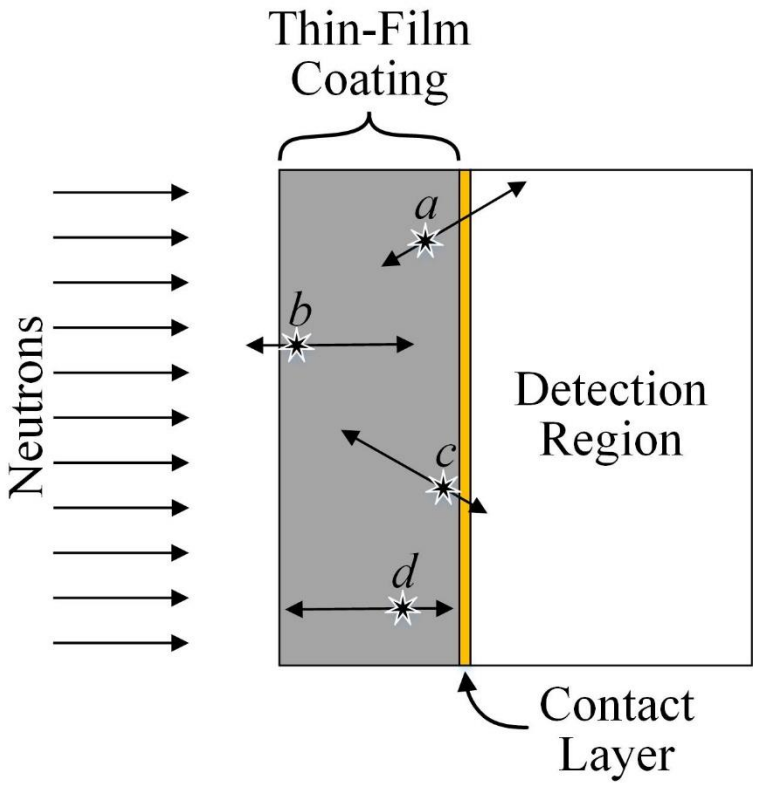

Figure 2.4. Examples of reaction-product trajectories based on the neutron-absorption location within the thin-film-coating layer. Scenarios a and c illustrate examples where one reaction-product can enter the detection region, while scenarios b and d depict examples of reaction-product self-absorption within the thin-film-coating layer.

In order to increase the ε_{th}, several thin-film-coated devices are typically combined [19, 59]. An alternative to combining several thin-film-coated devices is the MSND that consists of features, specifically trenches, etched into the semiconductor substrate, as illustrated in Figure 2.5 [27]. Conformal layers of *p*-type and *n*-type contacts are then deposited onto the surfaces of the etched semiconductor through diffusion processes to provide Schottky and ohmic contacts, respectively, prior to packing the trenches with neutron-converter material (typically ^{6}LiF) [27].

The geometry of the trenches allows for one or both reaction products to be measured within the adjacent fins, as depicted in Figure 2.5. The increased amount of neutron-converter material present in a MSND increases the ε_{th} by an order of magnitude over a single thin-film-coated semiconductor neutron detector. A measured ε_{th} of 53.54 ± 0.61% was recently reported for a dual-sided configuration of the MSND [43] and single-sided configurations have measured ε_{th} exceeding 35% [27]. The single- and dual-sided MSND configurations share many of the advantages of thin-film-coated semiconductor neutron detectors with the added improvement in ε_{th}. Unfortunately, MSNDs are also compact in size, thus requiring several MSNDs to be arrayed together to form a large effective-area device [27].

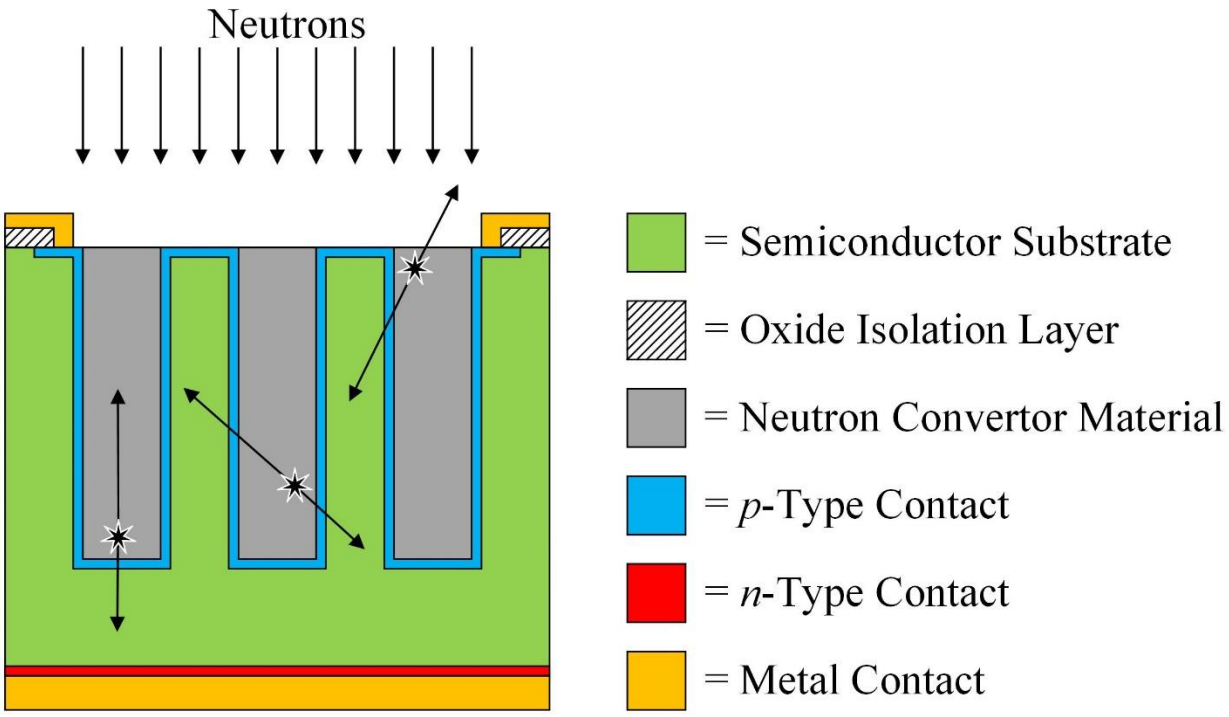

Figure 2.5. Cross-sectional schematic of a MSND showing that one or both reaction products can be measured within the fins adjacent to the trenches.

2.3.3 Gas-Filled Neutron Detectors

Gas-filled neutron detectors are frequently used for thermal-neutron detection applications, in which the gas functions as either: 1.) both the neutron converter and the proportional gas (e.g. ^{3}He or $^{10}BF_3$) or 2.) the proportional gas combined with a solid neutron converter (e.g. ^{10}B-lined). Both types of gas-filled proportional counters often feature a small-diameter anode wire (typically

25 – 100 μm in diameter) centered within a cylindrical housing. To avoid electrical discharge at the attachment points of the anode wire with the cylindrical housing, field tubes are used that result in inactive, "dead" regions near the anode-wire ends [87]. The field tubes reduce the electric field strength below the threshold necessary for Townsend avalanching [21, 87] (described in Section 3.3). Therefore, gas-filled proportional counters have two electric field regions, in which low electric field regions occur surrounding the field tubes and a high electric field region occurs within the detector volume where field tubes are not present. Finally, due to the presence of an anode wire centered within the cylindrical housing, proportional counter neutron detectors are susceptible to microphonic effects [88].

Gas-filled neutron detectors are often regarded as having desirable gamma-ray discrimination capabilities because the density of the gas is quite low relative to solid materials. However, when a gamma-ray interacts within a gas-filled neutron detector, Compton scattering can occur either within the gas or the cathode wall and the resulting Compton electron may produce a measurable pulse. If multiple gamma-ray interactions occur within the amplifier shaping time, pulse pile-up occurs resulting in a single, large-amplitude pulse relative to the amplitude of a pulse formed from an individual gamma-ray interaction. In this scenario, the resulting pulse amplitude may appear similar to a neutron-induced pulse and yield a false-positive result.

^{3}He proportional counters are capable of high ε_{th} and low sensitivity to gamma rays, and are among the most popular detectors used for thermal-neutron detection applications. ^{3}He proportional counters are capable of ε_{th} exceeding 80% [89] (depending on the detector volume and gas pressure) due, in part, to the combination of the $\sigma_{a,th}$ of ^{3}He and the gas functioning as both the neutron absorber and detector gas. However, the cost of ^{3}He-based devices is quite high due to the rarity of the isotope. Reaction products are emitted in opposite directions following the absorption of a slow or thermal neutron by the ^{3}He gas. Depending on the location of the ^{3}He(n, p)^{3}H reaction within the detector volume, the energy of one or both reaction products is deposited within the ^{3}He gas. As the reaction products ionize the ^{3}He gas, charge carriers are liberated that travel toward their respectively-charged electrodes due to the potential difference between the anode wire and the cathode wall.

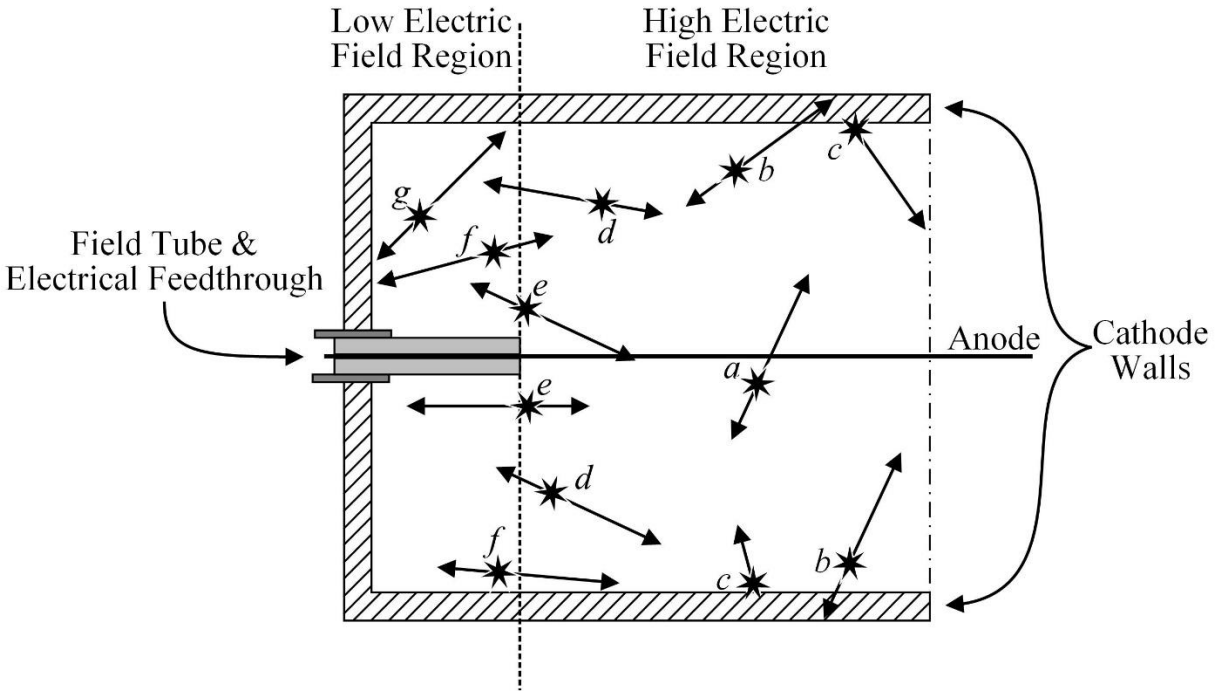

Figure 2.6. Examples of reaction-product trajectories in a gas-filled neutron detector. Scenario a illustrates an example of full kinetic energy deposition of both reaction-products within the high electric field region of the gas. Scenarios b and c depict examples of the wall effect that occur within the high electric field region. Scenarios d – g illustrate end effect examples where part or all of the kinetic energy of the reaction products is deposited within the low electric field region [After 21].

Illustrated in Figure 2.6 are examples of different reaction-product emission scenarios based on the location of the ^{3}He(n, p)^{3}H reaction within the detector volume. For neutron absorptions that occur within the high electric field region and a sufficient distance away from the cathode wall (thus preventing reaction products from colliding with the cathode wall), the full kinetic energy of both reaction products can be deposited within the gas (Figure 2.6, scenario *a*). The full-energy peak of the reaction-product pulse-height spectrum is formed with energy equal to the ^{3}He(n, p)^{3}H reaction Q-value of 0.764 MeV (shown in Figure 2.7). A portion of the kinetic energy of the reaction product can be deposited in the gas when neutron absorption occurs in close proximity to the cathode wall (Figure 2.6, scenario *b*). The residual kinetic energy of the reaction product is deposited within the cathode wall upon collision. The reduction in the total amount of reaction-product kinetic energy deposited within the high electric field region yields a smaller pulse amplitude relative to the full-energy deposition case (Figure 2.6, scenario *a*). The distribution

of pulse amplitudes resulting from partial energy deposition of one reaction product before collision with the cathode wall is called the *wall effect*.

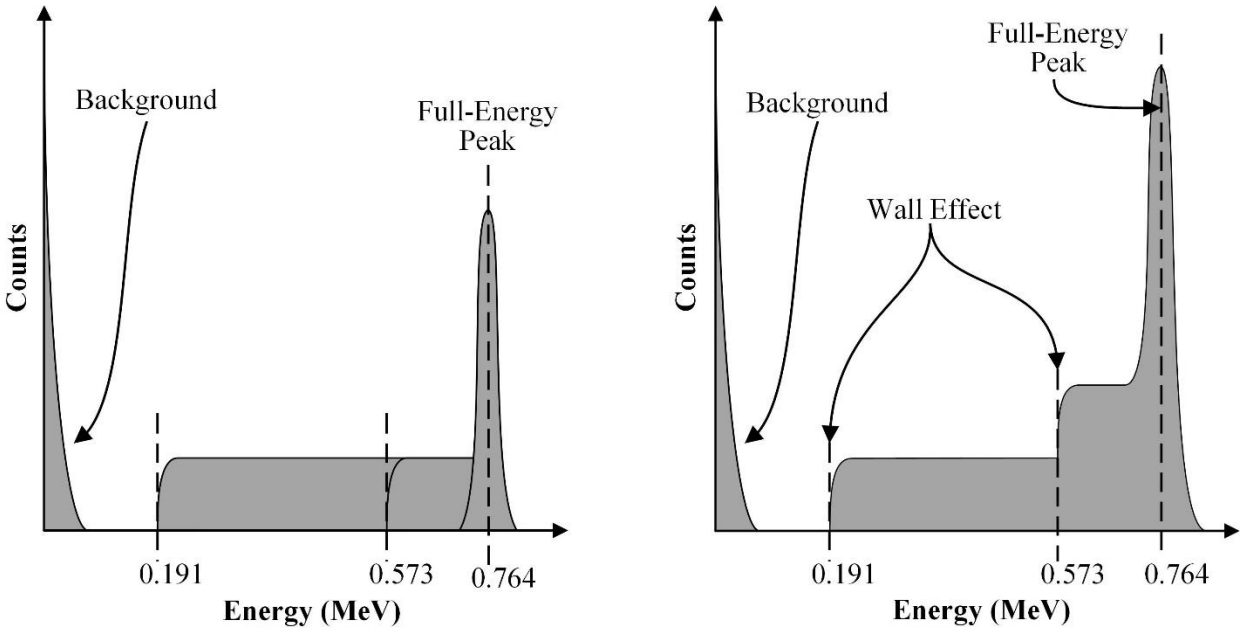

Figure 2.7. (left) Contributions of energy deposition from one or both reaction products within the high electric field region of the ^{3}He gas. The amount of energy deposited spans the energy range from the lower-energy reaction product (0.191 MeV triton) up to the ^{3}He(n, p)^{3}H reaction Q-value of 0.764 MeV. (right) Conceptual representation of a ^{3}He proportional counter reaction-product pulse-height spectrum. The wall-effect continuums overlap and, therefore, stack atop each other. The prominence of the wall effect is dependent on the size and pressure of the gas volume as well as the trajectories and creation site of the reaction products.

When neutron absorption occurs within the high electric field region and at the interface of the cathode wall and the detector gas, the kinetic energy of only one reaction product can be deposited within the gas while the entire kinetic energy of the other reaction product is deposited within the cathode wall (Figure 2.6, scenario *c*). Because the energy of only one reaction product is deposited within the gas, a discrete step feature appears in the reaction-product pulse-height spectrum. The discrete step represents the reaction-product kinetic energy deposited within the high electric field region (either 0.191 MeV or 0.573 MeV, depending on whether the kinetic energy of the triton or proton, respectively, is deposited within the detector volume). For situations when the full energy of one reaction product is deposited within the gas while only a portion of the energy of the other reaction product is deposited within the gas before colliding with the cathode wall (Figure 2.6, scenario *b*), a distribution of reaction-product kinetic energy is deposited

in the high electric field region. The amount of reaction-product kinetic energy deposited within the detector volume is dependent on the emission location of the reaction products, the reaction-product trajectories, the size of the detector volume, and the pressure of the gas. Due to the distribution of reaction-product energy deposited within the high electric field region, a continuum of energies occurs in the reaction-product pulse-height spectrum. The continuum of energies spans the energy range between the minimum energy (Figure 2.6, scenario *c*) and the full-energy peak (Figure 2.6, scenario *a*), as shown on the left of Figure 2.7. Because the continuums overlap beginning at an energy of 0.573 MeV, the higher energy continuum stacks atop the lower energy continuum, as depicted on the right of Figure 2.7. A *valley* occurs between the reaction-product pulse-height spectrum and the background radiation (and electronic noise) that appear in the low energy region. The valley provides the ability to set the lower level discriminator (LLD) in order to separate neutron-induced pulses from gamma rays and background events without significantly sacrificing ε_{th}.

The wall effect appears in the reaction-product pulse-height spectrum of a ^{3}He proportional counter regardless of the neutron environment surrounding the detector. However, a second effect, called the *end effect*, occurs when incident neutrons can interact within the regions of the detector where the field tubes are located. As stated previously, a low electric field region occurs surrounding the field tubes. Within the low electric field regions, the detector functions essentially as an ionization chamber and the resulting pulse amplitudes are lower than those produced within the high electric field region where Townsend avalanching occurs [21, 87]. Consequently, the lower-amplitude pulses appear in the lower energy channels of the pulse-height spectrum. The pulse formation process that occurs within ionization chambers and proportional counters, as well as discussion of Townsend avalanching, is provided in Ch. 3.

As depicted by scenario *d* of Figure 2.6, the end effect is produced for neutron absorptions occurring within the high electric field region near the ends of the anode wire where the field tubes are located [21]. The end effect occurs due to full energy deposition of one reaction product within the high electric field region and partial energy deposition from the other reaction product within the high electric field region before entering the low electric field region. The distribution of energy deposited within the high electric field region is similar to that depicted by scenario *b* of Figure 2.6. Neutron absorptions occurring along the border between the two electric field regions (Figure 2.6, scenario *e*) can result in the full energy of one reaction product being deposited in the high

electric field region while the full energy of the other reaction product is deposited in the low electric field region. For neutron absorptions occurring within the low electric field region, the kinetic energy of one (Figure 2.6, scenario *f*) or both (Figure 2.6, scenario *g*) reaction products can be deposited within the low electric field region. As depicted by scenario *f* of Figure 2.6, a portion of the kinetic energy of one reaction product can be deposited within the low electric field region before depositing the residual energy within the high electric field region. Thus, the amount of reaction-product kinetic energy deposited within the high electric field region of the detector volume ranges from zero up to the full energy of the reaction product, as illustrated on the left of Figure 2.8. The range of deposited energies is dependent on the emission location of the reaction products, the reaction product trajectories, the size of the detector volume, and the pressure of the gas. When the kinetic energy of both reaction products is deposited within the low electric field, as depicted by scenario *g* of Figure 2.6, the event is essentially lost.

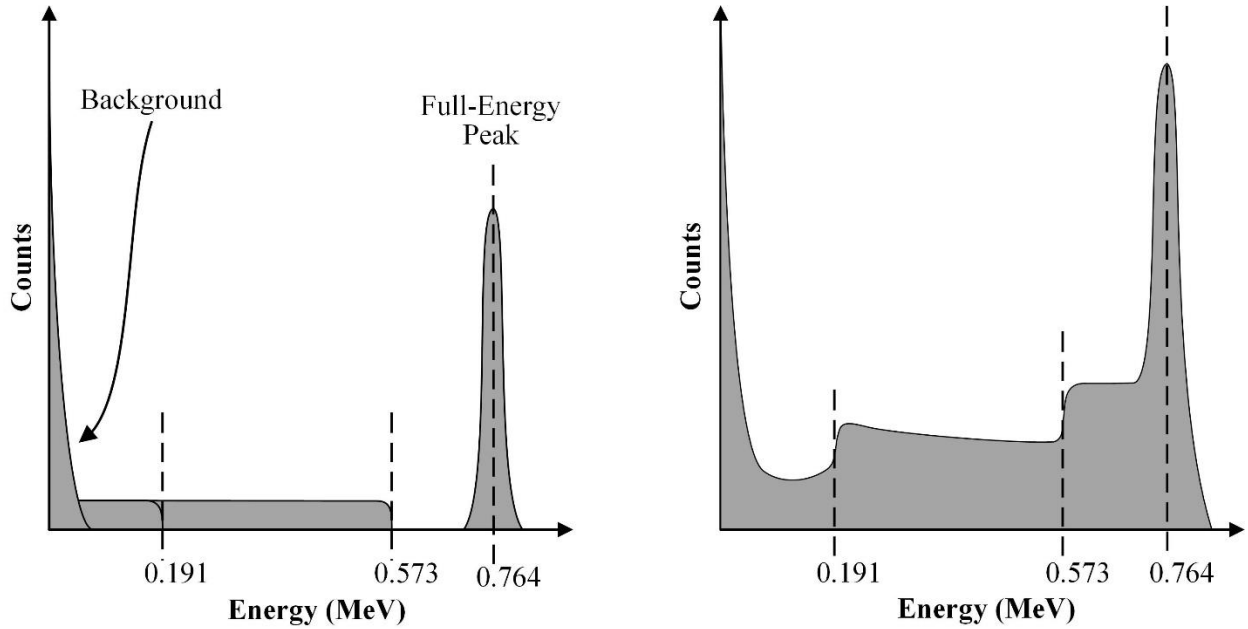

Figure 2.8. (left) Contributions of energy deposition from one or both reaction products within the low electric field region of the ^{3}He gas spanning the energy range from zero up to the full energy of either reaction product (either 0.191 MeV or 0.573 MeV corresponding to the triton and proton, respectively). (right) Conceptual representation of the reaction-product pulse-height spectrum with wall and end effects represented.

Shown on the right of Figure 2.8 is a conceptual representation of a ^{3}He reaction-product pulse-height spectrum with wall and end effects represented. The prominence of both effects, relative to the full energy peak, is dependent on the detector geometry. Thus, as detector length

increases, the ratio of the high electric field region to the low electric field region increases and the prominence of the end effect diminishes. Similarly, as the detector volume increases, the surface-to-volume ratio of the detector increases resulting in a decrease of the prominence of the wall effect [21].

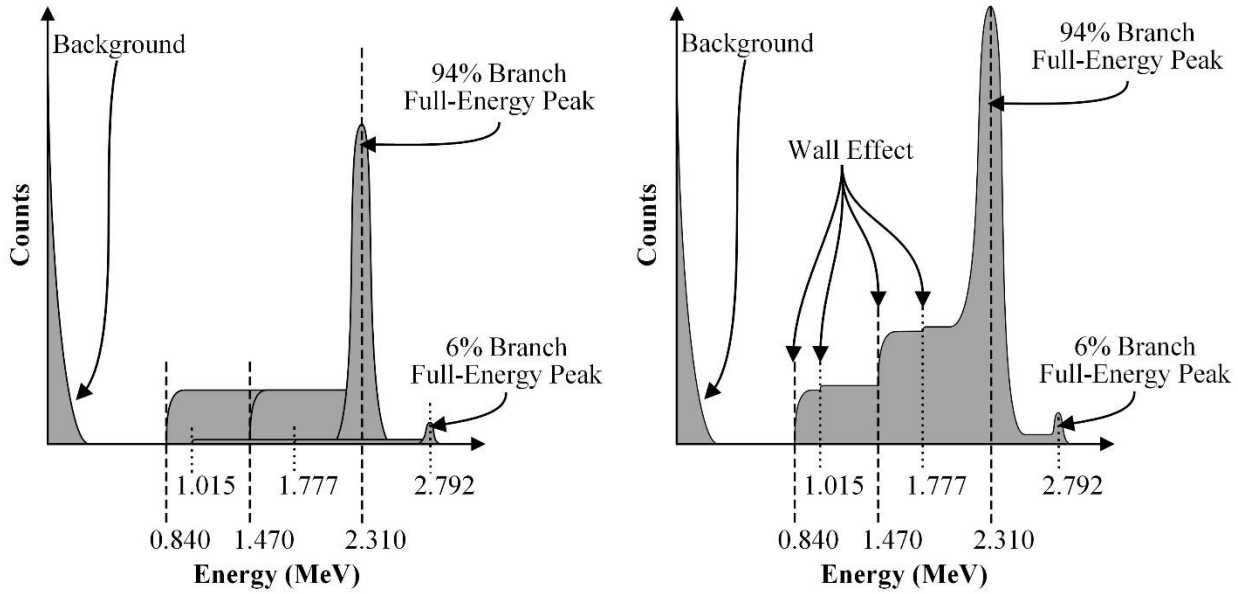

Figure 2.9. (left) Contributions of energy deposition from one or both reaction products within the high electric field region of the $^{10}BF_3$ gas from the 94% and 6% branches of the $^{10}B(n, \alpha)^7Li$ reaction. (right) Conceptual representation of a $^{10}BF_3$ proportional counter reaction-product pulse-height spectrum including the wall effect.

Similar to ^{3}He proportional counters, $^{10}BF_3$ proportional counters rely on the $^{10}BF_3$ gas as both the neutron converting material and the proportional gas. $^{10}BF_3$ proportional counters are typically operated with $^{10}BF_3$ gas pressures ranging from 0.2 to 2.0 atm [90] and the ε_{th} increases as the pressure is increased. The $^{10}BF_3$ gas pressure is limited due to the degradation in performance of $^{10}BF_3$ as a proportional gas at elevated pressures [90]. However, the diameter of $^{10}BF_3$ proportional counters can be increased in order to compensate for the pressure limitation [90]. Because the microscopic absorption cross section of ^{10}B is lower than that of ^{3}He, combined with the lower isotopic content of ^{10}B present in $^{10}BF_3$ relative to pure-^{3}He gas and the $^{10}BF_3$ gas pressure limitation, $^{10}BF_3$ proportional counters are a lower ε_{th} alternative to ^{3}He proportional counters. Illustrated in Figure 2.9 is a conceptual representation of the reaction-product pulse-height spectrum from a $^{10}BF_3$ proportional counter. The prominence of the wall effect features are

a function of the detector geometry and $^{10}BF_3$ gas pressure. Clear definition of the wall effect contributions from the 6% branch of the $^{10}B(n, \alpha)^7Li$ reaction is typically not possible due to the energy resolution of $^{10}BF_3$ proportional counters [21]. Although not shown in Figure 2.9, end effects can also appear in the reaction-product pulse height spectrum of a $^{10}BF_3$ proportional counter for scenarios when neutrons interact within the regions of the detector where the field tubes are located. A valley is also present in the reaction-product pulse-height spectrum from a $^{10}BF_3$ proportional counter. The valley occurs above background radiation and below the lowest-energy wall effect, allowing for sufficient LLD setting to discriminate background and gamma-rays from neutron-induced pulses. Thus, the gamma-ray discrimination capabilities of $^{10}BF_3$ proportional counters are similar to ^3He. Despite the lower cost of $^{10}BF_3$ relative to ^3He, the toxicity of $^{10}BF_3$ gas is a significant drawback compared to ^3He.

An alternative design to the $^{10}BF_3$ gas-filled proportional counter is the ^{10}B-lined proportional counter. ^{10}B-lined proportional counters are advantageous compared to $^{10}BF_3$ proportional counters because a more optimal proportional gas can be used instead of $^{10}BF_3$. The toxicity of $^{10}BF_3$ is also avoided when using a different proportional gas. However, ^{10}B-lined proportional counters are limited to a maximum ε_{th} of approximately 9% [90], which is significantly lower than that of ^3He and $^{10}BF_3$. Thermal-neutron absorption is a function of the thickness of the ^{10}B layer, much like thin-film-coated semiconductors. ^{10}B-lined proportional counters are fabricated by coating the interior of the cylindrical housing with a thin layer of ^{10}B (thickness of typically 1 – 3 μm [59]). The ^{10}B layer thickness should not exceed the maximum range of the highest energy reaction product from the 94% reaction branch, the 1.47 MeV alpha particle, or significant reaction-product self-absorption will occur within the ^{10}B layer. Because the interior surfaces of the cylindrical housing are coated with the ^{10}B, ^{10}B-lined proportional counters also suffer from the wall effect and only one reaction product is emitted into the proportional gas. Neutron absorptions occurring at the interface of the gas and ^{10}B coating result in the emission of one reaction product into the backfill gas. The full kinetic energy of one reaction product is deposited within the backfill gas and the kinetic energy of the other reaction product is deposited within the ^{10}B coating (and potentially the cathode wall for sufficiently-thin coatings). For neutron absorptions occurring within the ^{10}B coating, a portion of the kinetic energy of one reaction product is deposited within the ^{10}B coating before emerging from the coating to deposit the residual energy in the backfill gas. Self-absorption of both reaction products within the ^{10}B

coating may also occur, depending on the ^{10}B-coating thickness as well as the emission location and trajectories of the reaction products within the ^{10}B coating.

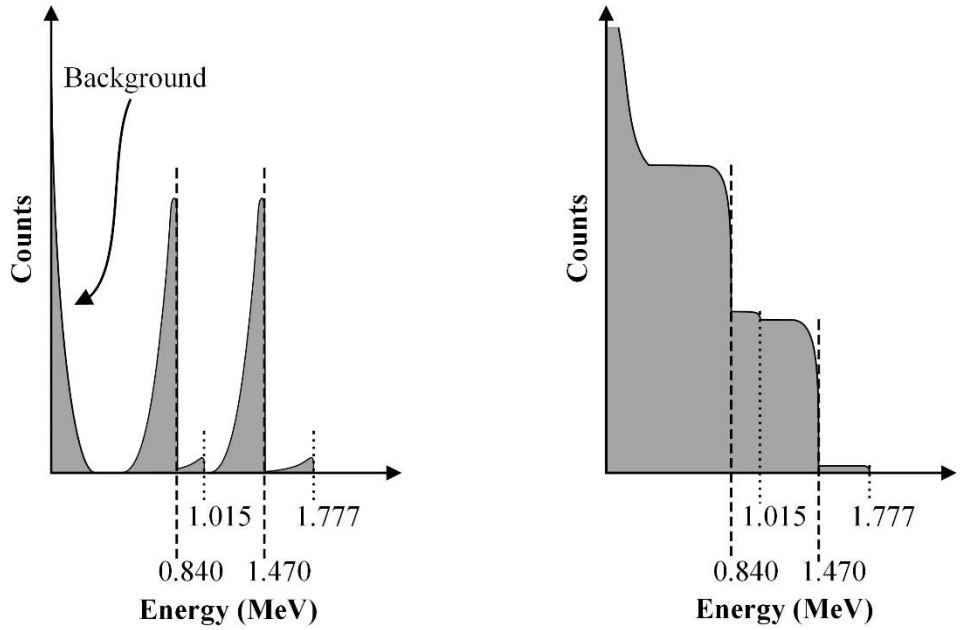

Figure 2.10. (left) Conceptual representation of a reaction-product pulse-height spectrum using a ^{10}B-lined proportional counter with a sufficiently thin ^{10}B coating that minimizes self-absorption effects. (right) Conceptual representation of a reaction-product pulse-height spectrum using a ^{10}B-lined proportional counter with a thick ^{10}B coating resulting in self-absorption effects.

For sufficiently-thin ^{10}B coatings, reaction-product self-absorption effects are minimized, yielding a reaction-product pulse-height spectrum with features similar to those shown on the left of Figure 2.10. As the thickness of the ^{10}B coating increases, the amount of self-absorption also increases. Based on the emission location and trajectories of the reaction products within the ^{10}B coating, a distribution of energies is deposited within the proportional gas, ranging from no energy up to the maximum energy that can be deposited from the 1.777 MeV alpha particle emitted from the interior surface of the ^{10}B layer (facing radially inward toward the anode wire). The reaction-product pulse-height spectrum has features similar to those shown on the right of Figure 2.10 where neutron events blend with electronic noise and gamma-ray events. Consequently, a valley does not exist in the reaction-product pulse-height spectrum that clearly and discretely separates neutron events from gamma-ray events and electronic noise. Thus, when setting a non-zero LLD to discriminate gamma-ray events from neutron events, neutron events that blend with gamma-ray events are also discriminated and the ε_{th} decreases accordingly.

2.4 Calculation of Intrinsic Thermal-Neutron Detection Efficiency (ε_{th})

The intrinsic thermal-neutron detection efficiency, ε_{th}, is commonly used as an evaluation criterion when comparing the neutron-detection performance of different neutron detectors and is defined as [19]

$$\varepsilon_{th} = \frac{\text{Number of incident neutrons counted}}{\text{Number of neutrons incident on detector}}. \tag{2.12}$$

Based on a typical neutron-detection process, the number of incident neutrons that are counted is dependent on the number of neutrons absorbed by the detector, the number of reaction products that ionize the sensitive volume of the detector, and the number of charge carriers that contribute to pulse formation within the detector. One method for calculating ε_{th} is by counting the number of neutrons emitted from a radioactive source, such as ^{252}Cf, as described by [71],

$$\varepsilon_{th} = \frac{\left(\frac{G_m}{t_{Gm}}\right)}{A \cdot BR \cdot \Omega_f}, \tag{2.13}$$

where G_m is the number of counts measured, t_{Gm} is the measurement time, A is the source activity at the time of the measurement, BR is the branching ratio of the radiation source, and Ω_f is the fractional solid angle between the source and the detector. The time-corrected source activity, $A(t)$ is defined as [51],

$$A(t) = A_0\, e^{-\lambda t}, \tag{2.14}$$

where A_0 is the assayed source activity, λ is the decay constant of the source, and t is the time that has elapsed between the time of measurement and assay date. The decay constant is defined by [51],

$$\lambda = \frac{\ln 2}{t_{1/2}}, \tag{2.15}$$

where $t_{1/2}$ is the half-life of the radioactive source. The fractional solid angle for a rectangular aperture detector is defined as [91],

$$\Omega_f = \frac{1}{\pi}\arctan\left[\frac{W \times L}{4 \times D \times \sqrt{\frac{W^2}{4} + \frac{L^2}{4} + D^2}}\right], \tag{2.16}$$

where *W* and *L* are the detector aperture width and length, respectively, and *D* is the distance separating the source from the detector.

ε_{th} can also be calculated by comparing the counting performance of the test detector to that of a calibrated, reference detector. The counting performance of each detector is commonly measured using a collimated, thermal-neutron beam with a constant flux, thus eliminating the source activity, *A*, and branching ratio, *BR*, terms shown in Eq. (2.13). Furthermore, the diameter of the thermal-neutron beam is constant for both detector measurements and is sufficiently small in order to ensure that neutrons are incident only on the sensitive volume of the detectors, thus eliminating the solid angle, Ω_f, term shown in Eq. (2.13). A ratio is established between the ε_{th} and the measured net count rate, *n*, for each detector as,

$$\frac{\varepsilon_{th,m}}{n_m} = \frac{\varepsilon_{th,r}}{n_r}, \tag{2.17}$$

where n_m and n_r are the measured net count rates using the test and reference detectors, respectively, and $\varepsilon_{th,m}$ and $\varepsilon_{th,r}$ are the measured intrinsic thermal-neutron detection efficiencies of the test and reference detectors, respectively. Rearranging Eq. (2.17) yields,

$$\varepsilon_{th,m} = \frac{n_m}{n_r}\varepsilon_{th,r}. \tag{2.18}$$

The net count rate is defined as the difference between the neutron-detection, *g*, and background, *b*, gross counts rates as,

$$n = g - b = \frac{G}{t_G} - \frac{B}{t_B}, \tag{2.19}$$

where *G* and *B* are the number of gross counts measured during the neutron-detection and background measurements, respectively, for the corresponding measurement times, t_G and t_B. Combining Eq. (2.18) and Eq. (2.19) yields,

$$\varepsilon_{th,m} = \frac{\left(\frac{G_m}{t_{Gm}} - \frac{B_m}{t_{Bm}}\right)}{\left(\frac{G_r}{t_{Gr}} - \frac{B_r}{t_{Br}}\right)}\varepsilon_{th,r}. \tag{2.20}$$

The error associated with $\varepsilon_{th,m}$ of the test detector, $\sigma_{\varepsilon th,m}$, is a function of the errors associated with G_m, B_m, G_r, B_r, and $\varepsilon_{th,r}$. The errors associated with the counting times can be assumed negligible due to the precision of modern counting and measurement equipment. Thus, $\sigma_{\varepsilon th,m}$ can be calculated by applying error propagation, yielding

$$\sigma_{\varepsilon th,m} = \sqrt{\left(\frac{\partial \varepsilon_{th,m}}{\partial G_m}\right)^2 \sigma_{Gm}^2 + \left(\frac{\partial \varepsilon_{th,m}}{\partial B_m}\right)^2 \sigma_{Bm}^2 + \left(\frac{\partial \varepsilon_{th,m}}{\partial G_r}\right)^2 \sigma_{Gr}^2 + \left(\frac{\partial \varepsilon_{th,m}}{\partial B_r}\right)^2 \sigma_{Br}^2 + \left(\frac{\partial \varepsilon_{th,m}}{\partial \varepsilon_{th,r}}\right)^2 \sigma_{\varepsilon th,r}^2}, \tag{2.21}$$

where σ_{Gm}, σ_{Bm}, σ_{Gr}, and σ_{Br} are the counting errors associated with G_m, B_m, G_r, and B_r, respectively. $\sigma_{\varepsilon th,r}$ is the error associated with the intrinsic thermal-neutron detection efficiency of the reference detector.

2.5 Calculation of Gamma-Ray Rejection Ratio (*GRR*)

A second evaluation criterion for thermal-neutron detectors is the ability for the detector to strictly measure neutrons without also detecting gamma rays. Thus, the gamma-ray sensitivity of the neutron detector is typically measured. One method for assessing the gamma-ray sensitivity of a neutron detector is to measure the intrinsic response of the neutron detector to the presence of a gamma-ray field without a neutron source present. The measurement of the intrinsic gamma-ray response indicates the neutron-to-gamma ray separation. Recently, this intrinsic response has been referred to as the gamma-ray rejection ratio (*GRR*) [91]. The *GRR* is typically assessed by measuring the detector response to a ^{60}Co exposure rate of 10 mR hr^{-1} using the following

$$GRR = \frac{\left(\frac{G_\gamma}{t_{G\gamma}}\right) - \left(\frac{B}{t_B}\right)}{A \cdot BR \cdot \Omega_f}, \tag{2.22}$$

where G_γ and B are the number of gross counts measured from the gamma-ray source and background measurements, respectively, for the corresponding measurement times, $t_{G\gamma}$ and t_B. As will be presented in Section 6.4.2, a ^{137}Cs exposure rate of 50 mR hr^{-1} was used when conducting *GRR* testing of SFMNDs. The 50 mR hr^{-1} ^{137}Cs exposure rate was used because a ^{60}Co source capable of a 10 mR hr^{-1} exposure rate was not available. The elevated exposure rate was selected to compensate for the lower-energy gamma rays emitted from ^{137}Cs relative to ^{60}Co. The error associated with the measurement of *GRR*, σ_{GRR}, is also calculated by applying error propagation as,

$$\sigma_{GRR} = \sqrt{\left(\frac{\partial GRR}{\partial G_\gamma}\right)^2 \sigma_{G\gamma}^2 + \left(\frac{\partial GRR}{\partial B}\right)^2 \sigma_B^2}, \tag{2.23}$$

based on the counting errors of the gamma-ray source and background measurements, $\sigma_{G\gamma}$ and σ_B, respectively.

CHAPTER 3
GAS-FILLED RADIATION DETECTOR THEORETICAL CONSIDERATIONS

It would be possible to describe everything scientifically,
but it would make no sense; it would be without meaning, as if you
described a Beethoven symphony as a variation of wave pressure.

Albert Einstein

Presented in this chapter are the underlying theoretical considerations pertaining to the operation of gas-filled radiation detectors. The general radiation detection process using a gas-filled device is addressed first (Section 3.1) before discussing properties of charged particles in gas-filled media (Section 3.2). Production of charge carriers, their properties, and their interaction phenomena are then described (Section 3.3). The operating properties of gas-filled radiation detectors are then presented followed by descriptions of ionization chambers, Frisch grids, proportional counters, and microstrip electrodes (Section 3.4).

3.1 General Detection Process Using a Gas-Filled Device

Gas-filled neutron detectors rely on either the gas or a solid medium as the neutron converter. Although the neutron-interaction phenomena have already been discussed, the remaining mechanisms that occur during the detection process need to be addressed as well. Consider the situation illustrated in Figure 3.1 depicting an *anode*, the collecting electrode, and a *cathode* positioned in a parallel-plate orientation and surrounded by gas. An alpha particle is shown incident on the *sensitive volume* (gray-shaded region in Figure 3.1), which is defined as the electrically-active volume contained between the electrodes. The electrodes are separated by a distance d and the x-axis of the electrode configuration is perpendicular to the electrodes with the origin located at the cathode. A positive voltage is applied to the anode, V_A, and the cathode is

maintained at ground potential. Assuming the absence of space charge, Poisson's equation reduces to Laplace's equation and the electrostatic field within the sensitive volume is defined as [92]

$$\nabla^2 V(\mathbf{r}) = 0, \tag{3.1}$$

and for a one-dimensional treatment in the *x*-direction as

$$\nabla^2 V(x) = \frac{d^2 V(x)}{dx^2} = 0. \tag{3.2}$$

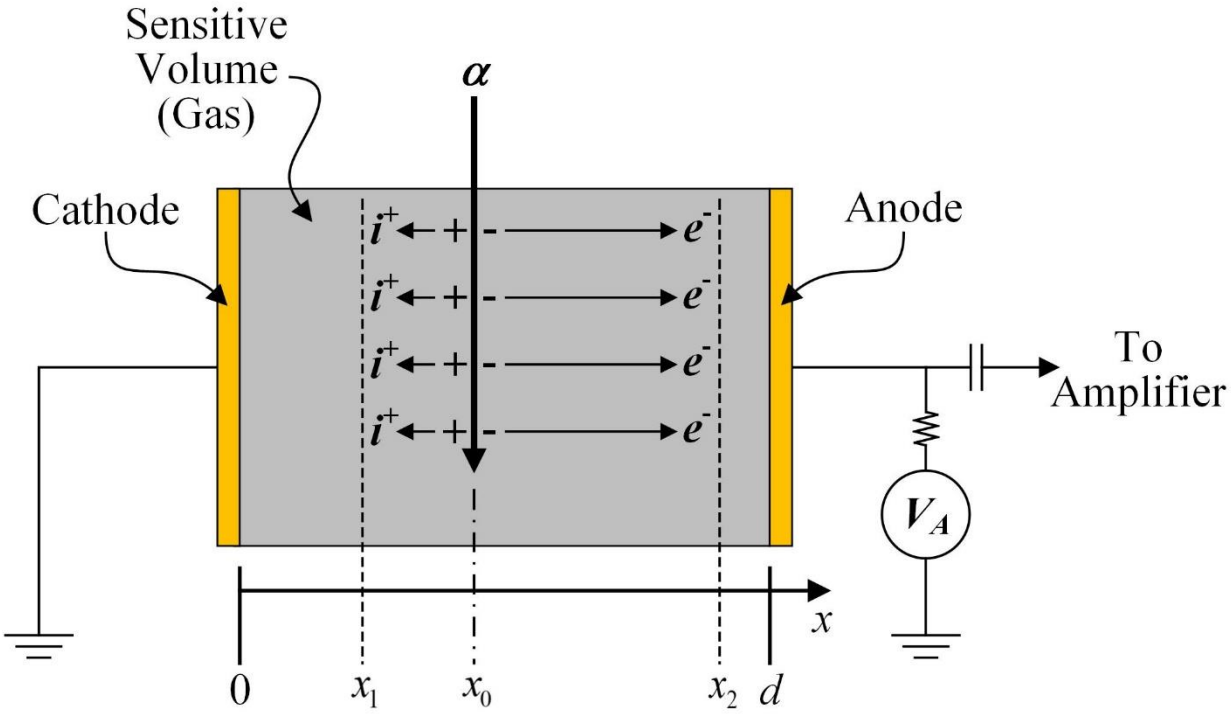

Figure 3.1. General depiction of the liberation of electrons (e^-) and positively-charged ions (i^+) as an alpha particle ionizes the gas between parallel-plate electrodes.

Integrating Eq. (3.2) twice and applying the boundary conditions $V(0) = 0$ and $V(d) = V_A$ yields integration constants of $C_1 = \frac{V_A}{d}$ and $C_2 = 0$. Thus, the potential distribution between the electrodes is defined by

$$V(x) = \frac{V_A}{d} x . \tag{3.3}$$

The electric field, $\vec{E}$, formed between the electrodes is defined by the gradient of the scalar potential, *V*, as [92]

$$\vec{E} = -\vec{\nabla} V . \tag{3.4}$$

As the alpha particle traverses the gas within the sensitive volume, charge carriers in the form of electrons and positively-charged ions are liberated through Coulombic interactions. The electrons, with charge *–q*, drift toward the anode and the positively-charged ions, with charge *q*, drift toward the cathode. The charge carriers drift toward their respectively-charged electrodes due to the force, $\vec{F}$, acting on the charges in the presence of the electric field, as defined by [92]

$$\vec{F} = q\vec{E} . \tag{3.5}$$

The motion of the charge carriers results in the flow of current in an external circuit due to *induction*. Thus, charge is induced on the collecting electrode as the charge carriers drift toward their respectively-charged electrodes.

The amount of charge induced can be calculated using *Green's reciprocation theorem*. Consider an isolated system of conductors called $a, b, \ldots$, in which charges $Q_a, Q_b, \ldots$, are placed on the conductors to produce the set of potentials $V_a, V_b, \ldots$. If these charges are replaced by different charges $Q'_a, Q'_b, \ldots$, that produce a different set of potentials $V'_a, V'_b, \ldots$, Green's reciprocation theorem states that the old charges and potentials are related to the new charges and potentials by [2, 57]

$$\sum_i Q_i V'_i = \sum_i Q'_i V_i . \tag{3.6}$$

Table 3.1. Green's reciprocation theorem conditions for analyzing charge induction in a parallel-plate gas-filled radiation detector.

	Condition 1			**Condition 2**		
Electrode	*c*	*a*	*m*	*c*	*a*	*m*
Charge	Q_c	Q_a	Q_0	Q_c'	Q_0	0
Potential	0	0	V_0	V_c'	V_a'	V_0'

Using Green's reciprocation theorem, the induced charge for a parallel-plate electrode setup is determined by applying the two sets of conditions listed in Table 3.1. In Condition 1, a charge Q_0 is placed on an indefinitely small electrode (electrode *m*) between the cathode and anode (electrodes *c* and *a*, respectively, in Table 3.1). As a result, electrodes *c* and *a* have induced charges of Q_c and Q_a, respectively, and the potentials on both electrodes are zero. In Condition 2, the charge Q_0 is removed from electrode *m* and placed on electrode *a*. Applying Eq. (3.6) to the described scenario yields

$$Q_c V_c' + Q_a V_a' + Q_m V_m' = Q_c' V_c + Q_a' V_a + Q_m' V_m, \tag{3.7}$$

which, upon application of Conditions 1 and 2, reduces to

$$Q_c V_c' + Q_a V_a' + Q_0 V_0' = 0. \tag{3.8}$$

Based on the assumption that the anode and cathode completely enclose electrode *m*, all of the lines of force from Q_0 end on either the anode or cathode, and thus [57]

$$Q_c + Q_a = -Q_0. \tag{3.9}$$

Combining Eq. (3.8) and Eq. (3.9) and solving yields the induced charges from Condition 1 as

$$Q_c = -Q_0 \frac{V_0' - V_a'}{V_c' - V_a'} \tag{3.10}$$

and

$$Q_a = -Q_0 \frac{V_c' - V_0'}{V_c' - V_a'}. \tag{3.11}$$

Using Eq. (3.10) and Eq. (3.11), the change in induced charge on either electrode can be calculated for the situation where the charge Q_0 is moved to a separate and new location. At the new location, the potential on electrode *m* is now V_n', resulting in the change in induced charge on the anode and cathode, respectively, of

$$\Delta Q_c = \left(-Q_0 \frac{V_n' - V_a'}{V_c' - V_a'} \right) - \left(-Q_0 \frac{V_0' - V_a'}{V_c' - V_c'} \right) = -Q_0 \frac{V_n' - V_0'}{V_c' - V_a'} = Q_0 \frac{V_0' - V_n'}{V_c' - V_a'} \tag{3.12}$$

and

$$\Delta Q_a = \left(-Q_0 \frac{V_c' - V_n'}{V_c' - V_a'} \right) - \left(-Q_0 \frac{V_c' - V_0'}{V_c' - V_a'} \right) = Q_0 \frac{V_n' - V_0'}{V_c' - V_a'} = -Q_0 \frac{V_0' - V_n'}{V_c' - V_a'}. \tag{3.13}$$

The results of Eq. (3.12) and Eq. (3.13) indicate that the change in induced charge on the anode is equal and opposite relative to the change on the cathode.

Recalling the scenario depicted in Figure 3.1, assume electrons drift toward the anode in the positive *x*-direction to position x_2 with potential $V'(x_2) = V_2'$ and positively-charged ions drift toward the cathode in the negative *x*-direction to position x_1 with potential $V'(x_1) = V_1'$. The change in induced charge on the anode, ΔQ_A, is [21]

$$\Delta Q_A = -Q_0 \frac{V_0' - V_2'}{V_c' - V_a'}\bigg|_{electrons} + Q_0 \frac{V_0' - V_1'}{V_c' - V_a'}\bigg|_{ions}. \tag{3.14}$$

When a unit negative charge is placed on the anode, resulting in a potential $-V_0$, the potential profile is defined using Eq. (3.3) as

$$V(x) = \frac{-V_0}{d} x. \tag{3.15}$$

Using Eq. (3.15), the normalized potential difference within the device is calculated as

$$\frac{V(x_2)}{-V_0} - \frac{V(x_1)}{-V_0} = \frac{x_2}{d} - \frac{x_1}{d} = \frac{x_2 - x_1}{d}, \tag{3.16}$$

and indicates that the potential difference between the electrodes is equal to the displaced distance divided by the distance separating the electrodes. Applying Eq. (3.16), the electron and positively-charged ion components shown in Eq. (3.14) become

$$-Q_0 \left.\frac{V_0' - V_2'}{V_c' - V_a'}\right|_{electrons} = -Q_0 \frac{x_0 - x_2}{d} \tag{3.17}$$

and

$$Q_0 \left.\frac{V_0' - V_1'}{V_c' - V_a'}\right|_{ions} = Q_0 \frac{x_0 - x_1}{d}. \tag{3.18}$$

Substitution of Eq. (3.17) and Eq. (3.18) into Eq. (3.14) yields the change in induced charge on the anode as

$$\Delta Q_A = -Q_0 \left.\frac{x_0 - x_2}{d}\right|_{electrons} + Q_0 \left.\frac{x_0 - x_1}{d}\right|_{ions} = Q_0 \frac{-x_0 - x_1 + x_0 + x_2}{d} = Q_0 \frac{x_2 - x_1}{d}. \tag{3.19}$$

A similar approach can be taken to calculate the change in induced charge on the anode when space charge is present between the anode and cathode. The result of such analysis is identical to

Eq. (3.19) and indicates that space charge has no effect on the change in induced charge attributed to the mobile charge [21]. Additional discussion of charge induction as well as the underlying theory are provided in the literature [2, 21, 57, 92-94].

The induced current resulting from the motion of charge carriers can be measured directly or stored in a capacitor. In the former case, the detector is operated in *current mode*, which is typically used in high radiation fields and provides a relative measure of the radiation environment. Due to the frequency of radiation interactions, individual radiation interactions often cannot be resolved [57]. The amount of induced current can be very small and difficult to measure when current mode is used under low irradiation conditions [21]. Under such conditions, the detector is operated in *pulse mode*, which requires that the induced current be stored in a capacitor and the resulting voltage measured across the capacitor. Pulse mode operation allows for counting of individual radiation interactions and is used for low radiation fields. When pulse mode operation is used in high radiation fields, *pulse pile up* can occur when a radiation interaction occurs while the capacitor is integrating or discharging the induced current from a previous radiation interaction. Significant detector *dead time*, the duration of time when the detector is insensitive to radiation interactions, can occur when pulse mode operation is used in a high radiation field, yielding inaccurate measurement results [21].

In order to adequately describe pulse mode operation, the definition of capacitance must be provided. Thus, the capacitance, C, of a parallel-plate electrode configuration is defined as [21]

$$C = \left| \frac{Q}{\Delta V} \right|, \tag{3.20}$$

based on the charge magnitude, Q, on either electrode and the magnitude of the potential difference, ΔV, between the electrodes. Rearranging Eq. (3.20), the voltage measured across the capacitor, V, is determined by the ratio of the charge stored in the capacitor, Q, to the capacitance, C, as

$$V = \frac{Q}{C} \ . \tag{3.21}$$

A relatively long duration of time is required for the positively-charged ions to fully induce charge due to their slow velocity relative to electrons (discussed in Section 3.3). The time response of the detector can be reduced by connecting an *RC* circuit [21, 87], however the capacitor typically discharges before all of the positively-charged ions are collected.

3.2 Heavy Charged-Particle Properties in Gas-Filled Media

Heavy charged particles are defined as particles with rest masses greater than or equal to the mass of a proton [21]. The mass of a heavy charged particle is on the order of at least 10^3 times larger than the mass of an electron. Due to the sizeable mass difference, heavy charged particles travel almost entirely in a straight line and negligible deflection occurs along the path of travel [95]. Rarely, deflection occurs due to nuclear elastic scattering, typically after most of the kinetic energy of the particle is lost [21, 95]. As a heavy charged particle traverses a gaseous medium, the kinetic energy of the particle is reduced almost entirely through a series of Coulombic interactions. The Coulombic interactions predominantly occur in the form of inelastic collisions with bound atomic electrons[1] resulting in the transition of one or more atomic electrons to an excited state (*excitation*) or an unbound state (*ionization*) [95]. Excitation occurs when the energy transferred to an atom or molecule of the surrounding media is less than the minimum ionization energy, I_0 [21]. Upon transitioning to the excited state, the atomic electron decays from the excited state resulting in the emission of conversion electrons and/or gamma rays [58]. Ionization occurs when the energy transferred to atomic electrons from Coulombic interactions is greater than I_0 resulting in the liberation of separate charge carriers [21].

[1] Heavy charged particles can also interact with the surrounding medium by other means that are described in detail in the literature [95].

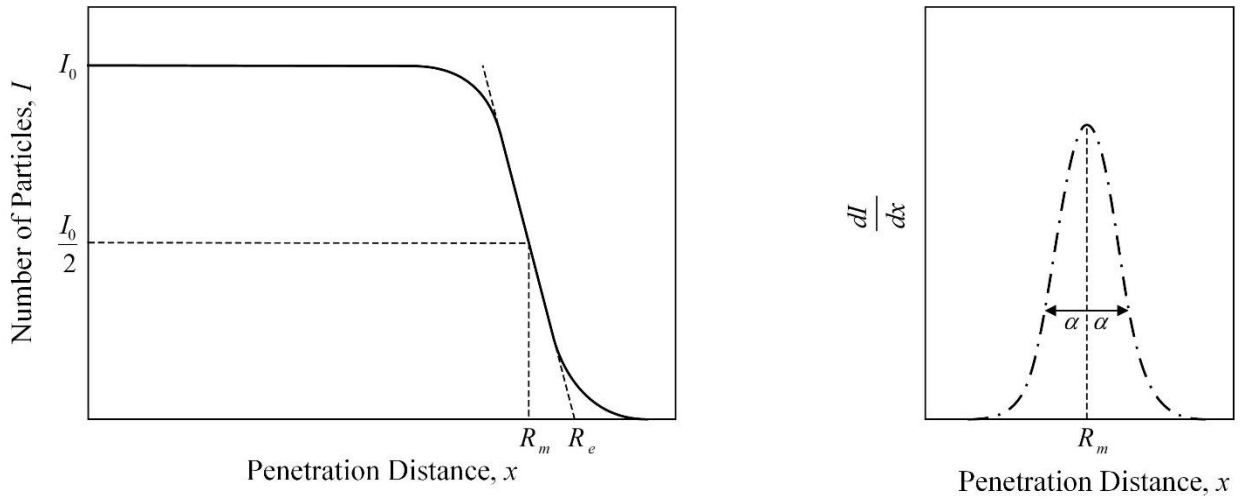

Figure 3.2. (left) Population of heavy charged particles as a function of penetration distance with the mean and extrapolated ranges, R_m and R_e, respectively, identified. (right) Gaussian distribution of heavy charged particle ranges about the mean range due to range-straggling effects. The range-straggling parameter, α, is defined based on the standard deviation, σ_R, about the mean range, R_m.

Initially, a heavy charged particle has a nuclear charge *qz* (where *z* is +2 for alpha particles, +1 for protons, etc.). However, exchange of electrons between the particle and the surrounding gas occurs (although loss of charge is more typical). When considering a beam of heavy charged particles with identical initial charge, the exchange of electrons as the particles traverse the gas results in an average charge that is smaller than the nuclear charge of the particle [95]. The frequency of the exchange of electrons increases as the particle velocity reduces near the end of its *range* [95], the maximum distance traveled by the particle before being stopped [21]. However, a beam of heavy charged particles of equal mass and initial kinetic energy traveling in a straight line will not have identical ranges. Shown on the left of Figure 3.2 is a conceptual representation of the distribution of particle ranges attributed to a beam of heavy charged particles of equal mass and initial kinetic energy traveling in a straight line. A Gaussian distribution of ranges appears about the *mean range*, R_m, the range when the beam intensity is halved [21, 95]. The Gaussian distribution occurs due to the stochastic nature of particle interactions as well as the potential for elastic nuclear scattering after most of the kinetic energy of the particle is lost, an effect called *range straggling* [21, 95]. Due to the approximately linear slope of the curve about the location of R_m, the *extrapolated range*, R_e, is defined by drawing the tangent to the curve at the point of

inflection about R_m and extrapolating the tangent to the *x*-axis [21]. As shown on the right of Figure 3.2, the distribution of range straggling is defined using the *range-straggling parameter*, α, which is a function of the *standard deviation about the mean range*, σ_R [95]. *Energy straggling* also occurs and is defined as the distribution of particle energies after the particles have traveled a given distance within the gas [95]. The distribution occurs due to fluctuations in the amount of particle energy lost based on the average number of Coulombic interactions that particles experience as a function of distance [95].

The amount of energy lost by a heavy charged particle from Coulombic interactions as a function of distance traveled within the gas is the *stopping power*, *S*, as represented by [58]

$$S = -\frac{dE}{dx}. \tag{3.22}$$

More specifically, the *Bethe-Bloch formula* defines the average amount of energy lost[1] per unit distance traveled by heavy charged particles with velocity, *v*, and charge, *z*, as [95]

$$-\frac{dE}{dx} = \frac{4\pi q^4 z^2}{m_0 v^2} N Z \left[\ln \frac{2 m_0 v^2}{I} - \ln\left(1 - \frac{v^2}{c^2}\right) - \frac{v^2}{c^2} \right], \tag{3.23}$$

where *q* and m_0 are the electron charge and rest mass, respectively, *c* is the speed of light, and *Z* is the atomic number of the absorber medium. The atomic density of the absorber medium, *N*, is a function of the density, ρ, of the absorber medium. The average ionization and excitation potential of the absorber medium, *I*, is a constant that cannot be calculated accurately from first principles and must be determined experimentally [95]. Eq. (3.23) is valid only if the particle energy is small enough that polarization of the medium is unimportant, *qz* remains constant and is not too large to strongly violate the Born approximation, and *v* greatly exceeds the speed of any atomic electron [95].

[1] From ionization and excitation.

The *specific ionization* is defined as the number of electron-ion pairs liberated per unit path length from a heavy charged particle traversing a gas and can be graphically represented by a *specific ionization curve* [95]. However, the specific ionization curve represents the Coulombic interactions experienced by an individual particle and, thus, does not account for straggling effects. A *Bragg ionization curve* is often used to depict the average specific ionization of a group of particles relative to the distance traveled by the particles [95]. Straggling effects appear in a Bragg ionization curve and are represented by a curved tail beyond the mean range [95]. Ziegler and Biersack developed a computational tool often used to determine the Bragg ionization curve of a specific particle type and energy traversing a given medium that also accounts for straggling effects known as *SRIM/TRIM* (*Stopping and Range of Ions in Matter*/*Transport of Ions in Matter*) [96]. Using *SRIM/TRIM* [96], the Bragg ionization curves and mean range of ions as a function of ion type, ion energy, and gas density are investigated based on the terms shown in Eq. (3.23). Different ion types (^{3}H, ^{4}He, and ^{7}Li) of equal initial energy (5 MeV) are considered within the same pressure of argon (Ar) gas. Next, different Ar gas pressures (1 – 5 atm in 1 atm increments), corresponding to different gas densities, for equal initial energy ^{4}He ions (5 MeV) are explored. Finally, different initial energies of ^{4}He ions (1 – 5 MeV in 1 MeV increments) within the same pressure of Ar gas (1 atm) are studied. In each scenario, the ions begin with their nuclear charge (qz = +1 for ^{3}H and ^{7}Li, qz = +2 for ^{4}He). Bragg ionization curves for each scenario are shown in Figure 3.3, Figure 3.4, and Figure 3.5, respectively, and correspond to the left ordinate of each figure with units of MeV/mm. The particle energy as a function of ion penetration distance is also shown in each of the figures and corresponds to the right ordinate with units of MeV. The mean ranges for each scenario are listed in Table 3.2.

Table 3.2. Summary of the ranges of different ion types with initial energy of 5 MeV traversing Ar gas pressurized to 1 atm (left column), 5 MeV ^{4}He ions traversing various pressures of Ar gas (center column), and different energies of ^{4}He ions traversing 1 atm of Ar gas (right column).

Ion Type		**Ar Gas Pressure**		**Alpha-Particle Energy**	
Ion	**Range (mm)**	**Pressure (atm)**	**Range (mm)**	**Energy (MeV)**	**Range (mm)**
^{3}H	164.11	1	36.35	5	36.35
^{4}He	36.35	2	18.17	4	26.40
^{7}Li	15.68	3	12.12	3	17.89
		4	9.09	2	10.87
		5	7.27	1	5.41

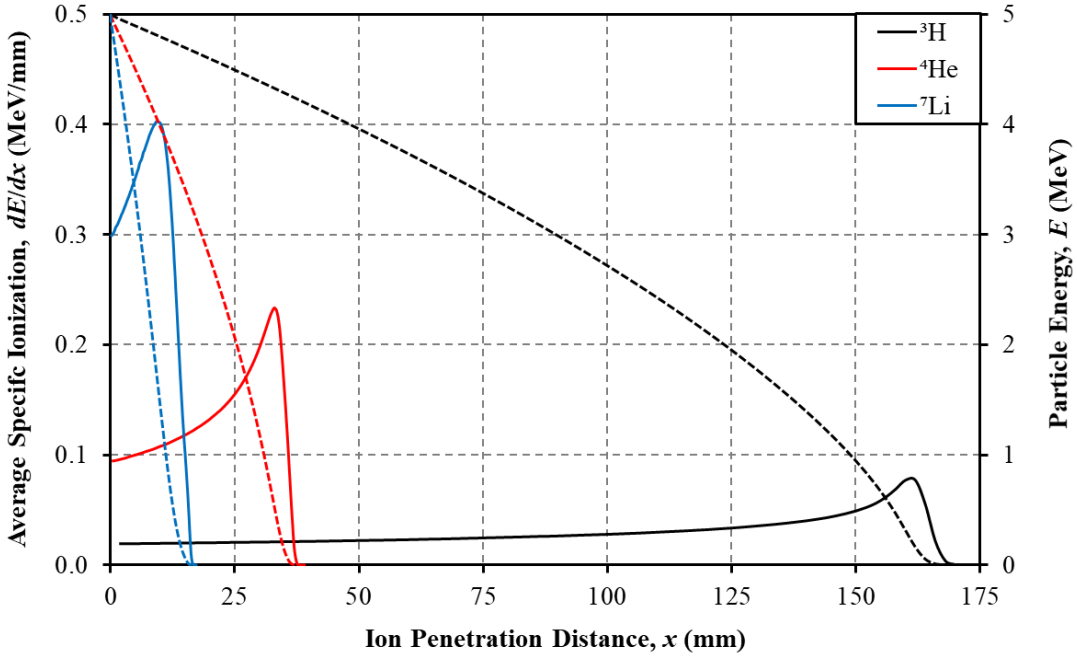

Figure 3.3. The solid lines, corresponding to the left ordinate, represent the Bragg ionization curves of 5 MeV ^{3}H, ^{4}He, and ^{7}Li ions in 1 atm of Ar gas. The dashed lines correspond to the right ordinate and represent the particle energy as a function of ion penetration distance.

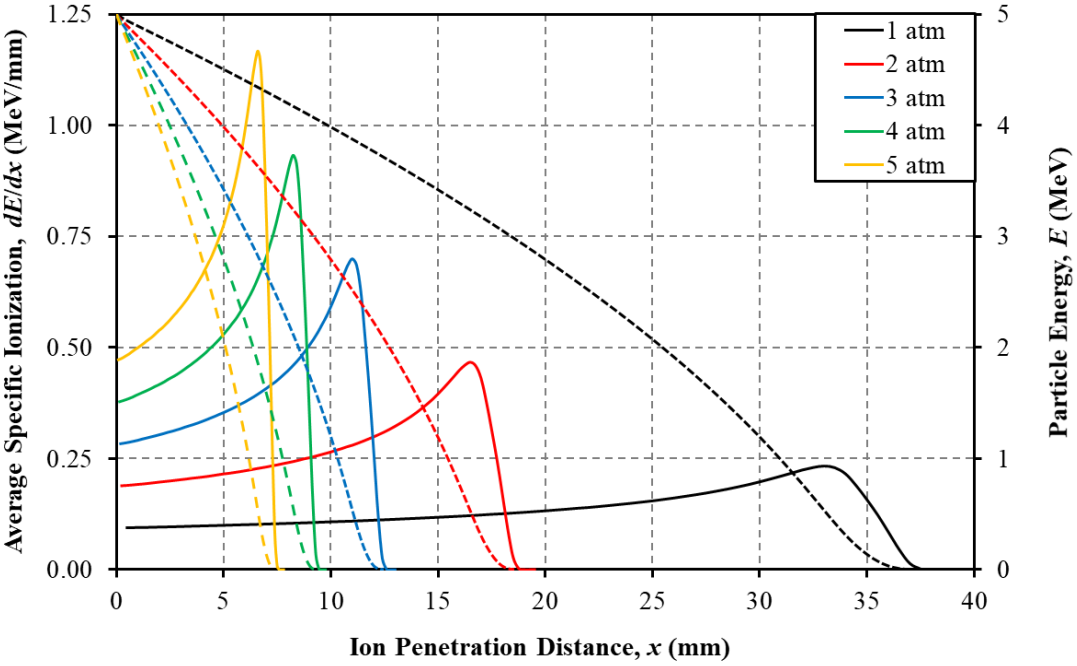

Figure 3.4. The Bragg ionization curves, represented by solid lines and corresponding to the left ordinate, of 5 MeV ^{4}He ions in Ar gas with pressures ranging from 1 to 5 atm. The energy of the ^{4}He ions as a function of penetration distance is denoted by the dashed line for each gas pressure and corresponds to the right ordinate.

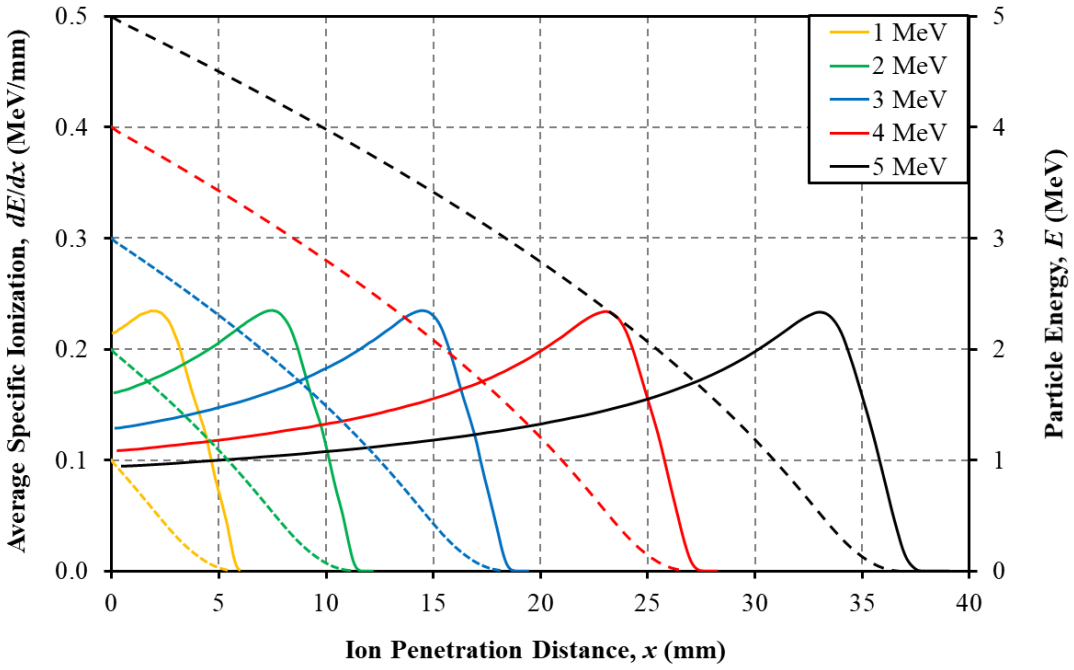

Figure 3.5. The solid lines correspond to the left ordinate and represent the Bragg ionization curves of ^{4}He ions with discrete initial energies ranging from 1 to 5 MeV in 1 atm of Ar gas. The dashed lines correspond to the right ordinate and represent the ^{4}He ion energy as a function of penetration distance.

3.3 Charge-Carrier Properties in Gases

Electron-ion pairs are produced due to the Coulombic interactions experienced by a heavy charged particle in a gaseous medium. The total number of electron-ion pairs created, N_T, based on the amount of particle energy absorbed, ΔE, is defined as [97]

$$N_T = \frac{\Delta E}{W}, \tag{3.24}$$

where W is the average energy required to produce an electron-ion pair. W is used instead of the minimum ionization energy I_0 due to the competing energy loss mechanisms that occur as the kinetic energy of a charged particle is reduced in a gaseous medium [21, 97]. Examples of W values for various gaseous media are provided in the literature [97].

Recalling Eq. (3.5), the force exerted by the electric field on a charge carrier causes the charge carrier to drift in the direction of the electric field. The drift direction is dependent on the charge of the charge carrier relative to the charges of the electrodes. The *charge-carrier drift velocity*, *v*, in the presence of an electric field, *E*, is defined as [93]

$$v = \mu E\,, \tag{3.25}$$

where μ is the *charge-carrier mobility*. The value of μ is dependent on the particle type as well as the pressure, *p*, and temperature, *T*, of the gas as defined by [98]

$$\mu(T, p) = \frac{T}{T_0}\frac{p_0}{p}\mu_0\left(T_0, p_0\right). \tag{3.26}$$

The term μ_0 is the mobility at standard temperature, T_0, and pressure, p_0, values of 20°C and 1 atm, respectively. As the velocity of electrons increases, the kinetic energy also increases. Eventually, the kinetic energy is sufficient to cause additional ionization, referred to as *impact ionization*, resulting in the production of additional electron-ion pairs. The additional ionization reduces the mean free path of the electrons and the electrons reach a saturation velocity at electric field strengths approaching the saturation electric field strength. Thus, Eq. (3.25) is valid for electrons drifting under the influence of electric fields below a saturation electric field strength. Beyond the saturation electric field strength, the drift velocity is determined by the amount of charged particle scattering that occurs [21]. The drift velocity of ions, however, typically follows Eq. (3.25) for electric field strengths commonly used in gas-filled radiation detectors due to the higher mass and lower mobility of ions relative to electrons [21]. Examples of charge-carrier mobilities and drift velocities for different ions and gas media as a function of *reduced electric field strength*[1], *E*/*p*, are provided in the literature [21, 99, 100].

[1] The reduced electric field strength is defined as the ratio of the electric field strength to the gas pressure, typically reported with units of V cm^{-1} Torr^{-1}.

The initial electron-ion pairs liberated from the incident radiation event due to *primary ionization* are referred to as *primary charge carriers.* Any subsequent impact ionization events are referred to as *secondary ionization* and the additional electron-ion pairs produced are referred to as *secondary charge carriers*[1]. Impact ionization can also occur from secondary electrons with sufficient kinetic energy [87]. The cascade of subsequently liberated electrons attributed to impact ionization is referred to as a *Townsend avalanche* [57]. The process is named after J.S. Townsend who characterized the increase in measured current, due to impact ionization, as a function of the reduced electric field strength [101]. The work resulted in the definition of the *first Townsend ionization coefficient*, α_M, which is the reciprocal of the mean free path for impact ionization, λ_i [2]. The first Townsend ionization coefficient is a representation of the number of secondary charge carriers produced from a single electron traveling 1 cm in the electric field direction of a given gas [93, 101]. Thus, the increase in the number of charge carriers, *dn*, produced by *n* electrons traveling a distance *dx* is defined as [93, 101]

$$dn = n\alpha_M \, dx . \tag{3.27}$$

Integrating Eq. (3.27), the number of charge carriers produced, $n(x)$, within a given distance x is

$$n(x) = n_0 \, e^{\alpha_M x}, \tag{3.28}$$

where n_0 is the initial quantity of charge carriers. Eq. (3.28) is an important relation that defines the *gas multiplication*, *M*, that occurs between the initial position of the primary ionization and the position *x*. Thus, *M* is defined by dividing $n(x)$ by n_0, yielding [98]

$$M = \frac{n(x)}{n_0} = e^{\alpha_M x}. \tag{3.29}$$

[1] At times, the term *secondary electrons* will be used when describing phenomena attributed to the electrons created from secondary ionization.

Following impact ionization, positively-charged ions are sometimes left in an excited state, which can result in the emission of a photon as the ion returns to the ground state. The photon can then undergo a photoelectric interaction within the cathode or elsewhere in the gas resulting in the liberation of a photoelectron. Photoelectrons can also be liberated by two different mechanisms once a positively-charged ion has arrived at the cathode wall. Both mechanisms rely on the energy difference between the ionization potential of the positively-charged ion and the work function of the cathode. The energy difference may be radiated as a photon, which can then undergo a photoelectric interaction within the cathode or elsewhere in the gas and produce a photoelectron, or may result in the radiationless liberation of a photoelectron from the cathode. In all cases when a photoelectron is liberated, additional Townsend avalanching can occur and potentially lead to a self-sustaining discharge (for sufficiently high electric field strengths) [21, 57, 93].

To prevent a self-sustaining discharge, the addition of a *quenching gas*, with a lower ionization potential than the host gas, is used and is typically a polyatomic gas. When primary ionization occurs, both the host and quenching gases are ionized. Unlike the host gas, the quenching gas dissociates upon returning from an excited state instead of emitting a photon. As both positively-charged ion types drift toward the cathode, collisions between the positively-charged ions of the host gas and the quenching gas molecules occur. The collisions result in almost all of the positive charge being transferred to the quenching gas molecule. The quenching gas molecule then carries the positive charge and continues to drift toward the cathode wall. Upon collision with the cathode wall or the absorption of a photon (liberated from the cathode or elsewhere in the gas), the quenching gas molecule dissociates [21, 57, 93].

Electron collisions can also elevate a positively-charged ion to a long-lived metastable state that cannot undergo radiative transitions to the ground state due to selection rules [93]. As a result, the metastable state does not produce ionization and, thus, does not contribute to the induced charge signal. However, a small amount of a gas can be added with a lower ionization potential relative to the energy of the excited metastable state. Through collision, the energy of the metastable state can be transferred to the additive gas and result in the liberation of an electron-ion pair. The energy transfer and subsequent ionization process is referred to as the *Penning effect*. The addition of a Penning gas can substantially increase ionization resulting in an increase in the amount of charge induced from the initial radiation interaction [21, 93].

Immediately following ionization, a dense charge cloud is formed and charge carriers diffuse within the gas toward regions with lower charge densities, as described by Fick's law of diffusion [93]. Electrons diffuse more rapidly, relative to positively-charged ions, due to their smaller masses and larger mean free paths. The diffusion occurs parallel and perpendicular to the electric field resulting in a Gaussian broadening of the charge-cloud distribution as a function of time. The uncertainty in the one-dimensional Gaussian distribution, referred to as the diffusion width, σ_D, as a function of time, *t*, is defined by [93]

$$\sigma_D = \sqrt{2Dt}, \tag{3.30}$$

where *D* is the diffusion coefficient. The relationship between the diffusion coefficient and mobility is defined using the *Nernst – Townsend formula*[1] as [97, 100]

$$\frac{D}{\mu} = \frac{kT}{q}, \tag{3.31}$$

where *k* is Boltzmann's constant.

As charge carriers drift under the influence of an electric field, they can also experience electron attachment, charge transfer, and recombination effects. *Electron attachment* occurs when a free electron becomes attached to a neutrally-charged gas molecule or atom. In some electron attachment processes, an electron is re-emitted and the electron attachment is effectively nullified. However, when electron attachment results in the formation of a stable, slow-moving, negatively-charged ion, the mobility of the negative charge carrier is reduced by three or more orders of magnitude [21]. The average probability of an electron attaching to a gas molecule per collision is defined by the *attachment coefficient* [97]. The number of collisions experienced by an electron is dependent on the gas type and pressure, the detector geometry, and the electric field strength [57]. Impurities such as O_2 and water vapor (H_2O) have high electron attachment coefficients.

[1] The Nernst-Townsend formula is sometimes called the Einstein relation because of Einstein's use of the formula in 1905 when conducting theoretical investigations of Brownian movement. However, Nernst first deduced the formula in 1889 for electrolytic ions and Townsend applied the formula to gases, as described in his 1899 paper [100].

Contamination of the detector gas with O_2 and/or water vapor can result in signal degradation due to electron attachment [57]. *Charge transfer* occurs when an electron is transferred from a neutrally-charge gas atom to a positively-charged ion. Often times, charge transfer is exploited by adding a second gas, with a lower ionization potential, to the host gas to alter the ion transport characteristics [93]. *Recombination* occurs when an electron combines with a positively-charged ion to form a neutral gas molecule. Three important types of recombination can occur which are volumetric recombination, columnar recombination, and preferential recombination. *Volumetric recombination* occurs between positively- and negatively-charged ions from separate and unrelated particle tracks. When the ionization density is initially very high, *columnar recombination* occurs between positively- and negatively-charged ions from separate parent atoms within the same particle track. Finally, *preferential recombination*, which is the only *true* form of recombination, occurs when an electron recombines with its positively-charged ion counterpart initially created from ionization [2].

3.4 Operating Properties of Gas-Filled Radiation Detectors

Gas-filled radiation detectors operate differently according to the strength of the electric field region that charge carriers traverse. Five regions of operation exist based on the measured pulse amplitude, or pulse height, as a function of the electric field strength, as shown by the *pulse-height curve* in Figure 3.6. The measured pulse amplitude is dependent on the amount of charge induced by charged carriers as they drift toward their respective electrodes within the time response defined by the *RC* time constant. The measured pulse amplitude is also dependent on the physics of charge-carrier production. When no electric field is present within a device, charge carriers thermally diffuse within the gas toward regions with lower charge densities, as described by Fick's law of diffusion [93], and eventually recombine. As the electric field strength is increased, recombination of charge carriers is reduced due to the force exerted on both charge-carrier types. The force exerted by the electric field accelerates the charge carriers toward their respectively-charged electrodes in the direction of the electric field lines.

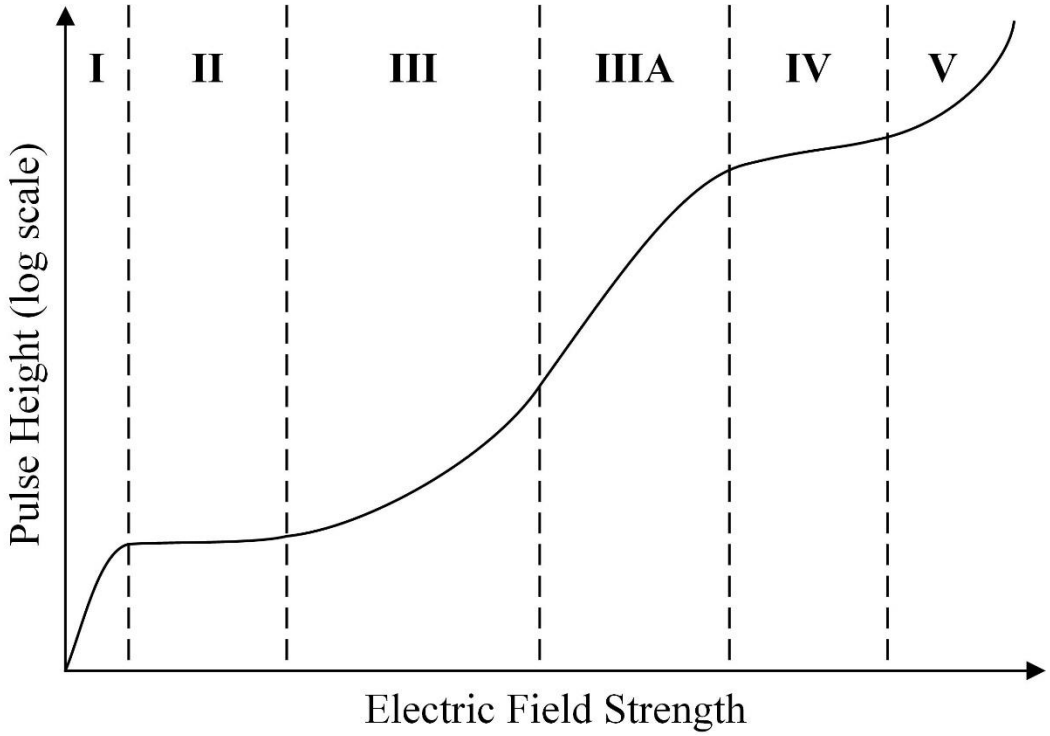

Figure 3.6. Gas-filled radiation detector operating regions defined by the measured pulse height as a function of electric field strength. Regions I – V are the recombination, ionization chamber, proportional, Geiger-Müller, and continuous-discharge regions, respectively. Region IIIA is the limited proportionality region.

In the first region of the pulse-height curve, the *recombination region*, the strength of the electric field is weak enough that charge carriers recombine following their liberation. As the electric field strength increases, the recombination rate decreases to effectively zero leading into region II. In region II, the *ionization chamber region*, charge carriers drift toward their respectively-charged electrodes and negligible recombination occurs. A plateau occurs within the ionization chamber region because recombination is minimal and no additional charge carriers are produced through multiplication. As the electric field strength is increased further, the kinetic energy of electrons increases and eventually is sufficient to cause impact ionization. An increase in pulse amplitude occurs due to the liberation of additional charge carriers from Townsend avalanching, as depicted by the *proportional region* (region III). The pulse amplitude is proportional to the amount of energy deposited by the initial radiation event. As the electric field strength increases, the amount of impact ionization also increases. Eventually, positive space charge begins to accumulate around the anode due to the slow motion of the positively-charged ions produced from Townsend avalanching. The amount of positive space charge is dependent on

the amount of Townsend avalanching, which is a function of the initial radiation energy deposited. The electric field strength decreases as positive space charge accumulates near the anode resulting in a slight decrease of gas multiplication. Therefore, the accumulation of positive space charge near the anode can introduce non-proportionality in the detector response, resulting in the *limited proportionality region* (region IIIA). Beyond region IIIA is region IV, the *Geiger-Müller region*. In region IV, the electric field strength results in a substantial amount of Townsend avalanching near the anode that produces a large and dense cloud of charge carriers. Positive space charge accumulates near the anode and eventually reduces the electric field strength below the threshold necessary for impact ionization. As a result, Townsend avalanching is halted and the electric field strength recovers as the positively-charged ions drift toward the cathode. Pulses formed in the Geiger-Müller region have nearly identical amplitudes that are independent of the type or energy of the incident radiation. Consequently, a device operated in the Geiger-Müller region can only function as a counter. Finally, region V, the *continuous-discharge region*, occurs when the electric field strength is so high that sporadic arcing can occur and potentially cause damage to the detector [2, 21, 102].

3.4.1 Ionization Chambers

Ionization chambers are detectors that are operated in region II of Figure 3.6. A common electrode configuration of an ionization chamber is a parallel-plate electrode setup, such as the one depicted in Figure 3.1, where the electrodes are separated by a distance *d* with the cathode positioned at $x = 0$. Recalling Eq. (3.24), N_T electron-ion pairs are liberated following a radiation interaction at position x_0, resulting in an initial charge, Q_0, of

$$Q_0 = q\,N_T\,. \tag{3.32}$$

The motion of the charge carriers as they drift toward their respectively-charged electrodes causes a change in induced charge on the electrodes (see Eq. (3.19)). The assumption is made that no electron attachment occurs, thus limiting the charge carriers to only electrons and positively-charged ions. The charge-carrier *sweep-out time* is defined as the distance displaced by the charge

carrier divided by the charge-carrier velocity. Thus, if a radiation interaction occurs at position x_0, the sweep-out times of electrons, t_e, and ions, t_i, are defined as

$$t_e = \frac{(d - x_0)}{v_e} \tag{3.33}$$

and

$$t_i = \frac{x_0}{v_i}, \tag{3.34}$$

where v_e and v_i are the electron and positively-charged ion velocities and $t_e \ll t_i$ because $v_e >> v_i$ (due to $\mu_e >> \mu_i$). Eq. (3.33) and Eq. (3.34) are defined assuming that sufficient time is provided for electrons and ions to drift the entire distance from x_0 toward their respective electrodes.

Assuming the detector is operated in pulse mode, the time-dependent rise in voltage from induced charge within the ionization chamber with intrinsic capacitance (see Eq. (3.21)) is [21]

$$V(t) = \frac{\Delta Q}{C} = \frac{q N_T t}{d C}(v_e + v_i), \tag{3.35}$$

where *t* is the duration of time following the radiation interaction event. However, commonly the *RC* time constant does not provide sufficient time for the positively-charged ions to contribute appreciably to the total induced charge. Thus, for $t_e \le t \ll t_i$, ion contributions are considered negligible and Eq. (3.35) can be approximated as [2, 21]

$$V(t) \approx \frac{q N_T t}{d C} v_e . \tag{3.36}$$

Applying Eq. (3.33) to Eq. (3.36) for $t = t_e$ yields

$$V(t) \approx \frac{q N_T}{d C}(d - x_0) = \frac{q N_T}{C}\left(1 - \frac{x_0}{d}\right). \tag{3.37}$$

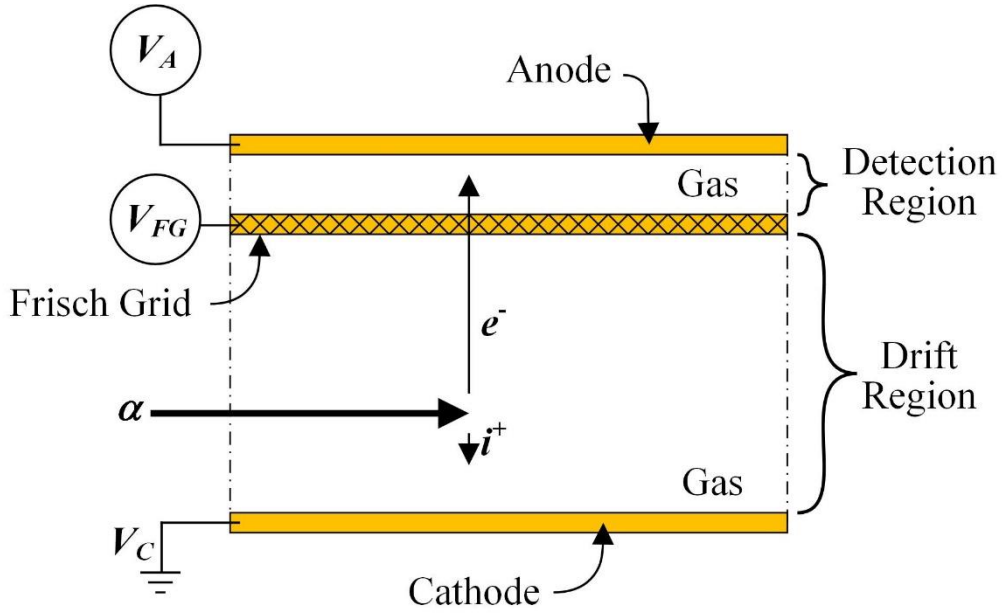

Figure 3.7. Frisch grid positioned between the anode and cathode of a parallel-plate ionization chamber. The operating voltage condition of $V_A > V_{FG} > V_C$ is required in order to drift electrons from their site of origin within the drift region, past the Frisch grid, and toward the anode in the detection region. Charge induction occurs only within the detection region.

Eq. (3.37) indicates that the pulse amplitudes measured using an ionization chamber are position-dependent. The position-dependency of an ionization chamber can be corrected by implementing a non-collecting grid electrode, such as a *Frisch grid*, between the anode and cathode. The Frisch grid was introduced in 1942 by Otto Frisch [103] and segments the sensitive volume of a device into two regions, the *drift region* and the *detection region*. Shown in Figure 3.7 is an alpha-particle incident on a parallel-plate ionization chamber with a Frisch grid. Electrons and positively-charged ions are liberated as the alpha particle ionizes the gas within the drift region. The electrons drift toward the Frisch grid and the positively-charged ions drift toward the cathode under the influence of the electric field formed by the potential difference between the operating voltages of the Frisch grid, V_{FG}, and cathode, V_C, where $V_{FG} > V_C$. Once beyond the Frisch grid, electrons drift toward the anode due to the potential difference between the operating voltages of

the Frisch grid and anode, V_A, where $V_A > V_{FG}$. The motion of electrons within the detection region induces charge on the anode. Although motion of the charge carriers occurs in the drift and detection regions, only charge induced within the detection region is measured and the resulting pulse amplitude is defined as [2, 21]

$$V(t) = \frac{q N_T t_m}{d_{FG} C} v_e , \tag{3.38}$$

where d_{FG} is the distance separating the anode and Frisch grid for a planar configuration and t_m is the drift time in the detection region. Under the assumption that radiation interactions occur only within the drift region, Eq. (3.38) indicates that the position dependence of pulse heights is eliminated with the implementation of a Frisch grid.

3.4.2 Proportional Counters

Detectors operated in region III of Figure 3.6 are referred to as *proportional counters* because the electric field strength within the device is sufficient to cause impact ionization, yielding pulse amplitudes that are proportional to the energy deposited by the initial radiation event. Proportional counters are commonly designed with a coaxial electrode configuration, in which a small-diameter anode wire is positioned axially within a cylinder that functions as the cathode. The potential distribution as a function of radial position, *r*, within a coaxial proportional counter is defined using Laplace's equation (see Eq. (3.1)) as [21]

$$V(r) = V_0 \frac{\ln(r/r_1)}{\ln(r_2/r_1)} . \tag{3.39}$$

Recalling Eq. (3.4) and differentiating Eq. (3.39) with respect to *r* yields the electric field strength distribution as

$$E(r) = \frac{V_0}{r \ln(r_2/r_1)} . \tag{3.40}$$

The form of Eq. (3.40) indicates that the electric field strength increases rapidly near the surface of the anode wire.

Because impact ionization occurs within a coaxial proportional counter, the change in induced charge, ΔQ, is a function of the initial charge, Q_0, and the gas multiplication factor, M, as defined by

$$Q = M\,Q_0 = M\,q\,N_T\,. \tag{3.41}$$

Following a radiation interaction event at an initial radial position r_0, electrons and positively-charged ions are liberated. The assumption is made that no electron attachment occurs, thus limiting the charge carriers to only electrons and positively-charged ions. Electrons drift toward the anode wire while the positively-charged ions drift toward the cathode wall. The change in induced charge within a coaxial proportional counter can be calculated using Green's reciprocation theorem (described in Section 3.1). Assuming the absence of space charge, the change in induced charge on the anode wire after electrons and ions drift to radial positions r_e and r_i, respectively, is [57]

$$\Delta Q_A = Q\frac{\left[-\ln\left(r_e/r_1\right)+\ln\left(r_i/r_1\right)\right]}{\ln\left(r_2/r_1\right)} = Q\frac{\ln\left(r_i/r_e\right)}{\ln\left(r_2/r_1\right)} = M\,q\,N_T\,\frac{\ln\left(r_i/r_e\right)}{\ln\left(r_2/r_1\right)}, \tag{3.42}$$

where the exterior radius of the anode is r_1 and the interior radius of the cathode is r_2. Assuming the detector is operated in pulse mode, application of Eq. (3.42) to Eq. (3.21) for a coaxial proportional counter with intrinsic capacitance defines the time-dependent rise in voltage as

$$V(t) = \frac{M\,q\,N_T}{C}\,\frac{\ln\left(r_i/r_e\right)}{\ln\left(r_2/r_1\right)}\,. \tag{3.43}$$

Recalling from Section 3.3, as the electric field strength increases, the kinetic energy of electrons also increases and eventually is sufficient to cause impact ionization. Thus, as electrons

drift within close proximity of the anode wire surface[1], Townsend avalanching occurs and produces a large cloud of electron-ion pairs. Due to the close proximity relative to the anode wire, electrons drift a relatively short distance before reaching the anode wire while the positively-charged ions produced from Townsend avalanching drift away from the anode wire toward the cathode wall. A substantial amount of charge is induced within the high electric field region surrounding the anode wire due to the motion of the positively-charged ions as they drift toward the cathode wall. The contribution to ΔQ_A from the motion of electrons before reaching the anode wire is very small and can be considered negligible. Thus, the time-dependent rise in voltage of a coaxial proportional counter is ion dominated and Eq. (3.43) reduces to

$$V(t) \approx \frac{M\, q\, N_T}{C} \frac{\ln(r_i)}{\ln(r_2/r_1)}. \tag{3.44}$$

The drift velocity of the positively-charged ions is defined by

$$v_i = \frac{dr_i}{dt} = \mu_i\, E = \frac{\mu_i\, V_0}{r \ln(r_2/r_1)}. \tag{3.45}$$

Integrating Eq. (3.45) defines r_i as a function of time t as [57]

$$r_i(t) = \sqrt{\frac{2V_0\, \mu_i\, t}{\ln(r_2/r_1)} + r_1^{\,2}}, \tag{3.46}$$

based on the approximation that all positively-charged ions start at r_1 when $t = 0$. Substitution of Eq. (3.46) into Eq. (3.44) yields

[1] The radial distance from the surface of the anode wire where Townsend avalanching occurs is dependent on the detector geometry, the gas pressure and type, and the applied voltage.

$$V(t) \approx \frac{M\,q\,N_T}{C} \frac{\ln\left(\sqrt{\frac{2\,\mu_{ion} V_0\,t}{r_1^{\,2}\ln(r_2/r_1)}+1}\right)}{\ln(r_2/r_1)}. \tag{3.47}$$

Finally, substituting $r_i = r_2$ into Eq. (3.46) defines the collection time for positively-charged ions as

$$t_i = \frac{\left(r_2^{\,2} - r_1^{\,2}\right)\ln(r_2/r_1)}{2V_0\,\mu_i}. \tag{3.48}$$

Similar to an ionization chamber, the *RC* time constant of a coaxial proportional counter often does not provide sufficient time for the positively-charged ions to drift the entire distance from the site of liberation to the cathode wall. However, typically half of the maximum pulse amplitude is achieved due to positively-charged ion motion within approximately 500 μm of the anode wire surface for common coaxial proportional counter designs [21]. Thus, the *RC* time constant can be set to provide sufficient time for large amplitude pulses to be formed without the significant risk of pulse pile-up occurring. Due to a majority of the pulse formation occurring near the anode from Townsend avalanching, the position dependence of pulse formation within a coaxial proportional counter is significantly reduced when measuring a monoenergetic radiation source. However, position dependence can still occur for radiation paths occurring within a coaxial proportional counter that are not parallel to the anode wire. In such a scenario, a distribution of distances are traveled by electrons before undergoing Townsend avalanching, resulting in a distribution of measured pulse amplitudes.

3.4.3 Microstrip Electrodes

In 1967, Charpak developed the first MWPC[1] due to the increasing demand for large-area, position-sensitive detectors in high-energy particle physics experiments [98, 104]. The success of

[1] The development would lead to Charpak receiving the 1992 Nobel Prize for Physics.

MWPCs combined with the increasing popularity of photolithography fabrication methods eventually led to the development of micropattern-electrode based detectors, the first of which was the microstrip gas counter (MSGC). The first MSGC was introduced in 1988 by Oed as an alternative to MWPCs with improved position resolution and rate capability [98, 105]. MSGCs feature a microstrip electrode positioned a distance away from a planar, drift electrode, as illustrated in Figure 3.8. The microstrip electrode is commonly fabricated using photolithography methods and has interdigitated metal anode and cathode strips adhered to an insulating substrate. Depending on the application, the range of widths of the anode and cathode strips are 8 – 30 μm and 90 – 500 μm, respectively with anode-to-anode pitches ranging from 200 to 1000 μm [105-109]. Microstrip electrodes are advantageous relative to MWPCs because the distance between neighboring anode and cathode strips can be reduced below the limiting distance between neighboring wires in MWPCs [105]. The anode strips are operated at a higher potential relative to the cathode strips. The difference in operating potential combined with the close proximity of the strips produces an electric field region of sufficient strength to cause impact ionization. A geometric weighting condition also exists due to the difference in strip width of the anode and cathode strips.

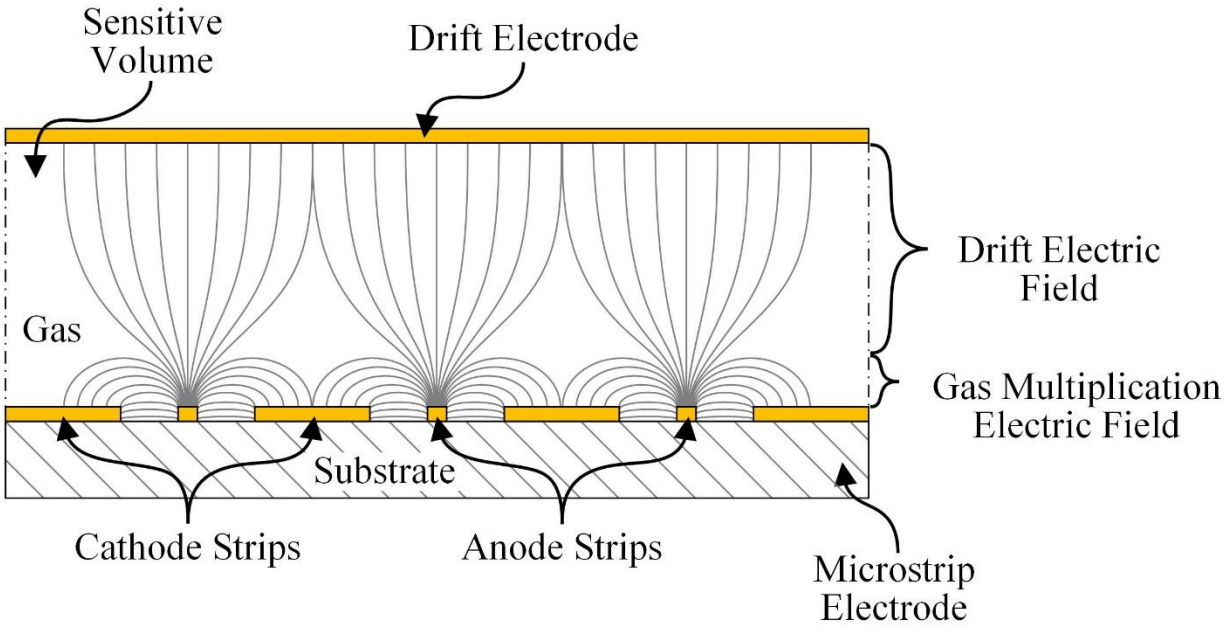

Figure 3.8. Example of a MSGC depicting the orientation of the microstrip and drift electrodes with gas located in between. The microstrip electrode is typically fabricated using photolithography processes and has interdigitated metal anode and cathode strips.

When an incident particle ionizes the gas, primary charge carriers are liberated. The charge carriers drift toward their respectively-charged electrodes under the influence of the electric field formed from the potential difference between the drift and microstrip electrodes. The drift electrode is maintained at a lower potential relative to the anode and cathode strips in order to drift electrons toward the microstrip electrode and positively-charged ions toward the drift electrode. As electrons approach the surface of the microstrip electrode, the electric field strength increases by several orders of magnitude and electrons gain sufficient kinetic energy to cause impact ionization. The region where Townsend avalanching occurs is denoted as the gas-multiplication electric field region in Figure 3.8. Secondary charge carriers are liberated due to Townsend avalanching which are rapidly swept to the nearest anode and cathode strips due to the close proximity of the strips and the high electric field strength.

3.4.4 Counting Curves

The measurement capabilities of gas-filled radiation detectors are inherently dependent on the electric field strength distribution within the device. Proportional counters and microstrip-electrode based devices are especially sensitive to changes in the electric field strength distribution that are attributed to fluctuations in the applied voltage setting(s). The sensitivity of proportional counters and microstrip-electrode based devices is attributed, in part, to Townsend avalanching that occurs during the charge induction process. Thus, *counting curves* are often defined to understand the counting stability when measuring a specific type of radiation with a device relying on Townsend avalanching. Before defining a counting curve, a series of measurements are conducted in order to sufficiently set the LLD of the counting system. Typically, the LLD is set to reject pulses with lower amplitudes than the pulse amplitudes produced from the radiation particle of interest. With the LLD set, the counting curve is developed by counting pulses with amplitudes above the LLD setting over a range of applied voltages. The pulses are attributed to a specific energy and type of particle emitted from a radioactive source. Each counting measurement is conducted for the same duration of time. When measuring a monoenergetic radiation source, as the applied voltage is increased, the pulse amplitude increases because the amount of charge induced on the anode increases. The increase in induced charge occurs due to an increase in charge-carrier velocity and, at sufficiently high electric field strength, Townsend avalanching. For pulses

with amplitudes below the LLD setting, no counts will be recorded. After the pulse amplitudes exceed the LLD setting, the measured count rate will increase. Eventually the count rate will stabilize because all of the pulses have amplitudes exceeding the LLD setting. The stable counting region where the count rate does not fluctuate appreciably is called the *counting curve plateau*. The counting curve plateau identifies the range of stable operating voltages for the detector to accurately count particles of a particular type and energy. The slope of the counting curve plateau is often calculated to provide a performance metric for a proportional counter. The slope is calculated based on the counts measured at the beginning, CTS_1, and end, CTS_2, of the counting curve plateau, as defined by [21]

$$CC_{Plateau\,slope} = \frac{(CTS_2 - CTS_1)}{V_2 - V_1}\left(\frac{2}{CTS_2 + CTS_1}\right), \tag{3.49}$$

where V_1 and V_2 are the applied voltage settings at the beginning and end of the counting curve plateau, respectively. The slope is also reported in percent change per 100 volts, as defined by

$$\%CC_{Plateau\,slope} = 100\left(\frac{100(CTS_2 - CTS_1)}{V_2 - V_1}\right)\left(\frac{2}{CTS_2 + CTS_1}\right). \tag{3.50}$$

As the applied voltage is further increased, the gas multiplication factor, *M*, will increase due to an increase in the electric field strength within the device. Eventually, the measured count rate will increase again with an increase in applied voltage. The increase in count rate occurs due to pulses created from background and low-energy events having amplitudes above the LLD setting. Once the counting curve plateau is defined, the applied voltage setting is set in the middle of the plateau region in order to minimize counting fluctuations attributed to variations in the applied voltage setting(s).

CHAPTER 4

PRELIMINARY EMBODIMENTS OF NEUTRON CONVERSION MEDIA: BACKGROUND, INVESTIGATION METHODS, AND RESULTS

An expert is a person who has made all the mistakes that can be made in a very narrow field.

Niels Bohr

Prior to selecting ^{6}Li foils as the neutron-conversion medium for SFMNDs, $^{10}B_4C$-coated RVC foam and aluminum honeycomb were investigated as neutron-conversion media. Thus, first, an overview of common thin-film-coating materials is provided (Section 4.1). A brief discussion of the general reaction-product emission scenarios associated with thin-film-coated substrates suspended within a gas-filled medium follows (Section 4.1). The background of each conversion medium is then discussed before detailing the methodology employed to characterize each medium. The characterization and neutron-sensitivity testing results follow for each medium (Section 4.2 for RVC foams and Section 4.3 for aluminum honeycomb). Finally, the simulation of thin-film-coated aluminum honeycomb is discussed and the results provided (Section 4.3).

4.1 Thin-Film-Coated Substrates Suspended in Gas-Filled Media

Illustrated in Figure 4.1 are three general reaction-product emission scenarios that can occur when using a thin-film-coated substrate for detecting neutrons. Because the thin-film coating must be applied to a substrate, only the energy of one reaction product can be deposited within the gas upon the reaction product escaping the thin-film coating (scenarios 1 and 2). The other reaction product is absorbed within the thin-film coating and/or the substrate material. The scenario also exists where both reaction products are absorbed within the thin-film coating layer and/or substrate

(scenario 3). The amount of reaction-product energy lost within the thin-film coating due to self-absorption effects is dependent on the position of reaction-product emission within the thin-film coating as well as the reaction-product trajectory. The amount of reaction-product energy deposited within the gas is dependent on the amount of energy retained by the reaction product upon escaping the thin-film coating. Thus, the full energy of one of the reaction products can be deposited within the gas for reaction products emitted at the interface of the gas and the thin-film coating. As the reaction product ionizes the gas, charge carriers are liberated. Charge is induced as charge carriers drift toward their respectively-charged electrodes under the influence of the electric field formed by the potential difference between the electrodes. Similar to ^{10}B-lined proportional counters and thin-film-coated semiconductors, the thin-film-coating thickness should not exceed the range of the highest energy reaction product or significant reaction-product self absorption likely will occur within the thin-film coating. Due to self-absorption effects within the thin-film coating, reaction-product pulse-height spectra measured with a thin-film-coated device typically have an energy distribution ranging from zero up to the highest energy reaction product (similar to the spectrum depicted in Figure 2.10 when using a ^{10}B-lined proportional counter) [86].

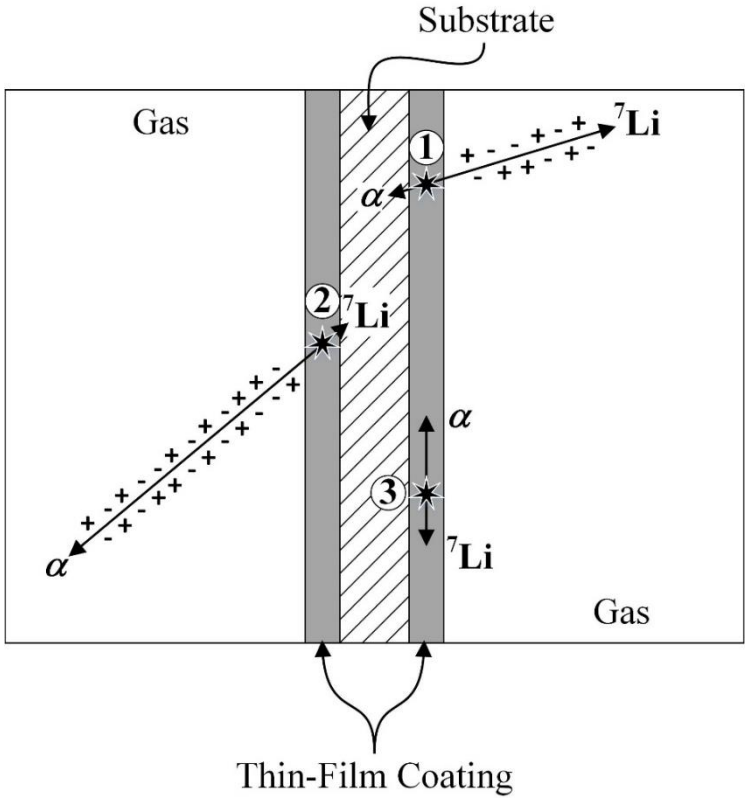

Figure 4.1. General reaction-product emission scenarios from conversion of neutrons using a thin-film-coated substrate surrounded by gas [110].

A single layer of ^{10}B or ^{6}LiF thin-film-coating has a maximum ε_{th} of approximately 4.5% [42, 59] and, therefore, several alternating converter-ionization volume layers are required to achieve the performance of commercially-available ^{3}He proportional counters [59]. In order to increase ε_{th}, a variety of approaches have been explored to implement consecutive thin-film coatings contained within various sizes and shapes of sensitive volumes [27, 44, 111-114]. RVC foam and aluminum-honeycomb substrates are capable of having a large number of coating surfaces, and thus a large amount of surface area, to apply thin-film coatings within a compact substrate size.

^{10}B, ^{10}BN, $^{10}B_4C$, and ^{6}LiF are some common thin-film-coating materials. Listed in Table 4.1 are the microscopic thermal-neutron interaction cross sections (σ) of the isotopes associated with ^{10}B, ^{10}BN, $^{10}B_4C$, and ^{6}LiF. ^{6}Li is provided for comparison despite not typically being used as a thin-film-coating material due to its reactive nature [59]. The σ values associated with ^{10}B and ^{6}Li represent absorption cross sections, while the σ values of N, C, and F are total interaction cross sections. Also listed in Table 4.1 are the material densities (ρ) and macroscopic thermal-neutron interaction cross sections (Σ) of ^{10}B, ^{10}BN, $^{10}B_4C$, ^{6}Li, and ^{6}LiF. The Σ values were calculated using Eq. (2.1) – (2.3).

Table 4.1. (left) Microscopic thermal-neutron interaction cross sections (σ) for the isotopes associated with ^{10}B, ^{10}BN, $^{10}B_4C$, ^{6}Li, and ^{6}LiF [60]. (right) Common neutron-conversion materials with associated densities (ρ) [59, 115, 116] and macroscopic thermal-neutron interaction cross sections (Σ).

Isotope	**σ (*b*)**	**Material**	**ρ (g cm^{-3})**	**Σ (cm^{-1})**
^{10}B	3842.6	^{10}B	2.16	499.5
N	11.8	^{10}BN	2.18	210.8
C	4.7	$^{10}B_4C$	2.45	436.0
^{6}Li	938.5	^{6}Li	0.463	43.5
F	3.7	^{6}LiF	2.54	57.7

Thin-film-coated devices commonly rely on either ^{10}B or ^{6}Li as the neutron-converting isotope, depending on the size and geometry of the neighboring ionization volume. For smaller ionization volumes, ^{10}B and ^{10}B-based compounds such as $^{10}B_4C$ and ^{10}BN are used due to the higher Σ compared to ^{6}Li and ^{6}LiF. Likewise, recalling Eq. (2.10) and Eq. (2.11), the $^{10}B(n, \alpha)^{7}Li$ reaction results in the emission of lower-energy reaction products with smaller ranges relative to

the $^{6}Li(n, \alpha)^{3}H$ reaction. $^{10}B_4C$ and ^{10}BN are often used instead of ^{10}B as a thin-film-coating material because of desirable material and adhesion properties [117-120]. As listed in Table 4.1, $^{10}B_4C$ has a slightly lower Σ and a higher ρ relative to ^{10}B. The Σ of ^{10}BN is significantly lower than that of ^{10}B and, therefore, $^{10}B_4C$ was selected as the thin-film-coating material for investigating RVC foam and aluminum-honeycomb substrates as thin-film-coated neutron-conversion materials.

4.2 $^{10}B_4C$-Coated Reticulated Vitreous Carbon Foam

RVC foams have recently emerged as a thin-film-coated substrate for neutron-detection applications [46, 121-124] due to the amount of coating surface area contained within a compact substrate size. RVC foam is produced by ERG Aerospace Corporation and features a semi-randomized network of pores, cells, and struts, in which the pores and cells are defined by the vacancies between neighboring struts [125], as shown in Figure 4.2. The size and number of struts defines the linear pore density of the material and RVC foams are produced with linear pore densities ranging from 5 to 100 pores per linear inch (PPI) [126], as shown in Figure 4.3. For linear pore densities of 5 to 80 PPI, pore diameters can range from 4.85 ± 0.81 mm to 0.63 ± 0.12 mm, respectively [124]. Similarly, the strut thicknesses can range from 418 ± 117 μm to 50 ± 11 μm for linear pore densities of 5 to 80 PPI, respectively [124]. Thus, an inverse relationship exists between the linear pore density of a sample and the size of the pores and struts contained within the sample. RVC foams are used for a variety of applications such as energy absorbers, heat shielding, and fuel cells [127] and, therefore, the manufacturing infrastructure already exists.

The intended neutron-detection process when using $^{10}B_4C$-coated RVC foam is similar to other thin-film-coated neutron-conversion media. Following neutron absorption within the $^{10}B_4C$ thin-film coating, charged-particle reaction products are emitted. One of the reaction products is absorbed within the $^{10}B_4C$ and/or the RVC foam and the other reaction product may escape the $^{10}B_4C$ to ionize the gas, as illustrated in Figure 4.4. Charge carriers are liberated as the reaction product ionizes the gas. Listed in Table 4.2 are the ranges of the $^{10}B(n, \alpha)^{7}Li$ reaction products in $^{10}B_4C$, RVC foam, and 1 atm of P-10 proportional gas (90% argon and 10% methane) [96]. Due to the network of pores, cells, and struts featured within the bulk of RVC foam, a reaction product

may ionize the gas within one or more pores and/or cells before stopping within the gas or colliding with a strut. Thus, a distribution of reaction-product energy can be deposited within the pore(s) and/or cell(s) contained within the bulk of RVC foam. The amount of reaction-product energy deposited is dependent on the size of the pore(s) and/or cell(s), the site of reaction-product emission within the $^{10}B_4C$, and the trajectory of the reaction product.

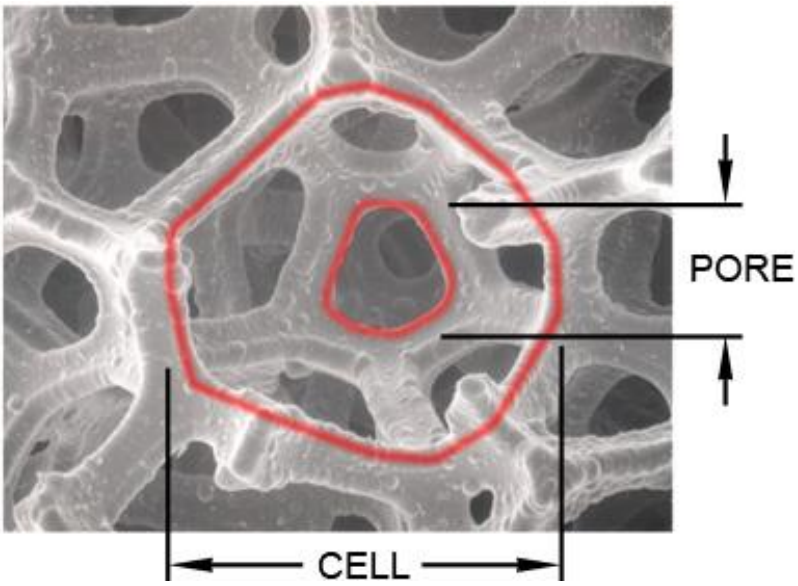

Figure 4.2. RVC foam structural definitions indicating the pores and cells formed by neighboring struts [125].

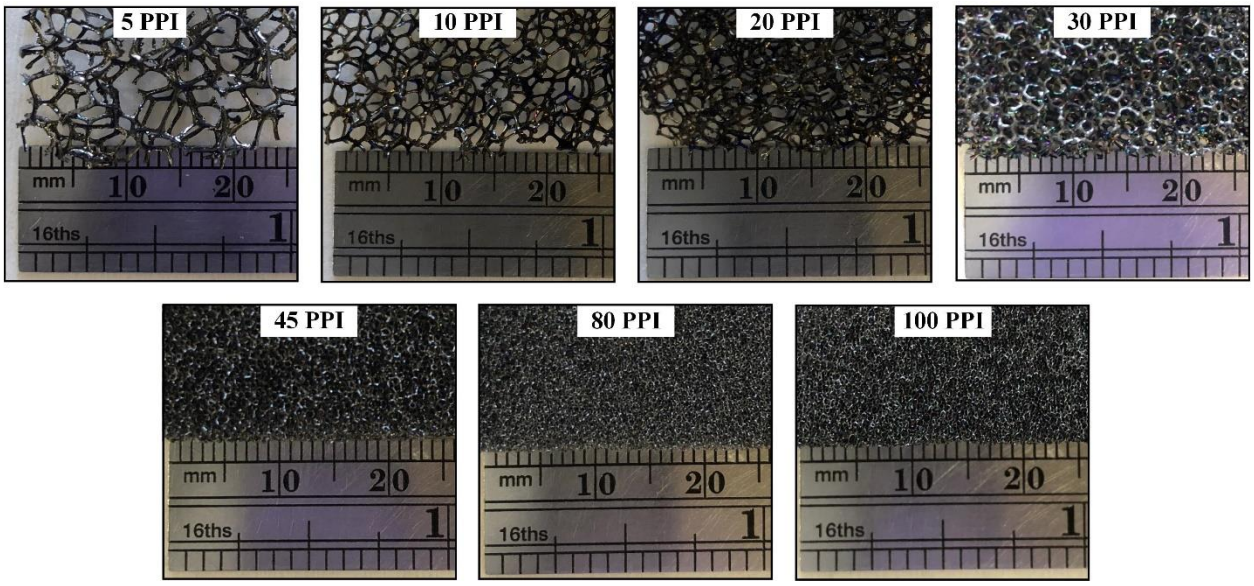

Figure 4.3. Sizes of pores, cells, and struts in RVC foam samples with linear pore densities of 5, 10, 20, 30, 45, 80, and 100 PPI.

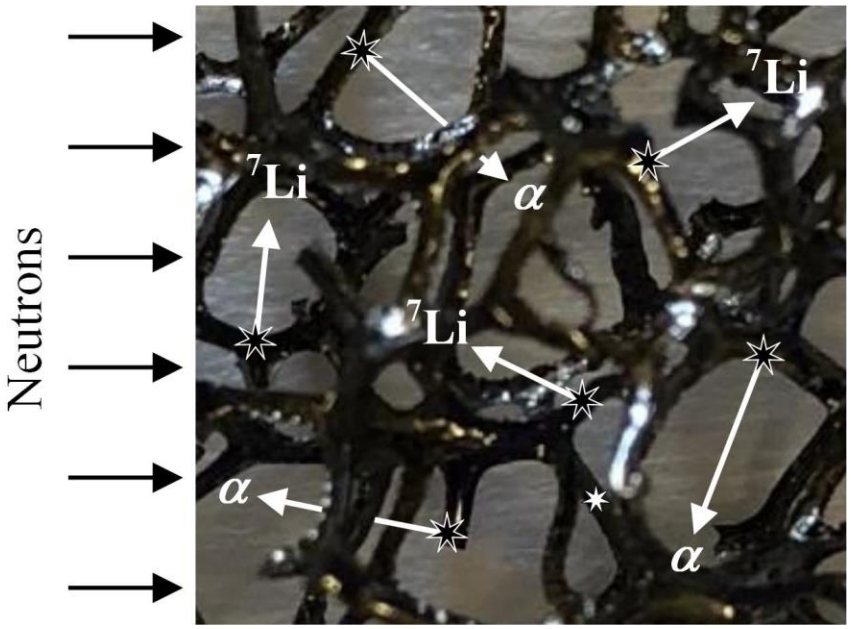

Figure 4.4. Illustration of potential reaction-product emission scenarios within the bulk of $^{10}B_4C$-coated RVC foam.

Table 4.2. The ranges of $^{10}B(n, \alpha)^7Li$ reaction products in $^{10}B_4C$, RVC foam, and 1 atm of P-10 gas [96]. The density, ρ, of each material is also listed [96, 115].

Material	**ρ (g cm^{-3})**	**0.840 MeV ^{7}Li (μm)**	**1.015 MeV ^{7}Li (μm)**	**1.470 MeV ^{4}He (μm)**	**1.777 MeV ^{4}He (μm)**
Thin-Film Coating					
$^{10}B_4C$	2.16	1.63	1.83	3.23	3.99
Substrate					
RVC Foam	2.20	1.87	2.1	4.01	4.91
P-10 Gas					
1 atm	0.00156	4210	4690	8040	9900

4.2.1 Charge-Carrier Propagation Properties

Although the neutron-detection capabilities of RVC foam have been studied both experimentally [46, 121, 122] and computationally [123, 124], the ability for charge carriers to drift through the bulk of the material was not previously characterized. Shown in Figure 4.5 is an illustration of potential reaction-product trajectories. Also depicted are the paths required of charge carriers to drift toward their respectively-charged electrodes. The charge carriers drift under the

influence of the electric field formed from the potential difference between the anode and cathode. If charge carriers are able to drift within the bulk of the material in the direction of the electric field and, therefore, induce charge on the electrodes, then the number of active thin-film-coating layers can be quite large for a compact substrate size. However, if charge carriers are not capable of drifting through the bulk of the substrate, then the motion of charge carriers liberated within the bulk of the material may not be measured. Therefore, charge induction may only occur due to the motion of charge carriers liberated at or near the exterior surfaces of the substrate.

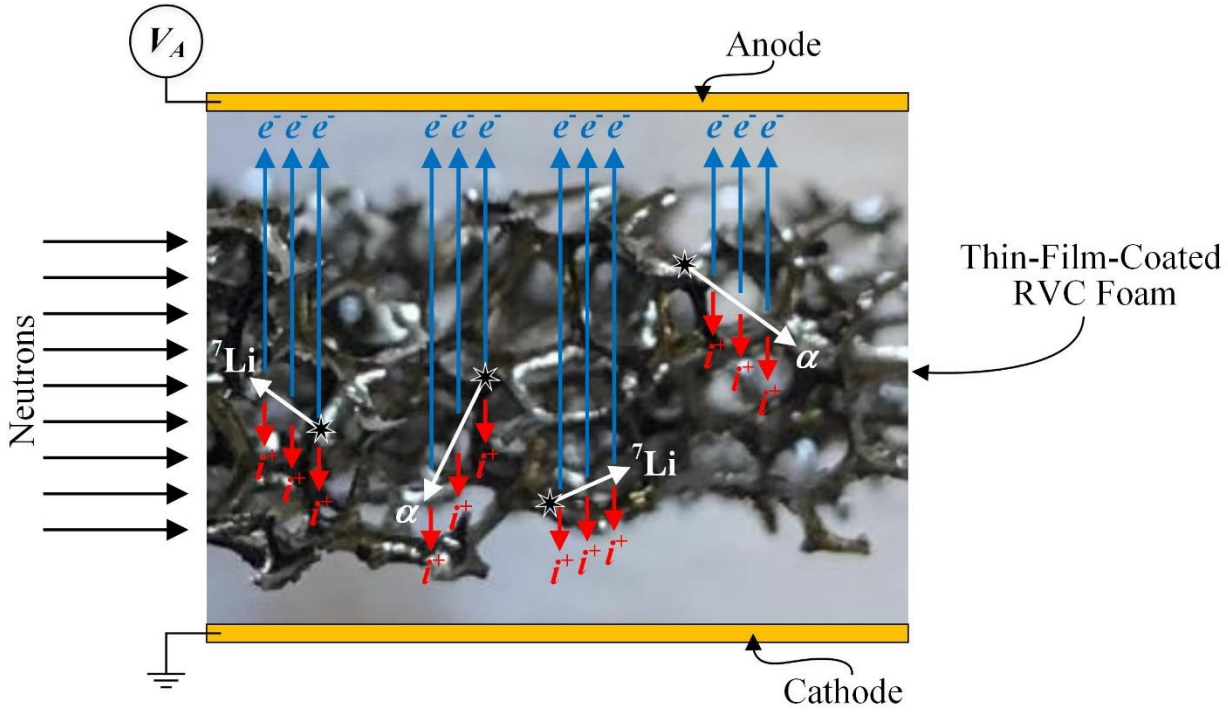

Figure 4.5. Illustration of reaction-product trajectories within the bulk of $^{10}B_4C$-coated RVC foam. The paths required of charge carriers to drift through the bulk of the RVC foam toward their respectively-charged electrodes are also shown.

Thus, a method was devised to determine whether electrons could traverse the bulk of RVC foam with linear pore densities ranging from 5 to 100 PPI. The pulse-height spectrum and count rate were measured for each sample. A parallel-plate electrode setup was assembled and each RVC foam sample was separately positioned between the parallel plate electrodes using a plastic support structure, as shown in Figure 4.6. The thickness and diameter of each RVC foam sample was approximately 6.35 mm (0.25 in.) and 25.4 mm (1 in.), respectively, and the samples were cut using a razor blade. The plastic support structure was fabricated using #6-32 nylon threaded rods, 1.5-mm (0.06-in.) thick nylon washers, and 0.76-mm (0.03-in.) thick polycarbonate film. The

nylon plastic washers had an inside diameter of 3.3 mm (0.13 in.) and an outside diameter of 7.4 mm (0.29 in.). The materials that were used for fabricating the plastic support structure were selected due to their availability within the laboratory. The planar, aluminum electrodes were waterjet-cut with a diameter of 12.7 mm (0.50 in.). The electrode diameter was intentionally designed to be smaller than the RVC foam sample diameter in order to ensure that charge carriers would drift through, rather than around, each RVC foam sample. Using the plastic support structure, the electrodes were separated by a distance of approximately 25.4 mm.

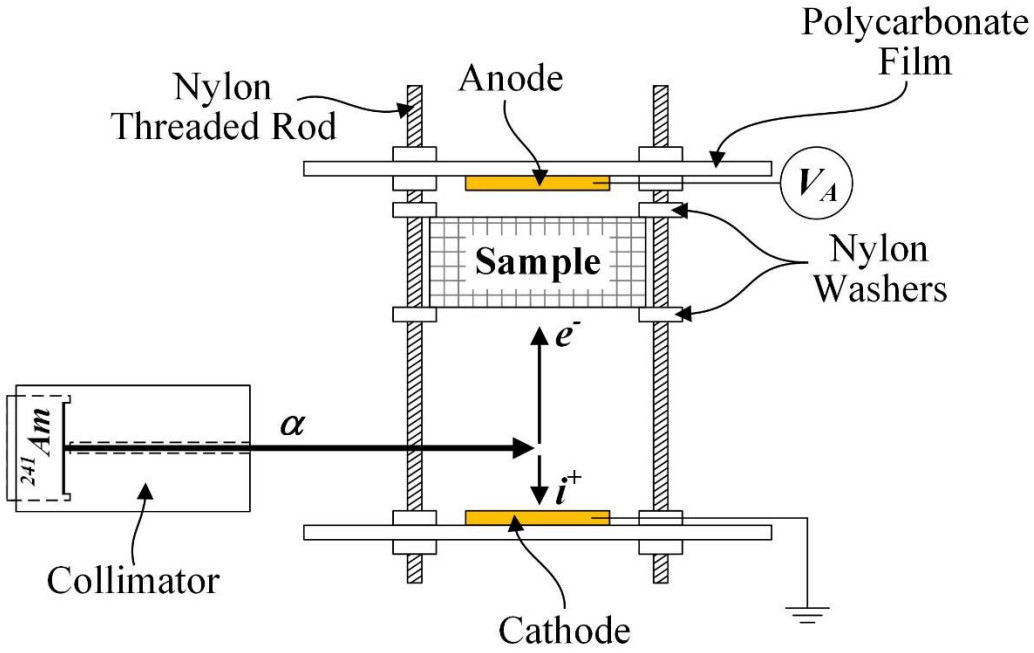

Figure 4.6. Parallel-plate electrode test configuration used for determining whether electrons could traverse the bulk of RVC foam. The collimated ^{241}Am alpha-particle was positioned in order to inject alpha particles between the cathode and RVC foam sample location [128].

Based on the Bragg ionization curve of alpha particles, a collimated ^{241}Am alpha-particle source was positioned so that a majority of the energy of the 5.48 MeV alpha particles was deposited between the RVC foam sample and cathode [96]. Charge carriers were liberated as the alpha particles ionized the gas between the cathode and RVC foam sample. The anode operating voltage, V_A, was 700 V and the cathode was maintained at ground potential to attain a reduced electric field strength of approximately 0.3 V cm^{-1} Torr^{-1} in 4 psig of P-10 gas [99, 129]. The potential difference between the electrodes resulted in electrons drifting toward the anode and positively-charged ions drifting toward the cathode. Throughout the duration of each

measurement, the testing apparatus and collimated ^{241}Am alpha-particle source were contained within a sealed aluminum enclosure backfilled with 4 psig of P-10 gas.

A two-hour measurement was conducted without an RVC foam sample that served as a control measurement. Subsequent two-hour measurements were then performed for RVC foam samples with linear pore densities of 5, 10, 20, 30, 45, 80, and 100 PPI. In each scenario with an RVC foam sample installed, the sample was consistently positioned above the cathode surface. The position of the collimated ^{241}Am alpha-particle source relative to the test configuration was maintained throughout all measurements to ensure that the same amount of energy was deposited between the cathode and RVC foam sample location. The consistent positioning of the RVC foam sample and collimated ^{241}Am alpha-particle source, relative to the anode and cathode, maintained the distance displaced by charge carriers as positively-charged ions drifted toward the cathode and electrons drifted toward the bottom of the sample in the direction of the anode.

The measured net count rates from the RVC foam samples are listed in Table 4.3 and suggest that charge induction occurred for all of the measurements. Shown in Figure 4.7 are the pulse-height spectra measured for each RVC foam sample relative to the no sample scenario. The down-shift in peak channel number of the pulse-height spectra measured with the RVC foam samples relative to the no sample case suggests that electrons drifted a shorter distance, thus less charge was induced when an RVC foam sample was present. Furthermore, the peak channel location of the 5 PPI RVC foam sample suggests that more charge was induced relative to the other RVC foam samples. Thus, the distance displaced by electrons was suspected to have occurred between the site of charge-carrier liberation and the sample, as well as potentially shallow depths within each sample.

Table 4.3. Net count rates measured using the testing configuration shown in Figure 4.6 [128].

Sample	**Net Count Rate (counts second^{-1})**
No Sample	2.66 ± 0.02
5 PPI	2.53 ± 0.02
10 PPI	2.52 ± 0.02
20 PPI	2.60 ± 0.02
30 PPI	2.54 ± 0.02
45 PPI	2.41 ± 0.02
80 PPI	2.40 ± 0.02
100 PPI	2.42 ± 0.02

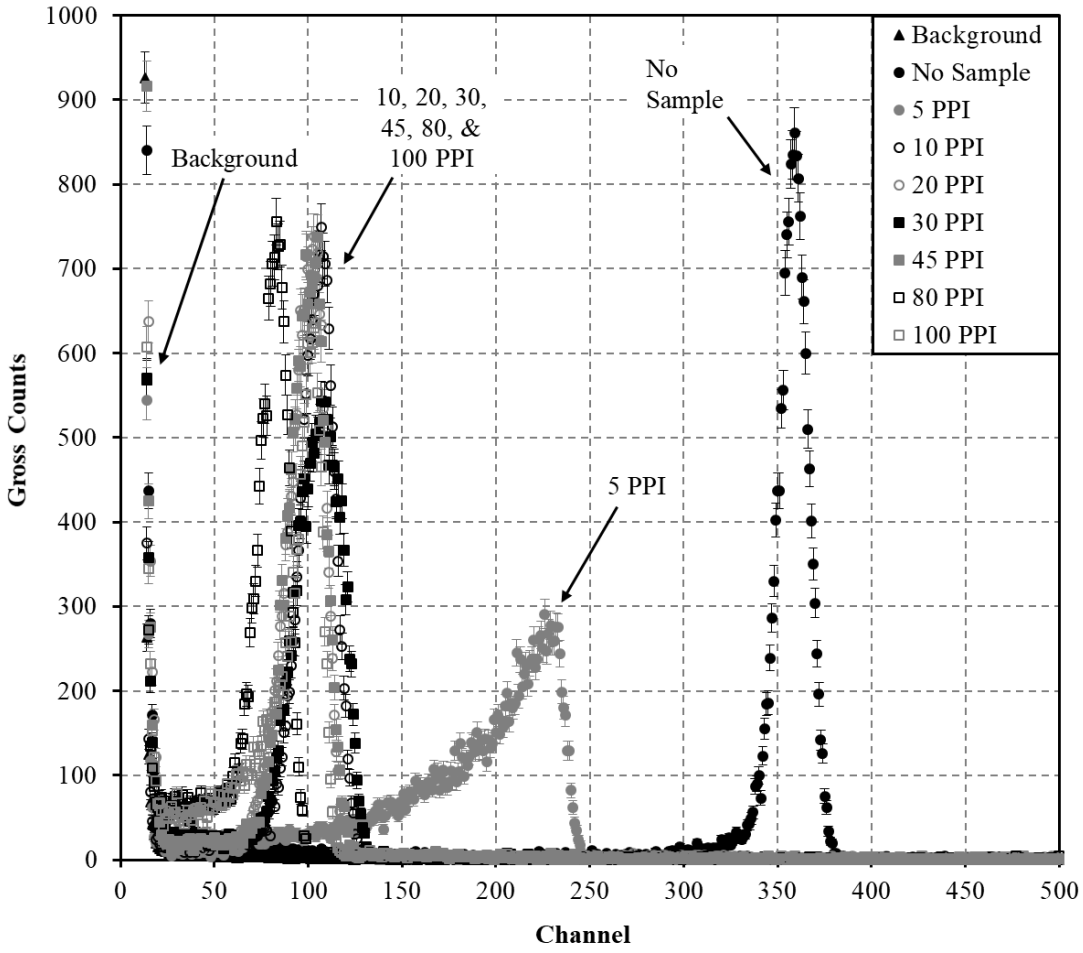

Figure 4.7. Pulse-height spectra measured using the testing configuration shown in Figure 4.6. The presence of pulses above background indicates that charge induction occurred, however the distance displaced by electrons was suspected to be between the site of charge-carrier liberation and the sample, as well as potentially shallow depths within each RVC foam sample [128].

In order to clarify whether electrons could traverse the bulk of RVC foam, the measurement method was refined. A parallel-plate electrode setup was again used, however a Frisch grid was installed between the sample location and the anode. The implementation of the Frisch grid allowed for determining whether electrons were actually traversing the thickness of each RVC foam sample because the measured pulse amplitude was defined by the distance displaced by electrons only between the Frisch grid and anode. However, prior to conducting measurements using the Frisch grid parallel-plate electrode setup, the parallel-plate electrode setup shown in Figure 4.8 was used to ensure that similar results to those listed Table 4.3 and shown in Figure 4.7 could be measured. The same plastic support structure and 6.35-mm (0.25-in.) thick, 25.4 mm (1-in.) diameter RVC foam samples were used. The 12.7-mm (0.50-in.) diameter planar, aluminum

electrodes were separated by a distance of approximately 29 mm. Teflon™ collars, with internal diameter of approximately 12.7 mm, were positioned between the RVC foam sample and the anode to ensure that electrons were streaming through, rather than around, the bulk of the RVC foam sample.

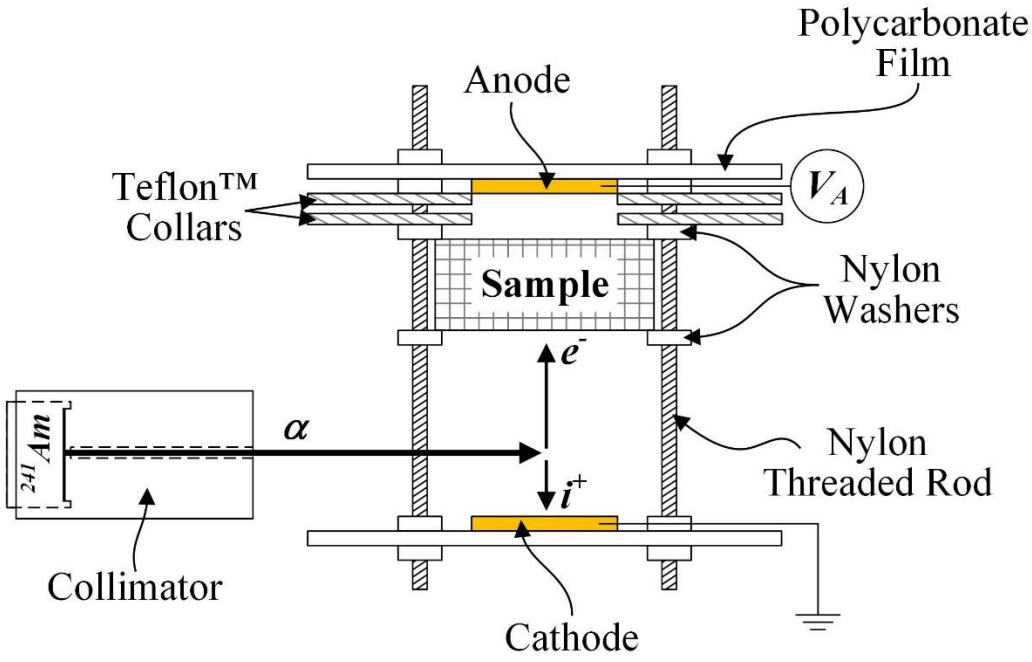

Figure 4.8. Refined parallel-plate electrode test configuration used for studying whether electrons could traverse the bulk of various linear pore densities of RVC foam [130].

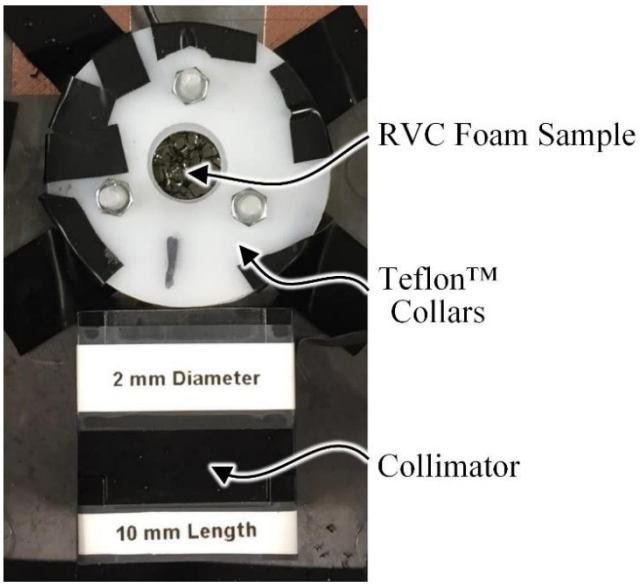

Figure 4.9. Top-down view of the collimated ^{241}Am alpha-particle source orientation relative to the test configuration. An RVC foam sample is positioned between the cathode and Teflon™ collars. The cathode is located below the sample.

A collimated ^{241}Am alpha-particle source was positioned so that a majority of the energy of the 5.48-MeV alpha particles was deposited between the RVC foam sample and cathode, based on the Bragg ionization curve of alpha particles in 1 psig of P-10 gas [96]. The anode operating voltage, V_A, was 700 V with the cathode maintained at ground potential to attain a reduced electric field strength of approximately 0.3 V cm^{-1} Torr^{-1} in 1 psig of P-10 [99, 129]. Throughout the duration of each measurement, the testing apparatus and collimated ^{241}Am alpha-particle source were contained within a sealed aluminum enclosure backfilled with a constant pressure of 1 psig of P-10 gas. Shown in Figure 4.9 is a top-down view of the test configuration with an RVC foam sample positioned between the cathode and Teflon™ collars. The position of the collimated ^{241}Am alpha-particle source relative to the test configuration is also shown.

The same testing procedure was used in which a two-hour measurement was conducted without an RVC foam sample that served as a control measurement. Two-hour measurements were then performed for RVC foam samples with linear pore densities of 5, 10, 20, 30, 45, 80, and 100 PPI. The sample was consistently positioned above the cathode surface to ensure that any charge motion occurring from the site of charge injection to either the cathode or the bottom of the sample was maintained throughout all trials. Likewise, the position of the collimated ^{241}Am alpha-particle source was maintained throughout all measurements to ensure that the same amount of energy was deposited between the cathode and RVC foam sample location.

The measured net count rates are listed in Table 4.4 and the pulse-height spectra are shown in Figure 4.10. The results are similar to those listed in Table 4.3 and shown in Figure 4.7 and suggest that charge induction occurred for each measurement. The same down-shift in peak channel number of the pulse-height spectra measured with the RVC foam samples relative to the no sample case occurred. The down-shift again suggests that electrons drifted a shorter distance, thus less charge was induced when an RVC foam sample was present. The pulse-height spectrum measured using the 5 PPI sample was not in the same location as shown in Figure 4.7, which suggests that electrons did not displace the same distance for both measurements. However, the measured net count rates and pulse-height spectra again suggest that the distance displaced by electrons was suspected to have occurred between the site of charge-carrier liberation and the sample, as well as potentially at shallow depths within each sample.

Table 4.4. Net count rates measured using the testing configuration shown in Figure 4.8. The collimated ^{241}Am alpha-particle source was positioned between the cathode and RVC foam sample locations [130].

Sample	Net Count Rate (counts second^{-1})
No Sample	3.47 ± 0.02
5 PPI	3.31 ± 0.03
10 PPI	3.37 ± 0.03
20 PPI	3.00 ± 0.03
30 PPI	2.74 ± 0.03
45 PPI	3.25 ± 0.03
80 PPI	3.04 ± 0.03
100 PPI	2.89 ± 0.03

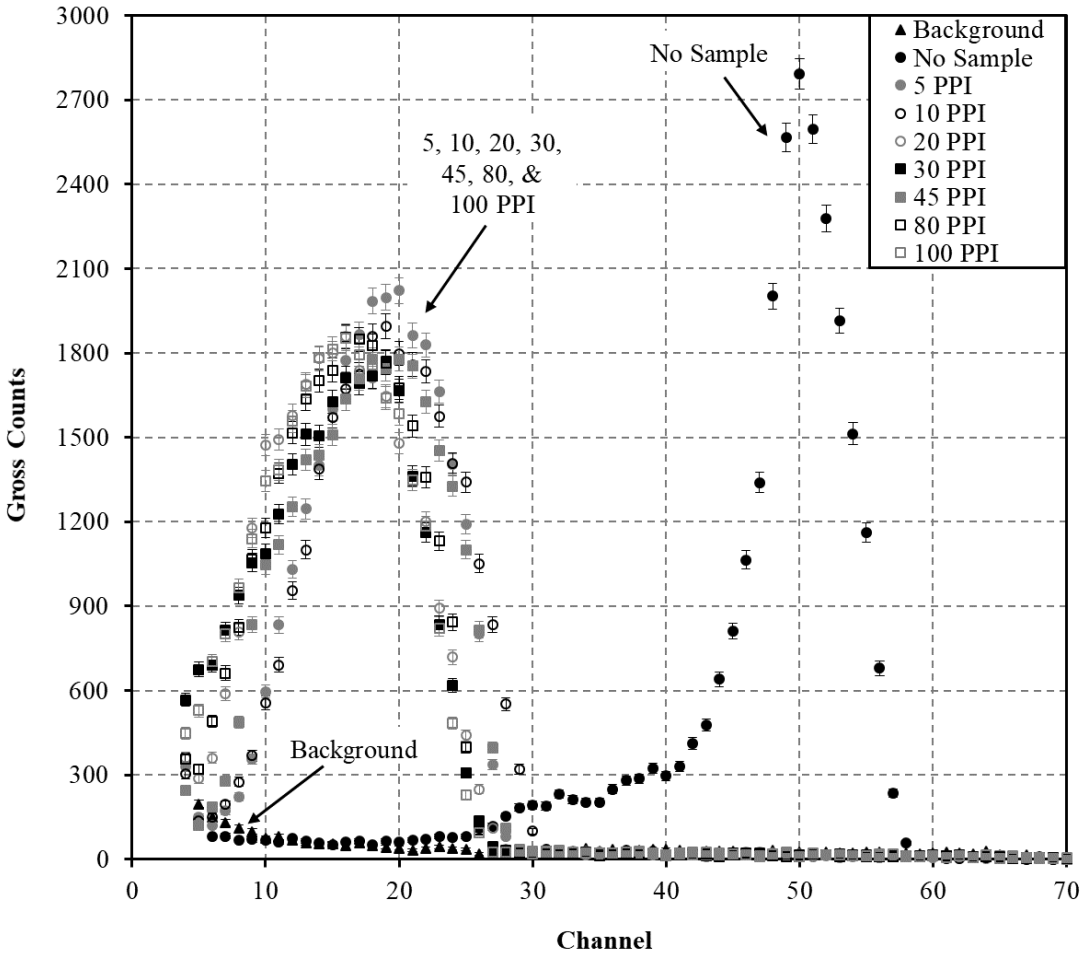

Figure 4.10. Pulse-height spectra measured using the testing configuration shown in Figure 4.8. The presence of pulses above background indicates that charge induction occurred, however the location of the charge induction was suspected to be between the site of charge-carrier liberation and the sample, as well as shallow depths within each RVC foam sample [130].

In order to determine whether electrons were traversing the bulk of the RVC foam samples, a Frisch grid was positioned approximately 0.79-mm below the surface of the anode, as shown in Figure 4.11. Using the testing configuration shown in Figure 4.11, the measured pulse-height spectrum and net count rate were representative of the charge-carrier motion only between the Frisch grid and anode. Shown in Figure 4.12 is the custom-designed 25.4-µm thick Frisch-grid electrode that was fabricated by Tech-Etch, Inc. The Frisch grid design featured 25.4-µm wide strips of BeCu with horizontal and vertical pitches of approximately 1.6 mm. The positions of the electrodes and collimated ^{241}Am alpha-particle source were the same as those used without the Frisch grid installed, as shown in Figure 4.13. P-10 gas at 1 psig was used for the measurements. Prior to inserting an RVC foam sample, the testing setup with the Frisch grid installed was characterized to determine the appropriate anode operating voltage. The Frisch-grid operating voltage, V_{FG}, was maintained at 700 V, and the cathode was maintained at ground potential. The anode operating voltage was increased in increments of 50 V from 0 V to 1650 V. The anode applied voltage was determined to be 1500 V. The RVC foam samples were then tested in the same manner as conducted without the Frisch grid installed.

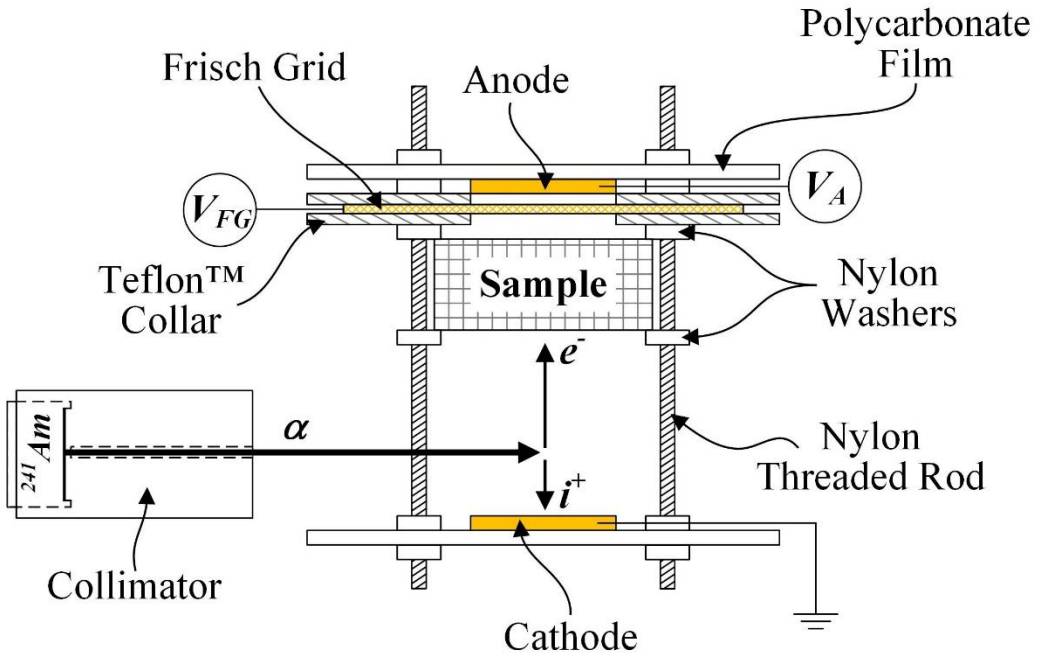

Figure 4.11. Parallel-plate electrode test configuration with a Frisch grid positioned between the sample and the anode [130].

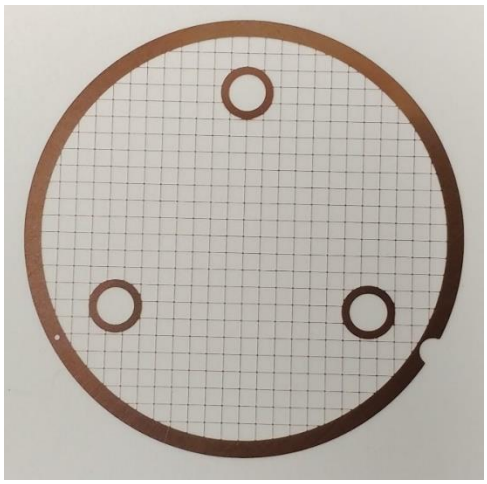

Figure 4.12. Frisch grid design featuring 25.4-µm wide strips of BeCu metal with vertical and horizontal pitches of approximately 1.6 mm [130].

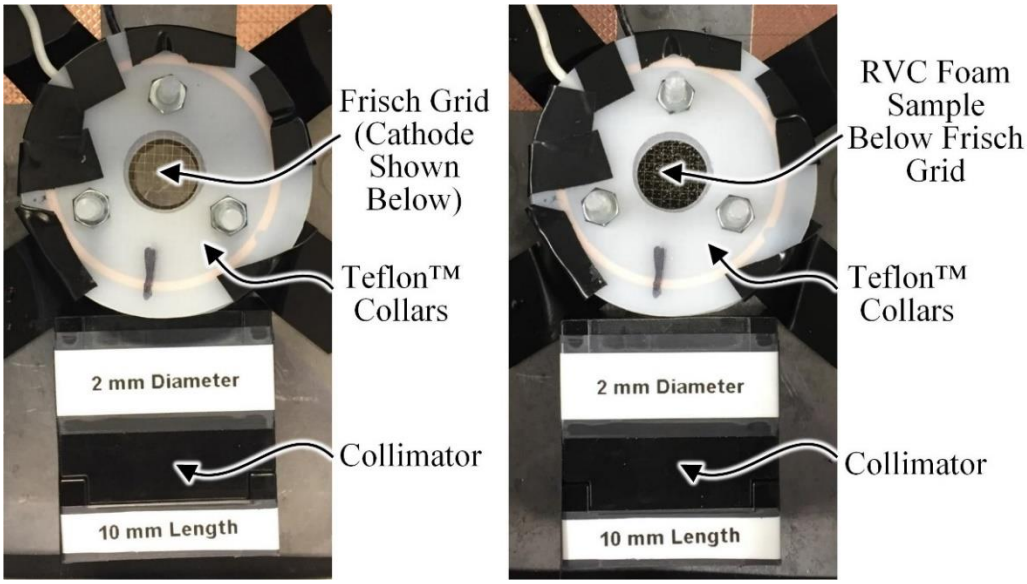

Figure 4.13. Top-down views of the test configuration, relative to the collimated ^{241}Am alpha-particle source, with (right) and without (left) an RVC foam sample positioned between the cathode and Teflon™ collars. The Frisch grid, positioned in between the Teflon™ collars, is also shown relative to the cathode (left) and RVC foam sample positioned above the cathode (right).

Shown in Figure 4.14 are the measured pulse-height spectra with the Frisch grid installed for the various RVC foam linear pore densities compared to the no sample case. Due to the blending of the measured pulse-height spectra with the background signal, negligible net count rates were measured for each of the RVC foam samples. Minimal, if any, charge motion occurred between the Frisch grid and anode for all RVC linear pore densities tested as indicated by the substantial reduction in peak channel number compared to the no sample case. Thus, electrons did

not traverse the bulk of RVC foam with linear pore densities ranging from 5 to 100 PPI, based on the measured pulse-height spectra and negligible net count rates for charge motion occurring between the Frisch grid and anode [130]. This result indicates that charge carriers liberated within the bulk of the substrate may not be measured and, therefore, only charge carriers created at or near the exterior substrate surfaces are capable of being measured. Thus, a $^{10}B_4C$-coated RVC foam sample is expected to be limited to functioning essentially as a thin-film-coated planar device. The maximum ε_{th} of $^{10}B_4C$-coated RVC foam is expected to be 4 – 5%, which is common for thin-film-coated planar devices [59].

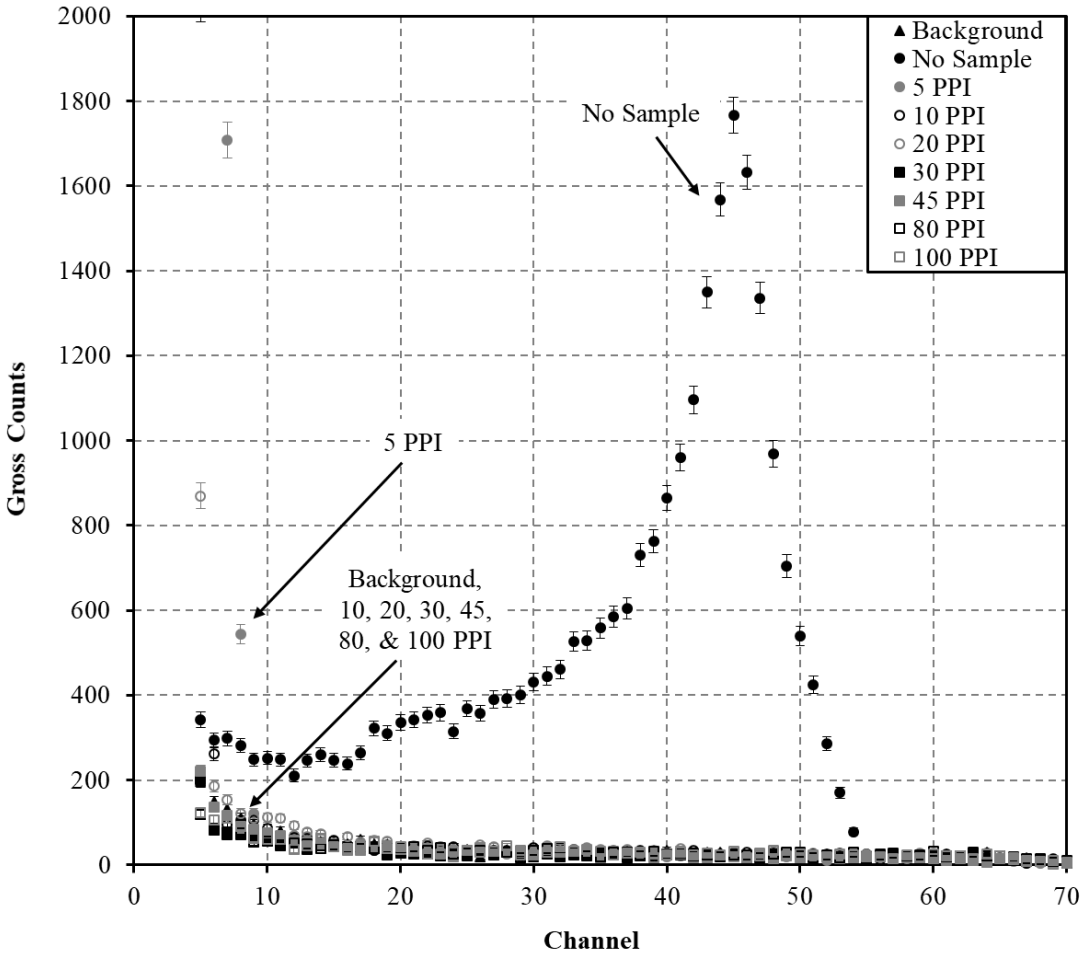

Figure 4.14. Measured pulse-height spectra resulting from electrons that traversed beyond the Frisch grid for various linear pore densities of RVC foam [130].

4.2.2 Neutron-Sensitivity Testing

Based on the results from the charge-carrier propagation study (Section 4.2.1), the ε_{th} of a $^{10}B_4C$-coated RVC foam sample was measured to determine if the sample would function essentially as a thin-film-coated planar substrate. A 6.35-mm (0.25-in.) thick 45 PPI RVC foam sample was waterjet-cut with a diameter of 4.1275 cm (1.625 in.). Exothermics, Inc. applied the $^{10}B_4C$ coating to the sample using magnetron sputtering. The desired coating thickness of the sample was specified as 0.4 µm in an attempt to achieve a ε_{th} of 53.2 ± 0.23% with a 75 keV LLD setting, as predicted in the literature [124]. However, the thickness of the $^{10}B_4C$ coating applied to the samples was measured to be 1.29 ± 0.47 µm using a Hitachi S-3400 N scanning electron microscope. Sixty-seven sample locations were measured in order to establish a distribution of coating thicknesses about the entire sample. Representative measurements of the $^{10}B_4C$ coating thickness are shown in Figure 4.15.

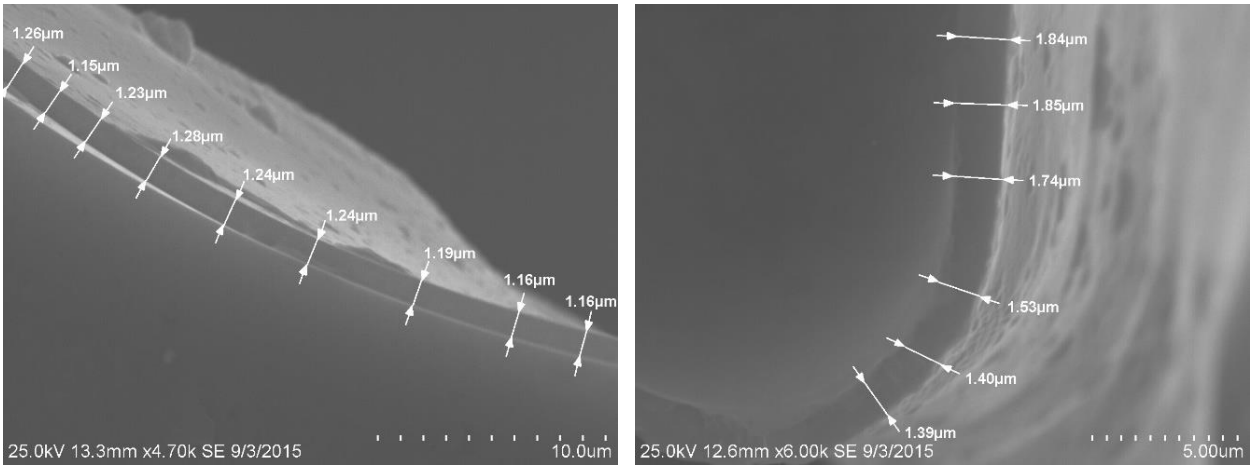

Figure 4.15. Scanning electron microscope images of $^{10}B_4C$ coatings applied to the 45 PPI RVC foam sample. An average $^{10}B_4C$ coating thickness distribution of 1.29 ± 0.47 µm was calculated based on the coating thicknesses measured at several sample locations.

Neutron-sensitivity measurements were conducted with the sample positioned within a continuous-gas-flow proportional counter, as shown in Figure 4.16. The continuous-gas-flow proportional counter featured a 25.4-µm diameter tungsten anode wire. The operating voltage of the anode wire was 700 V and the proportional counter walls were maintained at ground potential. P-10 gas was continuously flowed through the continuous-gas-flow proportional counter throughout the neutron-sensitivity measurements. ε_{th} measurements were conducted using the diffracted neutron beam of the KSU Training, Research, Isotopes, General Atomics (TRIGA)

Mark (Mk) II research reactor. The thermal-neutron beam was aligned with the side of the sample using a laser. The laser was previously calibrated to be aligned with the thermal-neutron beam. A 5-mm diameter aperture cadmium collimator was used to ensure the thermal-neutron beam was incident strictly on the side of the sample, thus eliminating solid-angle effects. The ε_{th} was calculated using Eq. (2.20) and Eq. (2.21) in reference to a 4.0-atm, 5.08-cm (2-in.) diameter, 15.24-cm (6-in.) long Reuter Stokes ^{3}He proportional counter with a measured ε_{th} of 80.7 ± 0.5% [89]. Energy calibration of the reaction-product pulse-height spectrum was conducted using a ^{148}Gd alpha-particle source. The energy calibration measurement was performed upon completion of neutron-sensitivity testing.

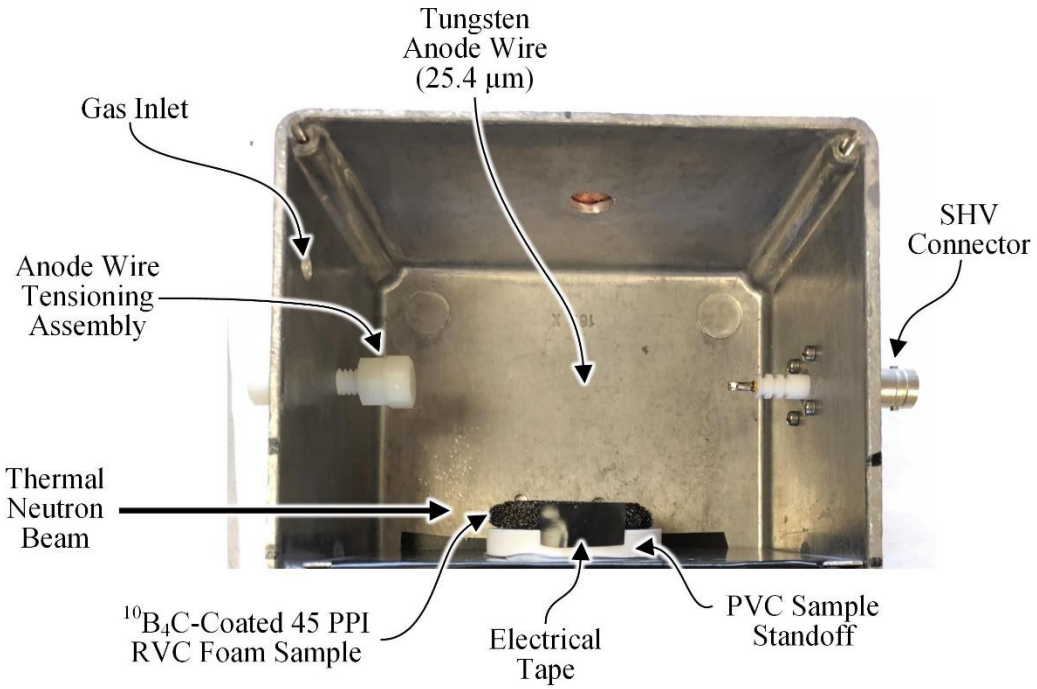

Figure 4.16. Top-down view of the 45 PPI RVC foam sample positioned within the continuous-gas-flow proportional counter testing device. The thermal-neutron beam was incident on the center of the side of the sample. During the ε_{th} and energy-calibration measurements, P-10 gas continuously flowed through the chamber.

Shown in Figure 4.17 are the reaction-product pulse-height spectra for the cases when the reactor was off (i.e. background), with the reactor on and the cadmium shutter closed, and with the reactor on and the cadmium shutter open. The ε_{th} was calculated to be 3.40 ± 0.09% for an LLD setting of 50 keV in reference to the energy-calibration measurement. The measured ε_{th} indicates that the $^{10}B_4C$-coated 45 PPI RVC foam sample functioned essentially as a thin-film-coated planar

device. Thus, the measured ε_{th} suggests that neutron-induced pulses are formed from charge carriers liberated at or near the exterior surfaces of the coated substrate and not from those liberated deep within the bulk of the sample. In order to achieve the performance of commercially-available ^{3}He proportional counters, several consecutive layers of thin-film-coated RVC foam substrates are required. Therefore, because of the observed results, further investigations of thin-film-coated RVC foams as neutron-conversion media were suspended.

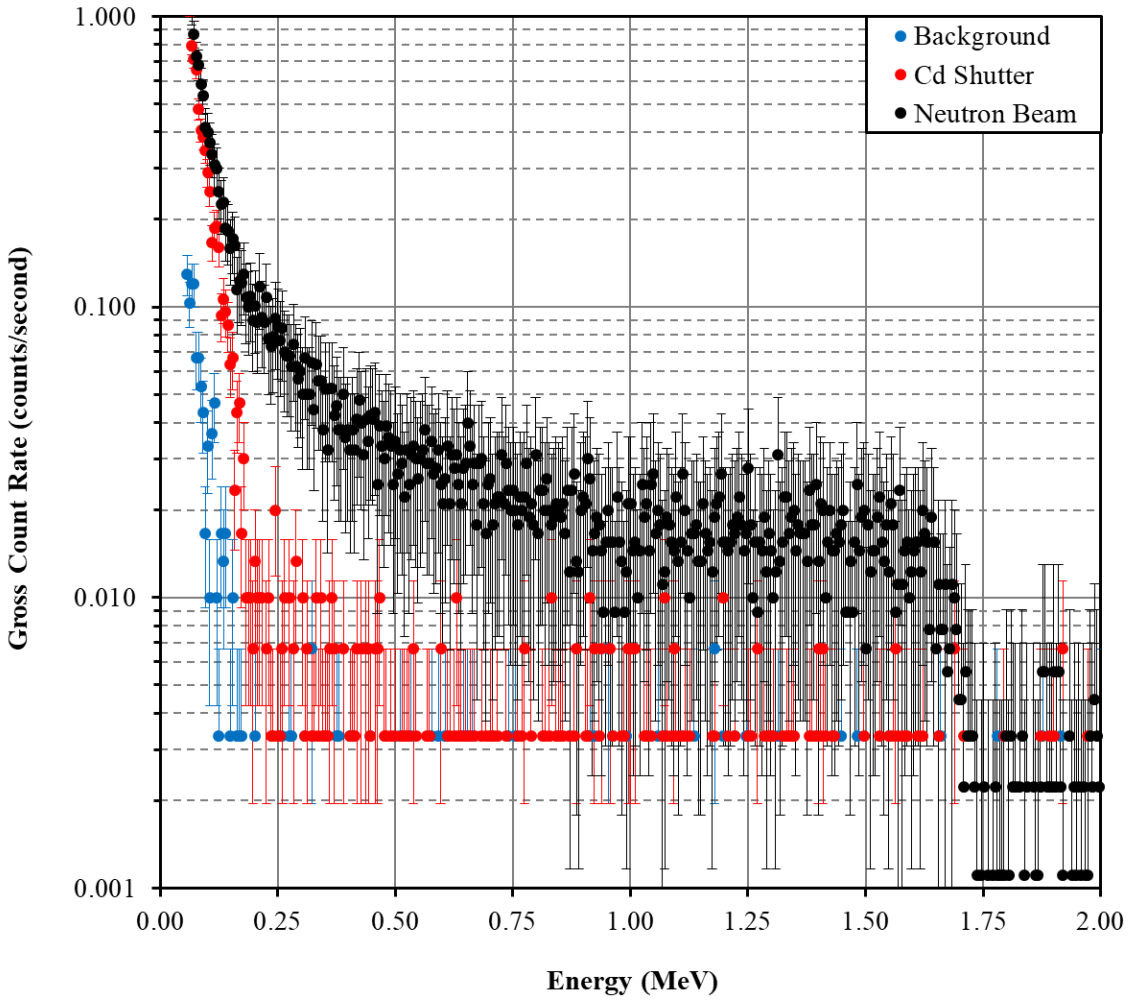

Figure 4.17. Measured reaction-product pulse-height spectrum of the $^{10}B_4C$-coated 45 PPI RVC foam sample relative to a background measurement and a measurement in which a cadmium shutter blocked the incident thermal-neutron beam. The LLD setting was calculated to be 50 keV [128].

4.3 $^{10}B_4C$-Coated Honeycomb Substrates

Honeycomb substrates have recently emerged as a thin-film-coated substrate for thermal-neutron detection applications [46, 113, 114, 131, 132] due to the amount of coating surface contained within a light-weight, compact substrate size. Honeycomb substrates feature an array of hexagonal cells, as shown in Figure 4.18. The cell size, wall thickness between neighboring hexagonal cells, and the thin-film coating thickness are defined in Figure 4.19. The nominal wall thickness between neighboring hexagonal cells ranges from approximately 36 – 200 μm (0.0007 – 0.004 in.), depending on the cell size [133]. Honeycomb substrates are commonly used in commercial industries as structural materials, directional flow guides, and energy absorbers due to their high strength-to-weight ratio [134]. Several companies manufacture honeycomb substrates [134-137] using materials such as aluminum and plastics and the size of the cells can be adjusted depending on the desired application [134, 135, 138]. Shown in Figure 4.20 are aluminum honeycomb samples with cell sizes of 0.635 cm (0.25 in.), 0.3175 cm (0.125 in.), or 0.15875 cm (0.0625 in.).

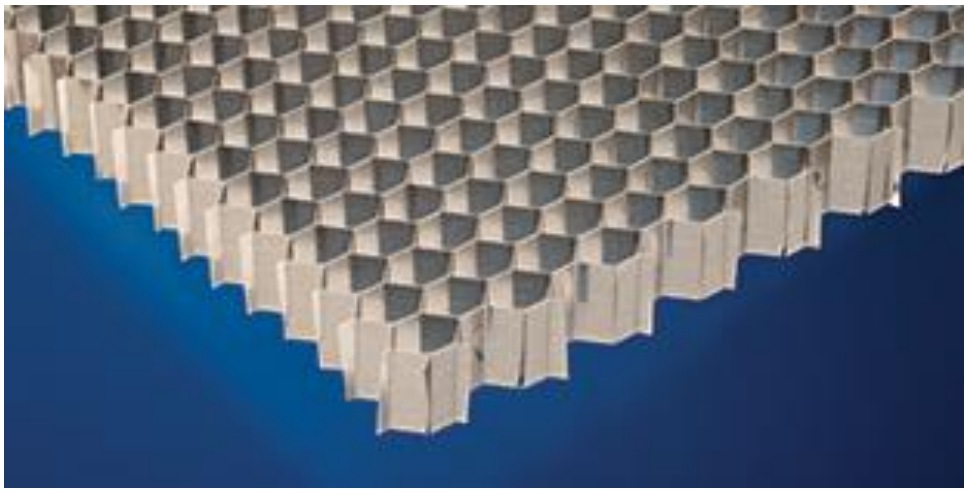

Figure 4.18. Lattice of hexagonal cells contained within an aluminum-honeycomb substrate [133]. A compact neutron counter capable of high ε_{th} can be fabricated by applying a thin-film-coating layer to the walls of the honeycomb substrate.

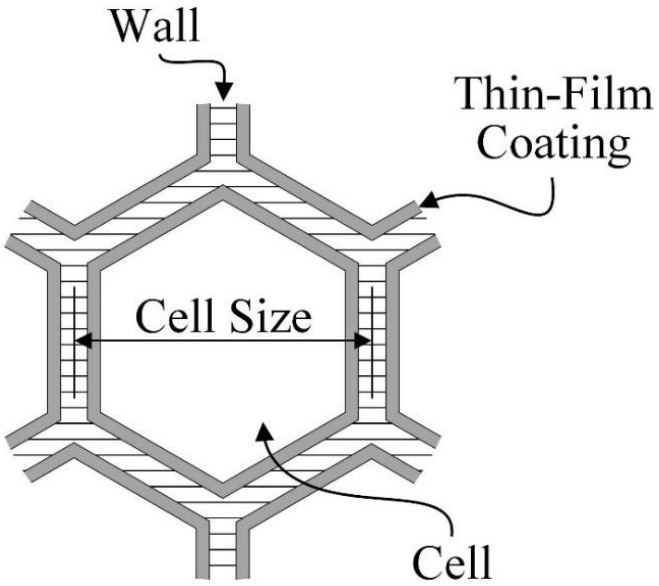

Figure 4.19. Top-down illustration of the thin-film coating (gray) relative to the honeycomb material (horizontal cross-hatching) and the gas contained within each cell (white) [110].

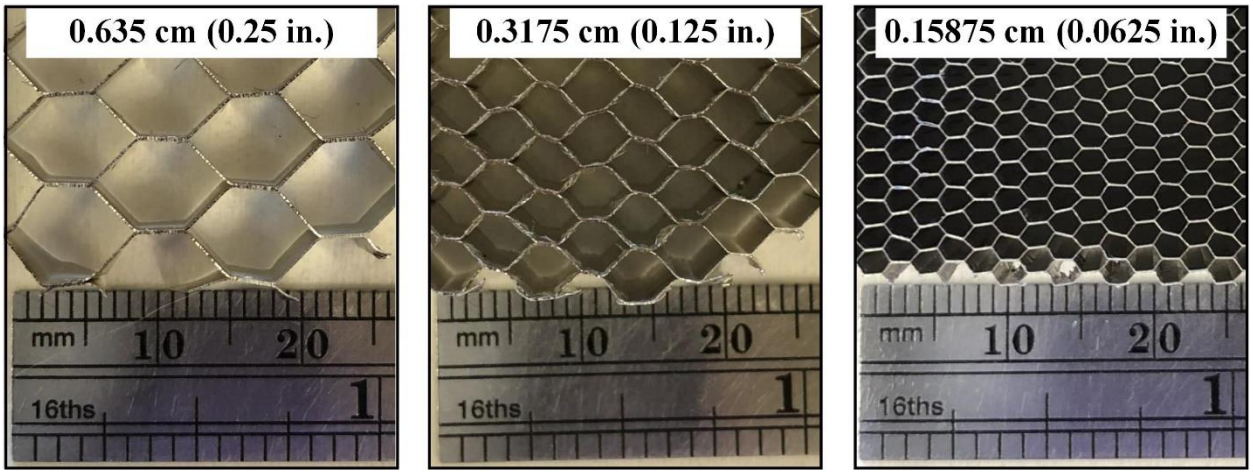

Figure 4.20. Aluminum honeycomb samples with cell sizes of 0.635 cm (left), 0.3175 cm (center), or 0.15875 cm (right).

The intended neutron-detection process using $^{10}B_4C$-coated aluminum honeycomb is similar to other thin-film-coated neutron-conversion media. Charged-particle reaction products are emitted following the absorption of a neutron within the $^{10}B_4C$ thin-film coating. Based on the ranges of the $^{10}B(n, \alpha)^7Li$ reaction products in aluminum and $^{10}B_4C$ (listed in Table 4.5 [96]), one of the reaction products is absorbed within the $^{10}B_4C$ and/or aluminum honeycomb substrate, while the other may escape the $^{10}B_4C$ to ionize the gas, as illustrated in Figure 4.21. Charge carriers are liberated as the reaction product ionizes the gas. The charge carriers then drift toward their

respectively-charged electrodes under the influence of the electric field formed by the potential difference between the anode and cathode.

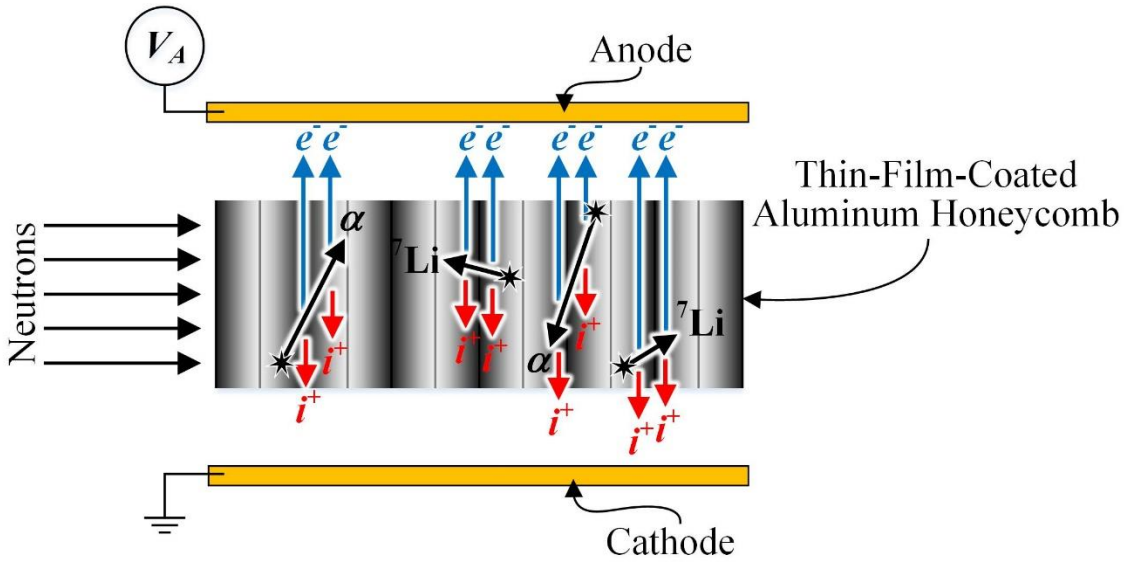

Figure 4.21. Neutron-detection process using a thin-film-coated aluminum honeycomb sample.

Table 4.5. The ranges of $^{10}B(n, \alpha)^7Li$ reaction products in $^{10}B_4C$, aluminum honeycomb, and 1 – 5 atm of P-10 gas [96]. The density, ρ, of each material is also listed [96, 115].

Material	**ρ (g cm^{-3})**	**0.840 MeV ^{7}Li (μm)**	**1.015 MeV ^{7}Li (μm)**	**1.470 MeV ^{4}He (μm)**	**1.777 MeV ^{4}He (μm)**
Thin-Film Coating					
$^{10}B_4C$	2.16	1.63	1.83	3.23	3.99
Substrate					
Aluminum Honeycomb	2.70	2.25	2.59	4.65	5.71
P-10 Gas					
1 atm	0.00156	4210	4690	8040	9900
2 atm	0.00312	2100	2340	4020	4950
3 atm	0.00468	1400	1560	2680	3300
4 atm	0.00624	1050	1170	2010	2470
5 atm	0.00780	842	939	1610	1980

A distribution of reaction-product energy can be deposited within the hexagonal cells depending on the cell size, the location of reaction-product emission within the $^{10}B_4C$ coating, and the trajectory of the reaction product. Shown in Figure 4.22 are the distribution of reaction-product trajectories for shorter- (^{7}Li ions) and longer-range (^{4}He ions) reaction products emitted at the interface of the $^{10}B_4C$ coating and the gas within the hexagonal cell. The distribution of reaction-

product trajectories depicted in scenario *a* shows the energy of the shorter-range reaction product (shaded yellow) being deposited within the cell without the reaction product colliding with the surrounding $^{10}B_4C$ coating (shaded gray). However, some of the longer-range reaction-product trajectories (shaded blue) result in a portion of the reaction-product energy being deposited within the cell before the reaction-product collides with a cell wall. When the reaction-product is emitted within close proximity of a nearby cell wall (scenario *b*), some of the shorter- and longer-range reaction-product trajectories result in a portion of the reaction-product energy being deposited within the cell before the reaction-product collides with any of the surrounding $^{10}B_4C$-coated cell walls.

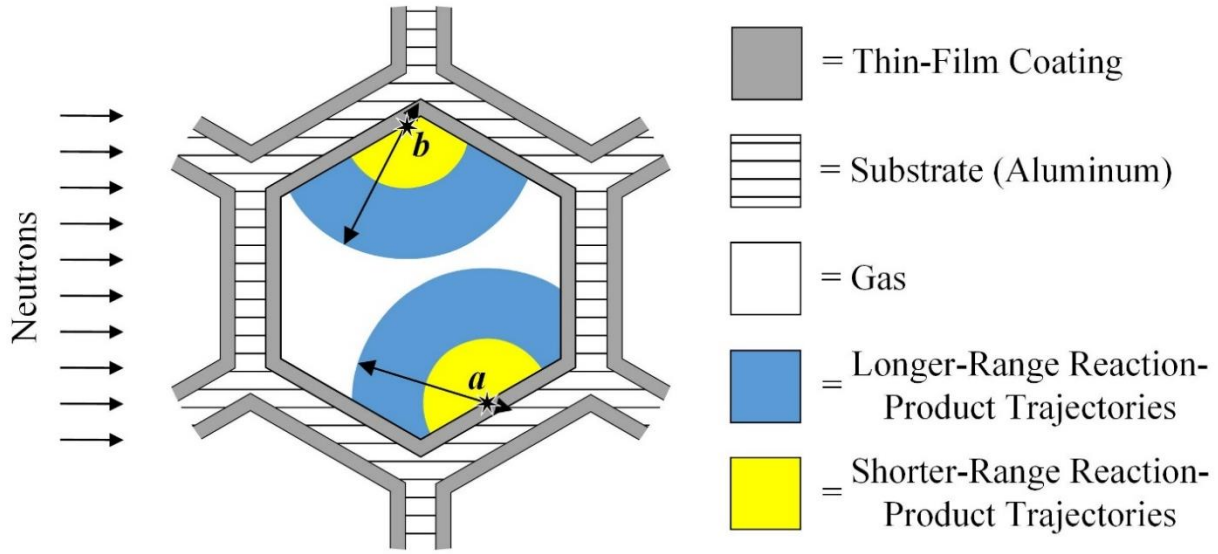

Figure 4.22. Distribution of potential reaction-product trajectories for reaction products emitted at the interface between the thin-film coating and the gas.

As the location of reaction-product emission occurs deeper within the $^{10}B_4C$ coating, self-absorption effects occur. Consequently, a portion of the reaction-product energy is deposited within the $^{10}B_4C$ coating before the reaction product escapes the $^{10}B_4C$ coating. Thus, the range of the reaction product within the gas is dependent on the amount of energy retained by the reaction product upon emerging from the $^{10}B_4C$ coating. The reduction in reaction-product range as a function of the location of reaction-product emission within the $^{10}B_4C$ coating is depicted in scenarios *c* – *e* of Figure 4.23. Therefore, the amount of reaction-product energy deposited within the hexagonal cells is dependent on the reaction-product emission location within the $^{10}B_4C$ coating as well as the reaction-product trajectory.

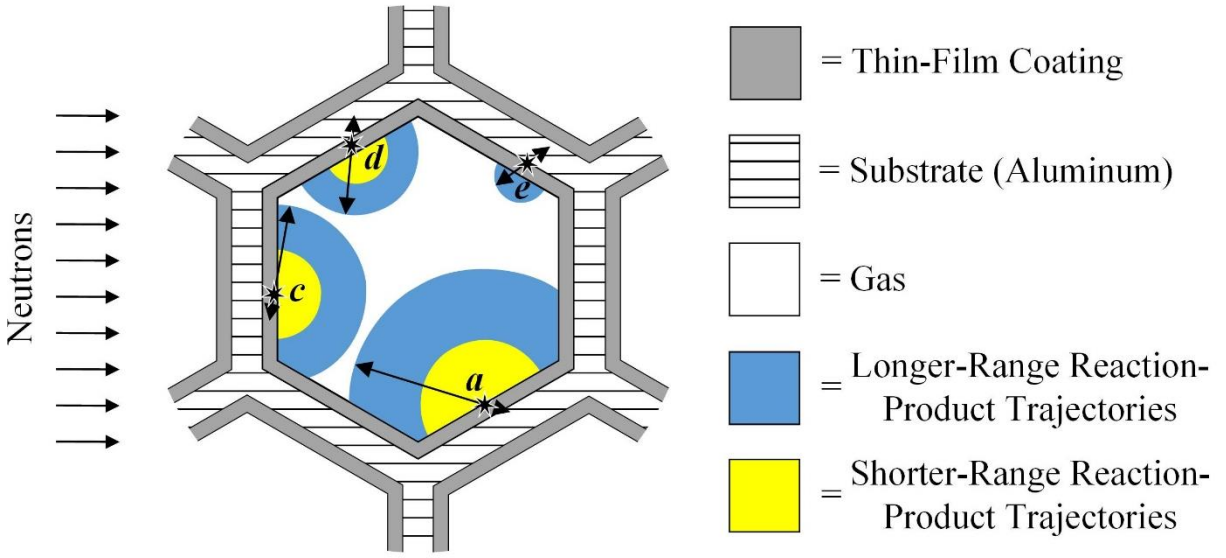

Figure 4.23. Examples of reaction-product emission locations within the thin-film coating of an aluminum honeycomb sample. The distribution of potential reaction-product trajectories are also shown.

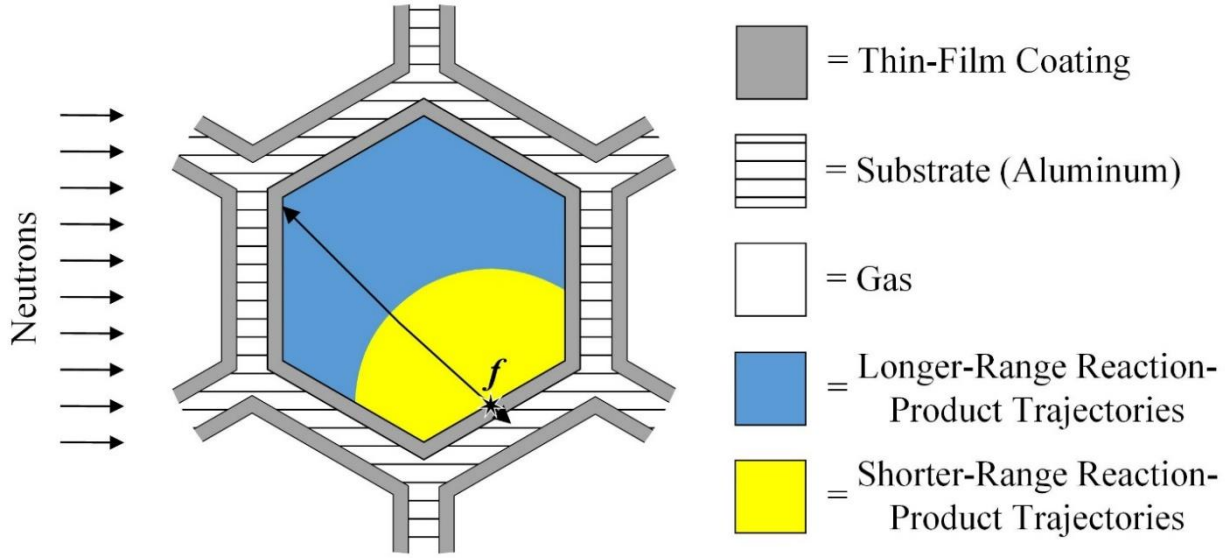

Figure 4.24. Example of a reaction-product trajectories when the cell size is sufficiently small that the longer-range reaction-product collides with the thin-film-coating layer.

The cell size of the honeycomb cells can also affect the amount of reaction-product energy deposited within a hexagonal cell. Consider scenario *f* depicted in Figure 4.24, in which the cell size is small enough that a portion of the longer-range reaction product is deposited within the cell before the reaction-product collides with the surrounding $^{10}B_4C$ coating, regardless of the reaction-

product trajectory. Some of the shorter-range reaction-product trajectories also result in a portion of the reaction-product energy being deposited within the cell before the reaction product collides with the surrounding $^{10}B_4C$ coatings. The range of the reaction products can be reduced by increasing the gas pressure within the cells. For sufficiently high gas pressures, the reaction-product ranges depicted in scenario *f* can be reduced to be similar to those depicted in scenario *a* of Figure 4.23. However, recalling Eq. (3.26), the charge-carrier mobilities will be affected by an increase in the gas pressure. Therefore, recalling Eq. (3.25), in order to retain the charge-carrier velocities, the electric field strength must be increased to compensate for the increase in gas pressure.

4.3.1 Neutron-sensitivity Testing

A 1.27-cm (0.5-in.) thick aluminum-honeycomb sample was waterjet-cut with a diameter of 4.1275 cm (1.625 in.). The sample contained hexagonal cells with a cell size of 0.15875 cm (0.0625 in.). Exothermics, Inc. applied the $^{10}B_4C$ coating using magnetron sputtering. Using a Hitachi S-3400N scanning electron microscopic, the $^{10}B_4C$ coating thickness was measured to be 4.68 ± 1.25 μm. Twenty-four sample locations were measured in order to establish a distribution of coating thicknesses about the entire sample. Representative measurements of the $^{10}B_4C$ coating thicknesses are shown in Figure 4.25.

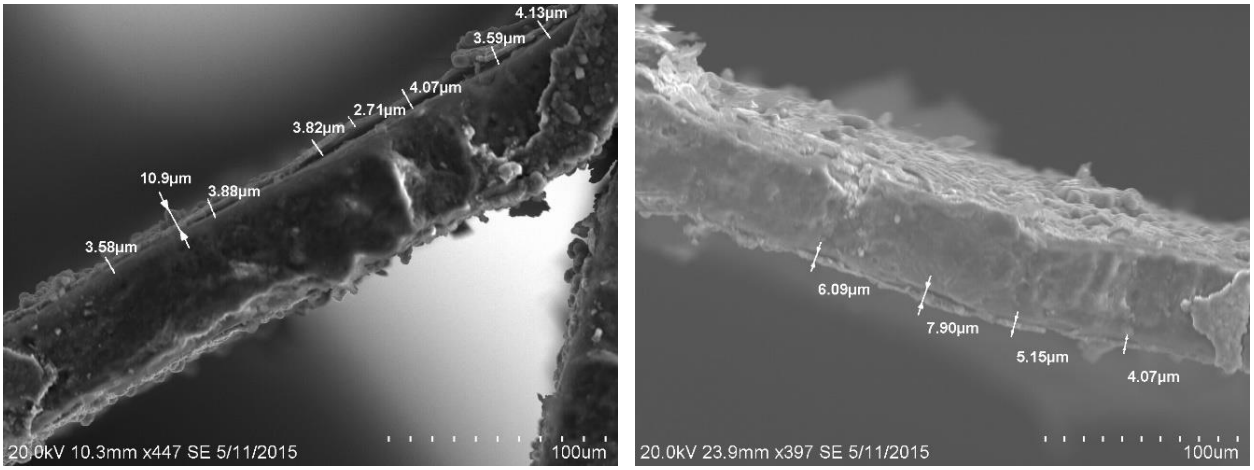

Figure 4.25. Scanning electron microscope measurements of the $^{10}B_4C$ coating thicknesses at different sample locations. An average $^{10}B_4C$ coating thickness distribution of 4.68 ± 1.25 μm was calculated based on the coating thicknesses measured at several sample locations [110].

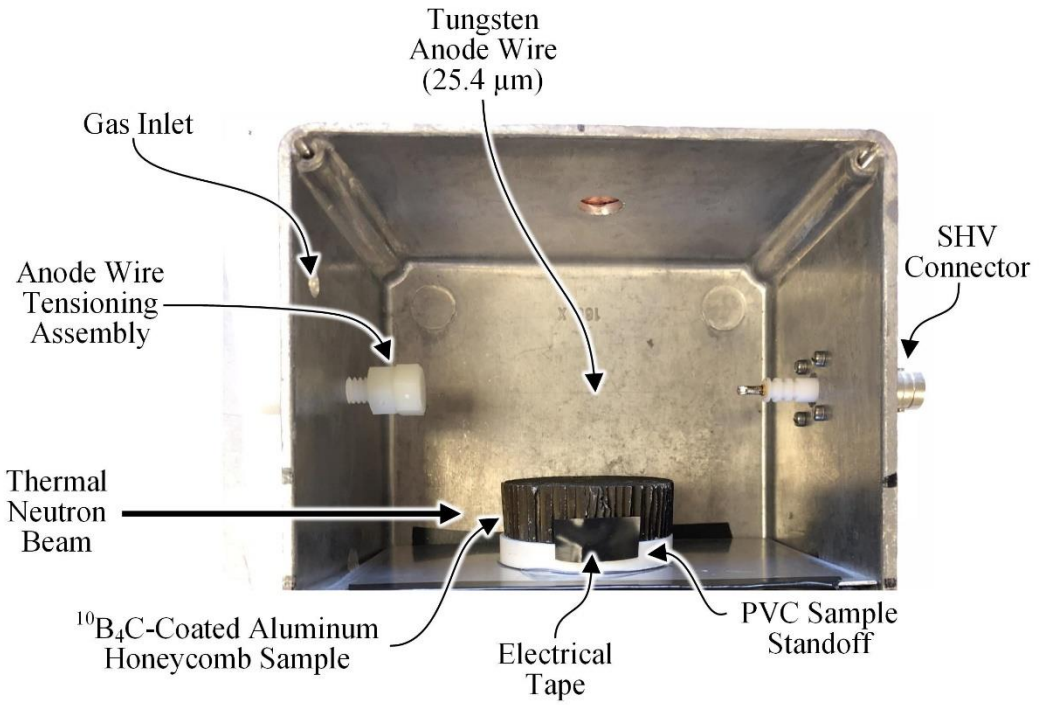

Figure 4.26. Top-down view of the $^{10}B_4C$-coated aluminum-honeycomb sample position relative to the thermal-neutron beam. The sample was positioned within a continuous-gas-flow proportional counter testing device. Throughout the ε_{th} and energy-calibration measurements, P-10 gas continuously flowed through the chamber.

Neutron-sensitivity measurements were conducted in the same manner as with $^{10}B_4C$-coated 45 PPI RVC foam. The sample was positioned within a continuous-gas-flow proportional counter featuring a 25.4-µm diameter tungsten anode wire, as illustrated in Figure 4.26. The operating voltage of the anode wire was 700 V and the proportional counter walls were maintained at ground potential. P-10 gas was supplied to the proportional counter throughout the duration of the ε_{th} measurements. The diffracted neutron beam of the KSU TRIGA Mk II research reactor was used to perform the ε_{th} measurements. A laser was used when aligning the thermal-neutron beam with the side of the sample. The laser was previously calibrated to be aligned with the thermal-neutron beam. A cadmium collimator with a 5-mm diameter aperture was used to ensure that the thermal-neutron beam was incident only on the sample. The measured ε_{th} of the $^{10}B_4C$-coated aluminum-honeycomb sample was calculated using Eq. (2.20) and Eq. (2.21). A 4.0 atm, 5.08-cm (2 in.) diameter, 15.24-cm (6 in.) long Reuter Stokes ^3He tube with a measured ε_{th} of 80.7 ± 0.5% [89] was used as a reference detector. After the neutron-sensitivity measurement, energy

calibration of the reaction-product spectrum was accomplished with a ^{148}Gd alpha-particle source positioned within the continuous-gas-flow proportional counter.

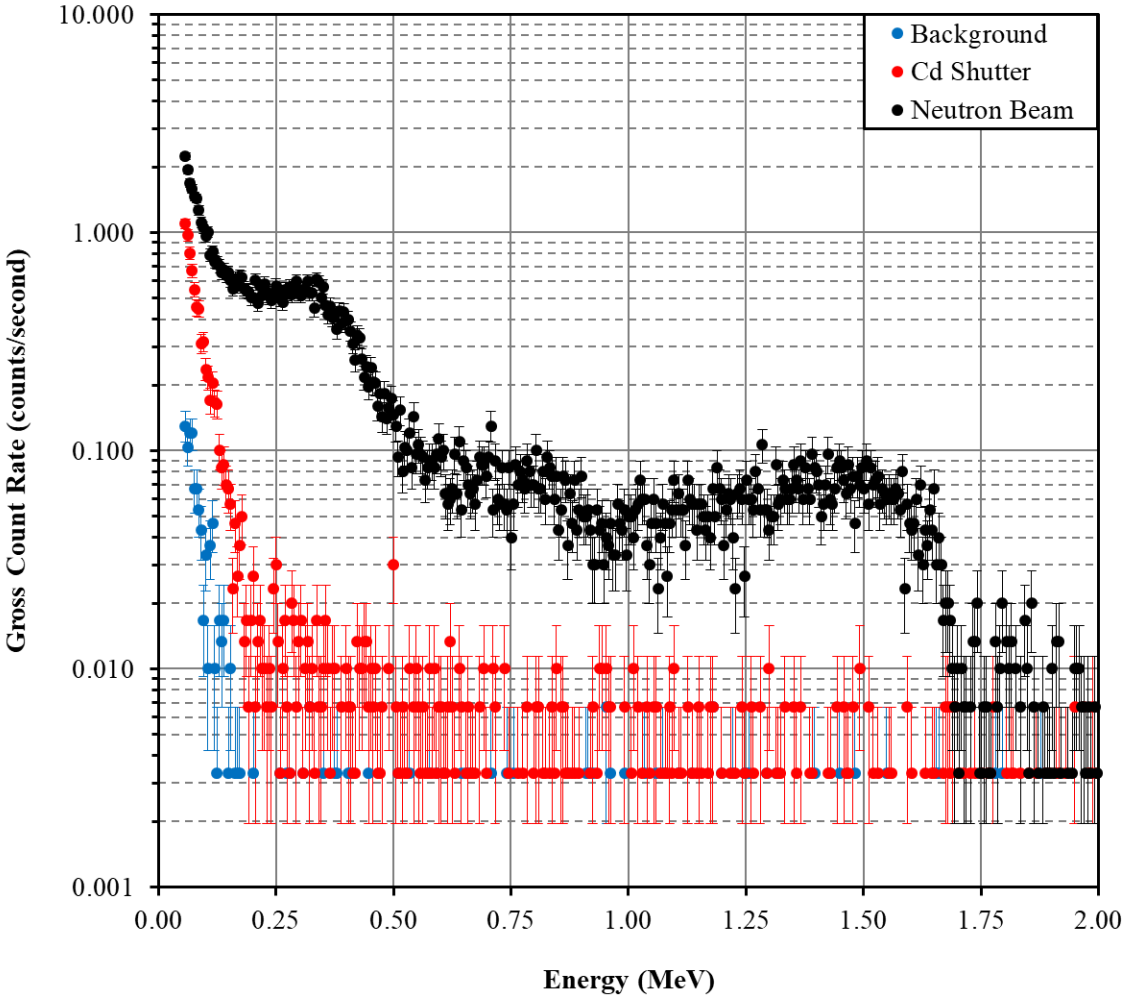

Figure 4.27. Reaction-product pulse-height spectrum measured for the $^{10}B_4C$-coated aluminum-honeycomb sample with an LLD setting of 50 keV relative to the background measurement. Also shown is the measurement when the neutron beam was blocked by the cadmium shutter [110].

Shown in Figure 4.27 are the measured reaction-product pulse-height spectra for the cases when the reactor was off (i.e. background), with the reactor on and cadmium shutter closed, and with the reactor on and the cadmium shutter open. For an LLD setting of 50 keV in reference to the energy-calibration measurement, the measured ε_{th} was calculated to be 21.45 ± 0.26%, which is the highest measured ε_{th} to date for coated honeycomb media. The measured ε_{th} was benchmarked by simulating the ε_{th} for the distribution of measured $^{10}B_4C$ coating thicknesses applied to the aluminum-honeycomb sample. The simulations were conducted using *MCNP6*. The

dimensions of the measured sample were used for the simulation (1.27-cm (0.5-in.) thick, 4.1275-cm (1.625-in.) diameter, 0.15875-cm (0.0625 in.) cell size). The simulation environment was modeled with P-10 proportional gas at ambient pressure and a 5-mm diameter thermal-neutron beam incident on the center of the side of the sample. The ε_{th} was simulated for uniform $^{10}B_4C$ coating thicknesses between 3.5 – 6.0 µm in 0.1 µm increments. The range of $^{10}B_4C$ coating thicknesses implemented into the simulations was based on the measured average coating thickness and associated error (4.68 ± 1.25 µm).

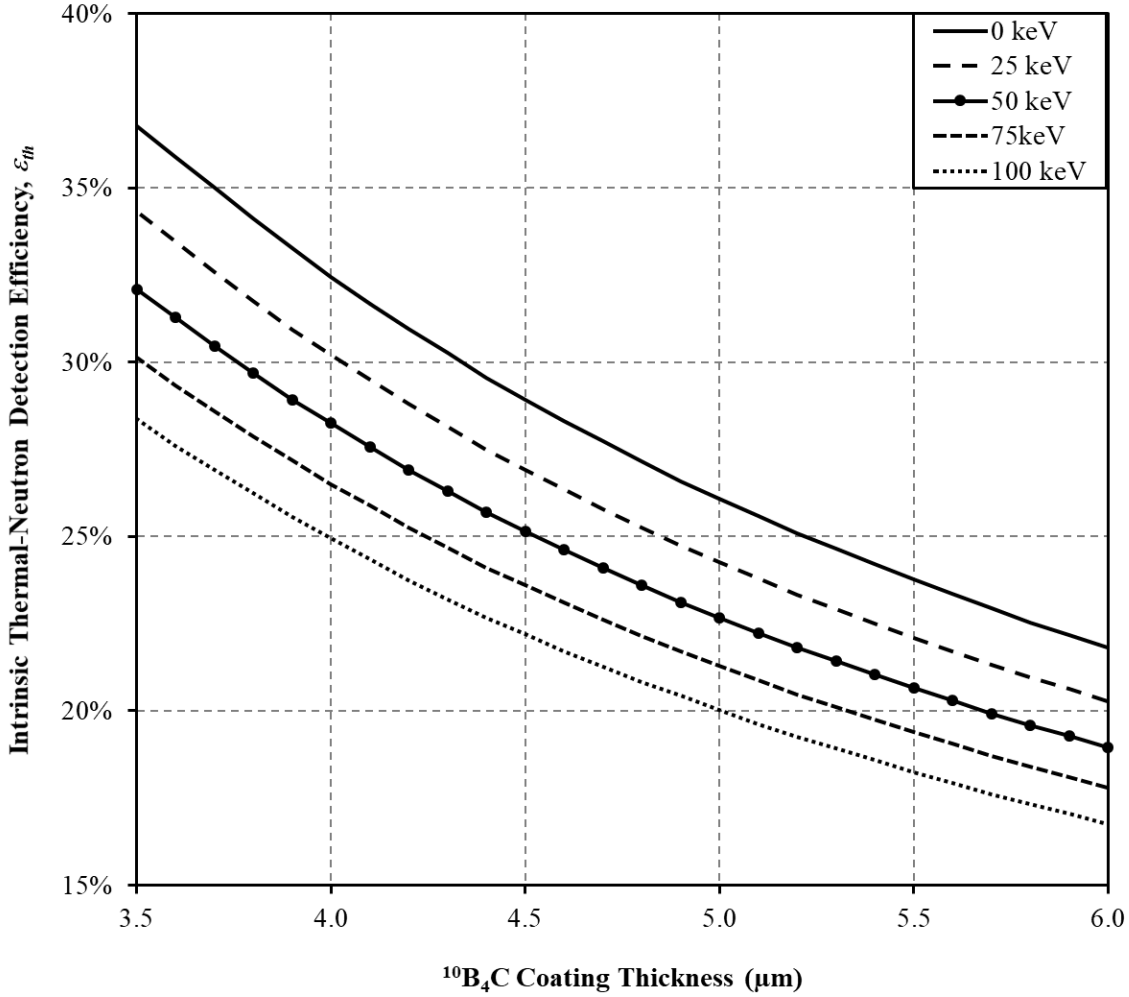

Figure 4.28. MCNP6-simulated ε_{th} as a function of $^{10}B_4C$ coating thickness ranging from 3.5 to 6.0 µm for various LLD settings. For a given coating thickness, the simulated ε_{th} decreases as the LLD setting is increased [110].

The distributions of simulated ε_{th} as a function of $^{10}B_4C$ coating thickness for LLD settings ranging from 0 to 100 keV are shown in Figure 4.28. For a 50 keV LLD setting, the simulated ε_{th}

varies from approximately 33% to 19% for $^{10}B_4C$ coating thicknesses ranging from 3.5 to 6.0 μm, respectively. A comparison of the measured and simulated ε_{th} reveals that the measured ε_{th} falls within the ranges of simulated values for similar LLD settings. Upon closer inspection, the simulated ε_{th} for a $^{10}B_4C$ coating thickness of 4.68 μm, the average coating thickness measured from the sample, was approximately 24% with an LLD setting of 50 keV. The difference between measured and simulated ε_{th} at the average coating thickness is suspected to be due to the measured distribution of $^{10}B_4C$ coating thicknesses. Specifically, the measured average coating thickness and associated error (4.68 ± 1.25 μm) were a representation of several locations measured on the exterior surfaces of the sample. A broader distribution of coating thicknesses may have been present about the sample for both internally- and externally-located coating surfaces.

4.3.2 Coating Thickness Optimization and Simulated Neutron Sensitivity

Simulation studies to define the thermal-neutron detection capabilities of thin-film-coated aluminum-honeycomb substrates are limited to either the benchmarked results described in Section 4.3.1 or the optimization of natural boron coatings [114, 131]. Therefore, additional *MCNP6* simulations of ε_{th} were performed to define the optimal $^{10}B_4C$ coating thickness for commercially-available honeycomb cell sizes of 0.635 cm (0.25 in.), 0.3175 cm (0.125 in.), and 0.15875 cm (0.0625 in.). The angular sensitivity of the substrate to incident neutrons was also simulated for each cell size. Finally, the effects of gas pressure on the ε_{th} as a function of LLD setting were studied to further-optimize the theoretical operating parameters of each cell size. For all simulation studies, the height and diameter of the substrate were defined as 1.27 cm (0.5 in.) and 4.1275 cm (1.625 in.), respectively. The wall thickness of the 5052 aluminum between neighboring cells was defined as 130 μm, 75 μm, or 60 μm corresponding to cell sizes of 0.635 cm (0.25 in.), 0.3175 cm (0.125 in.), or 0.15875 cm (0.0625 in.), respectively. The $^{10}B_4C$-coating thickness was assumed to be uniform about the interior of each cell.

MCNP6 simulations were performed to determine the optimal $^{10}B_4C$ coating thickness for each cell size. The ε_{th} was simulated for $^{10}B_4C$ coating thicknesses ranging from 0 to 5 μm in 0.1 μm increments. Shown in Figure 4.29 is an illustration of the simulation environment. The thin-film-coating, wall, and cell size definitions are also shown in Figure 4.29. P-10 gas at a pressure of 2.8 atm was initially defined as the backfill gas. The center of a 5-mm diameter thermal-neutron

beam was positioned at the center of the height of the substrate, normal to the substrate surface. The simulation environment was defined to emulate the expected testing environment for $^{10}B_4C$-coated aluminum-honeycomb samples that would be deployed as a ^{3}He-alternative technology with a similar form factor to commercially-available ^{3}He proportional counters. Therefore, the $^{10}B_4C$-coated aluminum-honeycomb sample was positioned within a 5.08-cm (2-in.) diameter cylindrical aluminum enclosure with a wall thickness of 0.15875 cm (0.0625 in.). A spacing of 0.3175 cm (0.125 in.) was implemented between the exterior surfaces of the $^{10}B_4C$-coated aluminum-honeycomb sample and the cylindrical aluminum enclosure interior surfaces.

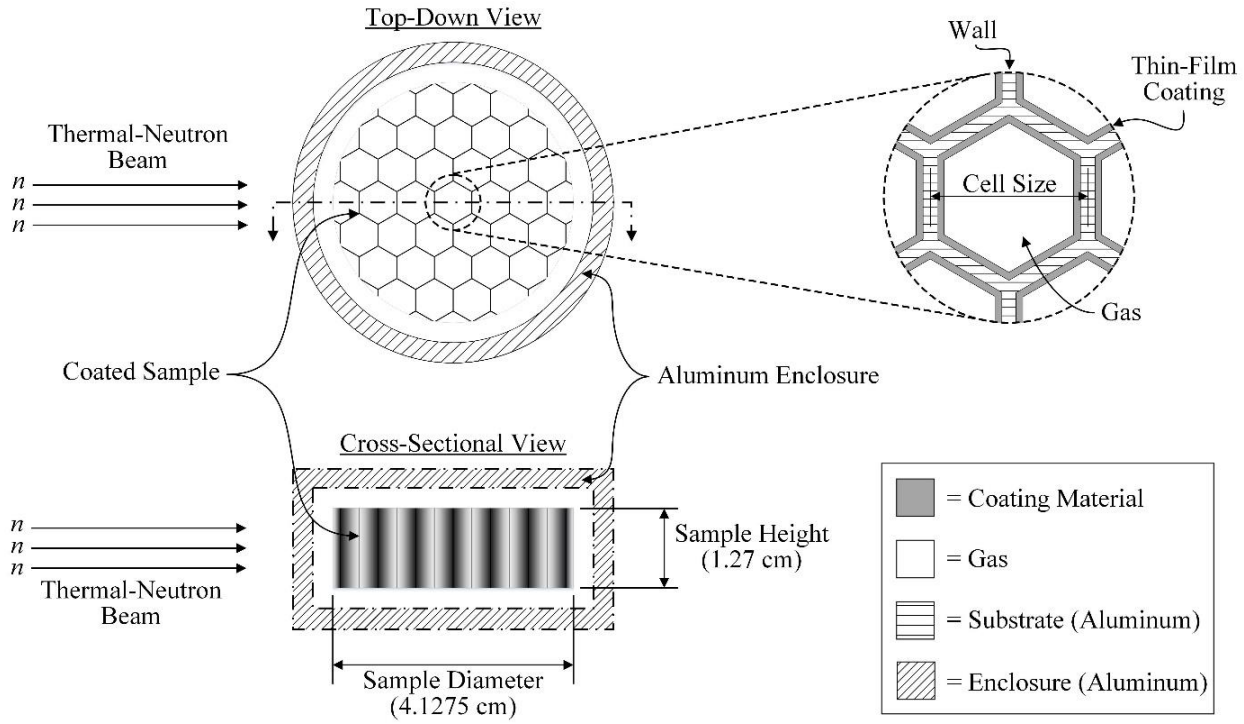

Figure 4.29. MCNP6 simulation environment used for determining the optimal $^{10}B_4C$ coating thickness of aluminum-honeycomb substrates.

Shown in Figure 4.30 are the simulated ε_{th} as a function of $^{10}B_4C$ coating thickness for the 0.635-cm (0.25-in.), 0.3175-cm (0.125-in.), and 0.15875-cm (0.0625-in.) cell sizes with a 0 keV LLD setting. A 0 keV LLD setting was used to simulate the ideal ε_{th} distribution as a function of $^{10}B_4C$ coating thickness for each cell size. However, a 0 keV LLD setting is rarely used when performing neutron-detection measurements due to the presence of electronic noise and undesirable low-energy radiation interactions attributed primarily to gamma rays. The maximum simulated ε_{th} with corresponding $^{10}B_4C$ coating thicknesses for each cell size are listed in Table

4.6. The number of $^{10}B_4C$ coating layers corresponding to each cell size are also listed in Table 4.6. The simulated ε_{th} is a function of the number of $^{10}B_4C$-coated layers, the neutron-absorption probability within the $^{10}B_4C$ coating, the probability that a reaction product enters the gas-filled cell upon escaping the $^{10}B_4C$ coating, and the LLD setting. Thus, as the cell size decreases and more thin-film-coated surfaces are present within the sample, the maximum ε_{th} occurs at a thinner $^{10}B_4C$ coating thickness. Further discussion of the ε_{th} as a function of thin-film-coating thickness and LLD setting is provided in the literature [59].

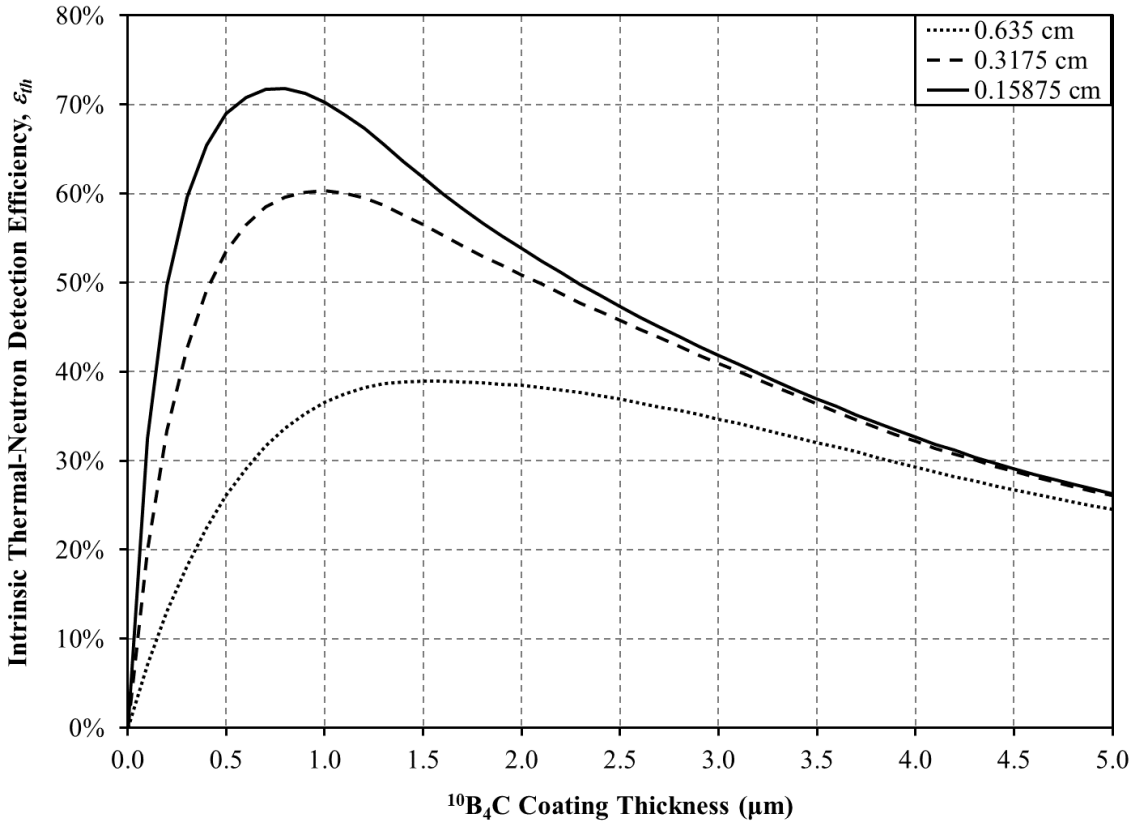

Figure 4.30. Simulated ε_{th} as a function of $^{10}B_4C$ coating thickness with a 0 keV LLD setting. A 1.27-cm (0.5-in.) tall, 4.1275-cm (1.625-in.) diameter aluminum-honeycomb substrate was simulated with cell sizes of 0.635 cm (0.25 in.), 0.3175 cm (0.125 in.), or 0.15875 cm (0.0625 in.).

Table 4.6. Simulated maximum ε_{th}, with corresponding $^{10}B_4C$ coating thickness, of the three honeycomb cell sizes with a 0 keV LLD setting.

Cell Size (cm)	Layers	ε_{th} (%)	Coating Thickness (µm)
0.635	12	38.92	1.6
0.3175	26	60.32	1.0
0.15875	52	71.78	0.8

Shown in Figure 4.31 are the simulated reaction-product pulse-height spectra, represented by solid lines and corresponding to the left ordinate with units of "Counts/Source Neutron", of the three cell sizes with the corresponding optimal $^{10}B_4C$ coating thicknesses (listed in Table 4.6). A down-shift in the energy range of the prominent spectral features occurs as the cell size is reduced, primarily because the amount of energy that can be deposited within each cell also reduces. The simulated ε_{th} distributions shown in Figure 4.31, represented by dashed lines and corresponding to the right ordinate, depict the ε_{th} as a function of LLD setting for each cell size. As the LLD setting is reduced, more low-energy events are tallied, and, therefore, the simulated ε_{th} increases.

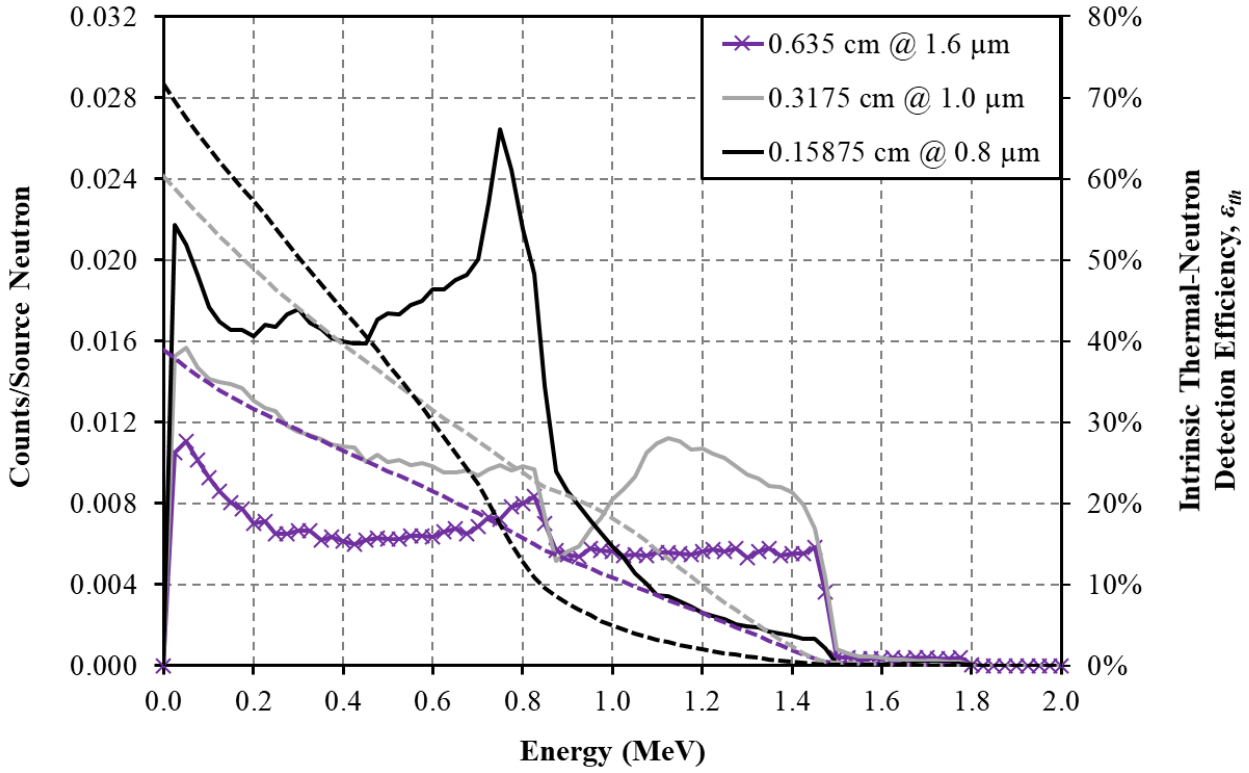

Figure 4.31. Simulated reaction-product pulse-height spectra (solid lines corresponding to the left ordinate with units of "Counts/Source Neutron") of the three cell sizes of $^{10}B_4C$-coated aluminum honeycomb. The dashed lines correspond to the right ordinate and illustrate the ε_{th} as a function of LLD setting for each cell size. The optimal $^{10}B_4C$ coating thickness listed in Table 4.6 was defined for each cell size.

Illustrated in Figure 4.32 are the simulation environments for studying the azimuthal and polar angular neutron-sensitivity distributions of the three cell sizes. The optimal $^{10}B_4C$ coating thickness for each cell size (Table 4.6) was implemented throughout the azimuthal and polar angular neutron-sensitivity simulations. The 5-mm diameter incident thermal-neutron beam was

adjusted in 15° increments within either the horizontal or vertical source plane and the ε_{th} was simulated at each beam position. For all azimuthal angular neutron-sensitivity simulations, the center of the 5-mm diameter incident thermal-neutron beam was directed toward the center of the sample at the midpoint of the sample height. For all vertical angular neutron-sensitivity simulations, the center of the incident thermal-neutron beam was directed toward the center of the sample within the vertical source plane.

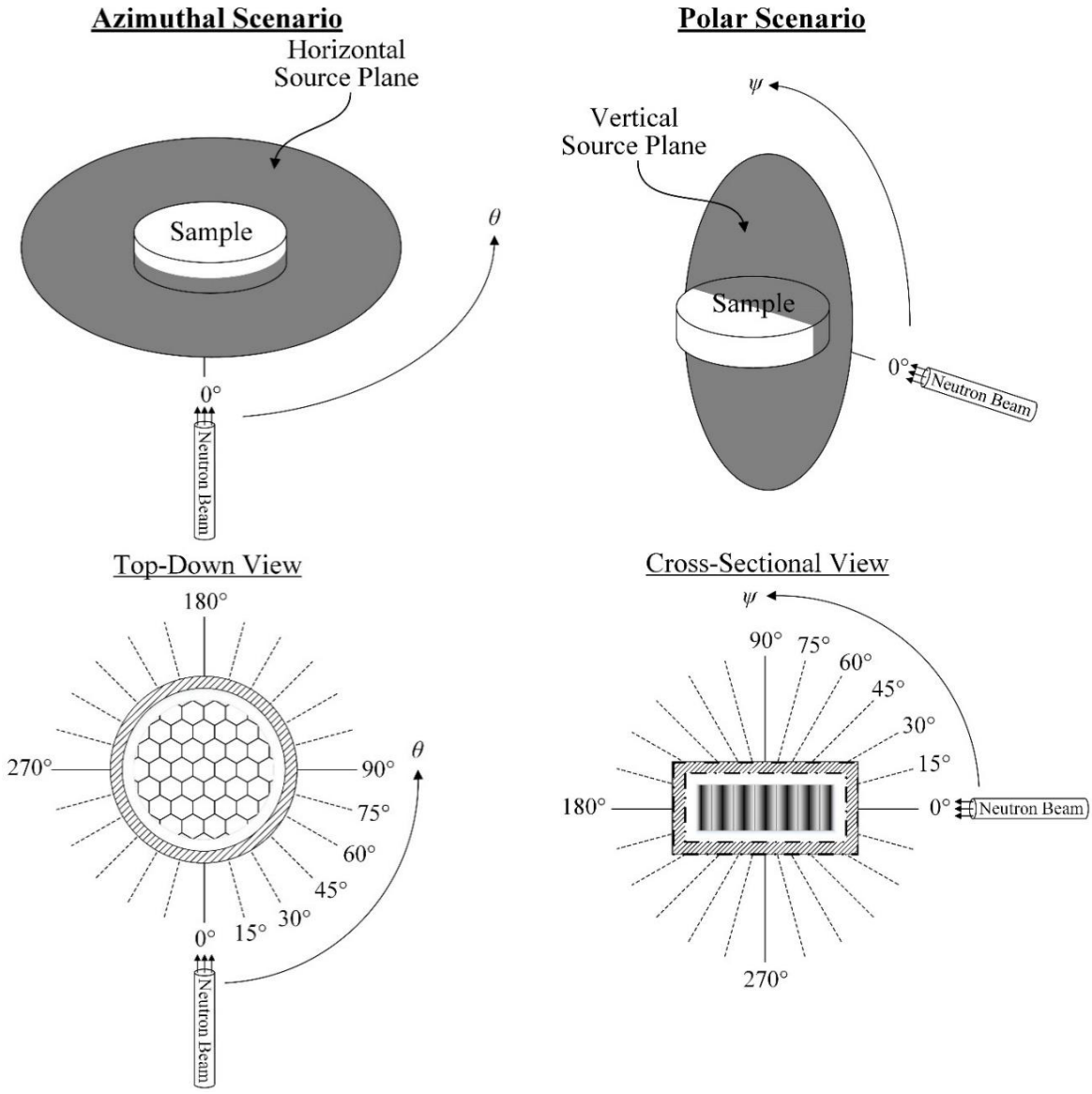

Figure 4.32. Simulation environments used for studying the azimuthal (left) and polar (right) angular neutron-sensitivity distributions. The orientation of the horizontal (left) and vertical (right) source planes, relative to the sample, are also illustrated with corresponding azimuthal and polar angular beam positions, respectively, indicated below.

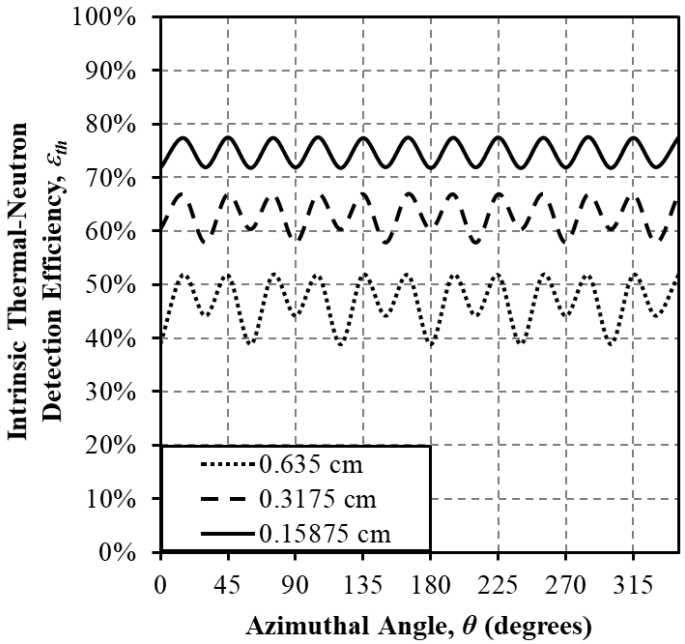

Figure 4.33. Simulated azimuthal angular neutron-sensitivity distributions of $^{10}B_4C$-coated aluminum-honeycomb substrates with cell sizes of 0.635 cm, 0.3175 cm, or 0.15875 cm and a 0 keV LLD setting. The distributions were simulated using the azimuthal scenario illustrated on the left of Figure 4.32.

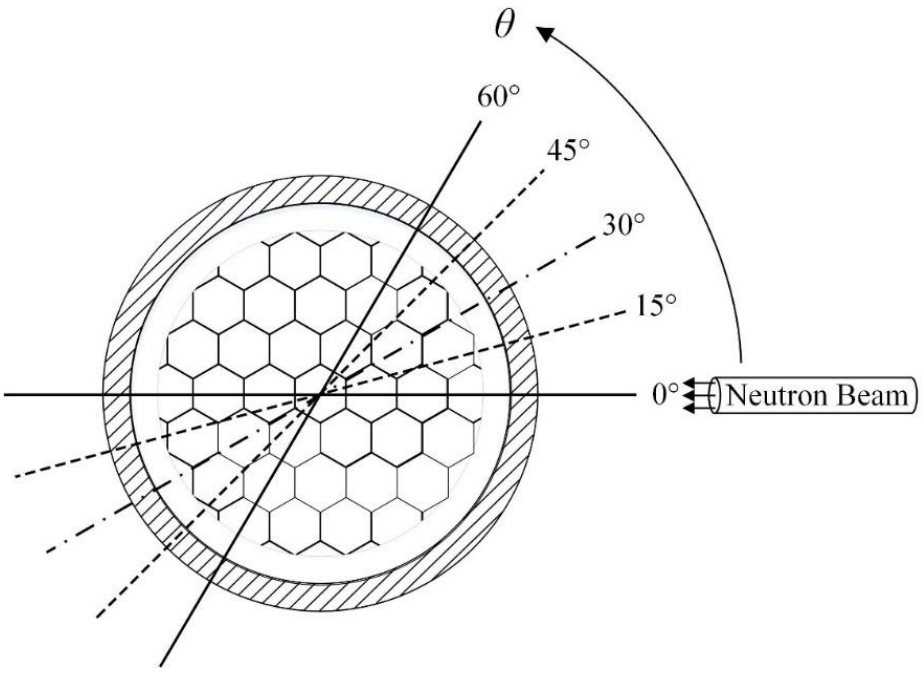

Figure 4.34. The number of thin-film-coating layers encountered by incident neutrons as a function of the azimuthal angle, θ, of incidence of thermal neutrons. The hexagonal cell geometry leads to a non-uniform azimuthal angular neutron-sensitivity distribution with a 60° period.

The simulated azimuthal angular neutron-sensitivity distributions for each cell size are shown in Figure 4.33. The azimuthal angles, θ, labeled on the x-axis of Figure 4.33 directly correspond to the angles illustrated on the left of Figure 4.32. A 60° periodic behavior occurs due to the change in the number of thin-film-coating layers that neutrons encounter as a function of the azimuthal angle of neutron incidence, as illustrated in Figure 4.34. The azimuthal angular neutron-sensitivity distribution becomes more uniformly periodic as the total number of thin-film-coating layers present within the sample increases.

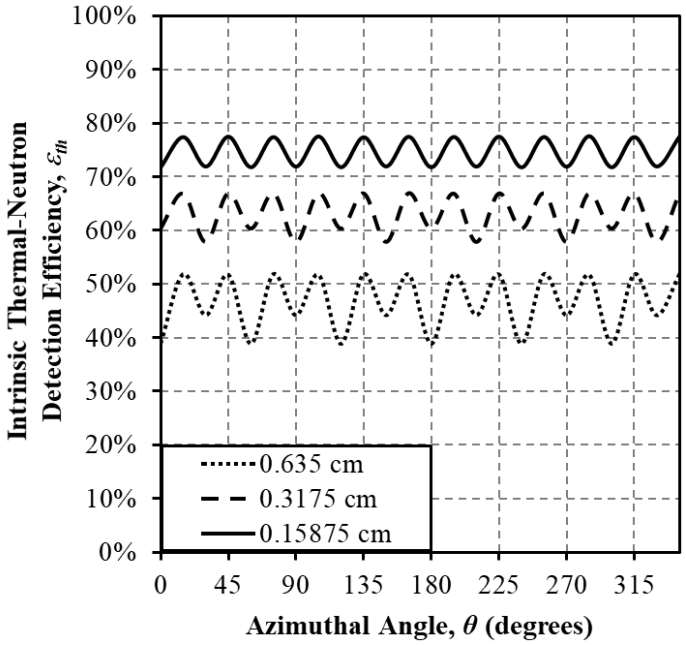

Figure 4.35. Simulated polar angular neutron-sensitivity distributions of $^{10}B_4C$-coated aluminum-honeycomb substrates with cell sizes of 0.635 cm, 0.3175 cm, or 0.15875 cm and a 0 keV LLD setting. The distributions were simulated using the polar scenario illustrated on the right of Figure 4.32.

The simulated polar angular neutron-sensitivity distributions for each cell size are shown in Figure 4.35. The polar angles, ψ, labeled on the x-axis of Figure 4.35 directly correspond to the polar angles illustrated on the right of Figure 4.32. As the incident thermal-neutron beam changes from the 0° and 180° polar angle positions, the probability of neutron absorption within the thin-film-coating layers decreases and neutron-streaming effects become more pronounced. At incident beam positions of 90° and 270°, the minimum polar angular neutron sensitivity occurs because incident neutrons are predominantly streaming through the substrate with a low probability of absorption within the vertical thin-film-coating layers lining the honeycomb cells. However, in a

scenario where consecutive $^{10}B_4C$-coated substrates are stacked on top of one another, neutron streaming effects can be mitigated by rotating and off-setting each honeycomb substrate.

The simulation environment shown in Figure 4.29 was used to simulate the effects of P-10 gas pressure on the theoretical ε_{th}. The optimized $^{10}B_4C$ coating thicknesses (listed in Table 4.6) were defined while conducting the P-10 gas pressure simulations. The P-10 gas pressure optimization study was conducted for gas pressures ranging from 1 to 5 atm in increments of 1 atm and the ε_{th} was simulated for each gas pressure. The distribution of simulated ε_{th} as a function of LLD setting was plotted and compared to the corresponding simulated reaction-product pulse-height spectrum at each gas pressure.

Shown in Figure 4.36 – Figure 4.38 are the simulated reaction-product pulse-height spectra, represented by solid lines and corresponding to the left ordinate with units of "Counts/Source Neutron", for the 0.635-cm, 0.3175-cm, and 0.15875-cm cell sizes, respectively. Also shown in Figure 4.36 – Figure 4.38 are the simulated ε_{th} as a function of LLD setting, which are represented by dashed lines and correspond to the right ordinate. For all cell sizes, the spectral features shift into higher energy bins as the P-10 gas pressure is increased. As listed in Table 4.5, the range of the reaction products decreases as the P-10 gas pressure is increased. Thus, the up-shift in energy occurs due to an increase in the amount of ionization that can occur within the honeycomb cells as the P-10 gas pressure is increased. As the cell size is reduced, this effect becomes more pronounced and, therefore, the 0.15875-cm cell size benefits the most from an increase in P-10 gas pressure. Due to the up-shift in energy of the reaction-product pulse-height spectral features as the gas pressure is increased, the reduction in the ε_{th} becomes less pronounced as the LLD setting is increased.

The simulation methods employed for defining optimal coating thickness, azimuthal and polar angular sensitivity, and gas pressure studies were also employed for thin-film coatings of ^{10}B, ^{10}BN, and ^{6}LiF and the results are provided in Appendices A – C, respectively. Despite the simulated results of thin-film-coated aluminum-honeycomb substrates as compact, high ε_{th} neutron-conversion media, applying uniform thin-film coatings still presents a significant challenge. Additionally, as with other thin-film-coated neutron detectors, the strong dependency of ε_{th} on the LLD setting presents a challenge when developing a device with low gamma-ray sensitivity that also is capable of high ε_{th}. Therefore, investigation of aluminum honeycomb as a thin-film-coated neutron-conversion medium has not progressed further.

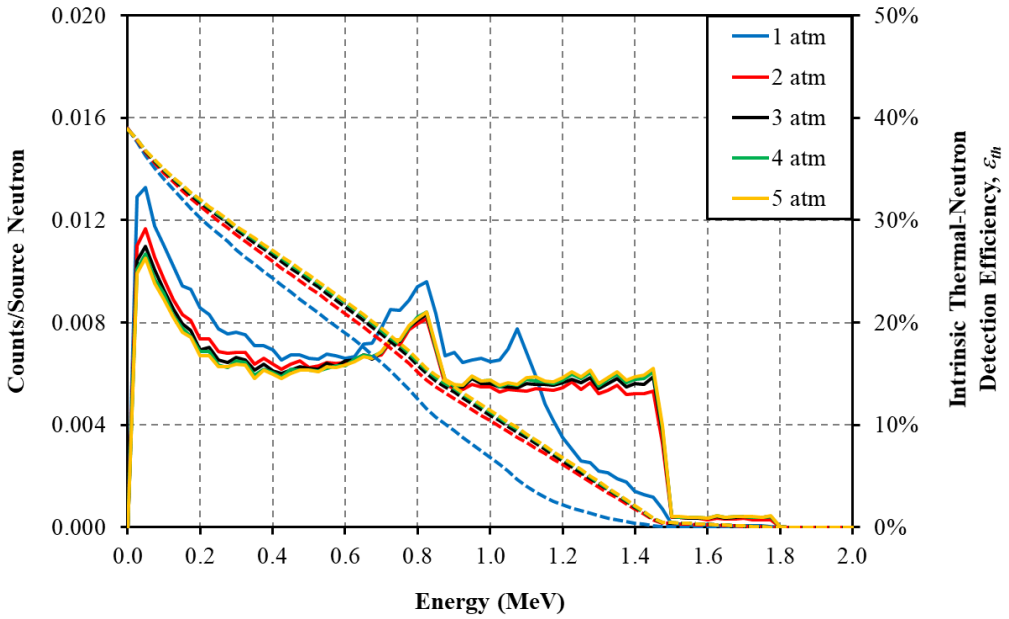

Figure 4.36. Simulated reaction-product pulse-height spectra (solid lines corresponding to the left ordinate with units of "Counts/Source Neutron") for a 0.635-cm cell size honeycomb substrate with P-10 gas pressures ranging from 1 to 5 atm. The dashed lines correspond to the right ordinate and illustrate the ε_{th} as a function of LLD setting for each cell size. The honeycomb sample contained hexagonal cells with a cell size of 0.635-cm that were coated with 1.6 µm of $^{10}B_4C$.

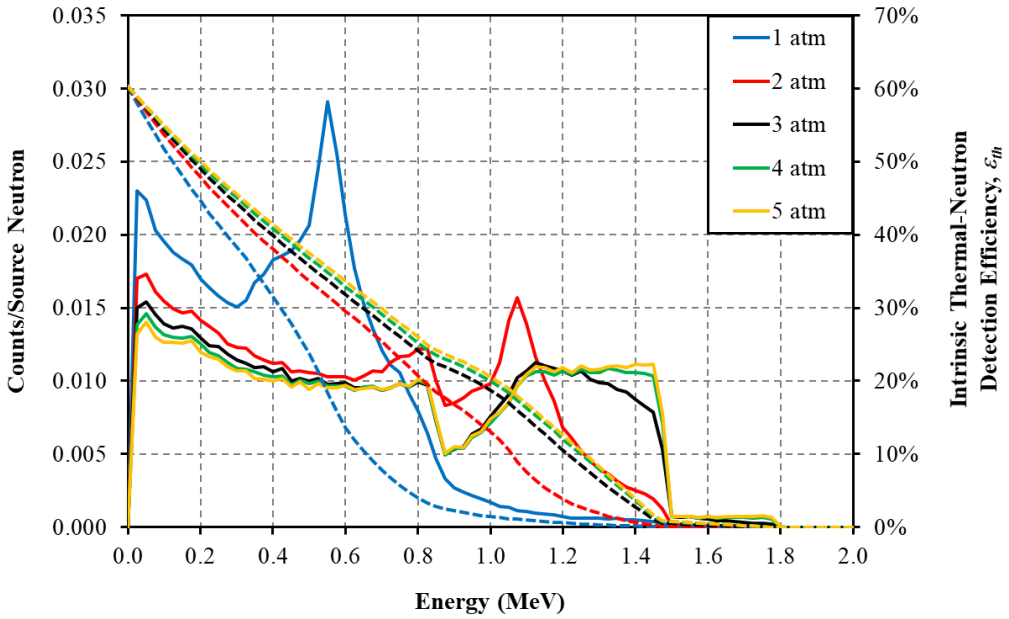

Figure 4.37. Simulated reaction-product pulse-height spectra (solid lines corresponding to the left ordinate with units of "Counts/Source Neutron") for a 0.3175-cm cell size honeycomb substrate with P-10 gas pressures ranging from 1 to 5 atm. The dashed lines correspond to the right ordinate and illustrate the ε_{th} as a function of LLD setting for each cell size. The honeycomb sample contained hexagonal cells with a cell size of 0.3175-cm that were coated with 1.0 µm of $^{10}B_4C$.

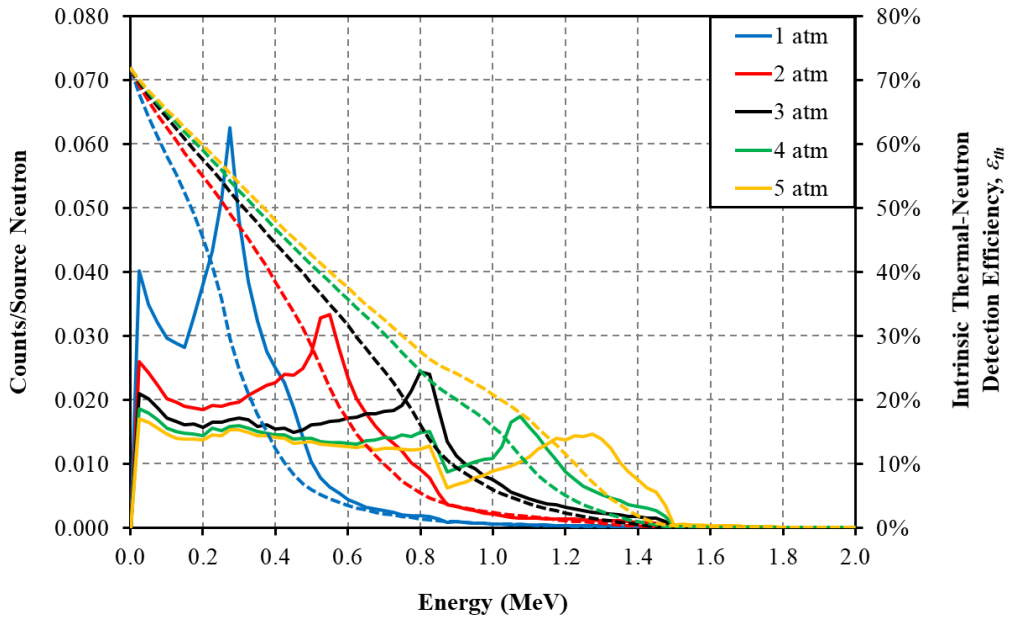

Figure 4.38. Simulated reaction-product pulse-height spectra (solid lines corresponding to the left ordinate with units of "Counts/Source Neutron") for a 0.15875-cm cell size honeycomb substrate with P-10 gas pressures ranging from 1 to 5 atm. The dashed lines correspond to the right ordinate and illustrate the ε_{th} as a function of LLD setting for each cell size. The honeycomb sample contained hexagonal cells with a cell size of 0.15875-cm that were coated with 0.8 µm of $^{10}B_4C$.

CHAPTER 5

SUSPENDED FOIL MICROSTRIP NEUTRON DETECTOR: DESIGN METHODOLOGY AND THEORETICAL CONSIDERATIONS

If we know what it was we were doing, it would not be called research, would it?

Albert Einstein

Described in the following chapter is the design methodology for the SFMNDs (Section 5.1). The reasoning for selecting lithium foils as the neutron-conversion medium and the decision to use microstrip electrodes are also discussed (Section 5.1). Description of the SFMND neutron detection process follows (Section 5.2). Finally, the simulated neutron detection capabilities of SFMNDs for different foil quantities and orientations are described to conclude the chapter (Section 5.3).

5.1 Design Methodology

The advancements in the lithium-ion battery industry have resulted in the fabrication of ^{6}Li foils with thicknesses as low as 55 μm [21], which, in turn, led to the development of Li-foil MWPCs. Li-foil MWPCs are a ^{3}He-alternative technology that feature suspended ^{6}Li foils positioned in between neighboring anode wire banks [26, 46-48, 139, 140]. The ^{6}Li foils are suspended in between anode wire banks by laminating each ^{6}Li foil to an aluminum frame. The laminated aluminum frames are then held in place relative to the anode wire banks. Depending on the thickness and quantity of ^{6}Li foils, Li-foil MWPCs are capable of ε_{th} exceeding 80% [46, 140]. Li-foil MWPCs have low gamma-ray sensitivity, with a reported *GRR* value of 7.67 x 10^{-9} measured using a five-foil device for a ^{60}Co exposure rate of 40 mR hr^{-1} [46, 48]. A valley is often

present in the reaction-product pulse-height spectrum (described in Section 2.3.3) measured using a Li-foil MWPC, a feature that is beneficial when discriminating gamma-rays and electronic noise from neutron events. However, the size of Li-foil MWPCs is limited due to the minimum space needed between neighboring ^{6}Li foils for anode wires. The anode wires are also susceptible to mechanical vibrations that induce microphonic noise.

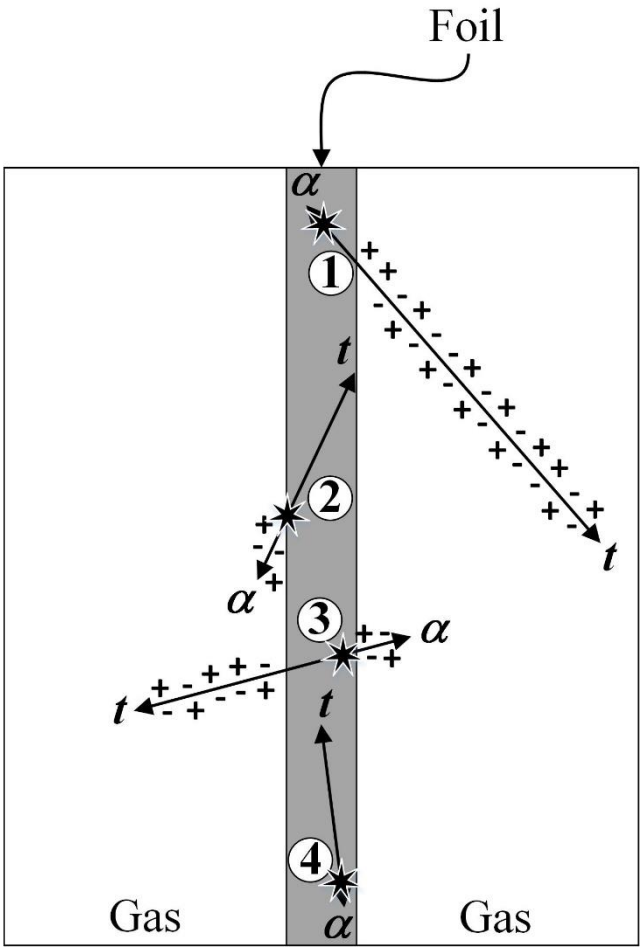

Figure 5.1. Examples of reaction-product trajectories from neutron absorption within a sufficiently-thin ^{6}Li foil. Scenarios 1 and 2 depict examples of one reaction product escaping the foil while the other reaction product is absorbed within the foil. Scenario 3 illustrates an example of both reaction products escaping the foil. Scenario 4 shows an example of both reaction products being absorbed within the foil.

Illustrated in Figure 5.1 are examples of reaction-product trajectories that can occur when using suspended ^{6}Li foil for detecting neutrons. One (scenario 1 and 2) or both (scenario 3) reaction products may escape the ^{6}Li foil to ionize the surrounding gas for sufficiently thin ^{6}Li foils [46, 48, 140]. Both reaction products can also be fully absorbed within the ^{6}Li foil (scenario 4) and,

thus, will not ionize the surrounding gas. The amount of reaction-product energy lost within the ^{6}Li foil due to self-absorption effects is dependent on the location of reaction-product emission within the ^{6}Li foil as well as the trajectory of the reaction product. The amount of reaction-product energy deposited within the gas is dependent on the amount of energy retained by the reaction product(s) upon escaping the ^{6}Li foil. Thus, the full energy of one of the reaction products can be deposited within the gas for reaction products emitted at the interface of the gas and the ^{6}Li foil. As the gas is ionized by the reaction product(s), charge carriers are liberated. Charge induction occurs as charge carriers drift toward their respectively-charged electrodes under the influence of the electric field formed by the potential difference between the electrodes.

Table 5.1. The ranges of ^{6}Li(n, α)^{3}H reaction products in ^{6}Li, aluminum, and 1 – 5 atm of P-10 gas [96]. The density, ρ, of each material is also listed [59, 96, 115].

Material	**ρ (g cm^{-3})**	**2.050 MeV ^{4}He (μm)**	**2.730 MeV ^{3}H (μm)**
Foil			
^{6}Li	0.463	23.2	134
Frame			
Aluminum	2.20	6.72	38.2
P-10 Gas			
1 atm	0.00156	11700	65900
2 atm	0.00312	5860	32900
3 atm	0.00468	3900	21900
4 atm	0.00624	2930	16400
5 atm	0.00780	2340	13100

Listed in Table 5.1 are the ranges of the ^{6}Li(n, α)^{3}H reaction products in ^{6}Li, aluminum, and 1 – 5 atm of P-10 gas [96]. The summed ranges of the ^{6}Li(n, α)^{3}H reaction products in ^{6}Li is 157.2 μm [96]. The probability of one or both reaction products escaping the foil is dependent on the foil thickness, the site of reaction-product emission within the ^{6}Li foil, and the trajectories of the reaction products. In order for both reaction products to be able to escape the foil, the thickness of the foil must not exceed the summed ranges of the ^{6}Li(n, α)^{3}H reaction products in ^{6}Li. Similarly, the thickness of the ^{6}Li foil should not exceed the range of the highest energy reaction product or significant reaction-product self absorption is likely to occur within the ^{6}Li foil. The amount of energy deposited by reaction products within the surrounding gas is dependent on the

foil thickness, the site of reaction-product emission within the ^{6}Li foil, and the trajectories of the reaction products. The amount of measureable reaction-product energy deposited within the surrounding gas is also dependent on the distance that reaction products can travel within the surrounding gas without colliding with other solid structures or escaping the sensitive volume.

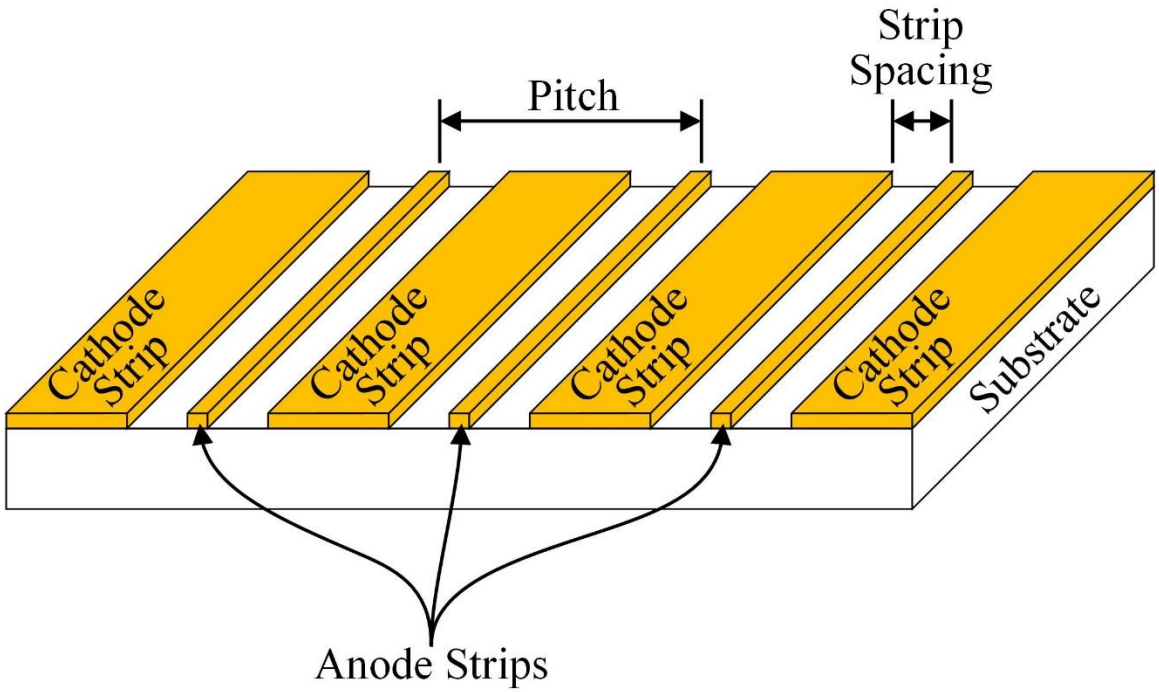

Figure 5.2. Definitions of the microstrip-electrode strip pitch and spacing relative to the interdigitated anode and cathode strips.

An alternative to using wires as anodes is to use a micropattern electrode such as the microstrip electrode (discussed in Section 3.4.3 and illustrated in Figure 3.8). Relative to anode wires, microstrip electrodes are inherently more robust and less prone to microphonic sensitivity because the metal strips are adhered to the substrate surface. Shown in Figure 5.2 is an illustration of the microstrip electrode parameters. The electrical qualities of a microstrip electrode are dependent on parameters such as the anode and cathode strip widths, the strip pitch (either anode-to-anode or cathode-to-cathode), and the strip spacing. The strip widths, strip pitch and spacing, and potential difference between neighboring anode and cathode strips affect the strength of the electric field produced above the microstrip electrode. The strip spacing must remain uniform in order to retain the uniformity of the electric field produced above the electrode surface. Careful selection of the strip metals is important to ensure proper adhesion to the substrate as well as other factors such as electrical stability, capacitance, and resistance. Each set of anode and cathode strips

can be interconnected to a common strip and the signal measured from the entire set of interconnected anode strips, as illustrated in Figure 5.3. The anode strip operating voltage is applied to the anode strip bond pad and the cathode strip operating voltage is applied to the cathode strip bond pad. However, in the scenario depicted in Figure 5.3, the microstrip-electrode capacitance is defined by the total number of neighboring anode and cathode strips. The capacitance can be reduced by segmenting the anode strips into separate groups, as depicted in Figure 5.4, where the signal from each anode strip group is sent to separate charge-sensitive preamplifier circuits. Finally, the substrate material can affect the gain stability of the microstrip electrode. The literature provides further discussion regarding the effect of various microstrip electrode parameters on the electrical performance of microstrip electrodes [98, 105-109, 141-146].

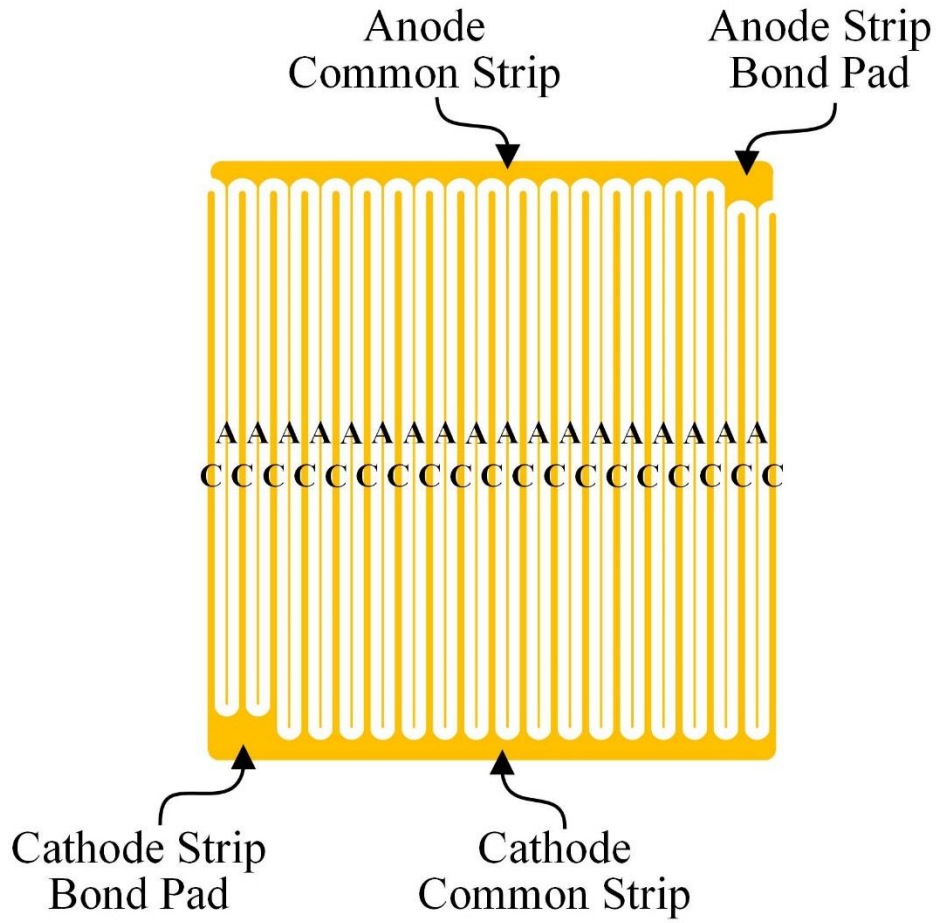

Figure 5.3. Example of a microstrip-electrode design where all anode strips (A) are interconnected to a common strip. The cathode strips (C) are interconnected in a similar manner. The signal is measured through the anode strip bond pad.

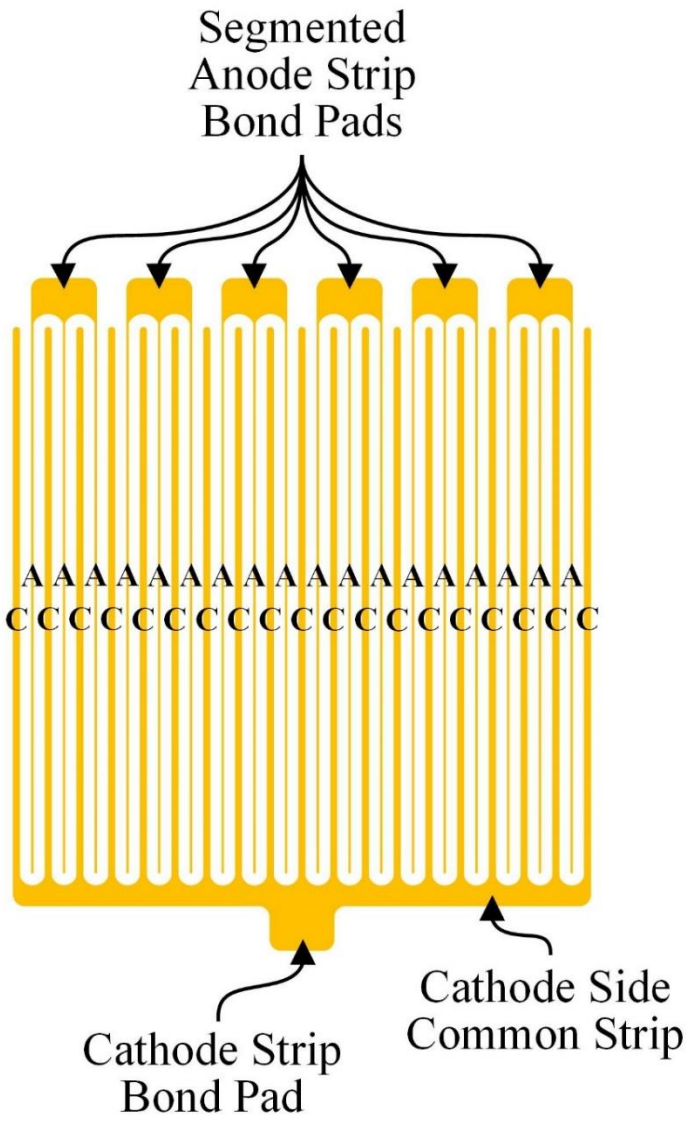

Figure 5.4. Example of a microstrip electrode with segmented groups of anode strips (A) relative to interconnected cathode strips (C). Each anode-strip group is interconnected by a bond pad and the signal from each group is measured using separate charge-sensitive preamplifier circuits.

Microstrip neutron detectors were previously developed for a variety of applications that primarily relied on ^{3}He gas as the neutron-conversion medium [63, 105, 109, 147-152]. Studies were also performed to develop microstrip neutron detectors that relied on a suspended foil as the neutron converter [62, 63, 108, 153]. As illustrated in Figure 5.5, the foil was positioned parallel to the top surface of the electrode(s). The suspended foil was composed of ^{nat}Gd [62], ^{157}Gd [108, 153], or ^{6}Li [108] and coated with a thin layer of CsI. The CsI functioned as a secondary electron emitter [62, 66, 108, 153]. Regardless of the foil material, the reliance on measuring low-energy

secondary electrons emitted from the CsI coating layer [62, 66] makes discrimination of gamma rays and electronic noise difficult without also sacrificing neutron-induced signals.

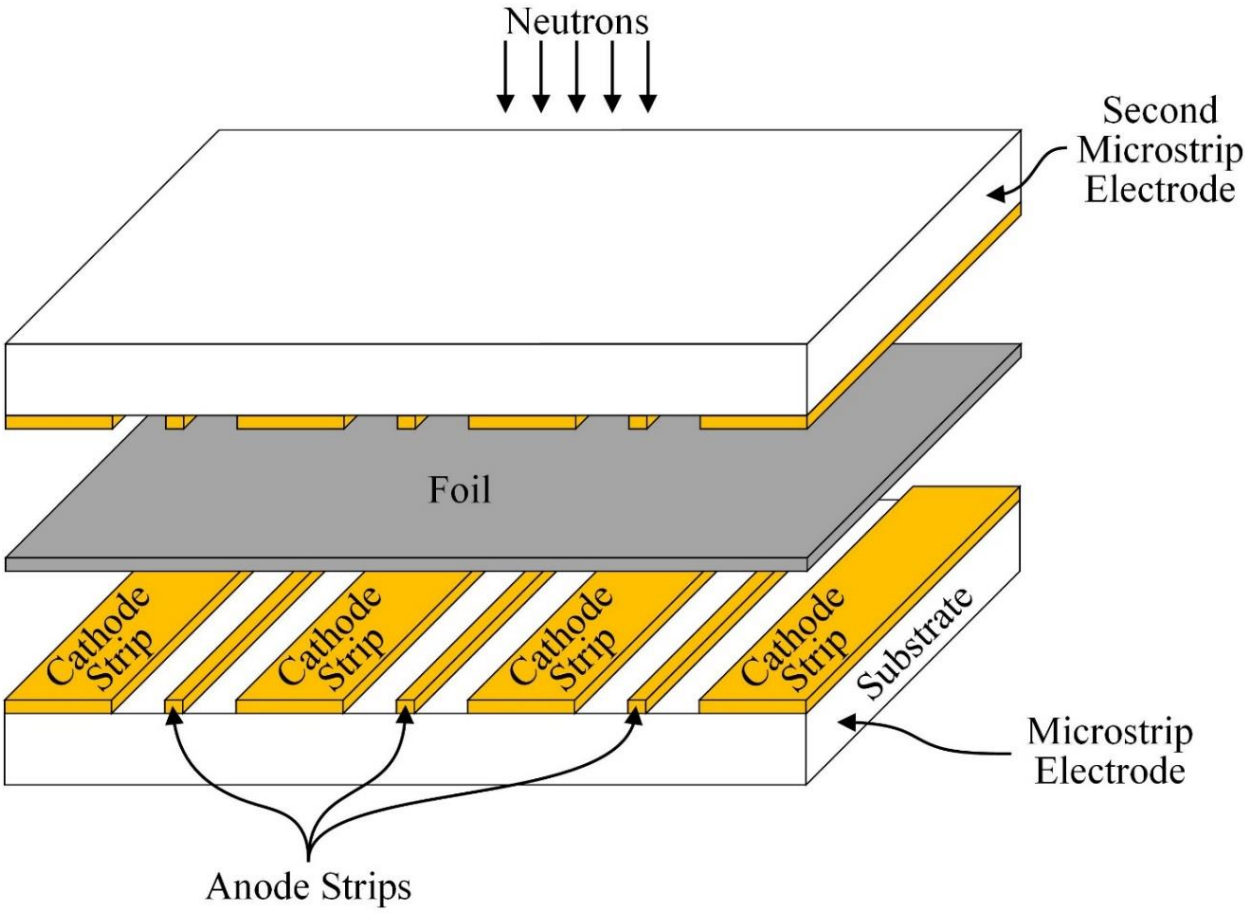

Figure 5.5. Example of the foil orientation previously used for CsI-coated ^{nat}Gd, ^{157}Gd, or ^{6}Li. In the case of the CsI-coated ^{nat}Gd, only one microstrip electrode was used.

SFMNDs were designed with the goal of developing a low-cost, robust, and compact ^{3}He alternative technology capable of achieving high ε_{th} with low gamma-ray sensitivity. Due to the limitations of anode wires contained within Li-foil MWPCs, the anode wires were replaced with a microstrip electrode and ^{6}Li foils were selected as the neutron-conversion medium to develop the first-ever SFMND [154], as illustrated in Figure 5.6. Thus, SFMNDs combine the mechanical and electrical capabilities of microstrip electrodes with the high ε_{th} capability and low gamma-ray sensitivity of ^{6}Li foils. Because SFMNDs do not rely on anode wires, neighboring foils can be positioned closer in proximity to one another, thereby allowing for smaller individual devices to be fabricated. The foils are oriented perpendicular to the surface of the electrodes and, therefore,

multiple ^{6}Li foils can be positioned between the microstrip and drift electrodes. Replacement of anode wires with a microstrip electrode eliminates the potential for failure from wire breakage while also reducing microphonic sensitivity. Cost analysis has not been conducted because SFMNDs are under prototypical investigation; however, the cost is expected to be lower relative to ^{3}He and other alternatives of similar size based on the materials and labor required to fabricate prototype devices. The compact size of the SFMNDs allows for the eventual development of modular devices, as illustrated in Figure 5.7. The modular devices could be arrayed together to form a variety of instrument geometries, such as a stacked column of devices, planar array of devices, etc., depending on the application.

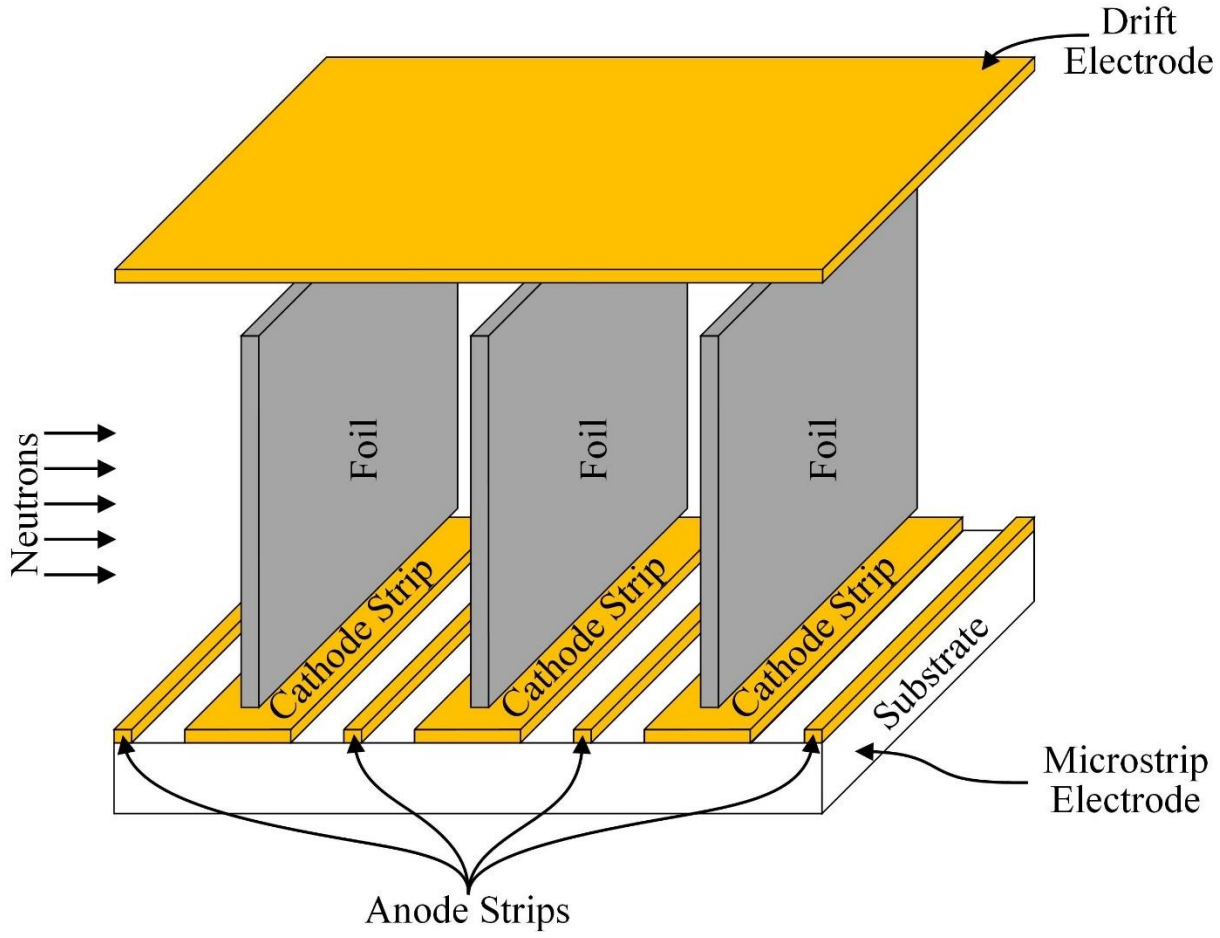

Figure 5.6. Configuration of a SFMND depicting the orientation of suspended foils relative to microstrip and drift electrodes [155].

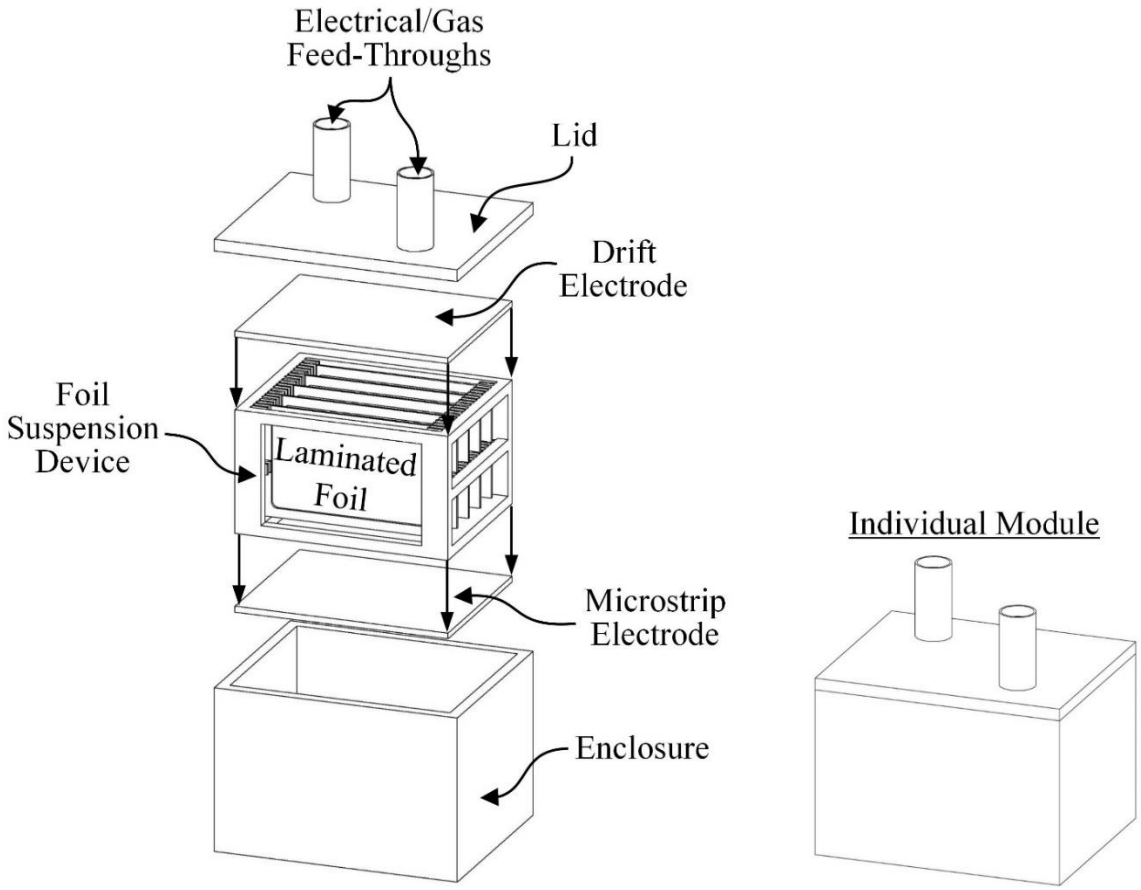

Figure 5.7. Example of a modular SFMND that is capable of being interconnected with other modular SFMNDs to produce an array of devices.

5.2 Neutron-Detection Process

Shown in Figure 5.8 is the neutron-detection process using a ^{6}Li-based SFMND. The neutron-detection process occurs by three main steps: 1.) neutron conversion, 2.) drift of charge carriers, and 3.) charge multiplication. The first step occurs when an incident slow neutron is absorbed by a ^{6}Li atom. The ensuing ^{6}Li(n, α)^{3}H reaction yields charged-particle reaction products that are emitted in opposite directions with energies described by Eq. (2.11). Upon exiting the ^{6}Li foil and entering the backfill gas, the reaction product(s) ionize the gas resulting in the liberation of charge carriers. The second step in the detection process occurs when charge carriers drift within the sensitive volume under the influence of the drift electric field. The drift electric field is produced from the potential difference between the operating voltage of the drift electrode, V_{DP}, and the operating voltages of the anode, V_A, and cathode, V_C, strips of the microstrip electrode.

The operating voltage condition of $V_{DP} < V_C < V_A$ is required to drift electrons towards the microstrip-electrode surface and positively-charged ions towards the drift electrode. Thus, the second step of the detection process is equivalent to the signal formation process that occurs in a parallel-plate ionization chamber (discussed in Section 3.4.1). As electrons approach the microstrip electrode, the electric field strength increases by several orders of magnitude and surpasses the threshold electric field strength necessary to cause Townsend avalanching, denoted in Figure 5.8 as the gas multiplication electric field region. The increase in electric field strength occurs due to the potential difference between neighboring anode and cathode strips positioned less than 1.0 mm apart, where $V_C < V_A$. Furthermore, the increase in electric field strength is also a function of the geometric weighting condition that occurs from the difference in anode and cathode strip widths. Therefore, the third step in the neutron-detection process occurs at the electric-field boundary where gas multiplication can occur. The amount of current induced on the anode strips is a combination of the distance displaced by primary charge carriers drifting within the drift electric field region as well as the motion of secondary charge carriers within the gas multiplication electric field as they are rapidly swept to the nearby anode and cathode strips.

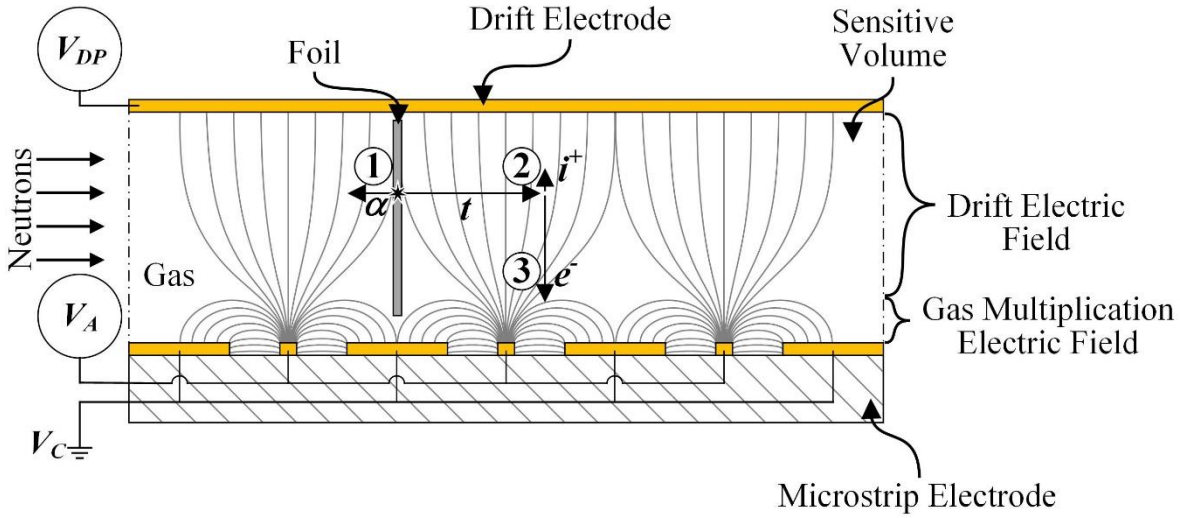

Figure 5.8. Three-step neutron-detection process of a ^{6}Li-based SFMND.

5.3 Simulated Intrinsic Thermal-Neutron Detection Efficiencies

The theoretical capabilities of the ^{6}Li-based SFMND were studied by simulating the ε_{th} for several scenarios using *MCNP6*. The ε_{th} was simulated as a function of ^{6}Li foil thickness for one,

five, ten, and twenty foils (Section 5.3.1). Next, the ε_{th} was simulated as a function of gas pressure and the resulting reaction-product pulse-height spectra were compared (Section 5.3.2). Finally, the ε_{th} was simulated as a function of foil width relative to the sensitive volume perimeter and the resulting reaction-product pulse-height spectra were compared (Section 5.3.3).

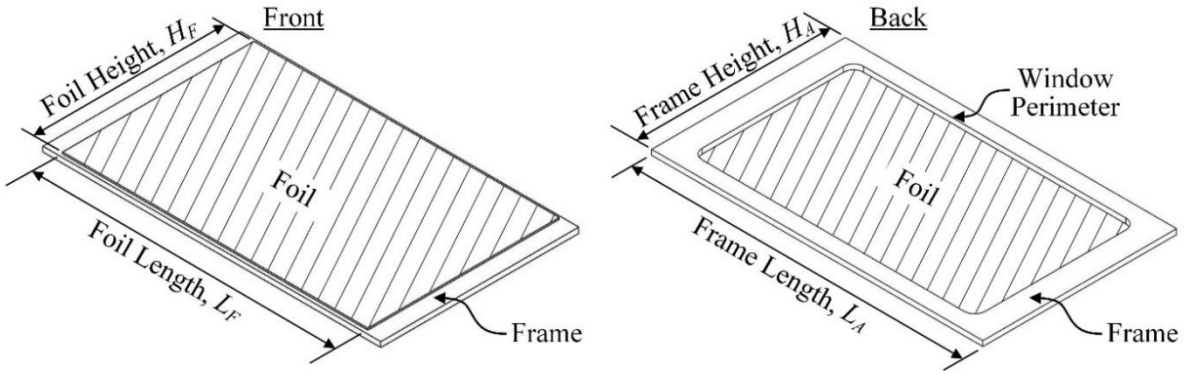

Figure 5.9. Illustrations of the aluminum frame positioned adjacent to the ^{6}Li foil (cross-hatched). The window in the frame, the opening in the center of the frame, allows reaction-products to escape from either side of the foil.

For all simulations, reaction-product energy deposition that occurred within the sensitive volume was tallied. In order to compare the simulation results to the experimental results (discussed in Section 6.4.2), the length, L_F, and height, H_F, of the 96%-enriched ^{6}Li foil(s) were defined as 5.00 cm and 2.95 cm, respectively. A 0.79-mm (1/32-in.) thick 6061 aluminum frame was positioned directly adjacent to each ^{6}Li foil, as illustrated in Figure 5.9. The aluminum frames were defined with a length, L_A, and height, H_A, of approximately 5.2 cm and 3.0 cm, respectively. Based on the reaction-product ranges in aluminum (Table 5.1), the thickness of the aluminum frames prevented reaction products from traveling through the aluminum frame and entering the surrounding gas. Thus, the aluminum frames were defined with an opening in the center, referred to as the *window*, to allow reaction products to escape from either side of the adjacent foil. The window perimeter had a length, L_W, and height, H_W, of approximately 4.45 cm and 2.54 cm, respectively. The microstrip and drift electrodes were defined as 525-μm thick borosilicate glass. The distance separating the microstrip and drift electrodes, D, was 3.9 cm. The electrodes were defined with square perimeters of length, L_M, and width, W_M. The sensitive volume was defined by the square perimeter of the electrodes (L_M x W_M) and the distance separating the electrodes, D. The gas surrounding the foils and frames within the sensitive volume was defined as P-10 proportional gas.

5.3.1 Effects of Foil Thickness & Quantity

The theoretical ε_{th} as a function of ^{6}Li foil thickness, t_F, was studied for SFMNDs containing one, five, ten, and twenty foils using the simulation environment illustrated in Figure 5.10. A 0.5-cm diameter thermal-neutron beam was incident on the center of the front face of the foil(s). The foils were separated a distance, d, of 5.73 mm, 3.82 mm, and 1.91 mm apart for the five, ten, and twenty foil scenarios, respectively. The length, L_M, and width, W_M, of the microstrip and drift electrodes were both defined as 4.1275 cm (1.625 in.). The gas surrounding the foil(s) within the sensitive volume was defined as 10 psig (1.68 atm) of P-10 gas.

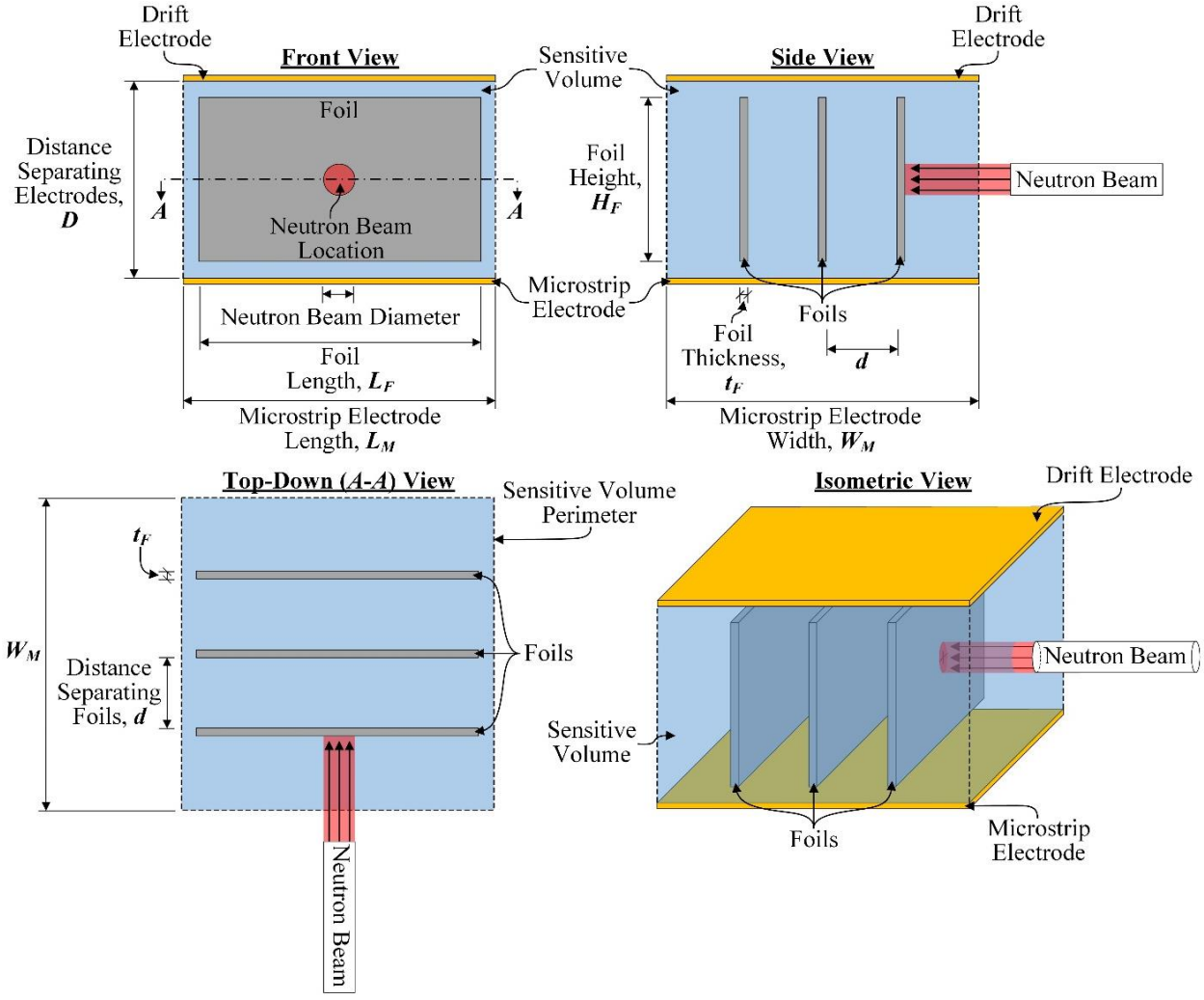

Figure 5.10. Simulation environment used for studying the theoretical ε_{th} as a function of foil thickness and quantity. The thermal-neutron beam is shaded red and the sensitive volume is shaded blue. The foils are shaded gray and the electrodes are shaded orange. The simulation environment was also used to study theoretical ε_{th} as a function of P-10 gas pressure for devices containing one and five foils.

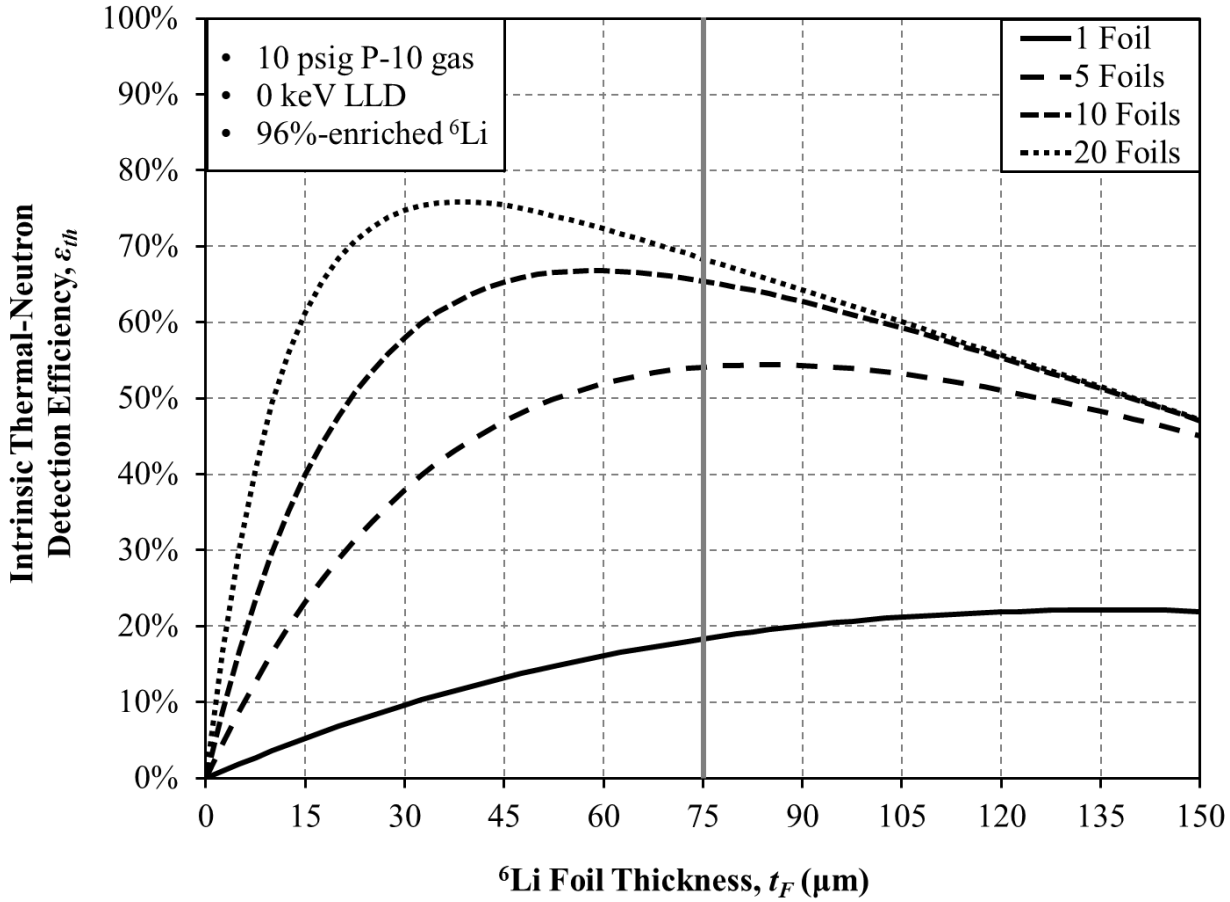

Figure 5.11. MCNP6-simulated ε_{th} curves as a function of ^{6}Li foil thickness for one, five, ten, and twenty foils in 10 psig (1.68 atm) of P-10 proportional gas. The foils were assumed to be 96%-enriched ^{6}Li and the ε_{th} curves are plotted for an LLD setting of 0 keV. The gray line indicates the simulated ε_{th} for a foil thickness of 75 µm.

Table 5.2. The foil spacing and maximum simulated ε_{th}, with corresponding foil thickness, for each foil quantity. The simulated ε_{th} for 75-µm thick foil(s) is listed on the right for each foil quantity.

Number of Foils	Foil Spacing (mm)	$\varepsilon_{th,max.}$	t_F (µm)	ε_{th} @ t = 75 µm
1	-	22.16%	137.5	18.36%
5	5.73	54.43%	85.0	54.08%
10	3.82	66.80%	60.0	65.43%
20	1.91	75.84%	37.5	68.36%

Shown in Figure 5.11 are the simulated ε_{th} as a function of ^{6}Li foil thickness for SFMNDs containing one, five, ten, and twenty foils with a 0 keV LLD setting. A 0 keV LLD setting was used to simulate the ideal ε_{th} distribution for each foil quantity. However, a 0 keV LLD setting is rarely used when performing neutron-detection measurements due to the presence of electronic

noise and undesirable low-energy radiation interactions attributed primarily to gamma rays. Similar to thin-film-coated aluminum honeycomb (described in Section 4.3.2), the simulated ε_{th} is a function of the neutron-absorption probability within the ^{6}Li foil, the probability that a reaction product enters the gas upon escaping the ^{6}Li foil, the quantity of ^{6}Li foils, and the LLD setting. Thus, as the foil quantity increases, the maximum ε_{th} occurs at thinner ^{6}Li foil thicknesses. The foil spacing, maximum ε_{th} with corresponding foil thickness, and ε_{th} for a foil thickness of 75 µm are listed in Table 5.2 for each foil quantity. A foil thickness of 75 µm was implemented for comparison to experimental efforts (discussed in Section 6.4).

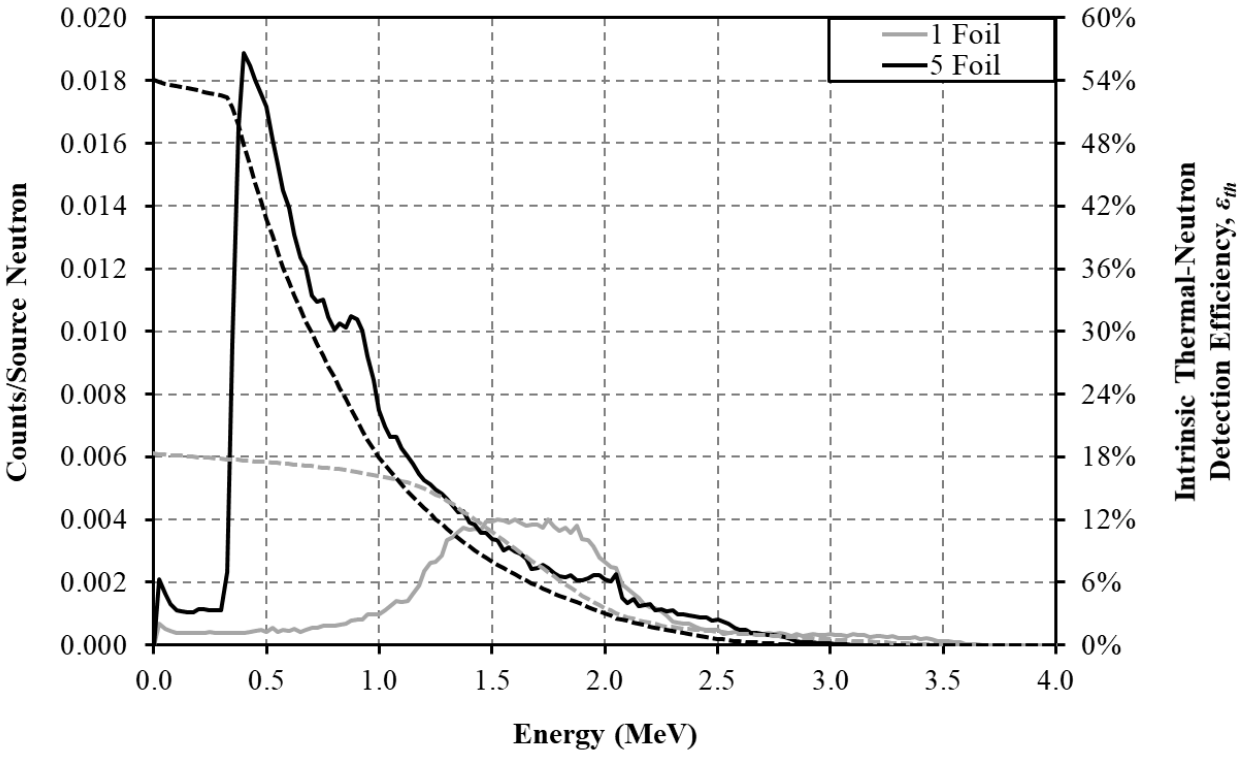

Figure 5.12. MCNP6-simulated reaction-product pulse-height spectra (left ordinate with units of "Counts/Source Neutron") for one (solid gray) and five (solid black) suspended ^{6}Li foils contained within 10 psig (1.68 atm) of P-10 proportional gas. The dashed gray and black lines correspond to the right ordinate and illustrate the ε_{th} as a function of LLD setting for one and five suspended ^{6}Li foils, respectively. As the LLD setting is increased, the ε_{th} reduces as a function of the prominence of the spectral features [155].

Shown in Figure 5.12 are the simulated reaction-product pulse-height spectra, represented by solid lines and corresponding to the left ordinate with units of "Counts/Source Neutron", for one and five 75-µm thick ^{6}Li foils. The simulated ε_{th} as a function of LLD setting are represented by dashed lines and correspond to the right ordinate of Figure 5.12. The simulated reaction-product

pulse-height spectra and ε_{th} as a function of LLD setting for ten and twenty ^{6}Li foils are shown in Figure D.1 of Appendix D. Although the remainder of the computational and experimental efforts focus on the implementation of one and five ^{6}Li foils, the ten and twenty foil scenarios are provided in order to convey the potential these foil scenarios have as high ε_{th} neutron detectors.

In both of the simulated reaction-product pulse-height spectra, a valley is present that separates the prominent spectral features from low-energy events. The difference in pulse-height spectra shown in Figure 5.12 is a consequence of differences in foil positions relative to the sensitive volume. Specifically, the location of neutron absorption and the reaction-product ranges, and corresponding particle trajectories relative to the sensitive volume, affect the shape of the pulse-height spectra [46, 48]. As described in Section 5.1, four reaction-product emission scenarios exist, based on the ranges of 2.05 MeV alpha particles and 2.73 MeV tritons in pure ^{6}Li foil (listed in Table 5.1) of 23.2 μm and 134 μm, respectively [96]. The ranges of 2.05 MeV alpha particles and 2.73 MeV tritons in 10 psig of P-10 gas are 7.50 mm and 43.20 mm, respectively [96].

The simulated ε_{th} changes as a function of the LLD setting based on the prominence of the simulated reaction-product spectral features. Consider the following example: if a 500 keV LLD setting is used with the one-foil ^{6}Li-based SFMND, the simulated ε_{th} reduces from 18.36% (0 keV LLD setting) to 17.50% (500 keV LLD setting). The reduction in simulated ε_{th} occurs because events below are 500 keV are discriminated. Because the prominent spectral features of the one-foil ^{6}Li-based SFMND occur within the energy range of approximately 1.0 – 2.5 MeV, the reduction in simulated ε_{th} is minimal. However, when using a 500 keV LLD setting with the five-foil ^{6}Li-based SFMND, the ε_{th} reduces from 54.08% (0 keV LLD setting) to 40.72% (500 keV LLD setting). The large reduction in simulated ε_{th} occurs because the prominent spectral features of the five-foil ^{6}Li-based SFMND occur within the energy range of approximately 0.3 – 1.0 MeV.

Illustrated in Figure 5.13 is the single-foil simulation scenario showing the foil positioned 1-mm laterally off-center within the sensitive volume. The perimeter of the sensitive volume is also shown, which is defined by the perimeter of the microstrip and drift electrodes (L_M x W_M). The foil position results in a minimum distance of approximately 20 – 21 mm, perpendicular to the foil surface, between the foil surface and the perimeter of the sensitive volume. Assuming full-energy reaction products are emitted into the backfill gas perpendicular to the foil surface (both polar and azimuthal), the alpha-particle energy will be fully absorbed within the sensitive volume, while approximately 0.93 – 0.98 MeV of the triton energy is absorbed within the sensitive volume

for particle trajectories ranging from approximately 20 to 21 mm, respectively [96]. However, before reaction products escape the foil and enter the backfill gas, a distribution of reaction-product energy is lost due to self-absorption within the foil. The amount of energy lost due to self-absorption is dependent on the site of creation and trajectories of the reaction products relative to the foil surface. Assuming the reaction product is not absorbed by other solid structures or escapes the sensitive volume, the amount of energy deposited within the P-10 gas increases as the polar and/or azimuthal angle of emission deviates from perpendicular to the foil surface. Therefore, the amount of reaction-product energy deposited within the P-10 gas is a continuous distribution that is dependent on the site of creation within the foil and the trajectory of the reaction products in both the foil and the P-10 gas.

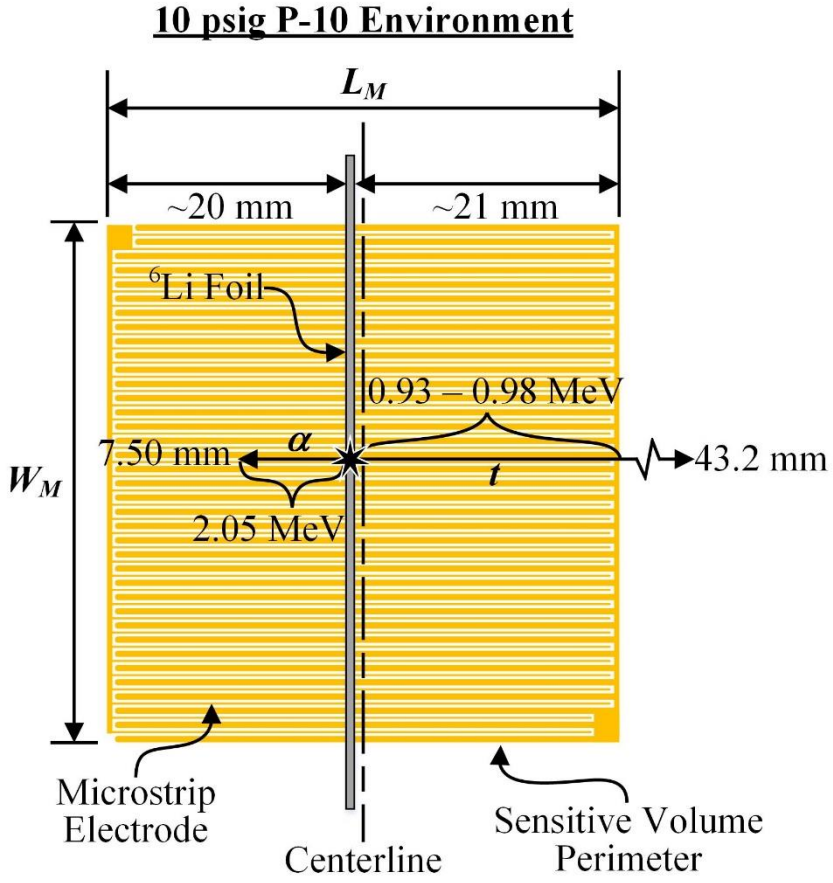

Figure 5.13. Top-down view of the MCNP6 simulation environment for the single-foil ^{6}Li-based SFMND showing the foil positioned 1-mm laterally off-center in the sensitive volume [155].

Illustrated in Figure 5.14 is the five-foil simulation scenario. Recalling Table 5.2, neighboring foils were positioned a distance, *d*, of 5.73 mm apart. Assuming full-energy reaction

products are emitted into the backfill gas perpendicular to the foil surface (both polar and azimuthal), the foil spacing allows for approximately 1.68 MeV and 0.25 MeV energy deposition of the alpha particles and tritons, respectively, to be absorbed within the backfill gas between neighboring foils [96]. For sufficiently-thin foils, the tritons are capable of ionizing the backfill gas between multiple foils by passing through one or more foils before being absorbed in a foil or the chamber wall. The amount of energy deposited between neighboring foils increases as the polar and/or azimuthal angle of emissions changes from perpendicular to the foil surface; however, the amount of energy lost from self-absorption within neighboring foils also increases for these trajectories. Thus, the distribution probability in the pulse-height spectrum decreases with energy deposition for the five-foil device compared to the single-foil device.

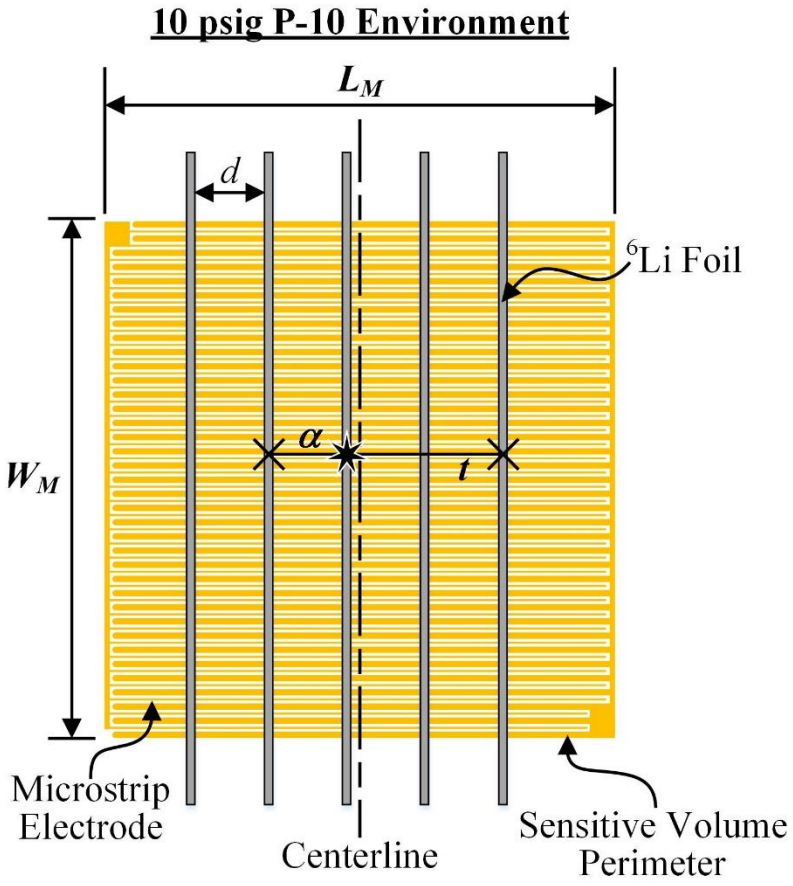

Figure 5.14. Top-down view of the five-foil simulation scenario showing the positions of the five foils relative to the sensitive volume perimeter. The distance between neighboring foils, d, is 5.73 mm. Alpha particles emitted from interior foils undergo self-absorption upon entering a neighboring foil, indicated by an X. Tritons are capable of traveling through adjacent foils before undergoing self-absorption within a foil or escaping the sensitive volume [155].

5.3.2 Effects of Gas Pressure

The ε_{th} and reaction-product pulse-height spectra as a function of P-10 gas pressure were simulated for one and five ^{6}Li foils using the simulation environment illustrated in Figure 5.10. The ε_{th} and reaction-product pulse-height spectra were simulated for P-10 gas pressures ranging from 1 to 5 atm in 1 atm increments. The ^{6}Li foils were defined with a thickness of 75 µm. The foil orientations and spacing were the same as those illustrated in Figure 5.13 and Figure 5.14 (listed in Table 5.2). A 0.5-cm diameter thermal-neutron beam was incident on the center of the front face of the foil(s). The square perimeter of the sensitive volume (L_M x W_M) was defined with dimensions of approximately 4.1275 cm x 4.1275 cm (1.625 in. x 1.625 in.).

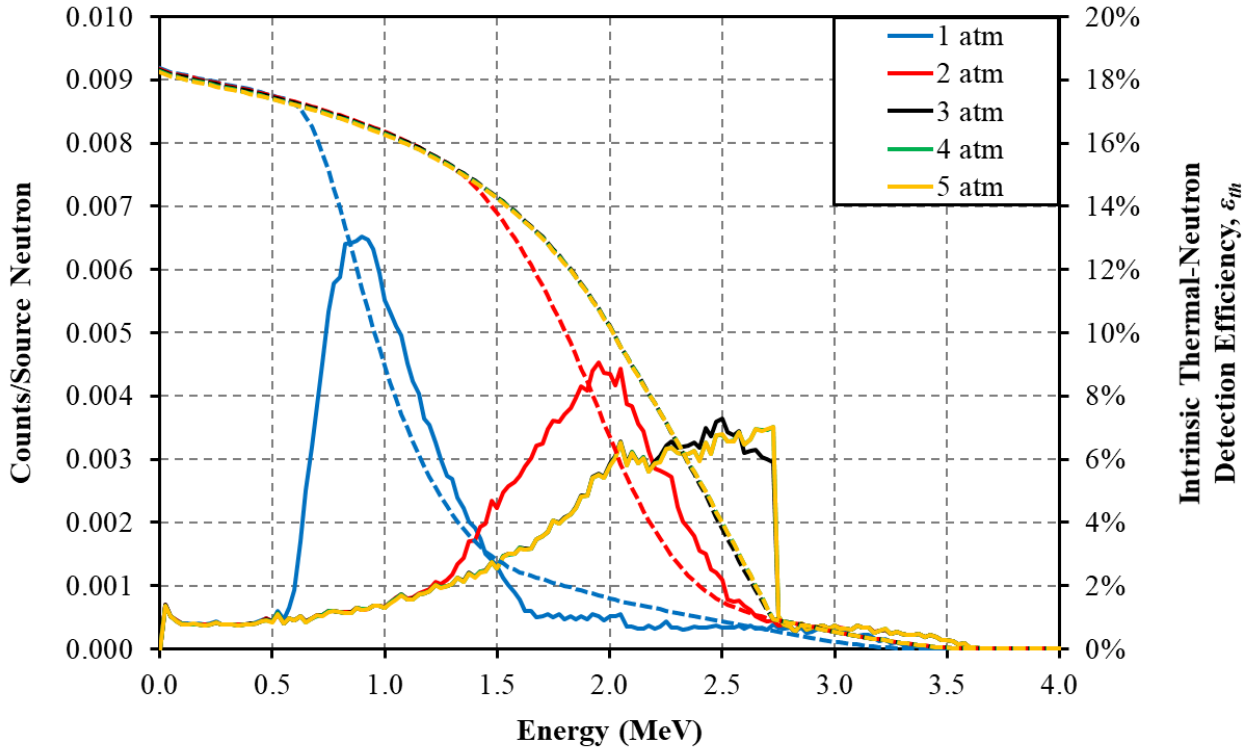

Figure 5.15. MCNP6-simulated reaction-product pulse-height spectra (solid lines corresponding to the left ordinate with units of counts/source neutron) for one suspended ^{6}Li foil surrounded by P-10 proportional gas with pressures ranging from 1 to 5 atm in 1 atm increments. The ε_{th} as a function of LLD setting are represented by dashed lines and corresponds to the right ordinate.

Shown in Figure 5.15 is the simulated reaction-product pulse-height spectra, represented by solid lines and corresponding to the left ordinate with units of "Counts/Source Neutron", of the single-foil ^{6}Li-based SFMND with P-10 gas pressures ranging from 1 to 5 atm. The simulated ε_{th}

as a function of LLD setting are represented by dashed lines and corresponds to the right ordinate of Figure 5.15. In all of the simulated reaction-product pulse-height spectra, a valley is present that separates the prominent spectral features from low-energy events. As the gas pressure is increased, and, thus, the density of the gas is increased, the reaction-product stopping power also increases, as defined by Eq. (3.22) and Eq. (3.23). Due to the increase in reaction-product stopping power as the gas pressure is increased, the ranges of the reaction products in the P-10 gas decrease (listed in Table 5.1). The reduction in reaction-product ranges as the gas pressure increases results in more reaction-product energy being deposited within the sensitive volume, assuming the reaction product does not collide with a solid structure or escape the sensitive volume.

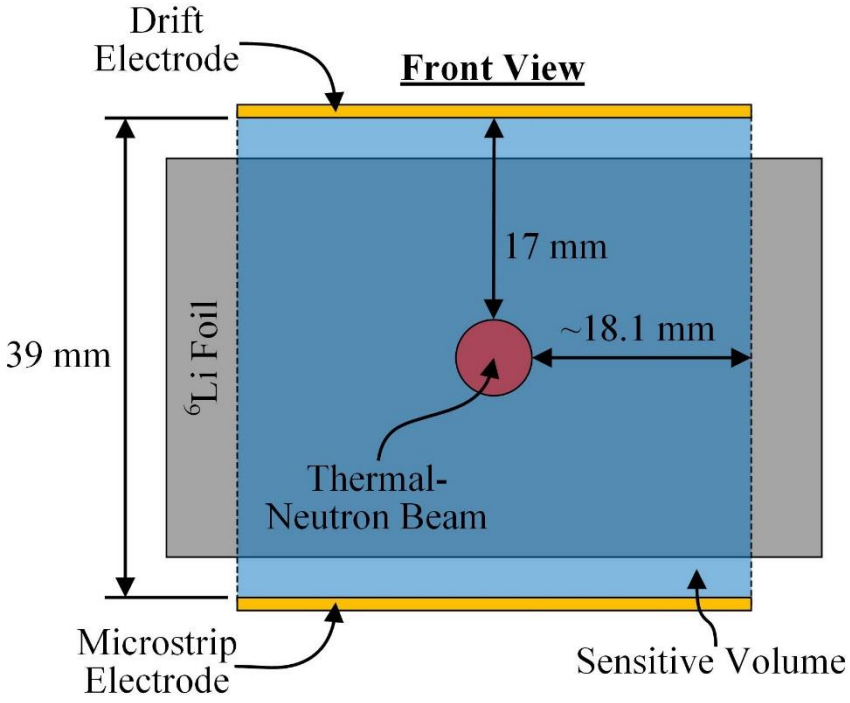

Figure 5.16. Illustration of the limiting distances between the perimeter of the thermal-neutron beam and the edge of the sensitive volume and electrode surfaces.

The increase in reaction-product energy deposition is represented in Figure 5.15 by an up-shift in energy of the reaction-product pulse-height spectral features as the gas pressure is increased from 1 to 3 atm. The energy range of the valley preceding the prominent spectral features also increases as the gas pressure is increased. The shape of the reaction-product pulse-height spectrum remains approximately constant for gas pressures exceeding 3 atm. The shape remains approximately constant because the reaction products are fully absorbed within the sensitive

volume due to the orientation of the foil within the sensitive volume and the location of the 0.5-cm thermal-neutron beam relative to the foil. Specifically, as illustrated in Figure 5.16, the range of the reaction products (listed in Table 5.1) is less than the limiting distance between the perimeter of the thermal-neutron beam and either the edge of the sensitive volume (approximately 18.1 mm) or the surface of either electrode (17 mm). Due to the up-shift in energy of the reaction-product pulse-height spectral features as the gas pressure is increased, the ε_{th} decreases less rapidly as the LLD setting is increased. Thus, as an example, a 500 keV LLD setting can be used for all P-10 gas pressures that were simulated without a significant reduction of ε_{th}.

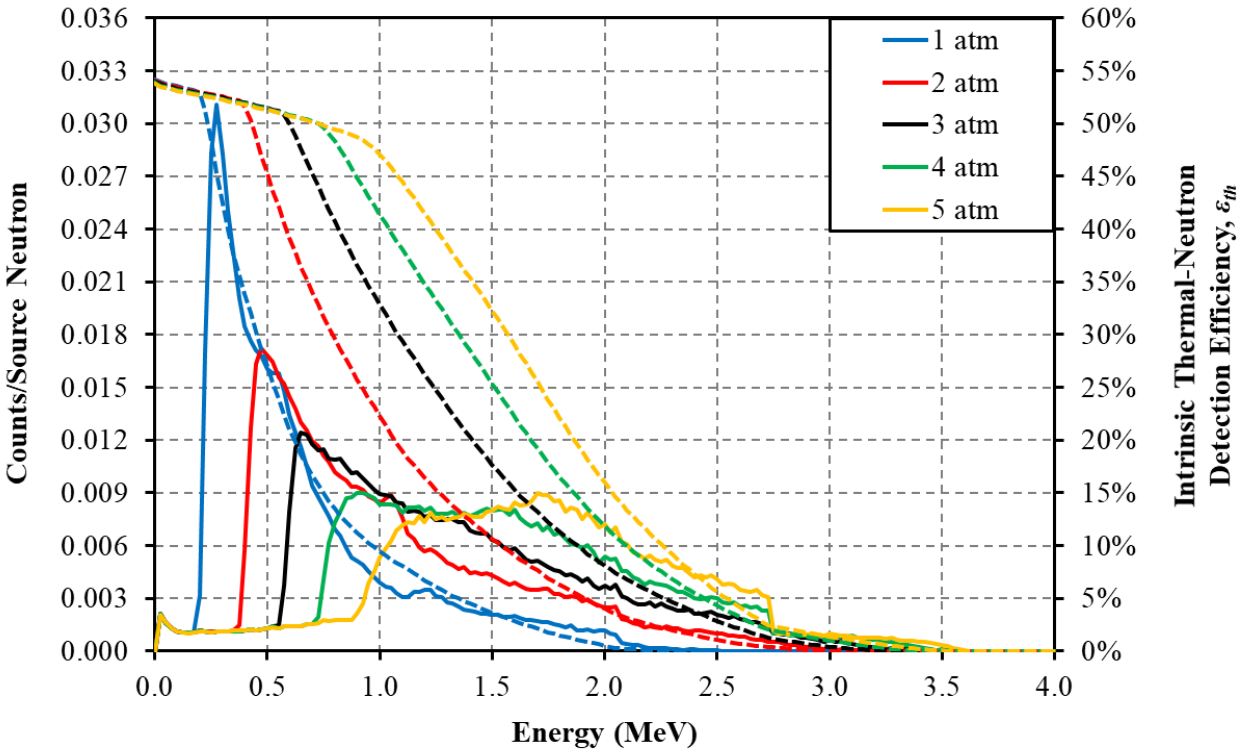

Figure 5.17. MCNP6-simulated reaction-product pulse-height spectra (left ordinate with units of counts/source neutron) for five suspended ^{6}Li foils surrounded by P-10 proportional gas with pressures ranging from 1 to 5 atm in 1 atm increments. The ε_{th} as a function of LLD setting are represented by the corresponding dashed lines for each gas pressure and corresponds to the right ordinate.

A similar trend is also depicted in Figure 5.17 for the five-foil scenario. The simulated reaction-product pulse-height spectra are represented by solid lines and correspond to the left ordinate with units of "Counts/Source Neutron". The simulated ε_{th} as a function of LLD setting are represented by dashed lines and corresponds to the right ordinate. Each increase in gas pressure

results in an up-shift in energy of the reaction-product pulse-height spectral features. Similar to the one-foil scenario, the up-shift in the energy range of the reaction-product pulse-height spectral features occurs because of the increase in the amount of reaction-product energy deposited within the sensitive volume combined with the decrease in probability of reaction-products escaping the sensitive volume. Likewise, the increase of the reaction-product stopping power as the gas pressure increases results in more reaction-product energy deposition between neighboring foils. As the gas pressure is increased, the energy range of the valley preceding the prominent spectral features increases. Thus, by increasing the gas pressure, a higher-energy LLD setting can be used without a significant reduction of ε_{th} (represented by the dashed lines of Figure 5.17). Although an increase in gas pressure is desirable for increasing the energy range of the valley in the reaction-product pulse-height spectrum, charge-carrier velocities reduce with an increase in gas pressure, as defined by Eq. (3.25) and Eq. (3.26). Thus, the operating voltage(s) must be adjusted in order compensate for the elevated gas pressure.

5.3.3 Effects of Foil Width Relative to Sensitive Volume Size

Due to the distribution of reaction-product emission sites about the face of the ^{6}Li foil(s), the effects of foil width relative to the perimeter of the sensitive volume were studied. Specifically, the changes in reaction-product pulse-height spectra and ε_{th} as a function of sensitive volume perimeter for one and five ^{6}Li foils were simulated. The simulations were performed by maintaining the ^{6}Li foil and frame dimensions (defined at the beginning of Section 5.3) and adjusting the size of the square sensitive volume perimeter, as illustrated in Figure 5.18 and Figure 5.19. The sensitive volume perimeter (L_M x W_M) was adjusted from 1.27 cm x 1.27 cm (0.5 in. x 0.5 in.) to 7.62 cm x 7.62 cm (3.0 in. x 3.0 in.) in 1.27 cm x 1.27 cm (0.5 in. x 0.5 in.) increments. The foil and frame dimensions (H_F, L_F, H_A, and L_A) were the same as those defined at the beginning of Section 5.3. The ^{6}Li foil thickness, t_F, was defined as 75 µm. The foil orientations and spacing, d, were the same as those used for the foil thickness and quantity simulations illustrated in Figure 5.13 and Figure 5.14, and listed in Table 5.2. The backfill gas was P-10 pressurized to 10 psig. A randomly-sampled rectangular beam of thermal neutrons was incident on the front face of the foil(s). The shape and sampling of the thermal-neutron beam was defined in order to study the

effects of reaction products emitted about the entire face of the foil(s) for different sensitive volume sizes.

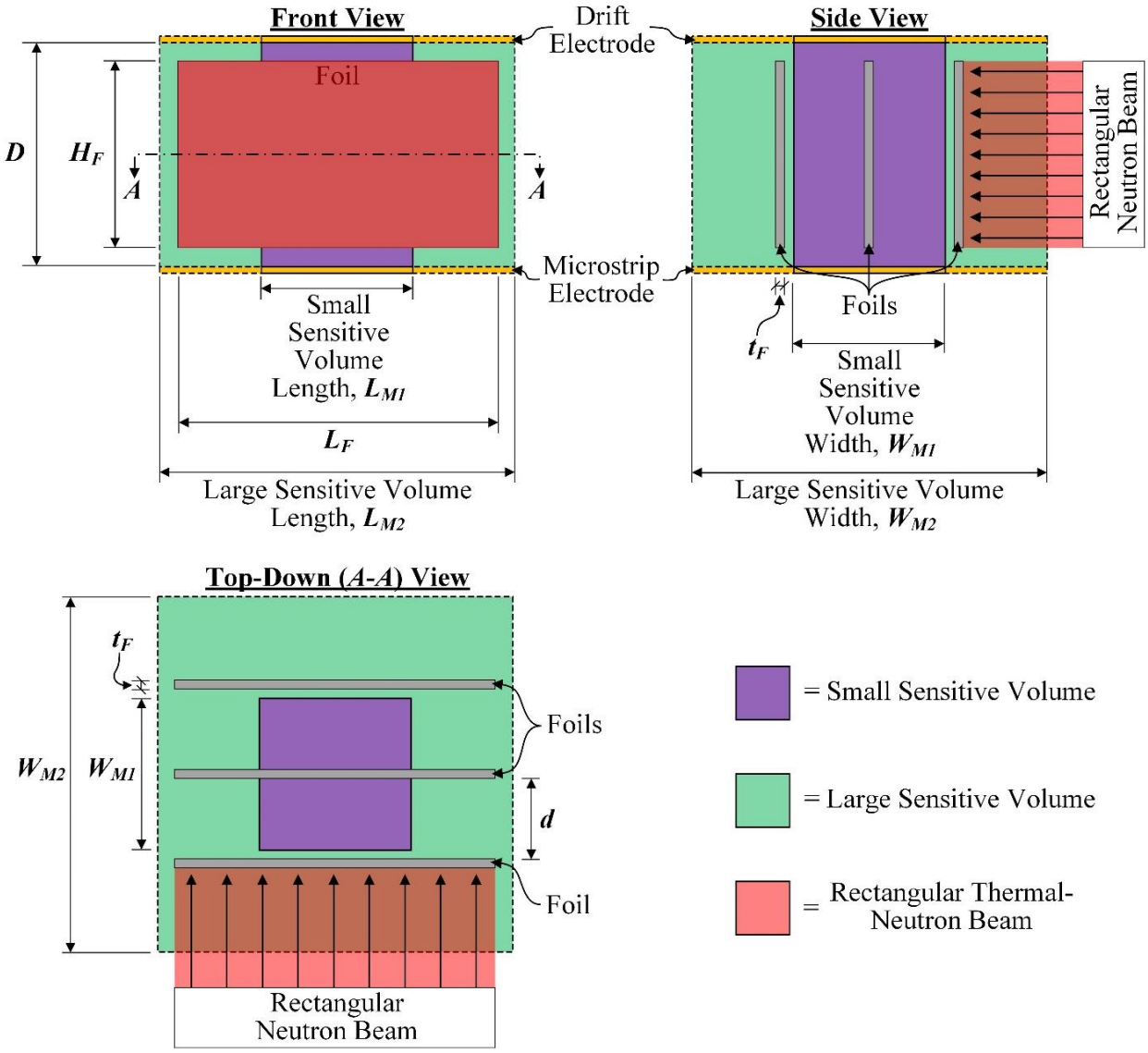

Figure 5.18. Illustrations depicting the width of the ^{6}Li foils relative to a small sensitive volume (shaded purple) and a large sensitive volume (shaded green). The thermal-neutron beam is shaded red, the foils are shaded gray, and the electrodes are shaded orange.

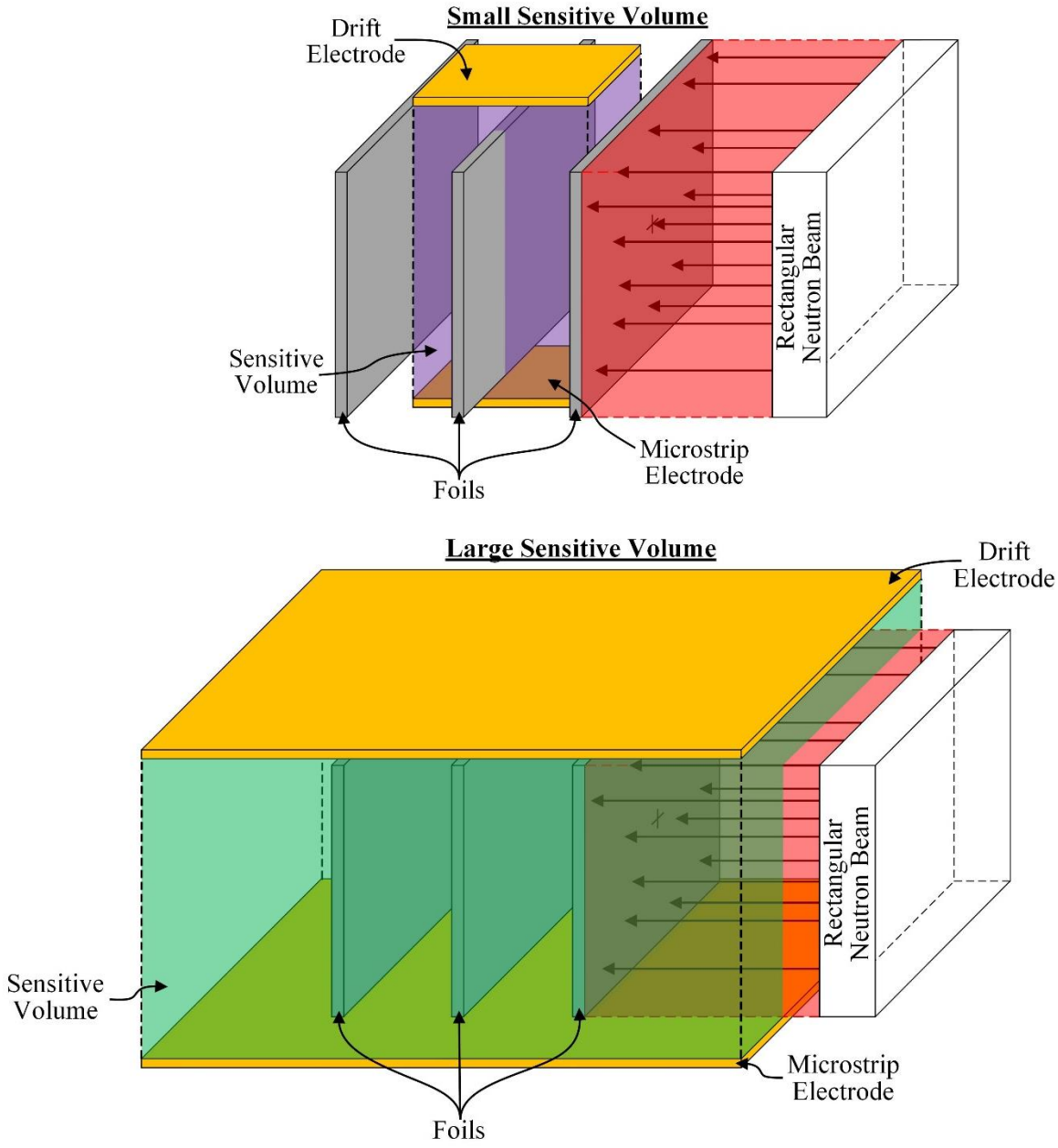

Figure 5.19. Illustrations of the ^{6}Li foil positions relative to a small sensitive volume (top – shaded purple) and a large sensitive volume (bottom – shaded green). The sensitive volume is defined by the perimeter of the electrodes and the distance separating the electrodes. The thermal-neutron beam is shaded red, the foils are shaded gray, and the electrodes are shaded orange.

In order to correlate the simulated reaction-product pulse-height spectra with the simulated ε_{th} as a function of LLD setting, the one- and five-foil device results were separately plotted for sensitive volume perimeters ranging from 1.27 cm x 1.27 cm to 5.08 cm x 5.08 cm and 5.08 cm x 5.08 cm to 7.62 cm x 7.62 cm. The single-foil results are shown in Figure 5.20 and Figure 5.21

and the five-foil results are shown in Figure 5.22 and Figure 5.23. The simulated reaction-product pulse-height spectra are represented by solid lines and correspond to the left ordinate of each plot with units of "Counts/Source Neutron". The ε_{th} as a function of LLD setting are represented by dashed lines and correspond to the right ordinate of each plot. For both the one- and five-foil scenarios, an up-shift of the energy range of the spectral features and an increase of ε_{th} occurs as the sensitive volume perimeter is increased from 1.27 cm x 1.27 cm to 5.08 cm x 5.08 cm. As the sensitive volume perimeter is increased, the probability of reaction products depositing more energy within the sensitive volume increases. An increase in ε_{th} also occurs because more neutron-absorption events occur within the sensitive volume as the sensitive volume perimeter is increased. However, for sensitive volume perimeters exceeding 5.08 cm x 5.08 cm, a majority of the reaction-product energy is already deposited within the sensitive volume. Thus, further increases of the sensitive volume perimeter do not yield a substantial increase in the energy range of the spectral features or ε_{th}.

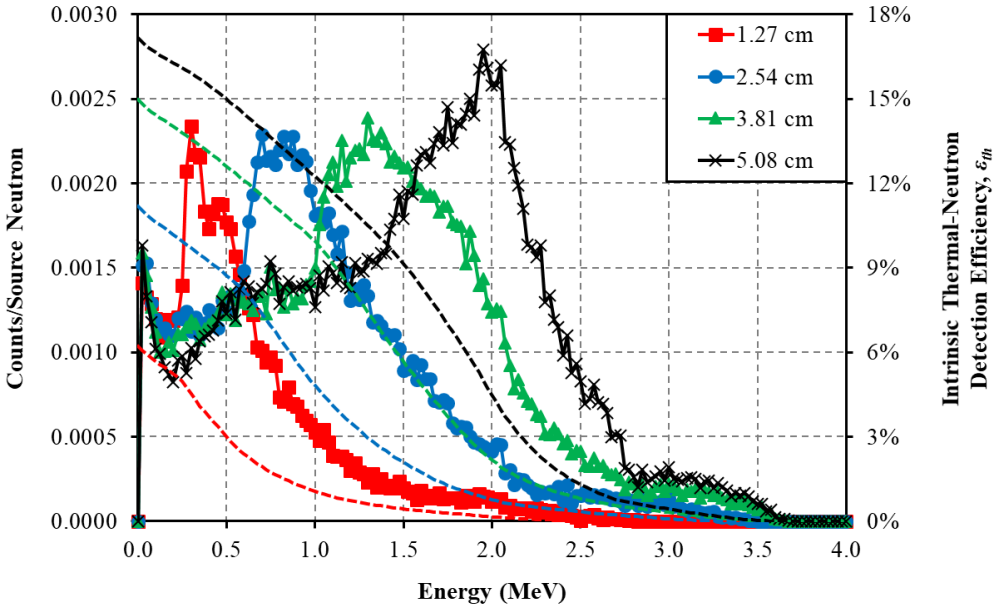

Figure 5.20. MCNP6-simulated reaction-product pulse-height spectra (left ordinate with units of counts/source neutron) for one ^{6}Li foil surrounded by 10 psig of P-10 proportional gas. The sensitive volume perimeters range from 1.27 cm x 1.27 cm (0.5 in. x 0.5 in.) to 5.08 cm x 5.08 cm (2.0 in. x 2.0 in.) in 1.27 cm (0.5 in.) increments. The ε_{th} as a function of LLD setting are represented by the corresponding dashed lines for each sensitive volume size.

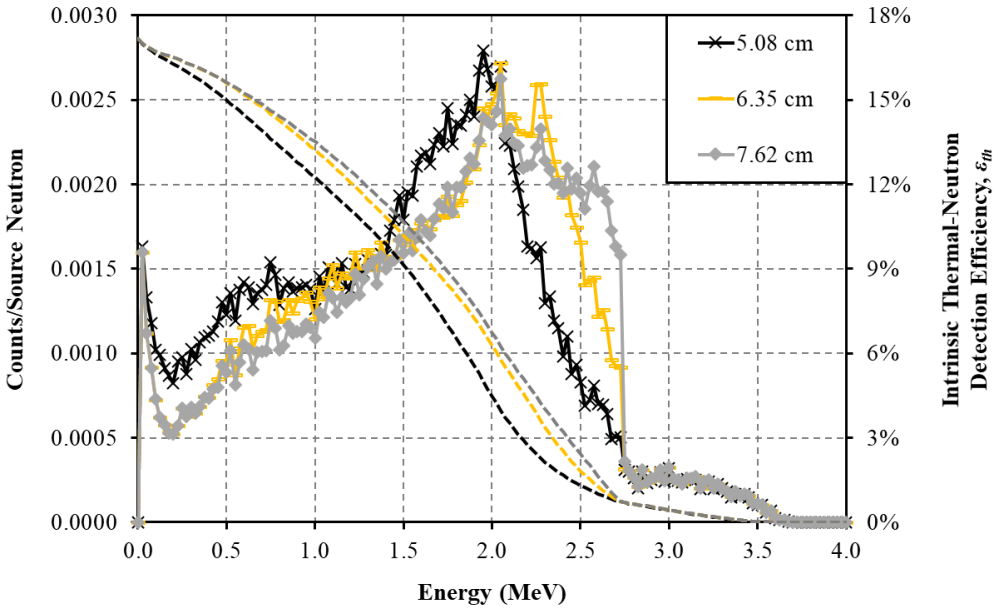

Figure 5.21. MCNP6-simulated reaction-product pulse-height spectra (left ordinate with units of counts/source neutron) for one ^{6}Li foil surrounded by 10 psig of P-10 proportional gas. The sensitive volume perimeters range from 5.08 cm x 5.08 cm (0.5 in. x 0.5 in.) to 7.62 cm x 7.62 cm (2.0 in. x 2.0 in.) in 1.27 cm (0.5 in.) increments. The ε_{th} as a function of LLD setting are represented by the corresponding dashed lines for each sensitive volume size.

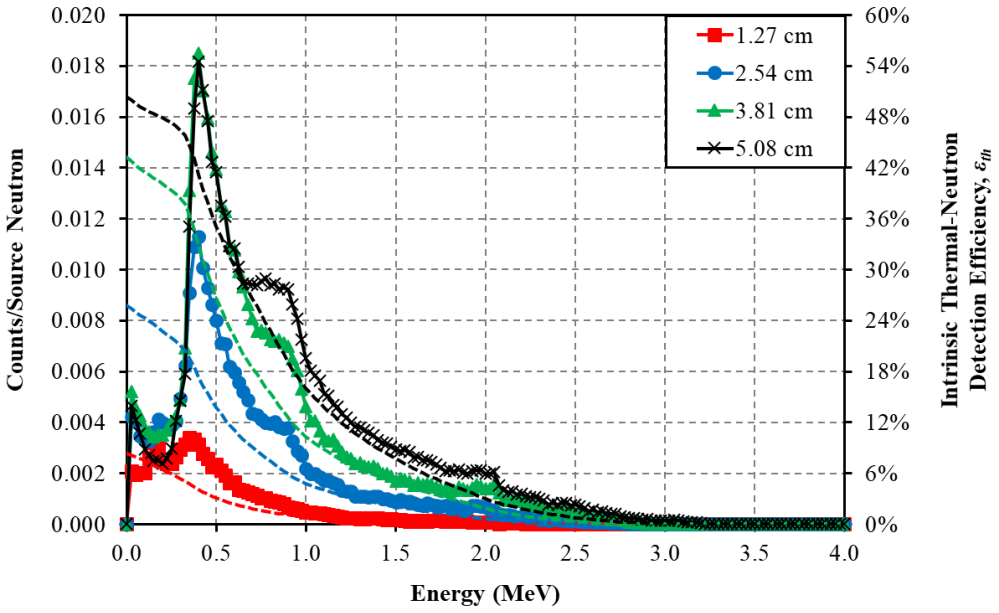

Figure 5.22. MCNP6-simulated reaction-product pulse-height spectra (left ordinate with units of counts/source neutron) for five ^{6}Li foils surrounded by 10 psig of P-10 proportional gas. The sensitive volume perimeters range from 1.27 cm x 1.27 cm (0.5 in. x 0.5 in.) to 5.08 cm x 5.08 cm (2.0 in. x 2.0 in.) in 1.27 cm (0.5 in.) increments. The ε_{th} as a function of LLD setting are represented by the corresponding dashed lines for each sensitive volume size.

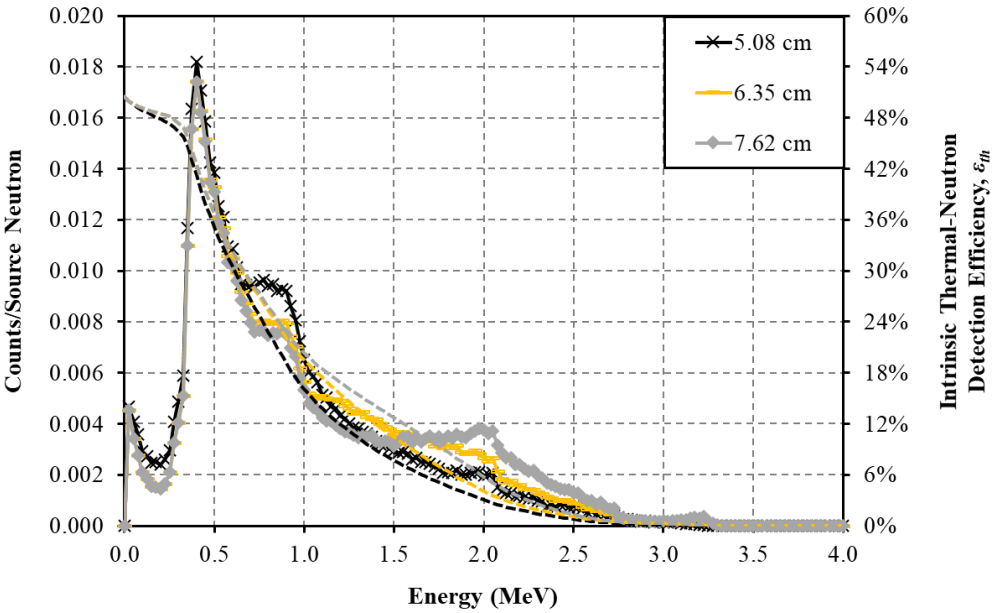

Figure 5.23. MCNP6-simulated reaction-product pulse-height spectra (left ordinate with units of counts/source neutron) for five ^{6}Li foils surrounded by 10 psig of P-10 proportional gas. The sensitive volume perimeters range from 5.08 cm x 5.08 cm (0.5 in. x 0.5 in.) to 7.62 cm x 7.62 cm (2.0 in. x 2.0 in.) in 1.27 cm (0.5 in.) increments. The ε_{th} as a function of LLD setting are represented by the corresponding dashed lines for each sensitive volume size.

To further explain the results shown in Figure 5.20 - Figure 5.23, a top-down cross-section view of the change in sensitive volume perimeter relative to the ^{6}Li foils, with fixed dimensions, is illustrated in Figure 5.24. The two-dimensional scenario also depicts examples of different reaction-product emission sites with corresponding reaction-product trajectory distributions. For the larger sensitive volume perimeter (shaded green), all reaction-product emission sites occur within the sensitive volume. Except for scenario *d*, all reaction-product trajectories result in full reaction-product energy deposition within the sensitive volume. However, in scenario *d*, reaction-product trajectories exist that prevent the deposition of all of the reaction-product energy within the sensitive volume before the reaction-product exits the sensitive volume. The distribution of reaction-product energy that is deposited within the sensitive volume becomes more pronounced as the sensitive volume perimeter is reduced in size relative to the foil width. Thus, for the smaller sensitive volume perimeter (shaded purple), only scenario *a* occurs within the sensitive volume. Furthermore, only the reaction-product trajectories of scenario *a* result in full reaction-product energy deposition within the sensitive volume. In scenario *b*, only one reaction product is capable of depositing a portion of its energy within the sensitive volume because the other reaction product

is emitted in the opposite direction and thus cannot also have a trajectory in the direction of the sensitive volume. Finally, scenarios *c*, *d*, and *e* illustrate examples where only the longer range reaction product is capable of depositing a portion of its energy within the sensitive volume.

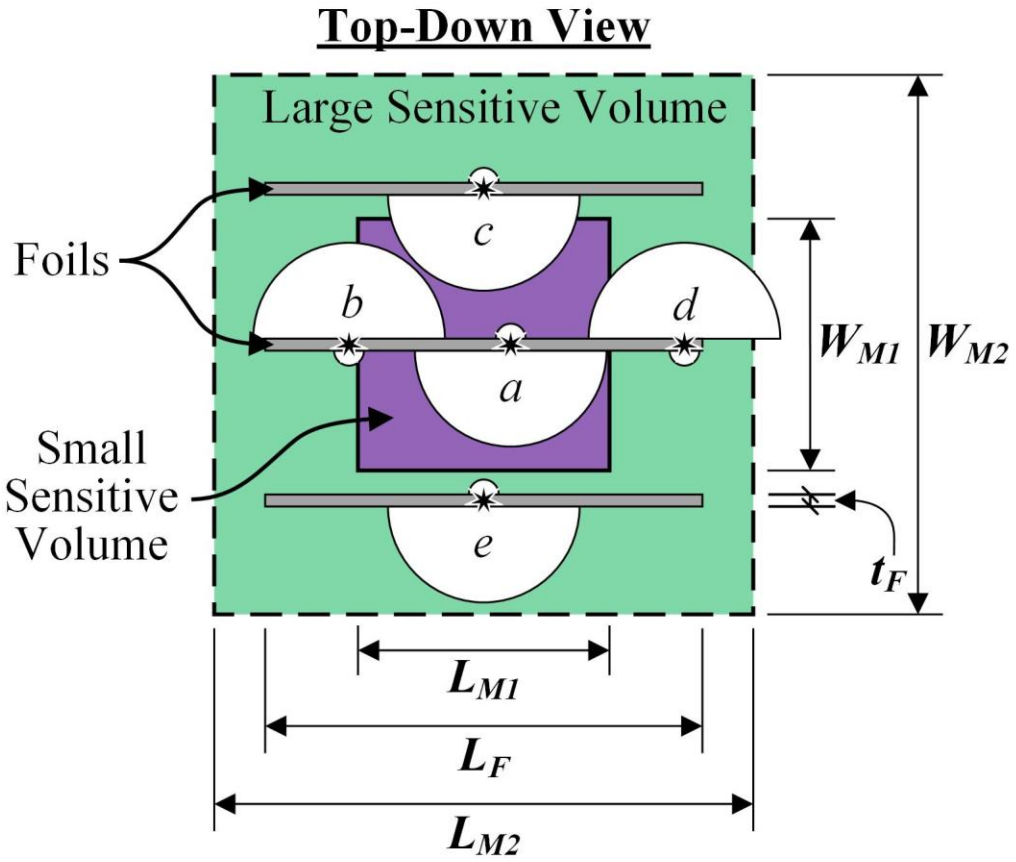

Figure 5.24. Top-down view of potential reaction-product trajectories for various reaction-product emission sites (a – e) occurring within two different sensitive volume sizes. The amount of reaction-product energy deposited within the sensitive volume is dependent on the emission-site and trajectory of the reaction-product relative to the perimeter of the sensitive volume.

CHAPTER 6

SUSPENDED FOIL MICROSTRIP NEUTRON DETECTOR: FABRICATION, CHARACTERIZATION TESTING METHODOLOGY, AND EXPERIMENTAL RESULTS

Measure what can be measured, and make measurable
what cannot be measured.

Galileo Galilei

Provided in this chapter is the microstrip-electrode fabrication process (Section 6.1). Discussion of the characterization methods employed to study the functionality of the microstrip electrodes follows (Section 6.2). The lithium foil suspension process is then described before discussing the SFMND assembly and fabrication methods (Section 6.3). Using the foil and electrode orientations discussed in Section 5.1 and shown in Figure 5.6, SFMNDs containing one and five ^{6}Li foils were fabricated (Section 6.3). The neutron-sensitivity measurement techniques are provided with corresponding results (Section 6.4). A discussion of the experimental results compared to theoretical considerations is provided. Finally, improvements to the SFMND design are proposed (Section 6.5).

6.1 **Microstrip-Electrode Fabrication**

The microstrip electrodes were fabricated in the KSU S.M.A.R.T. Laboratory class 100 clean room using metal lift-off photolithography techniques [156, 157]. Photolithography is the transfer of a pattern to a substrate using photoreactive chemicals, more commonly referred to as photoresist. Once exposed to ultraviolet (UV) light, the photoresist becomes more (*positive* tone) or less (*negative* tone) soluble in a solvent-based, photoresist developer solution. The basic

photolithography process occurs as follows. Upon coating the substrate surface with the desired thickness of photoresist, a photolithography mask is used to block specific regions of the substrate surface from the UV light. Following UV exposure, the substrate is immersed into a solvent-based developer solution and the regions of photoresist exposed to the UV light either are removed (positive tone) or remain (negative tone). The microstrip and drift electrode fabrication steps are illustrated in Figure 6.1 and discussed in Sections 6.1.1 – 6.1.7. Further discussion of metal lift-off photolithography methods and techniques is provided in the literature [157-160].

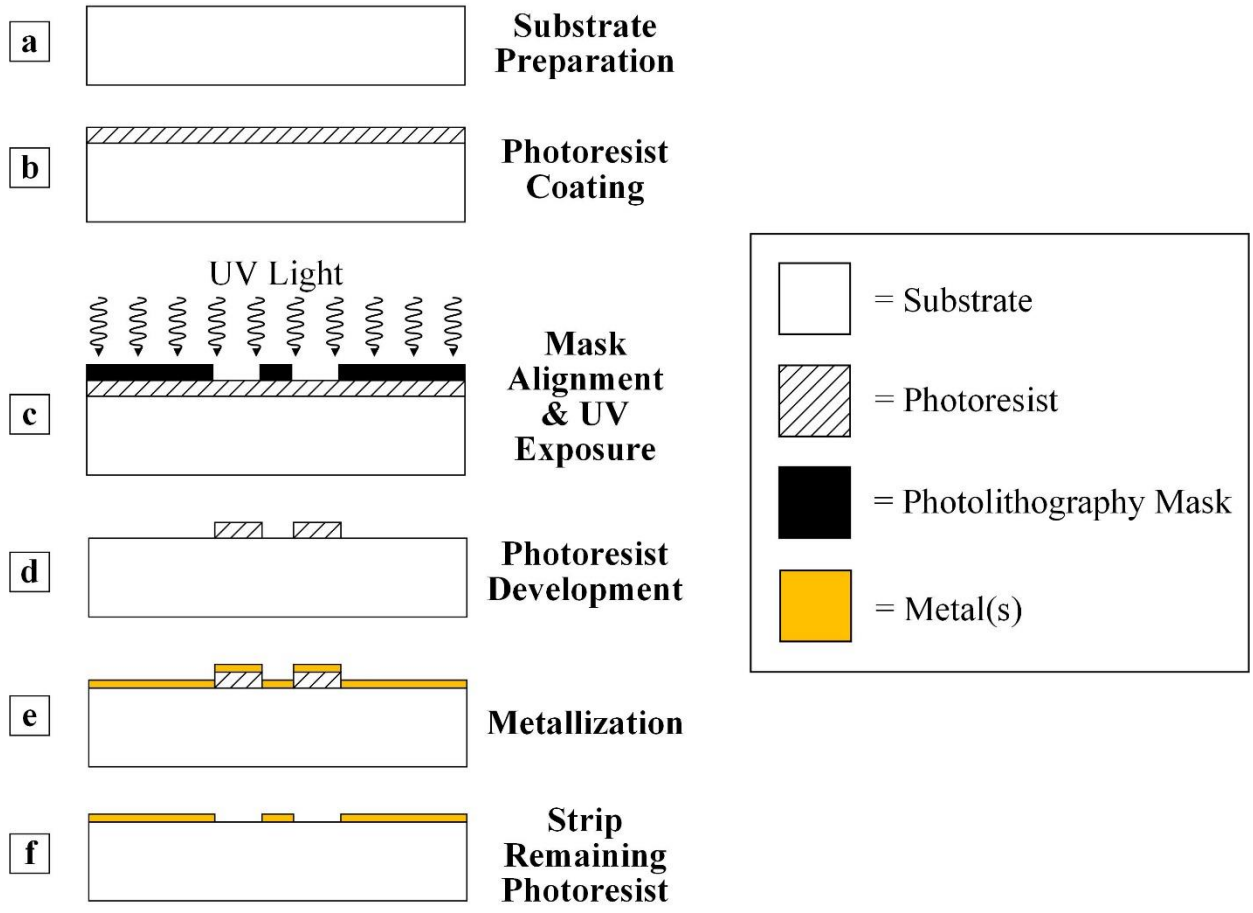

Figure 6.1. Metal lift-off photolithography processes used for fabricating the microstrip electrodes [161].

6.1.1 Substrate Selection

The microstrip electrodes were initially fabricated on 100-mm diameter, 525-µm thick silicon (Si) wafers with a volume resistivity, ρ_v, of 3 – 10 Ω cm and a dielectric constant, ε_r, of

11.9 [158]. Both surfaces of the Si wafers had a 3-µm thick layer of silicon dioxide (SiO_2). The volume resistivity and dielectric constant of SiO_2 are $10^{14} – 10^{17}$ Ω cm and 3.9, respectively [162, 163]. A gradual reduction in signal amplitude was observed when conducting electrode characterization (Section 6.2.5) and neutron-sensitivity (Section 6.4.1) measurements using the Si microstrip electrode. Due to the gradual reduction in signal amplitude, the literature was consulted [98, 107, 147]. Polarization of the SiO_2 layer was suspected to have occurred during the measurements leading to a gradual reduction of the gas gain (Section 6.2.5). Therefore, an electrically-stable substrate material was required.

Table 6.1. Comparison of the chemical composition and electrical properties of Schott Borofloat® 33 glass [164, 165] that was developed as a replacement to Corning 7740 glass [166, 167].

Name	**Chemical Composition**	**(%)**	**Volume Resistivity ρ_v (Ω cm) @ T(°C)**	**Dielectric Constant ε_r @ 25°C, 1 MHz**
Schott Borofloat® 33	SiO_2	(81)	1.0×10^8 @ 250°C	4.6
	B_2O_3	(13)	3.2×10^6 @ 350°C	
	Na_2O/K_2O	(4)		
	Al_2O_3	(2)		
Corning 7740	SiO_2	(80.6)	1.3×10^8 @ 250°C	4.6
	B_2O_3	(13.0)	4.0×10^6 @ 350°C	
	Na_2O	(4.0)		
	Al_2O_3	(2.3)		
	Misc. Traces	(0.1)		

Glass substrates such as Schott S8900 and Corning 7740 have previously been used as microstrip-electrode substrates because they are electrically stable over several hours [106, 107]. Schott S8900 is capable of long-term operational stability and has desirable electrical properties [106, 107, 168], but is not a common type of glass. Consequently, Schott S8900 is relatively expensive[1] compared to other substrate materials used for microstrip electrodes. Corning 7740 is a well-known, electrically-stable substrate, but is no longer available for purchase. However, Schott recently began producing a glass-substrate named Borofloat® 33 [164, 165] with a chemical composition and electrical properties nearly identical to Corning 7740 [166, 167], as listed in Table 6.1. Therefore, 100-mm diameter, 500-µm thick Schott Borofloat® 33 (SB33) substrates were

[1] The author received quotes from Schott Suisse SA ranging in price from $1583.60 to $174.60 per wafer for wafer quantities ranging from 1 to 100 wafers, respectively.

selected as a replacement to the Si substrates. The SB33 wafers cost $17.90 per wafer. Microstrip electrodes were also fabricated on the SB33 substrates.

6.1.2 Substrate Preparation

Prior to applying a photoresist coating to the substrate surface, the substrate surfaces were cleaned, dehydrated, and prepared with a photoresist adhesion promotor. The substrate surfaces were cleaned using a spin rinse dryer. Once cleaned, any residual water molecules were removed from the substrate surfaces to prevent partial or complete delamination of the photoresist coating during the subsequent photolithography processing steps. A dehydration bake-out procedure was performed by placing the substrate in a cleanroom oven with a temperature setting of 100°C for at least 20 min. Following the dehydration bake-out procedure, the substrate surfaces were coated with a photoresist adhesion promotor, hexamethyldisilazane (HMDS), due to the hydrophilic nature of the substrate surface (specifically SiO_2). HMDS removes the surface OH^- bonds and converts the surface state from hydrophilic to hydrophobic. The use of a photoresist adhesion promotor decreases the probability of water being trapped between the interface of the photoresist layer and the substrate surface, which can lead to delamination and poor feature resolution attributed to severe pattern undercutting. The HMDS was vapor deposited onto the substrate surfaces using a vapor prime oven with a temperature setting of 150°C. Prior to vapor depositing the HMDS, the substrate remained in the vapor prime oven for at least 10 min.

6.1.3 Photoresist Coating

Given that a metal lift-off photolithography process was used, which requires a controlled amount of pattern undercutting, negative photoresist was used. The top substrate surface was spin-coated with AZ® nLOF 2070 negative photoresist using a photoresist spinner. The photoresist was deposited onto the center of the substrate prior to initiating the spinning sequence. When depositing the photoresist onto the substrate surface, the substrate surface must remain free of dust and other airborne contaminants. Likewise, the photoresist was applied carefully to ensure no bubbles were incorporated into the photoresist prior to initiating the spin sequence. Should bubbles, dust, and/or other airborne contaminants be present on the substrate surface prior to initiating the spinning

sequence, streaks can appear in the photoresist that will alter the resolution of the photolithography pattern. During the spin-coating process, the photoresist is uniformly applied to the substrate surface and any residual photoresist is removed from the substrate. The photoresist viscosity, spin velocity of the substrate, and spin time define the thickness of photoresist applied to the substrate surface. Following spin-coating, the substrate was placed on a hotplate with a temperature setting of 105°C for 3 min. in order to perform a contact softbake. The softbake procedure is performed in order to remove solvent from the photoresist, which, in turn, hardens the photoresist and improves the photoresist adhesion to the substrate surface. The amount of solvent that is removed from the photoresist prior to UV exposure is dependent on the time and temperature parameters of the softbake procedure.

6.1.4 Mask Alignment & UV Exposure

The substrate was positioned beneath the photolithography mask shown in Figure 6.2 and exposed to UV light for 10 sec. A proximity gap of 6 µm was between the substrate and the photolithography mask during the UV exposure. The regions of photoresist that were not blocked by the photolithography mask features absorbed the UV light. When the photoresist absorbs UV light, the optical energy of the UV light is converted into chemical energy, which initiates a polymer-linking process referred to as *cross-linking*. Due to cross-linking, an increase in the average molecular weight of the cross-linked photoresist occurs. Consequently, the solubility of the cross-linked photoresist in a photoresist developer solution decreases.

The photolithography mask shown in Figure 6.2 was designed using *L-Edit* [169] and fabricated by Advanced Reproductions Corp. The mask design incorporated three microstrip electrode sizes, with perimeters of 1.27 cm x 1.27 cm (0.5 in. x 0.5 in.), 2.2225 cm x 2.2225 cm (0.875 in. x 0.875 in.), and 4.1275 cm x 4.1275 cm (1.625 in. x 1.625 in.). Although three microstrip electrode sizes were fabricated, only the 4.1275 cm x 4.1275 cm (1.625 in. x 1.625 in.) microstrip electrodes were characterized (Section 6.2) and used for neutron-sensitivity testing (Section 6.4). However, the capacitance of each electrode size was measured to compare the electrode capacitance as a function of electrode size (Section 6.2.1). The photolithography mask was designed in order to fabricate microstrip electrodes featuring 25-µm wide anode strips and 500-µm wide cathode strips with an anode-to-anode pitch of 1000 µm. As shown in Figure 6.2,

the anode and cathode strips were interconnected to separate 2 mm x 2 mm bond pads. For all electrode sizes shown in Figure 6.2, the anode strip bond pad is located at the top-right and the cathode strip bond pad is located at the bottom-left. The spacing between anode and cathode strips was maintained throughout the length of the strips as well as at the strip ends, as shown in Figure 6.2.

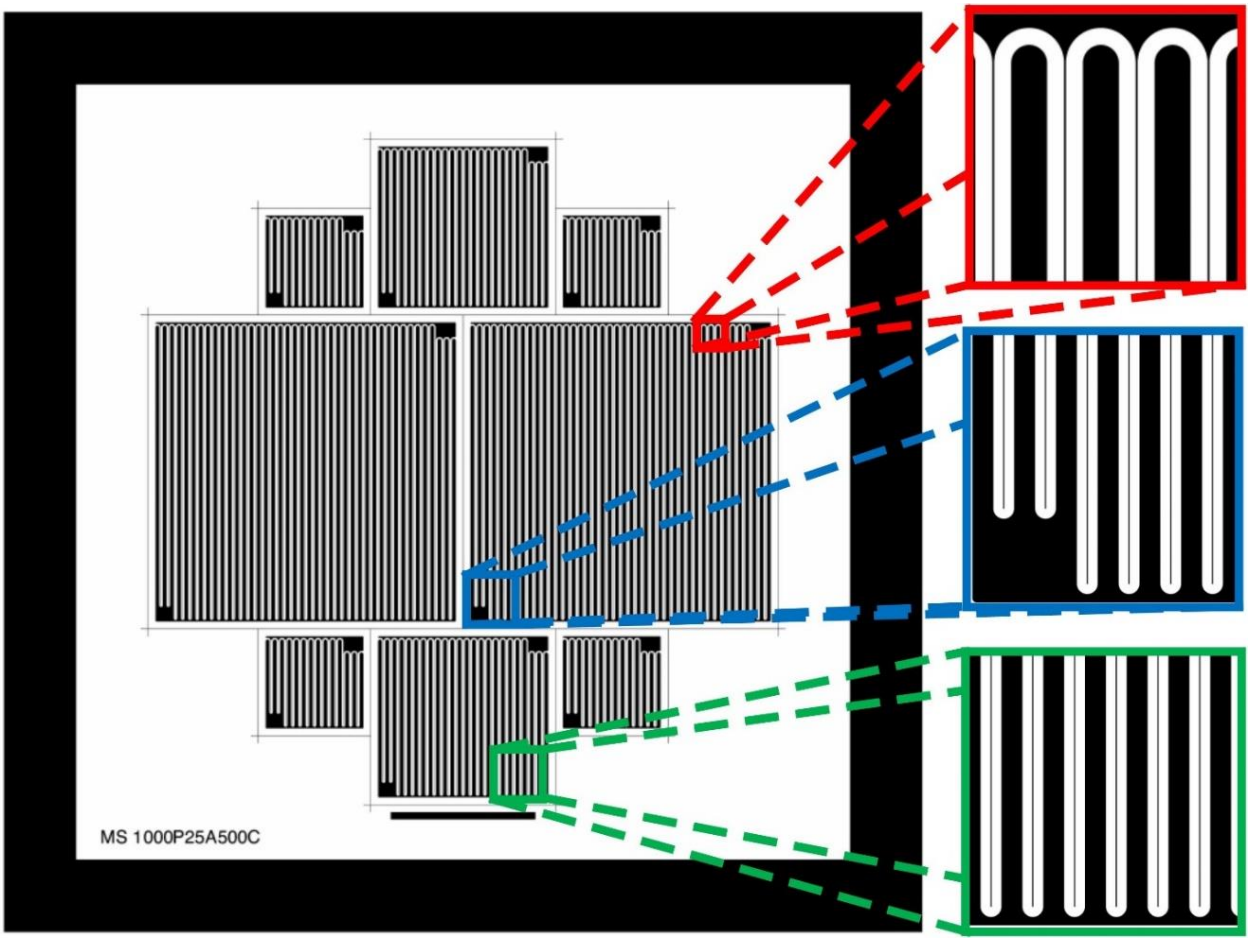

Figure 6.2. Photolithography mask used for fabricating three sizes of microstrip electrodes. The red-outlined box highlights the 500-µm wide cathode strip ends relative to the interconnected 25-µm wide anode strips. The blue-outlined box highlights the 2 mm x 2 mm bond pad for the cathode strips. A 2 mm x 2 mm bond pad was also used for measuring the signal from the anode strips (located in the top-right of each electrode pattern). The green-outlined box highlights the anode strip ends relative to the interconnected cathode strips.

6.1.5 Photoresist Development

Following UV exposure, the substrate was placed on a hotplate with a temperature setting of 115°C to perform a post-exposure baking (PEB) procedure for 1 min. The PEB procedure

further hardens the photoresist, improves photoresist adhesion to the substrate surface, and reduces striations caused by standing wave effects during UV exposure. The substrate was then submerged in AZ® MIF 300, a metal ion free (MIF), tetramethylammonium hydroxide (TMAH) photoresist developer solution. The photoresist developer dissolves the regions of photoresist that were not exposed to UV light. Consequently, following the development step, the remaining photoresist on the substrate surface is the inverse image of the photolithography mask pattern.

The substrate was visually inspected using optical microscopy to determine the amount of development that occurred. The degree of pattern undercut was also monitored. Pattern undercut is important when performing metal lift-off photolithography to ensure that the desired pattern is retained during the metallization process. When necessary, further development was performed until sufficient pattern undercut was achieved. The substrate surfaces were then cleaned using a spin rinse dryer. The substrate surfaces not coated by photoresist were then prepared for metallization. An O_2 plasma ash was performed for 2 min. to remove any residual photoresist remaining on the substrate surface where the microstrip electrode features would eventually exist. The substrate was then placed in a bath of buffered oxide etch (BOE) for 30 sec. to etch a thin layer of the substrate surface in preparation for metallization. Finally, prior to positioning the substrate(s) within an electron-beam (e-beam) evaporator, a cleaning process was performed using the spin rinse dryer.

6.1.6 Metallization

Metallization of the microstrip anode and cathode strips as well as the drift electrodes was accomplished using e-beam evaporation, a physical vapor deposition (PVD) method. The metals used were Cr, Cu, and Au at thicknesses of 500 Å, 3000 Å, and 1000 Å, respectively. The metals were selected based on their functionality. The Cr functioned as the adhesion layer to the substrate surface, the Cu as the conductive layer, and the Au as the encapsulating layer to prevent oxidation of the Cu conductive layer. Following the metallization process, the substrate was placed in a bath of AZ® Kwik Strip photoresist remover to remove the remaining photoresist. The substrate remained in the AZ® Kwik Strip photoresist remover bath overnight and the microstrip electrode features were inspected the following morning. The microstrip electrodes that were fabricated using 100-mm diameter, 525-µm thick Si wafers are shown in Figure 6.3 and the microstrip

electrodes that were fabricated using 100-mm diameter, 500-µm thick SB33 substrates are shown in Figure 6.4.

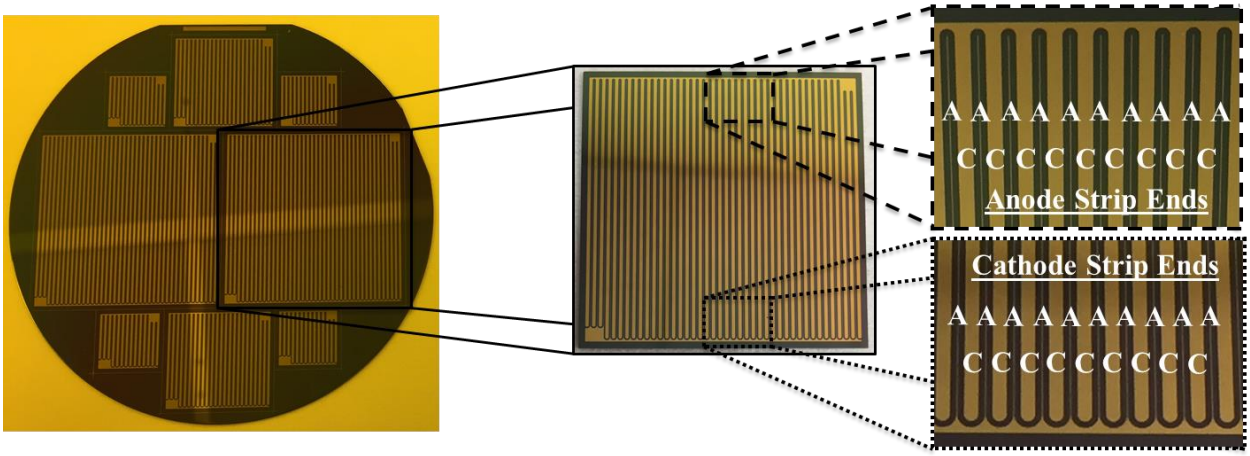

Figure 6.3. Microstrip electrodes fabricated using 100-mm diameter, 525-µm thick low-resistivity silicon wafers with a 3-µm thick layer of SiO_2 on both surfaces of the substrate. Anode strips are labeled with "A" and cathode strips are labeled with "C" [161].

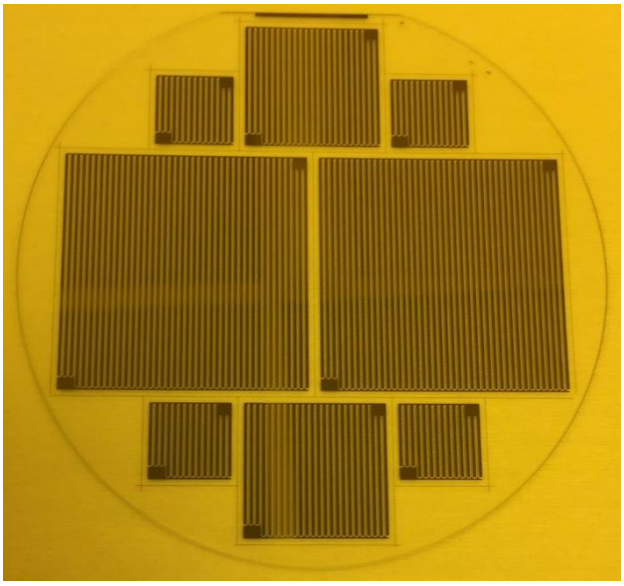

Figure 6.4. Microstrip electrodes fabricated using 100-mm diameter, 500-µm thick Schott Borofloat® 33 substrates.

The photolithography methods were used only when fabricating the microstrip electrodes. Due to the planar geometry of the drift electrodes, fewer fabrication steps were inherently required. First, the substrate surface was cleaned using the spin rinse dryer. The substrate was then inserted into the e-beam evaporator for metallization. Because no photolithography processing was

performed, a planar metal layer was deposited on the surface. When fabricating the drift electrodes, the same metals were used in the same order and with the same thicknesses.

6.1.7 Wafer Dicing

The microstrip and drift electrodes were cut and removed from the wafer using a wafer dicing saw. During the dicing process, the position of the wafer was maintained using UV dicing tape. The UV dicing tape features an adhesive surface that the wafer is mounted atop. The dicing process occurred by orienting the dicing blade relative to the dicing lines defined from the photolithography mask (Figure 6.2). Once properly aligned, the dicing blade was slowly passed through the wafer. As the wafer was diced, a mixture of deionized (D.I.) water and cutting fluid was injected at the cutting site to improve wetting and lubricity, and remove wafer saw dust. Following the wafer dicing process, the electrodes were rinsed using D.I. water. In order to remove the electrodes from the dicing tape, the dicing tape was exposed to UV light which reduces the adhesion between the tape and the wafer/electrodes. The electrodes were then removed, rinsed with D.I. water, and dried.

6.2 Microstrip-Electrode Characterization

The microstrip electrodes were characterized by first measuring the capacitance as a function of time (Section 6.2.1). Next, counting and gas-multiplication curves were defined for each substrate (Section 6.2.4). The gain stability of both substrates was then measured and compared (Section 6.2.5). Finally, the drift electric field strength distribution was measured using the SB33 microstrip electrode (Section 6.2.6).

6.2.1 Electrode Capacitance Measurements

Capacitance measurements were conducted using a BK Precision 879 LCR (inductance – L, capacitance – C, resistance – R) meter. The capacitance between the interconnected anode and cathode strips, C_M, was measured with the probes positioned a distance d_C apart, as illustrated in

Figure 6.5. The positive probe was positioned at the anode strip bond pad and the ground probe was positioned at the cathode strip bond pad. Because the measurement of C_M includes the capacitance between the probes, C_P, the capacitance was measured between the probes without positioning the probes on the anode and cathode strip bond pads. The probes were positioned the same distance, d_C, apart from one another. The net capacitance, C_N, was then calculated by subtracting the probe capacitance, C_P, from the capacitance measured with the probes positioned on the anode and cathode strip bond pads, C_M, as described by,

$$C_N = C_M - C_P . \tag{6.1}$$

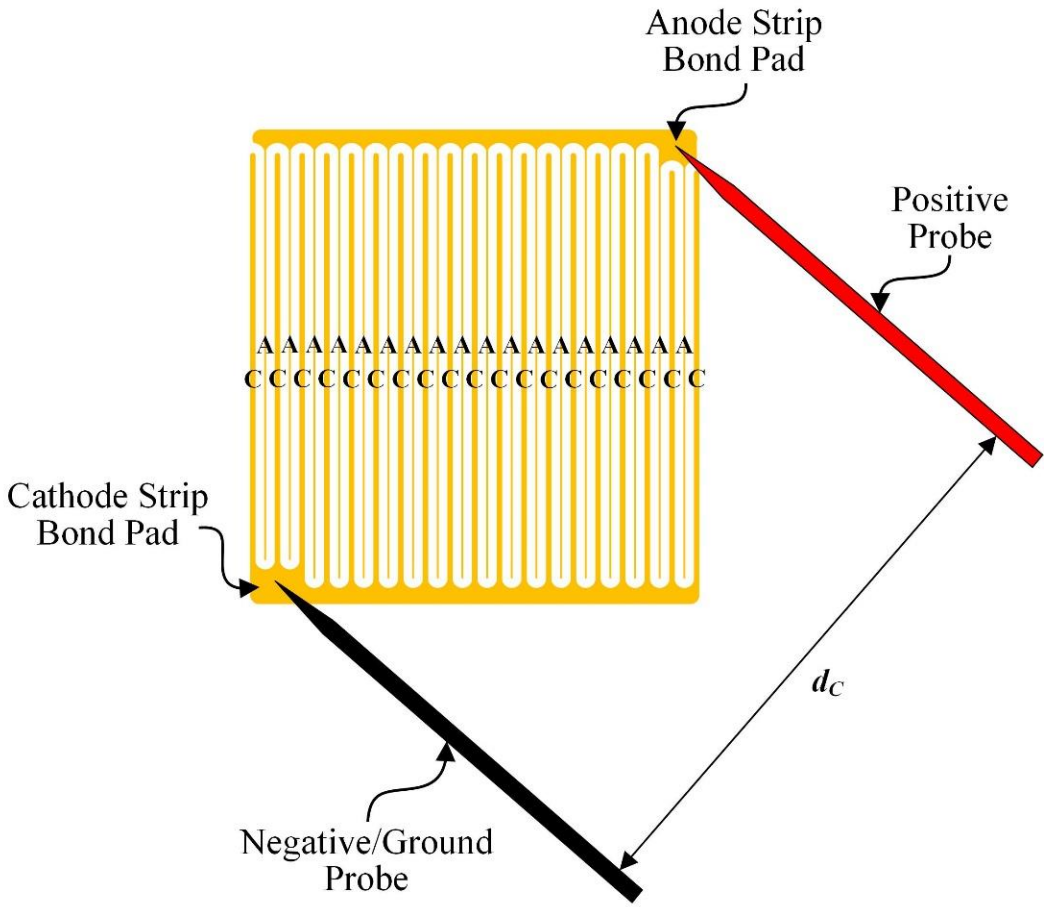

Figure 6.5. Illustration of the method for measuring the capacitance of the microstrip electrodes.

Listed in Table 6.2 are the measured net capacitances of the Si and SB33 microstrip electrodes for each electrode size. The capacitance measurements were conducted for frequencies of 100 Hz, 1 kHz, and 10 kHz. As the electrode size decreases, the net capacitance also decreases.

Fewer anode and cathode strips are incorporated within the microstrip electrode as the electrode size decreases. Thus, fewer anode strips are adjacent to neighboring cathode strips, resulting in a decrease in capacitance. A reduction in capacitance should yield an increase in measured pulse amplitude (Eq. (3.21)), which, in turn, should improve the signal-to-noise ratio. The reduction in capacitance as a function of electrode size indicates that segmentation of anode strips may prove beneficial for reducing the capacitance of the electrode. A difference of over an order of magnitude in capacitance was measured between the two substrate types for all electrode sizes. For each electrode size, the change in capacitance as a function of substrate type is suspected to be attributed to the difference between the Si and SB33 dielectric constants, ε_r, and the substrate thicknesses.

Table 6.2. Comparison of the silicon (Si) and Schott Borofloat® 33 (SB33) microstrip-electrode capacitances, in pF, measured for each electrode size.

	1.2700 cm x 1.2700 cm		2.2225 cm x 2.2225 cm		4.1275 cm x 4.1275 cm	
Frequency	**Si**	**SB33**	**Si**	**SB33**	**Si**	**SB33**
100 Hz	142	6	314	22	754	63
1 kHz	138	4	305	21	755	61
10 kHz	138	4	303	23	756	62

6.2.2 Electrical Connections & Electrode Positioning

Following electrode capacitance measurements, electrical connections were made to the 4.1275 cm x 4.1275 cm electrodes in preparation for conducting microstrip-electrode characterization measurements. The electrical connections were made by soldering separate 22 AWG silver-plated copper wires to the anode and cathode strip bond pads as well as the surface of the drift electrode. Once soldered, the electrodes were rinsed using isopropyl alcohol and dried.

The vertical and horizontal positions of the microstrip and drift electrodes were maintained during microstrip-electrode characterization and SFMND neutron-sensitivity measurements using the plastic support structure shown in Figure 6.6 and Figure 6.7. The plastic support structure was designed so that the microstrip and drift electrodes were vertically aligned. The design of the plastic support structure also allowed for adjusting the distance separating the electrodes, *D*. The plastic support structure was fabricated using #6-32 nylon threaded rods, 1.5-mm (0.06-in.) thick nylon plastic washers, and 0.76-mm (0.03-in.) thick polycarbonate film. The nylon plastic washers had an inside diameter of 3.3 mm (0.13 in.) and an outside diameter of 7.4 mm (0.29 in.). The

materials that were used for fabricating the plastic support structure were selected due to their availability within the laboratory.

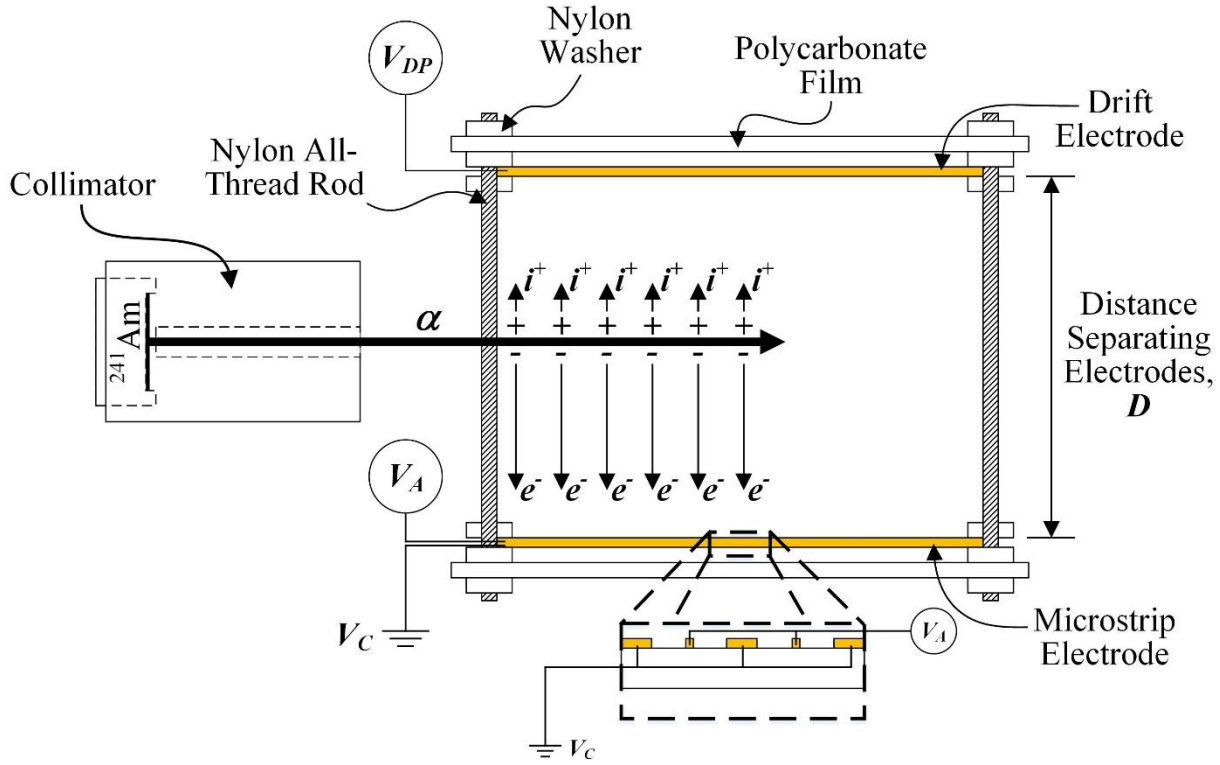

Figure 6.6. Illustration of the plastic support structure used for maintaining the positions of the electrodes while conducting microstrip-electrode characterization and SFMND neutron-sensitivity measurements.

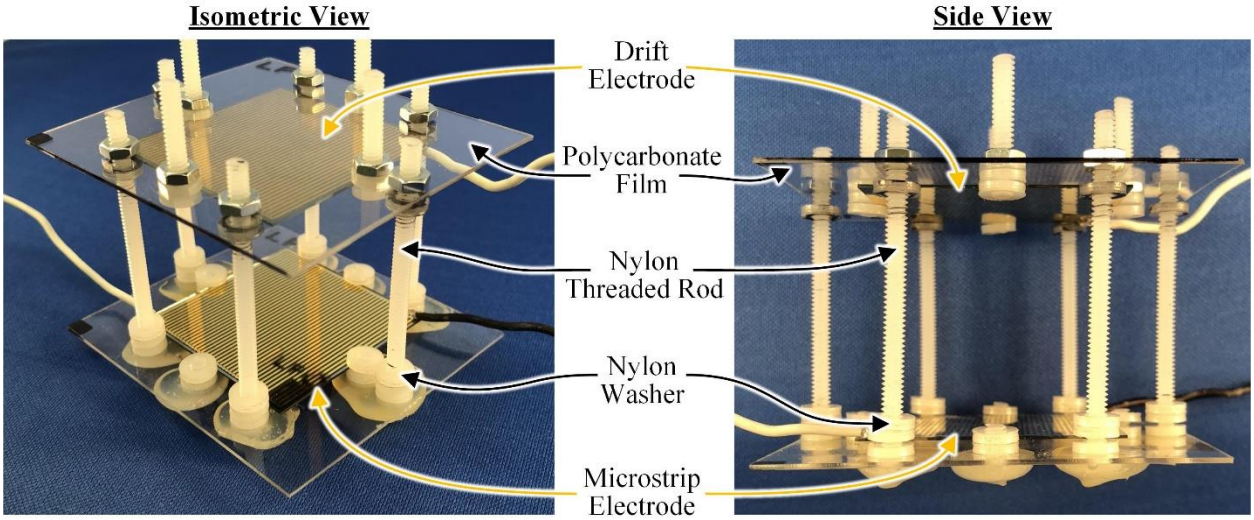

Figure 6.7. Isometric (left) and side (right) view photographs of the plastic support structure.

6.2.3 Testing Instrumentation

The remainder of the microstrip-electrode characterization and the SFMND neutron-sensitivity measurements were conducted using an aluminum testing enclosure with exterior length, width, and height of 20.32 cm (8 in.), 20.32 cm (8 in.), and 18.415 cm (7.25 in.), respectively, and a wall thickness of 0.9525 cm (0.375 in.) (Figure 6.8). The enclosure had two SHV feedthroughs to separately apply voltages to the microstrip and drift electrodes. Also shown in Figure 6.8 is the gas-pressure monitoring system that was used to monitor the enclosure pressure. The gas-pressure monitoring system provided the option to connect a gas cylinder to the enclosure. For gas pressures exceeding 30 psig, a SSI Technologies, Inc. MGA-100-A-9V digital pressure gauge was used to monitor the enclosure pressure, with a maximum pressure rating of 100 psig and a resolution of 0.1 psig [170]. For gas pressures below 30 psig, a SSI Technologies, Inc. MGA-30-A-9V-R digital pressure gauge was used, with a maximum pressure rating of 30 psig and a resolution of 0.01 psig [170]. When the enclosure pressure deviated during operation, the gas-pressure monitoring system was used to add or remove gas from the enclosure.

Shown in Figure 6.9 is the mobile testing station that was used to conduct microstrip-electrode characterization and SFMND neutron-sensitivity measurements. The mobile testing station was equipped with the components listed in Table 6.3. Diagrams of the equipment configurations used for microstrip-electrode characterization and SFMND neutron-sensitivity measurements are shown in Figure E.1 and Figure E.2, respectively, of Appendix E. While performing measurements, the operating voltage of the anode strips was monitored using a Fluke IV True RMS digital multimeter and the drift electrode operating voltage was monitored using a Fluke 8010A digital multimeter. The DC voltage ranges, with corresponding resolutions, for each digital multimeter are listed in Table 6.4.

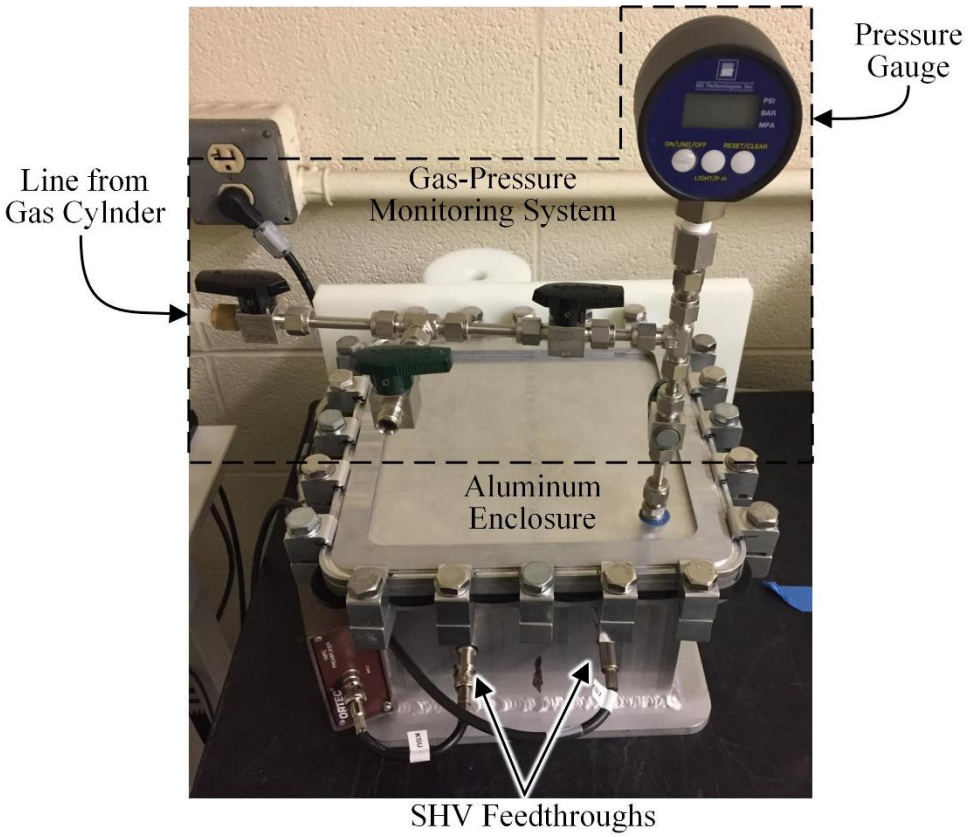

Figure 6.8. Aluminum testing enclosure used for microstrip-electrode characterization and neutron-sensitivity measurements. The enclosure had two SHV feedthroughs to separately apply operating voltages to the microstrip and drift electrodes. Also shown is the gas-pressure monitoring system with a digital pressure gauge and valve assembly for pressure balancing. A gas cylinder could be attached to the enclosure using a quarter-turn valve (upper left).

Table 6.3. Mobile testing station components. The numbers correspond to those shown in Figure 6.9 B.

Component	**Brand**	**Model Number**
1.) Microstrip-Electrode Digital Multimeter	Fluke	89 IV True RMS
2.) Oscilloscope	Tektronix	TDS 2004B
3.) PC Equipped with Multi-Channel Analyzer	Ortec	TRUMP-PCI
4.) Uninterruptible Power Supply	APC	XS 1000
5.) Tail-Pulse Generator	BNC	BH-1
6.) Microstrip-Electrode High Voltage Power Supply	Canberra	3106D
7.) Shaping Amplifier	Canberra	2022
8.) Integral Dual Discriminator	Canberra	2032
9.) Dual Counter/Timer	Canberra	512
10.) Drift-Electrode High Voltage Power Supply	Canberra	3105
Drift Electrode Digital Multimeter	Fluke	8010A
10X Voltage Divider Circuit	Custom Built	
Preamplifier (not shown in Figure 6.9)	Ortec	142PC

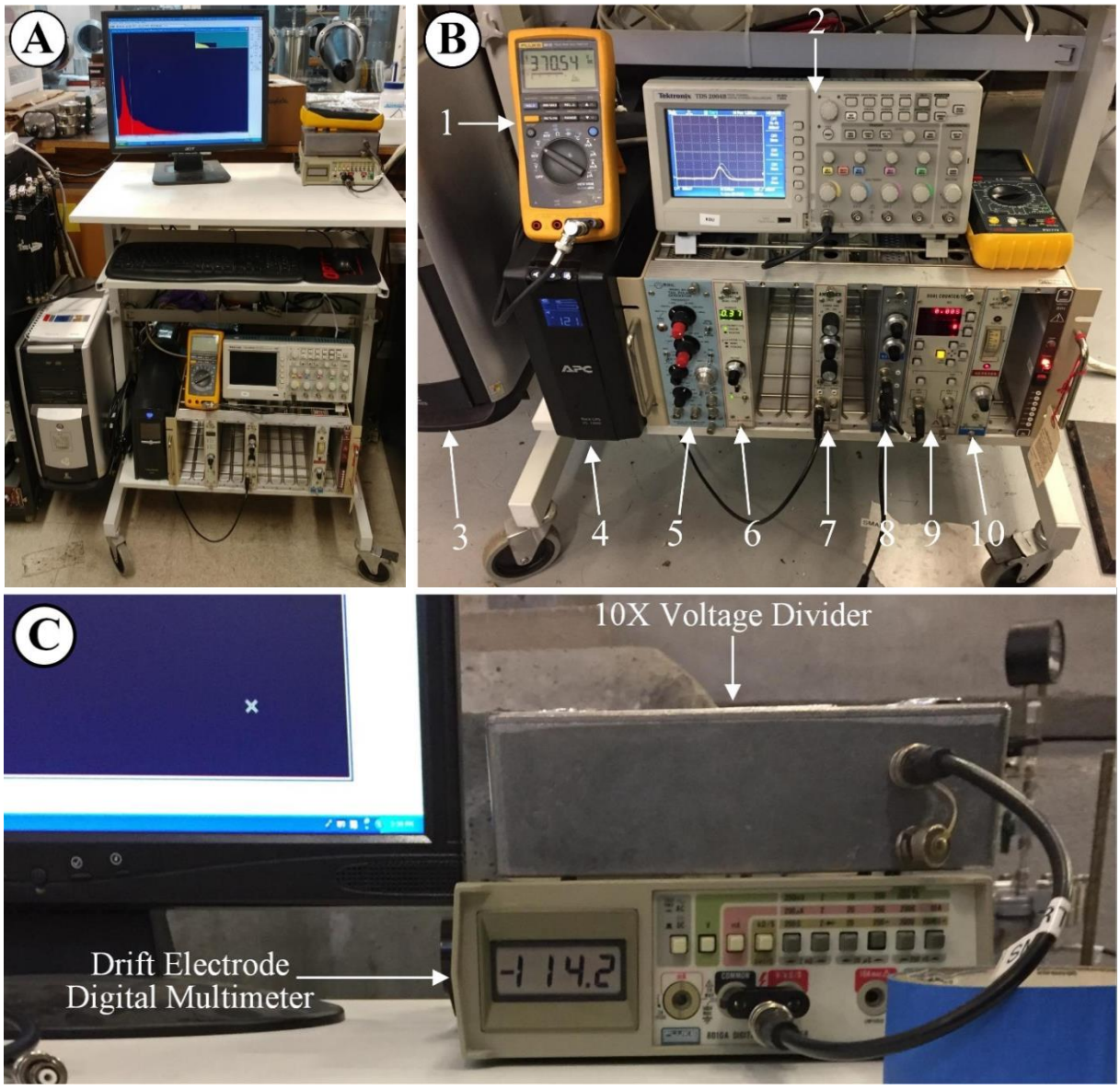

*Figure 6.9. (**A**) Mobile testing station used for characterizing the microstrip electrodes and performing neutron-sensitivity measurements. (**B**) Measurement components with numbers corresponding to those listed in Table 6.3. (**C**) Fluke 8010A digital multimeter connected to a 10X voltage divider used for monitoring the drift electrode operating voltage.*

Table 6.4. Digital multimeters used for monitoring the operating voltages of the anode strips and drift electrode [171, 172].

Digital Multimeter	DC Voltage Range (V)	Resolution (V)
Fluke IV True RMS	±500	0.01
	±1000	0.1
Fluke 8010A	±200	0.1
	±1000	1

When performing measurements, the drift electrode operating voltage setting often exceeded -1000 V. To prevent damaging the Fluke 8010A digital multimeter, a 10X voltage divider circuit (Figure 6.10) was designed and connected between the Canberra 3105 high voltage power supply and the Fluke 8010A digital multimeter. The 5 MΩ potentiometer (R_4 in Figure 6.10) was used to fine-tune the series resistance of the voltage divider circuit ($R_1 + R_2 + R_3 + R_4$). The series resistance was fined-tuned to ensure an accurate 10X reduction in voltage across the voltage divider, based on the input impedance of the digital multimeter.

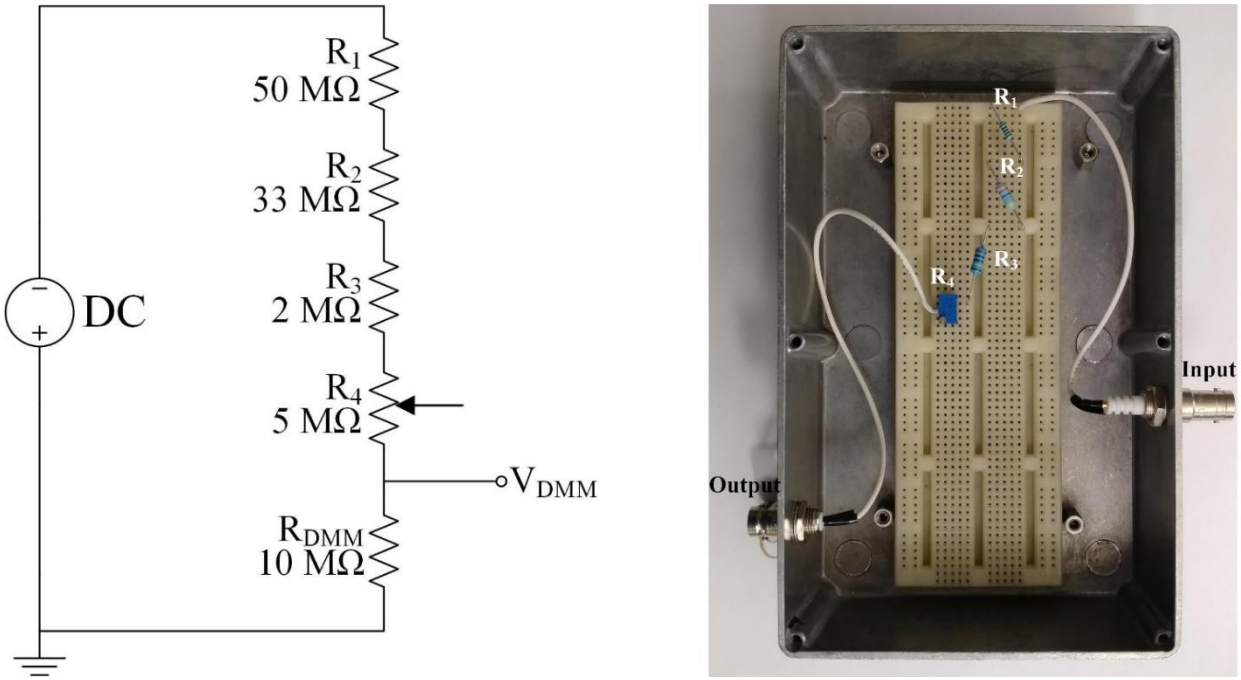

Figure 6.10. (left) Voltage divider circuit designed to provide a 10X reduction in voltage. (right) The voltage divider circuit that was fabricated and used for measurements.

6.2.4 Counting & Gas-Multiplication Curves

Counting and gas-multiplication curves were simultaneously defined for the Si microstrip electrode. Separately, the curves were also simultaneously defined for the SB33 microstrip electrode. During the measurements, the total number of counts tallied during the measurement time and the pulse amplitudes were monitored using a multi-channel analyzer. The counting curve was defined by plotting the measured count rate, the total number of counts tallied divided by the measurement time, as a function of anode strip applied voltage. The gas multiplication curve

represents the distribution of gas multiplication factors measured as a function of anode strip applied voltage. The gas multiplication factor, *M*, was calculated as

$$M = \frac{P_i}{P_0}, \tag{6.2}$$

where P_i is the measured pulse amplitude for a given applied voltage setting, V_i, and P_0 is the pulse amplitude measured for an anode strip operating voltage of approximately 0 V [173]. The most prominent pulse amplitude at each applied voltage setting was used when calculating *M*. During the measurements, the drift electrode operating voltage was maintained at -500 V or -1000 V when using the Si or SB33 microstrip electrode, respectively, and the cathode strips were maintained at ground potential. The operating voltage of the anode strips was incrementally increased until the measured pulse amplitudes exceeded the capabilities of the nuclear instrument module (NIM) equipment.

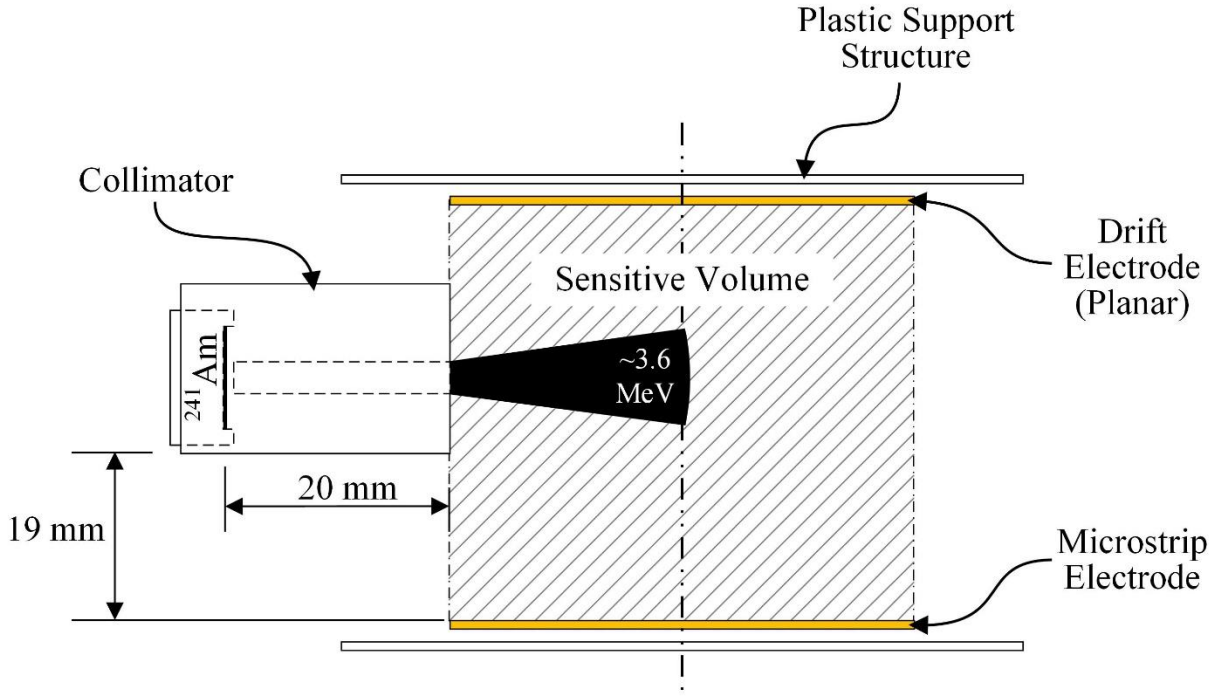

Figure 6.11. Illustration of the testing apparatus used for defining the counting and gas-multiplication curves using either the Si or SB33 microstrip electrode positioned at a distance of approximately 4 cm from the planar, drift electrode [161].

The counting and gas multiplication curves were defined using the testing configuration illustrated in Figure 6.11. The positions of the microstrip and drift electrodes were maintained using the plastic support structure shown in Figure 6.6 and Figure 6.7. The electrodes were separated by a distance, *D*, of approximately 4 cm. A collimated ^{241}Am alpha-particle source was used in order to inject energy between the microstrip and drift electrodes. The diameter of the collimator aperture was approximately 2.5 mm. The collimated ^{241}Am alpha-particle source was positioned 19 mm above the surface of the microstrip electrode. The surface of the alpha-particle source and the perimeter of the sensitive volume were separated by a distance of 20 mm. Because the position of the collimated ^{241}Am alpha-particle source remained constant relative to the testing configuration, the amount of energy deposited by alpha particles within the sensitive volume was approximately constant. Shown in Figure 6.12 is a top-down view of the collimator containing the ^{241}Am alpha-particle source relative to the microstrip electrode and plastic support structure.

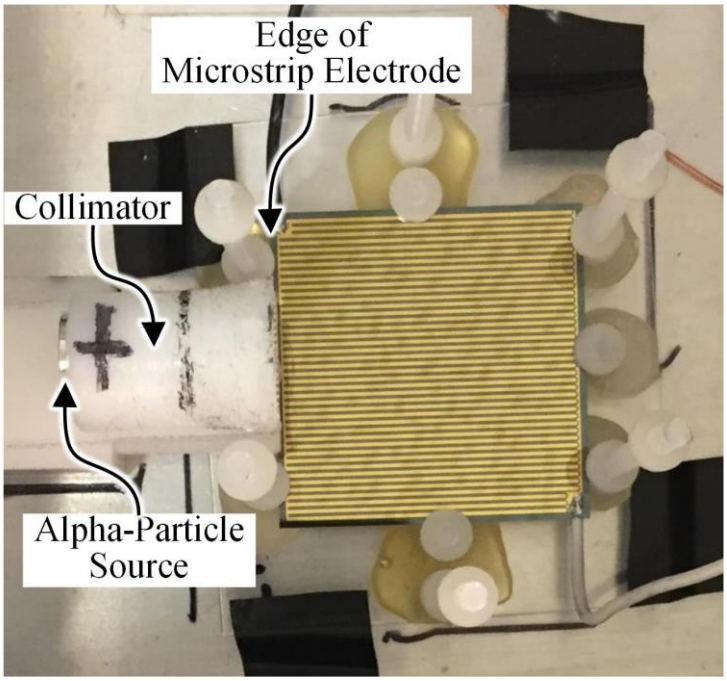

Figure 6.12. Top-down view of the source collimator orientation relative to the microstrip electrode. A small portion of the alpha-particle source is visible on the left side of the collimator.

The counting and gas-multiplication curves were defined with the testing apparatus (Figure 6.11 and Figure 6.12) contained within the aluminum testing enclosure (Figure 6.8). The components were thoroughly cleaned using isopropyl alcohol and dried prior to assembling the testing configuration. The testing configuration was assembled within the aluminum testing

enclosure and the enclosure was sealed. Prior to conducting measurements, the sealed, aluminum testing enclosure was maintained under rough vacuum overnight and pressurized with P-10 gas the following morning. The aluminum testing enclosure was pressurized with 3.7 psig (1.25 atm) of P-10 gas. Thus, the combination of the alpha-particle source position relative to the sensitive volume and the P-10 gas pressure resulted in approximately 3.6 MeV of the energy of the incident alpha particles being deposited within the sensitive volume. The energy deposited between the electrodes was estimated based on the characteristic Bragg ionization curve of 5.48 MeV alpha particles in 3.7 psig of P-10 gas [96].

Shown in Figure 6.13 are the counting and gas-multiplication curves of the Si microstrip electrode. The curves were defined by increasing the operating voltage of the anode strips from 0 to 350 V in 10 volt increments. The counting curve plateau occurs between applied voltages of 70 – 350 V. The percent change in count rate of the counting curve plateau was calculated using Eq. (3.50) to be 2.5% per 100 V. The increase in gas multiplication factor as the operating voltage of the anode strips was increased indicates that Townsend avalanching occurred, and, therefore, the device was operating in proportional mode.

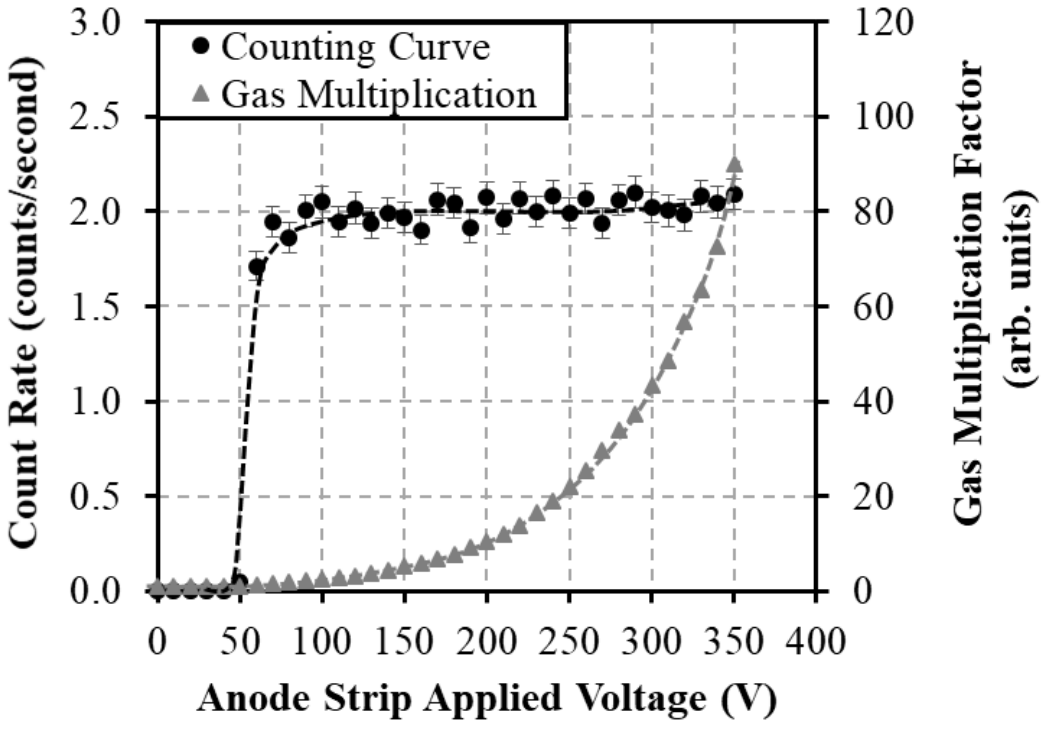

Figure 6.13. Counting and gas-multiplication curves measured from a collimated ^{241}Am alpha-particle source using the Si microstrip electrode for various anode strip operating voltages.

The counting and gas-multiplication curves of the SB33 microstrip electrode are shown in Figure 6.14. The curves were defined by increasing the operating voltage of the anode strips from 0 to 550 V in 25 volt increments. The counting curve plateau occurs between applied voltages of 50 – 500 V. The percent change in count rate of the counting curve plateau was calculated using Eq. (3.50) to be 4.6% per 100 V. Like the Si microstrip electrode, the increase in gas multiplication factor as the operating voltage of the anode strips was increased indicates that Townsend avalanching occurred.

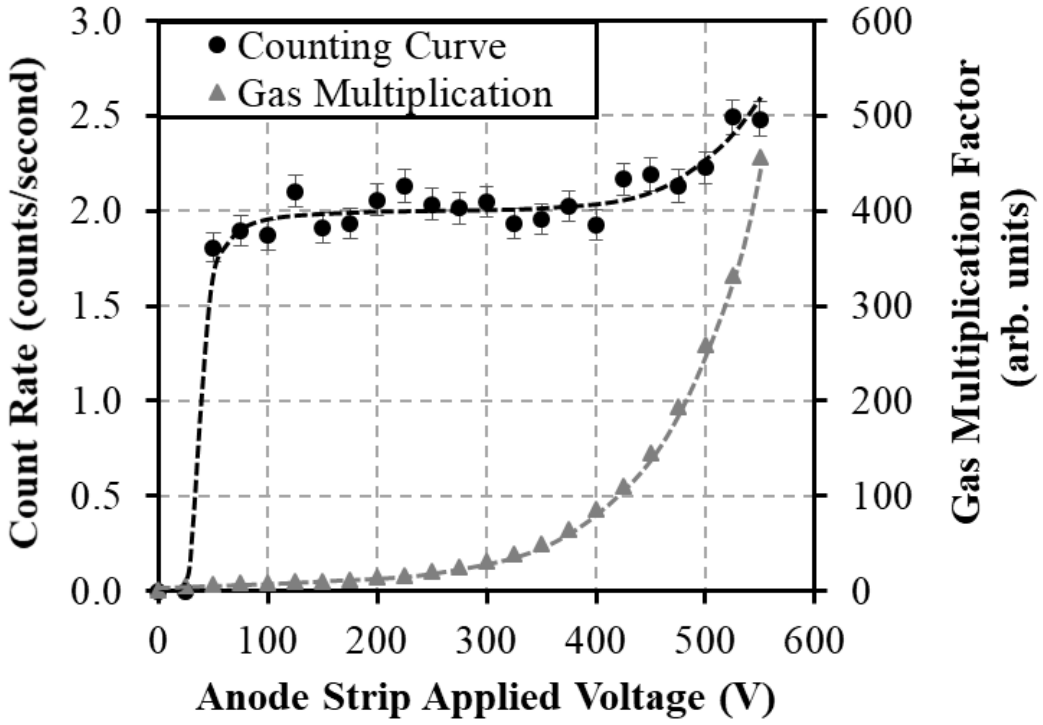

Figure 6.14. Counting and gas-multiplication curves measured from a collimated ^{241}Am alpha-particle source using the SB33 microstrip electrode for various anode strip applied voltages [161].

6.2.5 Gain Stability Measurements

The testing configuration illustrated in Figure 6.11 was also used to compare the gain stability of the Si and SB33 microstrip electrodes. The gain stability was measured by monitoring the most prominent pulse amplitude as a function of time. The measurements were conducted for approximately 24 hours and the pulse amplitudes were monitored using a multi-channel analyzer. The pulse amplitudes were attributed to energy deposited within the sensitive volume from alpha particles emitted from a collimated ^{241}Am alpha-particle source. The horizontal and vertical

positions of the collimated ^{241}Am alpha-particle source remained constant relative to the testing configuration for all measurements. Because the position of the collimated ^{241}Am alpha-particle source remained constant relative to the testing configuration, the amount of energy deposited by alpha particles within the sensitive volume was approximately constant.

Like the counting and gas multiplication curves measurements, the positions of the microstrip and drift electrodes were maintained using the plastic support structure shown in Figure 6.6 and Figure 6.7. The electrodes were separated by a distance, *D*, of approximately 4 cm. The ^{241}Am alpha-particle source was positioned within a collimator with a 2.5-mm diameter aperture. The horizontal and vertical positions of the collimated ^{241}Am alpha-particle source were the same as those used to define the counting and gas multiplication curves. Likewise, the same cleaning and assembly procedures were performed as were used for defining the counting and gas multiplication curves (Section 6.2.4). Once the testing configuration was assembled and installed, the aluminum testing enclosure (Figure 6.8) was sealed, maintained under rough vacuum overnight, and pressurized with 3.7 psig (1.25 atm) of P-10 gas the following morning. The combination of the alpha-particle source position relative to the sensitive volume and the P-10 gas pressure resulted in approximately 3.6 MeV of the energy of the incident alpha particles being deposited within the sensitive volume. The energy deposited between the electrodes was estimated based on the characteristic Bragg ionization curve of 5.48 MeV alpha particles in 3.7 psig of P-10 gas [96].

During the measurements, constant operating voltages were applied to the anode and cathode strips as well as the drift electrode. The cathode strips were maintained at ground potential and the operating voltage of the drift electrode was maintained at -1000 V. The operating voltage of the anode strips was maintained at 300 V when using the Si microstrip electrode and 400 V when using the SB33 microstrip electrode. The operating voltages of the anode strips were selected based on the counting curve results. The drift electrode operating voltage was defined in order to achieve a reduced electric field strength of approximately 0.35 V cm^{-1} Torr^{-1} in 3.7 psig of P-10 gas [99, 129].

Shown in Figure 6.15 is the relative gain as a function of time of the SB33 microstrip electrode compared to the Si microstrip electrode. The relative gain, G_t, at time *t* was calculated by normalizing the pulse amplitude, P_t, measured at time *t* relative to the maximum measured pulse amplitude, P_{MAX}, as defined by,

$$G_t = \frac{P_t}{P_{MAX}}. \tag{6.3}$$

During the first hour of measurements, the relative gain of both microstrip electrodes increased. The initial increase in relative gain was suspected to be attributed to charging of the substrate surface after initially applying voltage. Furthermore, the increase was suspected to have occurred until an equilibrium operating condition was reached [106]. After the first hour, the SB33 microstrip electrode remained electrically stable for approximately 23 hours. However, the relative gain of the Si microstrip electrode began to decrease immediately following the first hour of operation. The decrease in relative gain of the Si microstrip electrode was suspected to be from polarization of the SiO_2 surface layer [107, 147].

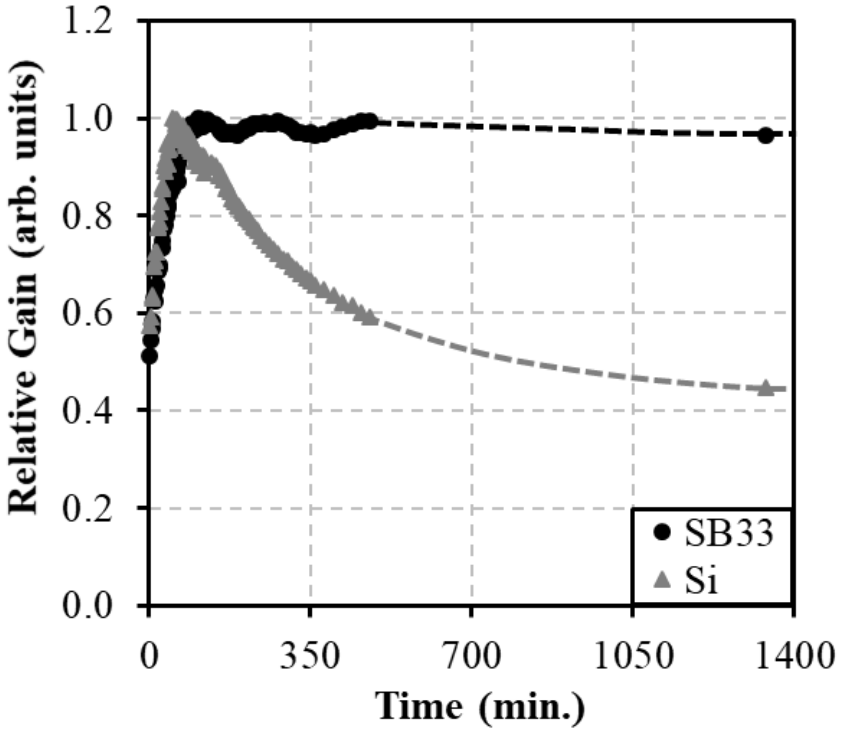

Figure 6.15. Relative gain as a function of time of the Si and SB33 microstrip electrodes. The operating voltages of the microstrip and drift electrodes were maintained for approximately 24 hours for each measurement scenario [161].

6.2.6 Drift Electric Field Profiling

Using the experimental setup illustrated in Figure 6.16, the electric field strength distribution was measured between an anode (either planar electrode or SB33 microstrip electrode) and the planar, drift electrode. Measurements were performed after an initial one hour duration of time for the electrode setup to reach a stable operating condition. The study was not conducted using the Si microstrip electrode due to the electrical instability previously measured (Section 6.2.5). The electric field strength distribution was measured by monitoring the most prominent pulse amplitude as a function of the vertical position of a collimated ^{241}Am alpha-particle source. The pulse amplitudes were attributed to the energy deposited by alpha particles within the sensitive volume and were monitored using a multi-channel analyzer. The collimated ^{241}Am alpha-particle source was positioned at five discrete vertical positions along the length of the drift electric field region between the electrodes, as illustrated in Figure 6.16. Although the vertical position of the collimated ^{241}Am alpha-particle source did not remain constant, the horizontal position of the source relative to the testing configuration remained approximately constant for all measurements. Consequently, the amount of alpha-particle energy deposited within the sensitive volume was approximately constant for all measurements.

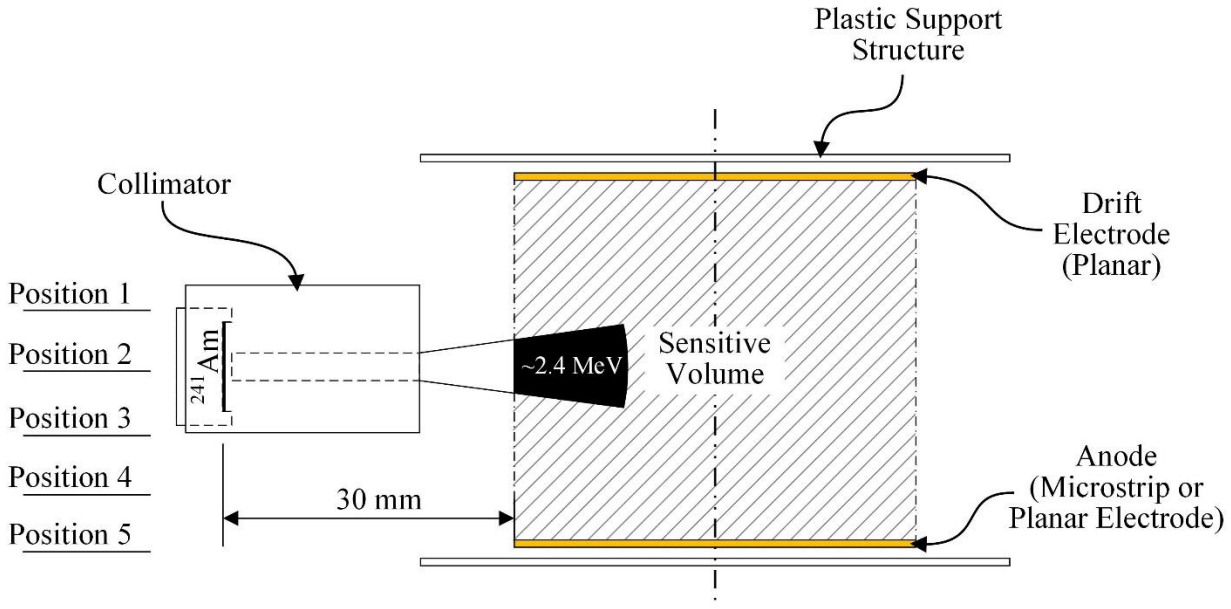

Figure 6.16. Illustration of the testing assembly used for measuring the drift electric field strength distribution between an anode (either planar or SB33 microstrip electrode) and the planar, drift electrode [161].

The plastic support structure shown in Figure 6.6 and Figure 6.7 was used to maintain the positions of the electrodes while conducting the electric field strength distribution measurements. The electrodes were separated by a distance, *D*, of approximately 4 cm. The ^{241}Am alpha-particle source was positioned within a collimator with a 2.5-mm diameter aperture. The surface of the alpha-particle source and the edge of the microstrip electrode were separated by a distance of 30 mm. Shown in Figure 6.17 is a top-down view of the orientation of the collimated ^{241}Am alpha-particle source relative to the electrode assembly.

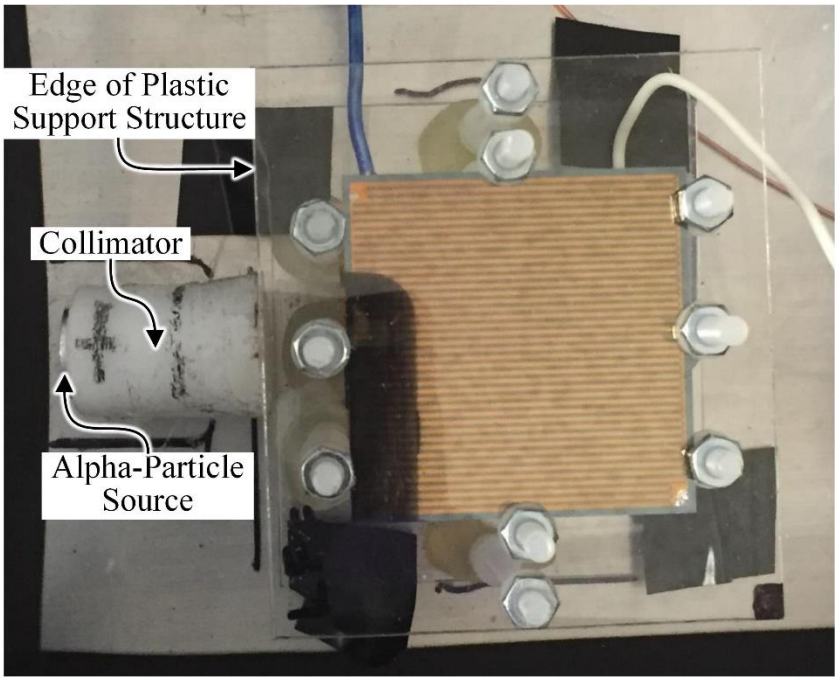

Figure 6.17. Top-down view of the source collimator orientation relative to the testing assembly containing the microstrip or planar electrode (anode) and drift electrode.

The same cleaning procedures and assembly procedures were performed as were used for defining the counting and gas multiplication curves (Section 6.2.4) as well as for performing the gain stability measurements (Section 6.2.5). Once the testing configuration was assembled and installed, the aluminum testing enclosure (Figure 6.8) was sealed, maintained under rough vacuum overnight, and pressurized with 1.0 psig (1.07 atm) of P-10 gas the following morning. The alpha-particle source horizontal position relative to the sensitive volume combined with the P-10 gas pressure resulted in approximately 2.4 MeV of the energy of the incident alpha particles being deposited within the sensitive volume. The energy deposited between the electrodes was estimated

based on the characteristic Bragg ionization curve of 5.48 MeV alpha particles in 1.0 psig of P-10 gas [96].

Constant operating voltages were applied to the anode and cathode strips as well as the drift electrode while conducting the measurements. The operating voltage of the anode (either planar electrode or SB33 microstrip-electrode anode strips) was maintained at 400 V and the drift electrode was maintained at -1000 V for all measurements. When using the SB33 microstrip electrode, the cathode strips were maintained at ground potential. The anode operating voltage was selected based on the counting curve results measured using the SB33 microstrip electrode (Section 6.2.4). The drift electrode operating voltage was defined in order to achieve a reduced electric field strength of approximately 0.35 V cm^{-1} $Torr^{-1}$ in 3.7 psig of P-10 gas [99, 129].

Listed in Table 6.5 are the pulse amplitude values measured using either the planar anode or the SB33 microstrip electrode with corresponding source heights. Shown in Figure 6.18 are the distributions of measured pulse amplitudes (indicated on the *x*-axis as "Peak Channel"). The peak channel of each source position corresponds to the most prominent channel of the pulse-height spectrum measured using Ortec's multi-channel analyzer program Maestro®. Recalling Eq. (3.37), which states that pulse amplitudes measured using an ionization chamber are position-dependent, the distribution of pulse amplitudes measured with the planar scenario was consistent with a parallel-plate ionization chamber.

Table 6.5. Vertical positions of the collimated ^{241}Am alpha-particle source used for measuring the pulse amplitude distribution [161].

Position	Source Height From Anode Surface (cm)	Planar Peak Channel	SB33-Microstrip Peak Channel
1	3.20	54.23	109.62
2	2.55	66.84	118.22
3	1.90	58.70	128.84
4	1.25	50.42	199.30
5	0.60	37.21	255.69

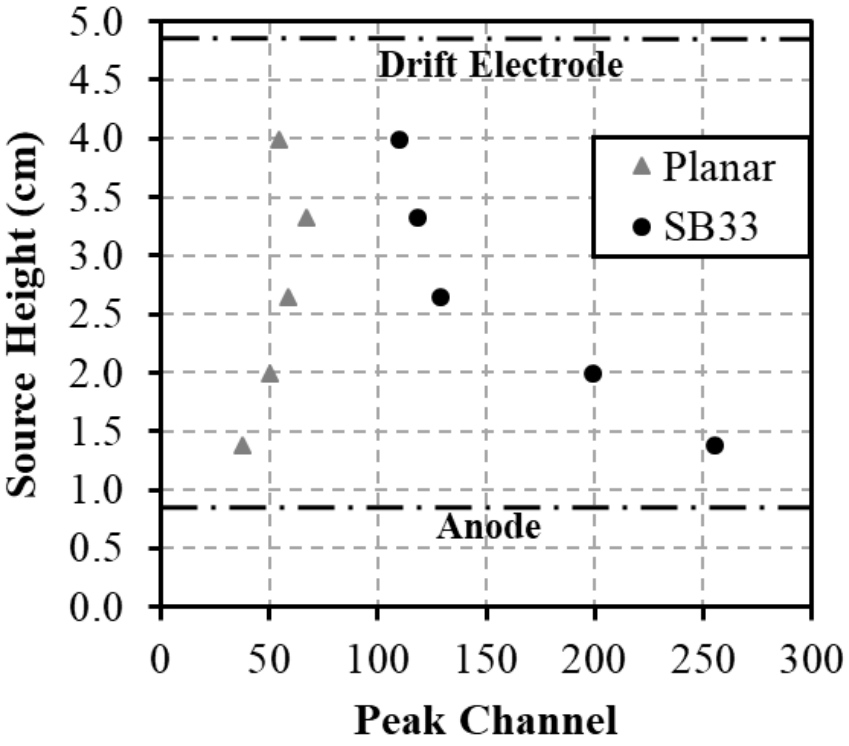

Figure 6.18. Comparison of the measured pulse-amplitude (peak channel) distribution as a function of the position of a collimated ^{241}Am alpha-particle source for an anode using either a planar electrode or a SB33 microstrip electrode [161].

A non-uniform pulse amplitude distribution is evident for the SB33 microstrip-electrode scenario. The pulse amplitude increases slightly up to approximately half-way between the drift and microstrip electrodes (source height of approximately 2.6 cm). Between the microstrip electrode (anode) and a source height of approximately 2.6 cm, a substantial increase in pulse amplitude occurs for each source position as the collimated ^{241}Am alpha-particle source is positioned closer to the microstrip electrode surface. Because the horizontal position of the ^{241}Am alpha-particle source relative to the testing configuration remained approximately constant, the amount of energy deposited within the sensitive volume also remained approximately constant. Thus, the increase in measured pulse amplitude was suspected to have occurred due to a change in the electric field strength. Specifically, the electric field strength is suspected to increase as the microstrip electrode surface is approached. The increase in electric field strength, in turn, affects the velocity of charge carriers. Consequently, as the electric field strength increases, charge carriers can displace longer distances during the time response of the pulse formation process (defined by the *RC* time constant), resulting in the formation of a larger amplitude pulse.

Given the distribution of pulse amplitudes measured with the SB33 scenario, simulations of the electric field strength distribution were performed using the 3D electric field analysis software *COULOMB* [174]. The microstrip and drift electrode geometries used for testing (Section 6.1) were implemented into the simulation environment. The drift electrode surface was oriented parallel to the microstrip electrode surface and the electrodes were separated by a distance of approximately 4 cm. The anode strips were defined in the simulation environment with an operating voltage of 400 V and the operating voltage of the cathode strips were defined at ground potential (0 V). The drift electrode was defined with an operating voltage of -1000 V. Although 1.0 psig of P-10 gas was used for the measurements, Ar gas at atmospheric pressure was selected as the dielectric material between the microstrip and drift electrodes to provide a close approximation to P-10 gas.

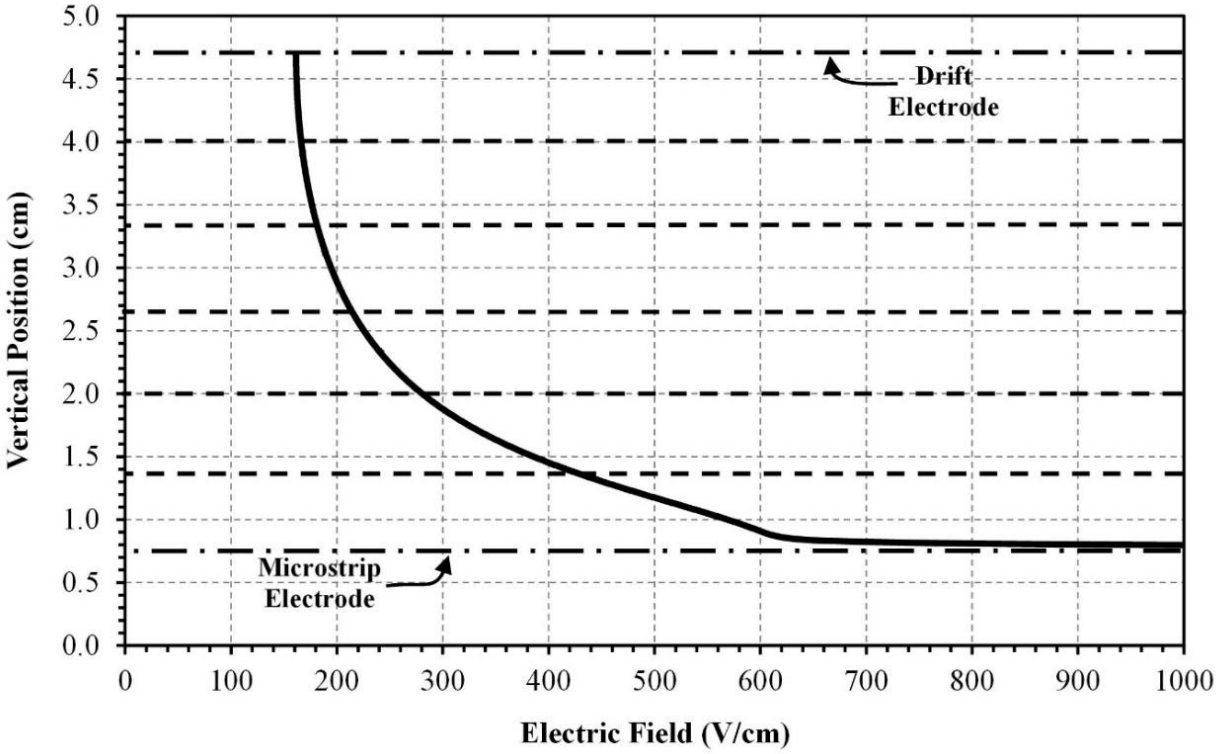

Figure 6.19. COULOMB simulation results for the electric field strength distribution (in linear scale) as a function of vertical distance between the microstrip and drift electrodes. The dashed lines provide a frame of reference for the vertical positions of the collimated ^{241}Am alpha-particle source positions defined from Figure 6.18 and Table 6.5.

Shown in Figure 6.19 is the simulated electric field strength distribution as a function of vertical position, defined using *COULOMB*. The positions of the microstrip and drift electrodes

are indicated by dot-dashed lines (— · —). The microstrip electrode is located at a vertical position of 0.75 cm and the drift electrode is located at a vertical position of 4.7 cm. The dashed lines (- - -) indicate the approximate vertical positions above the microstrip-electrode surface where the collimated ^{241}Am alpha-particle source was measured (Figure 6.18 and Table 6.5). A non-uniform electric field strength distribution occurs between the microstrip and drift electrodes. Recalling Eq. (3.25), the velocity of charge carriers is dependent on the electric field strength. The distribution of electric field strength should have minimal effect on electron drift because electrons will eventually achieve saturation velocity for a sufficiently high electric field strength. Consequently, electrons should be capable of drifting the full distance between the site of charge-carrier liberation and the collecting electrode during the time response of the pulse formation process. However, the velocity of positively-charged ions will be dependent on the local electric field strength. Thus, the distance displaced by positively-charged ions during the time response of the pulse formation process will also be dependent on the local electric field strength. Recalling from Chapter 3, the pulse amplitude is dependent on the change in induced charge on the collecting electrode, which is dependent on the distance displaced by charge carriers during the time response of the pulse formation process (defined by the *RC* time constant). Therefore, the distribution of distances displaced by positively-charged ions during the time response of the pulse formation process yields a distribution of pulse amplitudes.

The shape of the simulated electric field strength distribution shown in Figure 6.19 is similar to the measured pulse amplitude distribution measurement results shown in Figure 6.18. Thus, in order to further study the distribution of pulse amplitudes measured experimentally, the electric field strength values at the dashed line locations shown in Figure 6.19 were normalized and plotted in comparison to the normalized pulse amplitudes shown in Figure 6.18. The electric field strength values and measured pulse amplitudes were normalized relative to the values reported at the position closest to the microstrip electrode surface. A comparison of the two normalized data sets is shown in Figure 6.20. The normalized pulse amplitude distribution corresponds to the left ordinate and the normalized electric field strength distribution corresponds to the right ordinate. Both data sets have similar shapes, which suggests that a non-uniform electric field strength distribution may have been present within the device when conducting the experimental measurements (Figure 6.18). Consequently, a non-uniform distribution of pulse amplitudes was measured.

Although not accounted for in the *COULOMB* simulations, nylon and other high-outgassing materials were used to construct the plastic support structure (Figure 6.6 and Figure 6.7) due to the availability of the materials in the laboratory. Thus, in addition to the suspected non-uniform electric field strength distribution present within the device while conducting measurements, electron attachment [93, 97] was also suspected to have occurred during the drift electric field profiling measurements. The components that were composed of nylon and other high-outgassing materials may have resulted in O_2, water vapor/moisture (H_2O), and/or other volatiles being present within the testing enclosure during the measurements. Consequently, the presence of O_2, H_2O, and/or other volatiles within the testing enclosure may have resulted in electron attachment. Recalling Section 3.3, if electron attachment occurred, the population of electrons that arrive at the microstrip electrode would have varied as a function of position between the microstrip and drift electrodes. Consequently, a degradation in pulse amplitude may have occurred as the collimated ^{241}Am alpha-particle source was positioned further away from the microstrip-electrode surface.

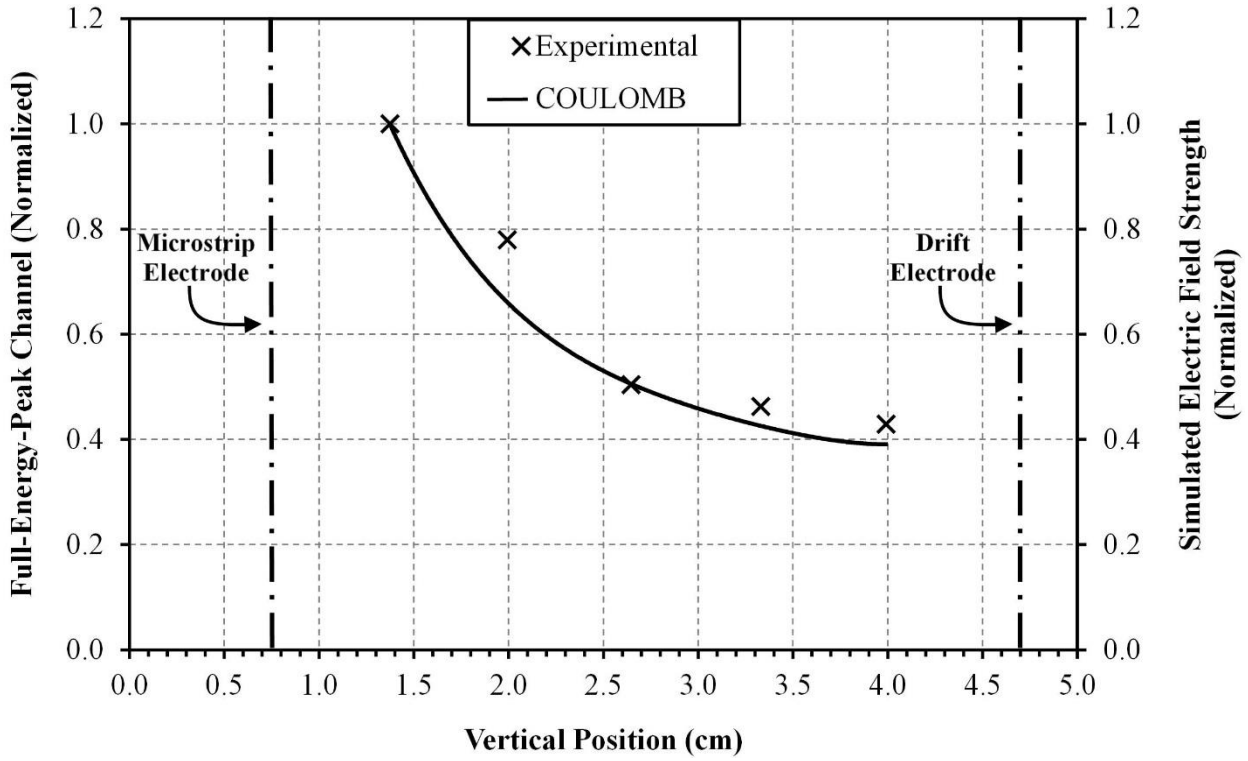

Figure 6.20. Comparison of the measured pulse-amplitude distribution to the COULOMB-simulated electric field strength distribution. Both data sets were separately normalized in order to provide a comparison of the two distributions.

6.3 SFMND Assembly & Fabrication Processes

The following sections describe the design and assembly of the SFMND components. First, the design attributes of the 3D-printed support device and aluminum frames are described (Section 6.3.1). The plastic support structure was used to maintain the position of the 3D-printed support device relative to the electrodes and is also discussed (Section 6.3.1). The second section provides the steps and procedures required for fabricating SFMNDs (Section 6.3.2).

6.3.1 Design of SFMND Components

Recalling from Figure 5.6, the SFMND consists of ^{6}Li foil(s) positioned in between microstrip and drift electrodes and oriented perpendicular to the electrode surfaces. Thus, in order to fabricate a testable SFMND, components were designed to suspend the ^{6}Li foil(s) between the electrodes. Due to the malleable nature of lithium metal, the ^{6}Li foils were adhered to rigid, aluminum frames. The frames also aided in maintaining the positions of the foils between the electrodes. The aluminum frames were designed with a length, L_A, and height, H_A, of approximately 5.2 cm and 3.0 cm, respectively, because the length, L_F, and height, H_F, of the 96%-enriched ^{6}Li foil(s) were 5.00 cm and 2.95 cm, respectively. The aluminum frames featured a window in the center to allow reaction products to escape from either side of the ^{6}Li foil (Figure 5.9). The perimeter of the window had a length, L_W, of approximately 4.45 cm and a height, H_W, of 2.54 cm. The aluminum frames were water-jet cut from a single sheet of 0.79-mm (1/32-in.) thick 6061 aluminum. The ^{6}Li foil and aluminum frame design parameters were defined in order to compare the experimental neutron-sensitivity results (Section 6.4) to the simulated results (Section 5.3).

A suspension device was designed that could maintain the positions of the aluminum frames between the electrodes. The suspension device was designed using *SolidWorks* [175] with dimensions of approximately 4.3 cm x 5.9 cm x 3.4 cm, as shown in Figure 6.21. The suspension device contained twenty 1-mm wide frame slots, which allowed for the position and spacing of the foils to be adjustable. Neighboring frame slots were separated from one another by 1-mm thick dividers. A mock-up of the suspension device with a non-laminated aluminum frame is shown in Figure 6.22. The suspension device was 3D printed using ABS plastic and will be henceforth

referred to as the 3D-printed support device. Although the 3D-printed support device had twenty frame slots, only devices with one or five suspended foils were fabricated and tested. The orientation of the 3D-printed support device relative to the electrodes is illustrated in Figure 6.23.

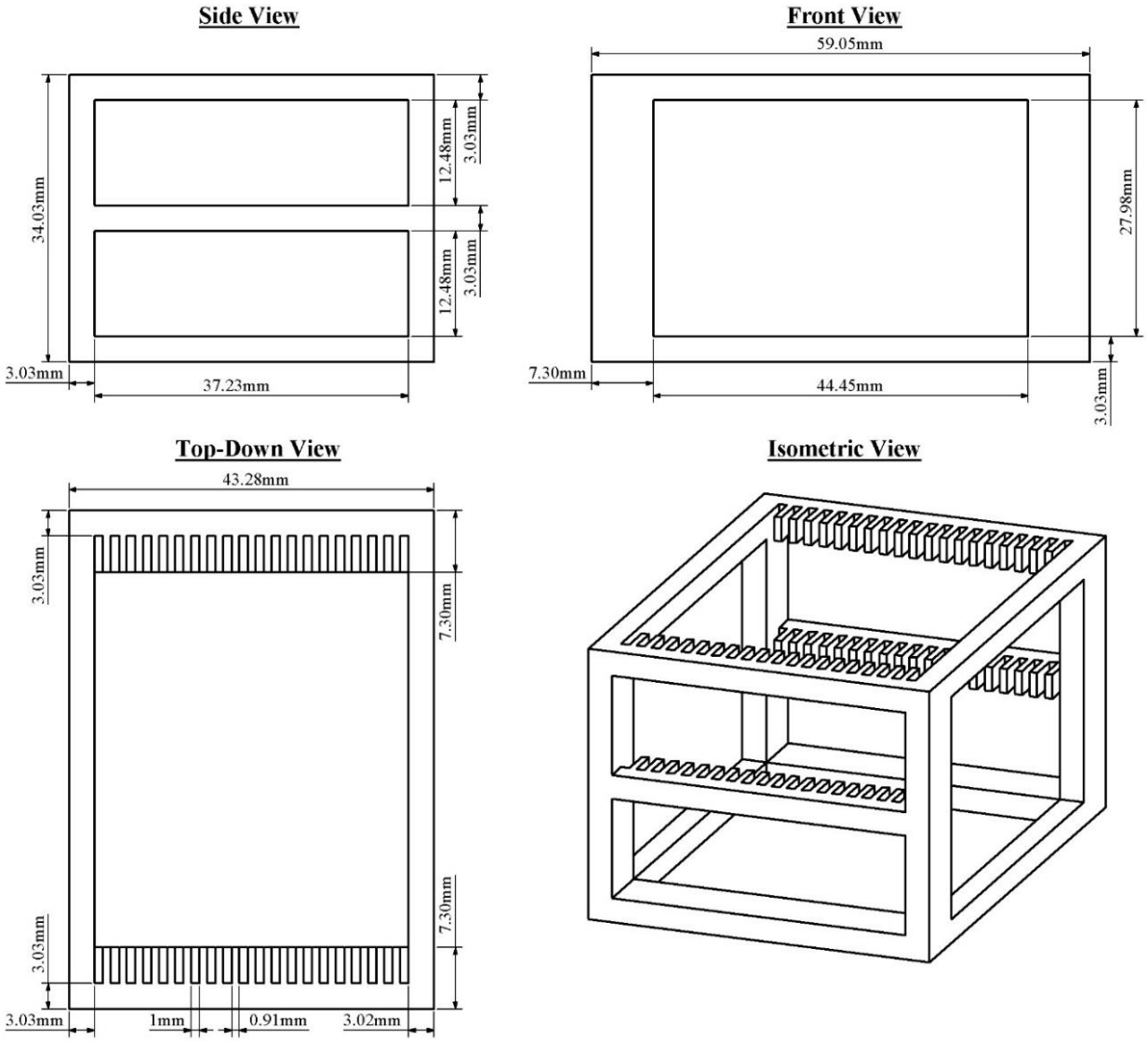

Figure 6.21. Design attributes of the 3D-printed support device used for maintaining the position(s) of the foil(s) during SFMND neutron-sensitivity testing.

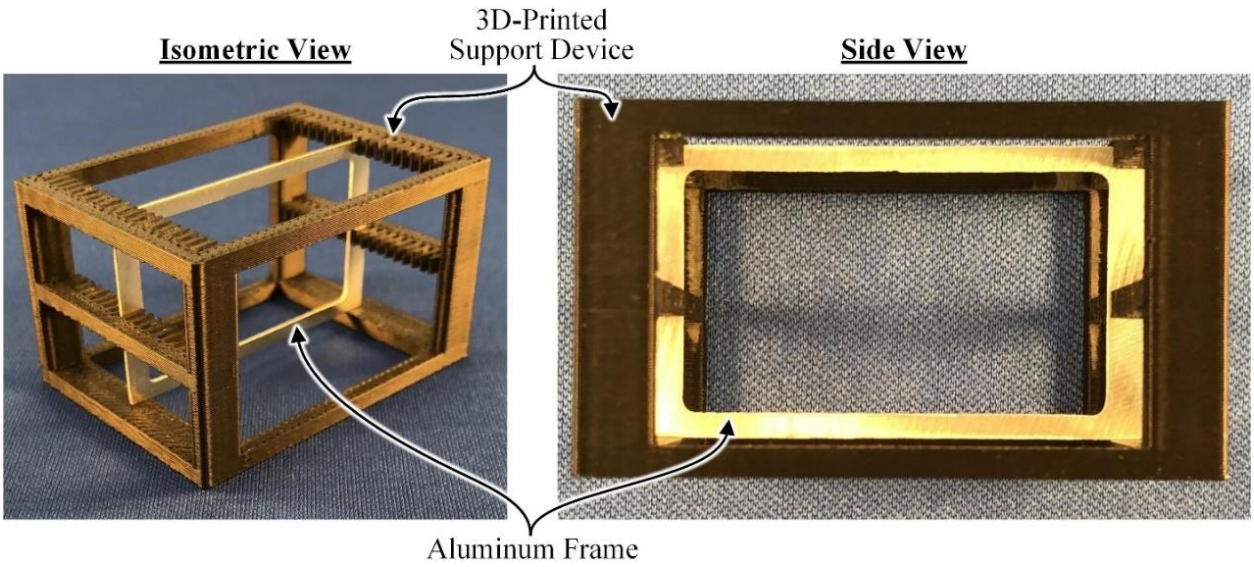

Figure 6.22. Isometric (left) and side (right) view photographs of the suspension device (3D-printed support device) containing a non-laminated aluminum frame.

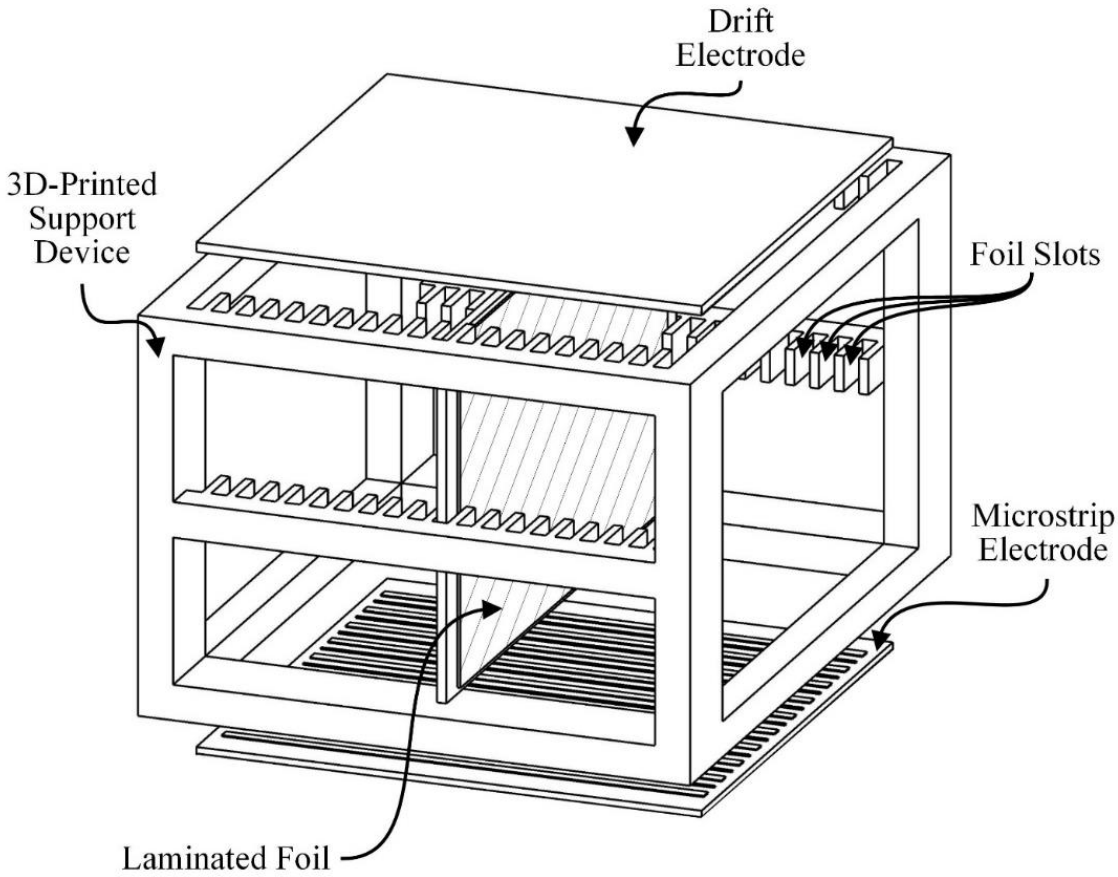

Figure 6.23. Orientation of the 3D-printed support device containing a laminated foil relative to the microstrip and drift electrodes.

The plastic support structure (Figure 6.6 and Figure 6.7) was used to maintain the position and orientation of the 3D-printed support device relative to the electrodes, as illustrated in Figure 6.24. A mock-up of the 3D-printed support device and electrodes, with positions maintained using the plastic support structure, is shown in Figure 6.25. The nylon washers (threaded on the nylon threaded rods) were used to support and maintain the orientation of the 3D-printed support device. Thus, the vertical position of the 3D-printed support structure was established by adjusting the vertical positions of the nylon washers. The vertical positions of the nylon washers were set in order to maintain a vertical distance of 3 mm between the electrodes and the 3D-printed support device. The horizontal position of the 3D-printed support device, relative to the electrodes, was maintained due to the established positions of the nylon threaded rods of the plastic support structure.

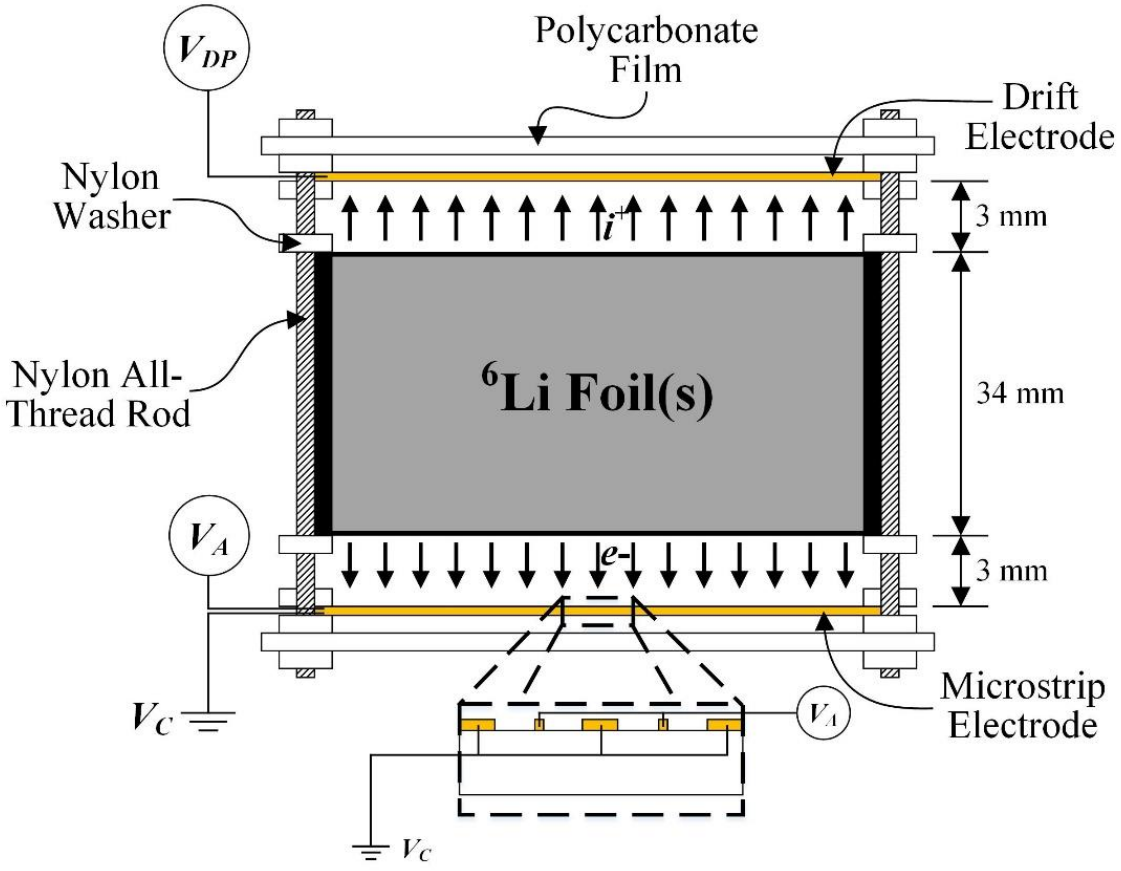

Figure 6.24. Illustration of the plastic support structure used for maintaining the orientation of the 3D-printed support device relative to the microstrip and drift electrodes.

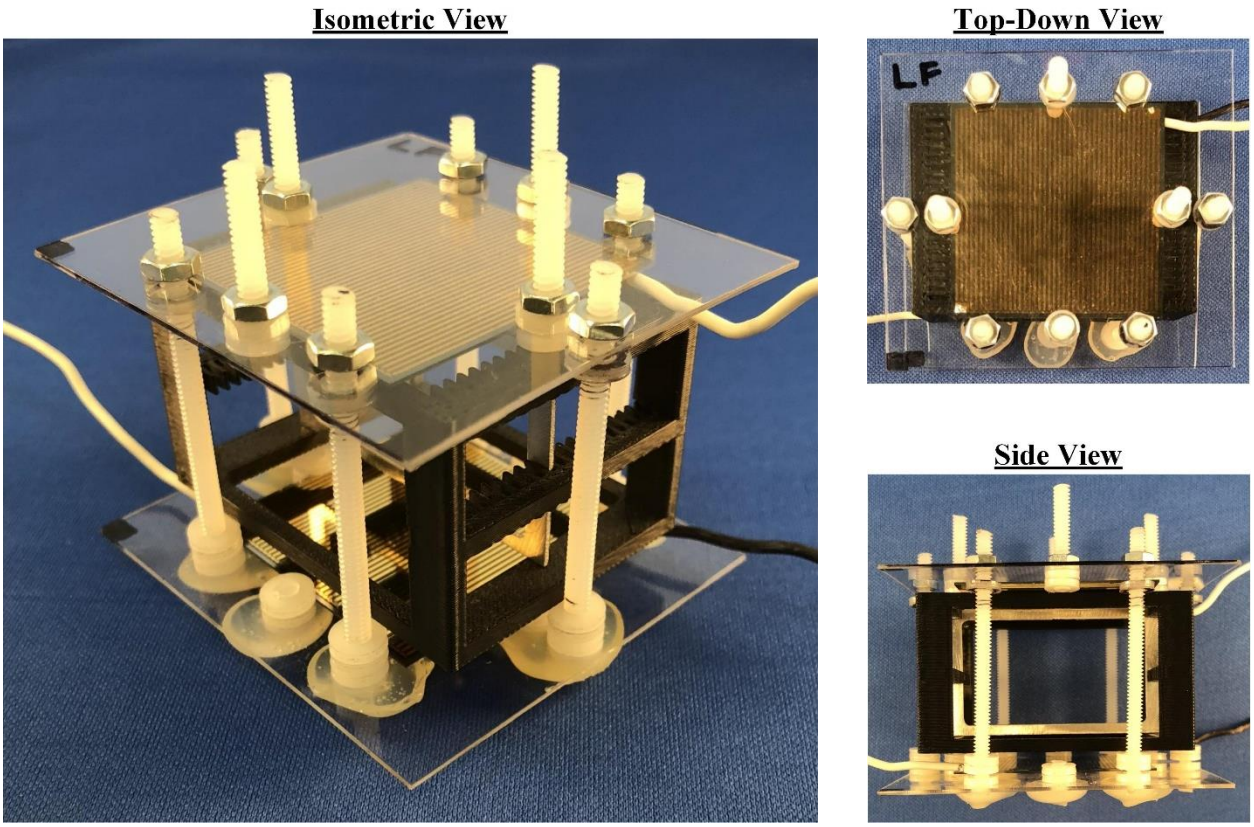

Figure 6.25. Isometric (left), top-down (top-right), and side (bottom-right) view photographs of the plastic support structure containing the 3D-printed support device. The orientation of the 3D-printed support device, containing a non-laminated aluminum frame, is shown relative to the microstrip and drift electrodes.

6.3.2 Assembly of SFMNDs

The first-ever SFMNDs were fabricated using Si microstrip electrodes and contained either one or five ^{6}Li foils. Once SB33 microstrip electrodes were identified as an electrically-stable alternative, SFMNDs containing one and five ^{6}Li foils were also fabricated and tested. The SFMNDs were fabricated within the confines of a Vigor SG2400/1000TS glovebox with an argon atmosphere due to the reactivity of ^{6}Li metal in open atmosphere. Prior to being inserted into the glovebox, the SFMND components (3D-printed support device, aluminum enclosure, aluminum frames, plastic support structure, and electrodes) were thoroughly cleaned using isopropyl alcohol and dried. The SFMND components were inserted into the antechamber of the glovebox and a purge cycle was conducted three times. During each purge cycle, the antechamber was maintained under rough vacuum for 30 minutes and then repressurized using the argon glovebox environment.

Once inside the glovebox, the 75-μm thick, 96%-enriched ^{6}Li foils were adhered to the aluminum frames using a lamination process. The foils were laminated to the frames to allow the non-laminated face of the ^{6}Li foil to be uniformly-capable of allowing reaction products to escape the foil and enter the backfilled gas. The ^{6}Li foils were cut using scissors and care was taken to ensure that the foil did not stretch or tear during the cutting process. Each foil was carefully positioned atop an aluminum frame. The foil and frame were sandwiched between sheets of Teflon® to prevent the foil from tearing during the lamination process. Each sandwiched foil and frame was then fed through an Apache AL13P laminator with a temperature setting of 200°F. Two lamination processes were performed for each foil. The foil was inspected following the lamination processes to ensure proper foil adhesion was achieved. Shown in Figure 6.26 are the front (left) and back (right) of a ^{6}Li-laminated aluminum frame.

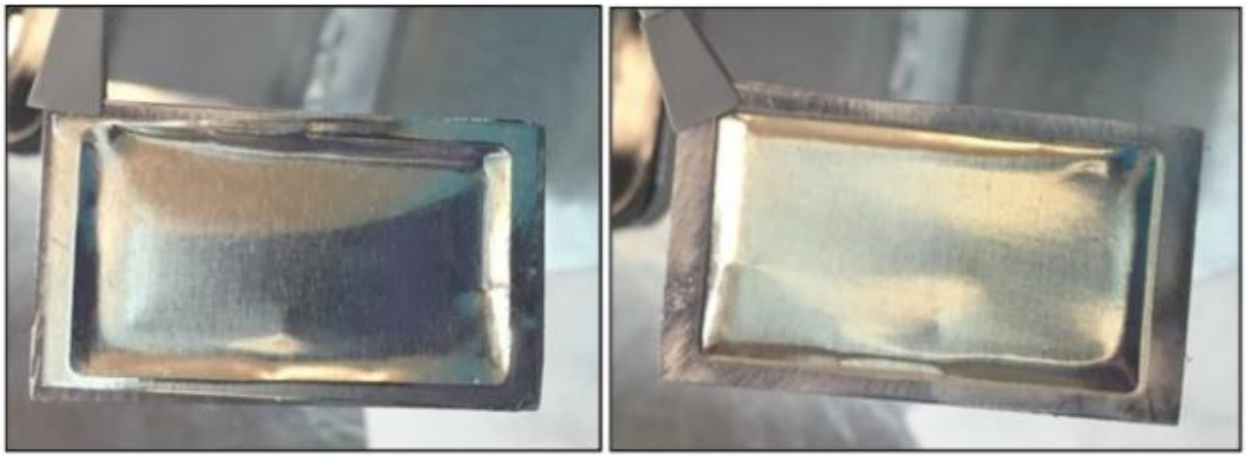

Figure 6.26. (Left) Front of a 0.79-mm (1/32-in.) thick aluminum frame with a laminated ^{6}Li foil adhered to the surface. The entire face of the laminated ^{6}Li foil is capable of allowing reaction products to escape the ^{6}Li foil and enter the detector gas. (Right) Backside of an aluminum frame showing that only the center opening of the frame allows reaction products to escape the ^{6}Li foil and enter the detector gas [155].

The laminated frames were then carefully inserted into the 3D-printed support device. Shown in Figure 6.27 is the 3D-printed support device containing one (left) and five (right) ^{6}Li-laminated aluminum frames. The position of the single foil was offset from center by 1 mm within the 3D-printed support device (illustrated in Figure 5.13). For the five-foil SFMNDs, the spacing between neighboring foils, *d*, was 7.64 mm when using the Si microstrip electrode and 5.73 mm when using the SB33 microstrip electrode. The 3D-printed support device was positioned between the microstrip and drift electrodes using the plastic support structure, as shown in Figure 6.24 and

Figure 6.25. Shown in Figure 6.28 is the 3D-printed support device containing one (left) and five (right) laminated ^{6}Li foils positioned above a microstrip electrode.

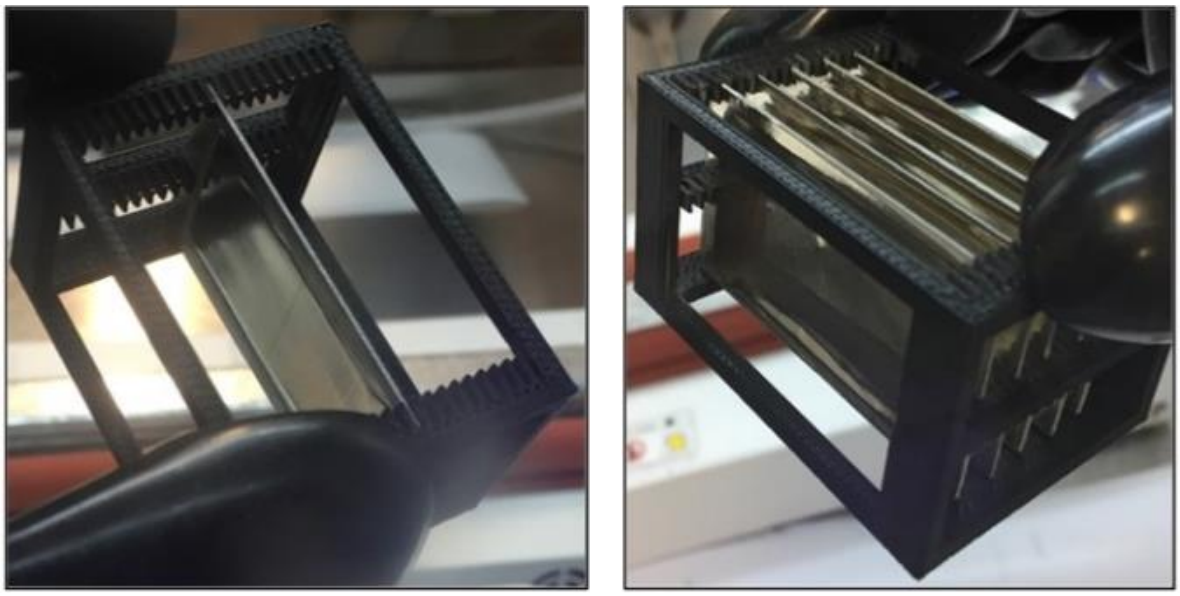

Figure 6.27. 3D-printed plastic support device containing one (left) and five (right) ^{6}Li foil(s) used for suspending ^{6}Li foil(s) between microstrip and drift electrodes [155].

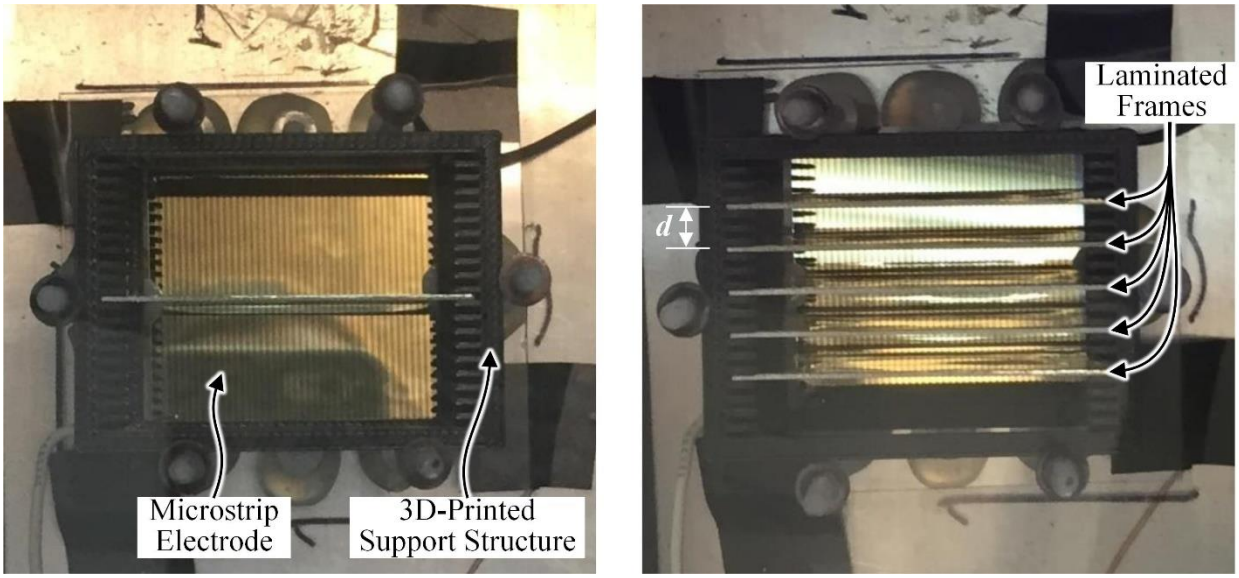

Figure 6.28. Top-down views of the 3D-printed support device containing one (left) and five (right) laminated ^{6}Li foils. The microstrip electrode is shown below.

The entire testing assembly was positioned within the aluminum enclosure (Figure 6.8). The aluminum enclosure, containing atmospheric pressure of the argon glovebox environment,

was sealed before being removed from the glovebox. Immediately following removal from the glovebox, the aluminum enclosure was connected to a gas-filling system. Heat tape was wrapped around the enclosure and a bake-out procedure was performed with the aluminum enclosure maintained under rough vacuum overnight. The bake-out procedure was performed in an attempt to remove O_2, H_2O, and other volatiles. Following the bake-out procedure, the test enclosure was pressurized with P-10 gas.

6.4 Neutron-Sensitivity Testing

The following sections describe the testing methodology employed to measure the neutron sensitivity of one- and five-foil SFMNDs fabricated with either a Si or SB33 microstrip electrode. One- and five-foil SFMNDs with a Si microstrip electrode were initially fabricated and tested (Section 6.4.1). The reaction-product pulse-height spectra and ε_{th} were measured and compared to *MCNP6* simulation results. Following the identification of SB33 as an electrically-stable microstrip electrode, one- and five-foil SFMNDs with a SB33 microstrip electrode were fabricated and neutron-sensitivity measurements were performed (Section 6.4.2). The measured ε_{th} values and reaction-product pulse-height spectra were compared to simulated results. Gamma-ray rejection ratio measurements were also conducted using the SB33-based SFMNDs. The ε_{th} of each device was calculated using Eq. (2.20) and Eq. (2.21) in reference to a 4.0 atm, 5.08-cm diameter, 15.24-cm long Reuter Stokes ^{3}He tube with an ε_{th} of 80.7 ± 0.5% [89].

6.4.1 Silicon Microstrip Electrode

One- and five-foil SFMNDs with a Si microstrip electrode were separately contained within the aluminum testing enclosure (Figure 6.8) pressurized with 30.4 psig (3.07 atm) of P-10 gas while conducting neutron-sensitivity testing. Elevated P-10 pressures were initially used to increase the amount of reaction-product ionization that could occur within the sensitive volume. In order to maintain a reduced electric field strength of approximately 0.3 V cm^{-1} Torr^{-1} [99, 129], the operating voltages of the drift electrode, V_{DP}, and anode strips, V_A, were -2350 V and 380 V, respectively. The operating voltage of the cathode strips, V_C, was maintained at ground potential.

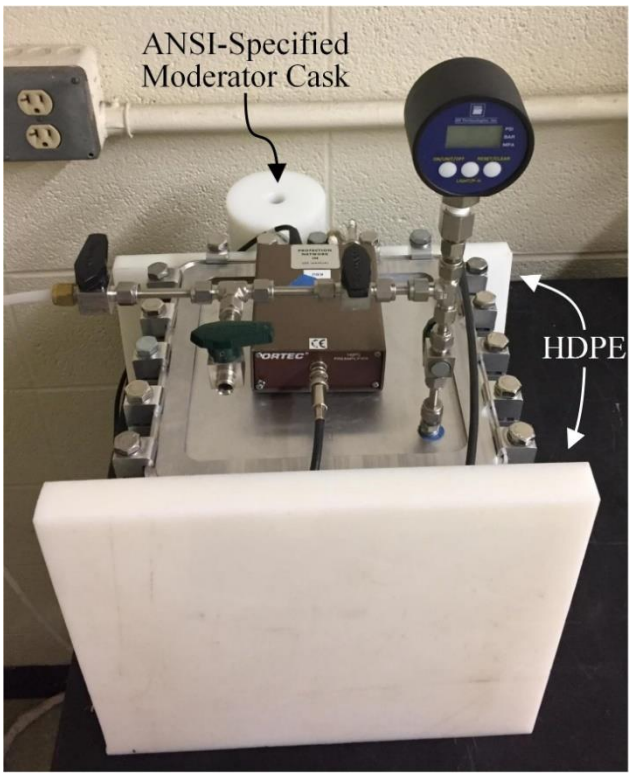

Figure 6.29. Orientation of HDPE slabs and the ANSI-specified moderator cask containing the 26-ng ^{252}Cf source relative to the aluminum testing enclosure.

Initially, neutron-sensitivity measurements were conducted using a 26-ng ^{252}Cf source surrounded by an ANSI-specified moderator cask [176]. The moderated ^{252}Cf measurements were performed to measure the reaction-product pulse-height spectra for each device. The orientation of the aluminum testing enclosure relative to the ANSI-specified moderator cask is shown in Figure 6.29. Slabs of high-density polyethylene (HDPE) moderator were positioned in front and behind the aluminum enclosure to moderate the fast neutrons emitted from the spontaneous fission of the ^{252}Cf source. The HDPE slabs each had a thickness of 2.54 cm (1 in.). The ^{252}Cf measurements were conducted prior to understanding the gain instability of the Si microstrip electrode. One-hour ^{252}Cf measurements were conducted for each device. As consecutive one-hour ^{252}Cf measurements were performed, the spectral features gradually shifted into lower channels. The gradual shift to lower channels was eventually attributed to the suspected gain instability of the Si microstrip electrode. The best reaction-product pulse-height spectrum measured for each device are shown in Figure 6.30. The reaction-product pulse-height spectra shown in Figure 6.30 are some of the first-ever spectra measured using SFMNDs.

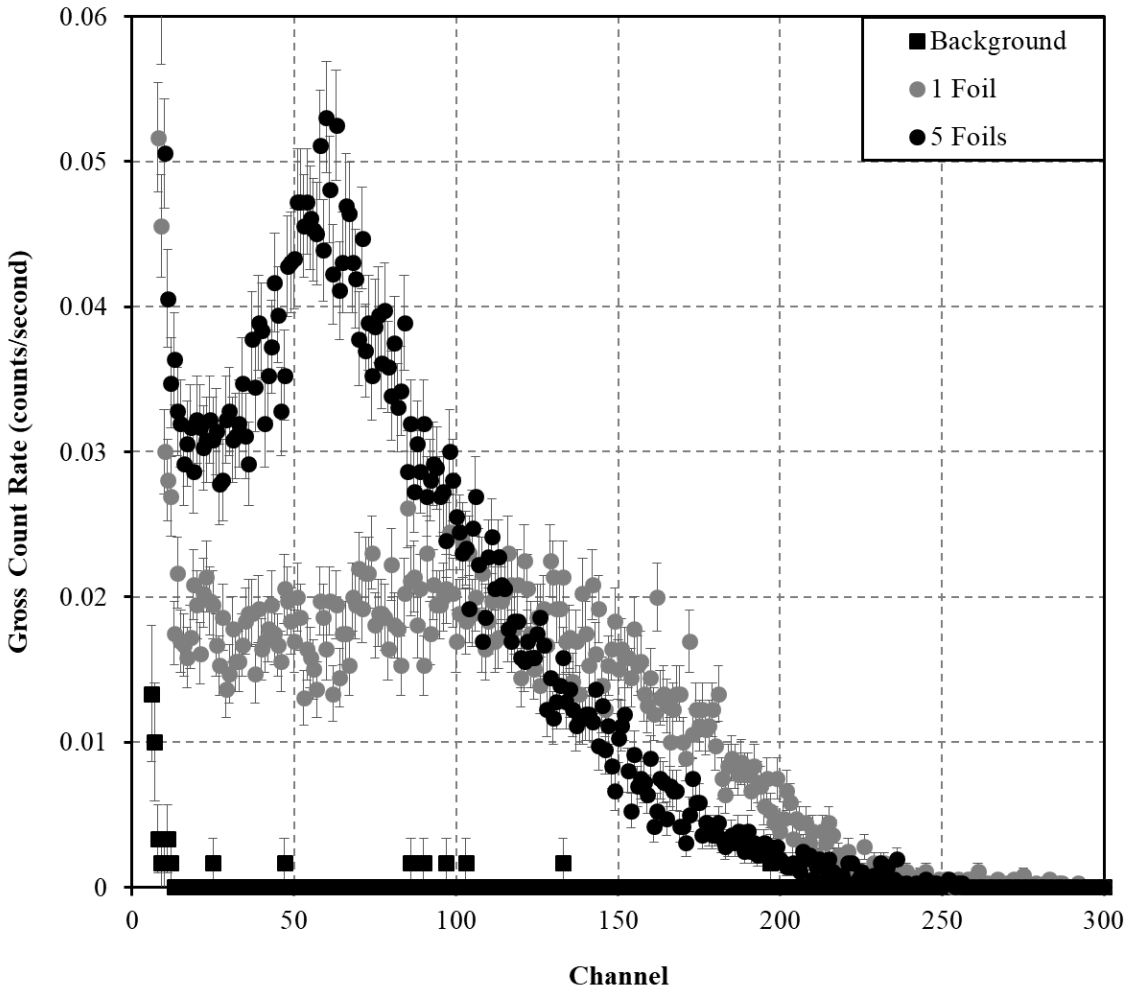

Figure 6.30. Reaction-product pulse-height spectra of one- and five-foil SFMNDs measured from a ^{252}Cf source housed within an ANSI-specified moderator cask. The SFMNDs were fabricated using a Si microstrip electrode.

MCNP6 simulations were also conducted for each device to compare the measured and simulated reaction-product pulse-height spectra of each device. The *MCNP6* simulation environments were defined in order to mimic the measurement scenarios. Thus, the materials, positions, and orientations of the electrodes, ^{6}Li foil(s), and foil frames were approximately the same as those used for conducting measurements. Likewise, the gas pressure and type were defined as 30.4 psig (3.07 atm) of P-10 gas. Shown in Figure 6.31 and Figure 6.32 are top-down views comparing the *MCNP6* simulation environment to the experimental configurations for one- and five-foil devices. The *MCNP6* simulations were also used for comparing measured and simulated values of ε_{th} for each device. Thus, the simulations were defined with a 5-mm diameter thermal-neutron beam incident on the center of the face of the ^{6}Li foil(s). Shown in Figure 6.33 are the

simulated reaction-product pulse-height spectra of one- and five-foil SFMNDs with a Si microstrip electrode. The shapes of the measured (Figure 6.30) and simulated (Figure 6.33) reaction-product pulse-height spectra appear similar, however the measured spectral features appear to be down-shifted relative to the simulated spectral features.

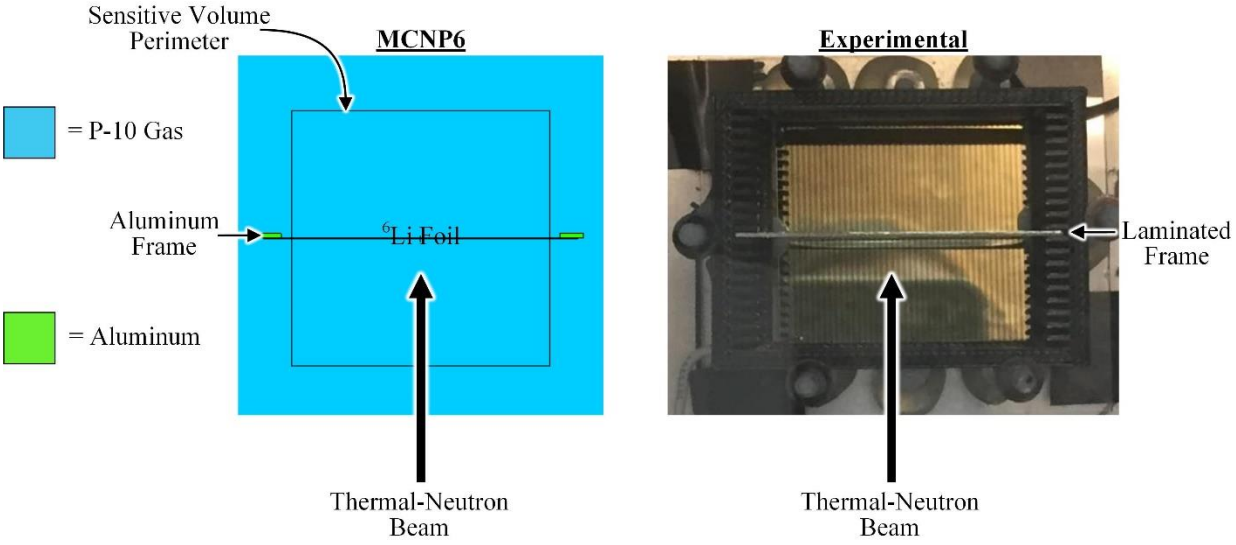

Figure 6.31. Top-down views of the MCNP6 simulation environment (left) to the experimental configuration (right) used for comparing the measured and simulated reaction-product pulse-height spectra and ε_{th} of a one-foil SFMND with a Si microstrip electrode.

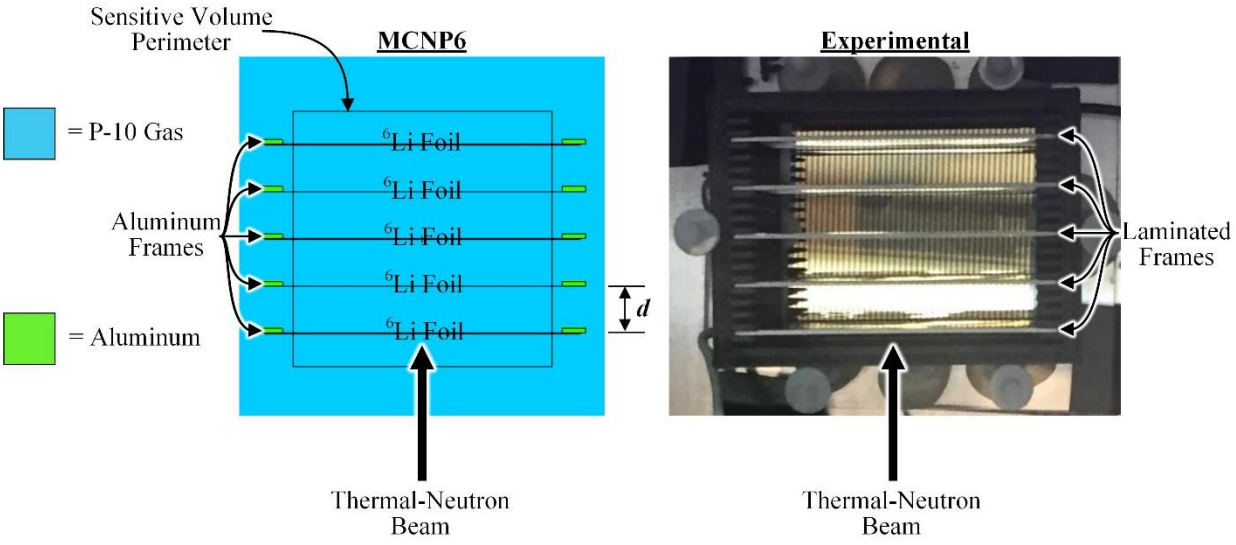

Figure 6.32. Top-down views of the MCNP6 simulation environment (left) to the experimental configuration (right) used for comparing the measured and simulated reaction-product pulse-height spectra and ε_{th} of a five-foil SFMND with a Si microstrip electrode.

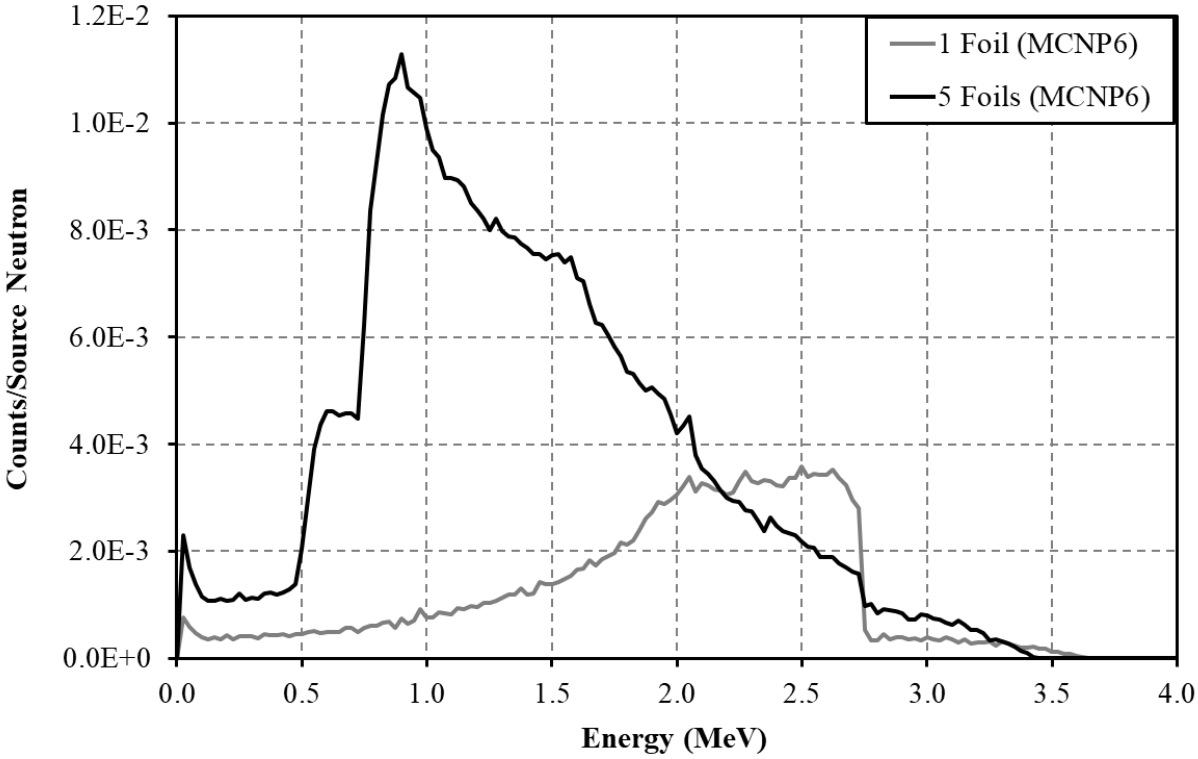

Figure 6.33. MCNP6-simulated reaction-product pulse-height spectra of SFMNDs containing one and five ^{6}Li foils.

Measurements of ε_{th} were conducted using the tangential beam port of the KSU TRIGA Mk II research reactor and compared to values simulated using *MCNP6*. The neutron beam emerging from the tangential beam port was collimated using a 5-mm diameter cadmium collimator. The aluminum enclosure was positioned relative to the neutron beam in order to align the center of the neutron beam with the center of the ^{6}Li foil(s). The measured net count rate of the one-foil SFMND was 3.25 ± 0.04 counts per second, yielding an ε_{th} of 4.02 ± 0.04%. The measured net count rate of the five-foil SFMND was 10.62 ± 0.14 counts per second, yielding an ε_{th} of 14.58 ± 0.11%. Simulated ε_{th} of the one- and five-foil devices were 19.06% and 54.91%, respectively.

The down-shift in spectral features observed from the ^{252}Cf measurements combined with the difference between measured and simulated ε_{th} was suspected to have occurred due to a combination of the measured capacitance (Section 6.2.1) and the gain instability (Section 6.2.5) of the Si microstrip electrode. The measured capacitance of the Si microstrip electrode may have resulted in a signal-to-noise ratio that led to lower-energy events blending with electronic noise. Consequently, if lower-energy events blended with electronic noise, those events would not

contribute to the measured ε_{th}, thus yielding a lower ε_{th} relative to the predicted value. The suspected polarization of the SiO_2 surface layer may have resulted in the gradual reduction of electric field strength and thus a gradual reduction in signal amplitude as a function of time. Therefore, better agreement between measured and simulated reaction-product pulse-height spectra and ε_{th} may have been possible, but would require the use of a lower capacitance, electrically-stable microstrip electrode.

6.4.2 Schott Borofloat® 33 Microstrip Electrode

One- and five-foil SFMNDs with a SB33 microstrip electrode were separately contained within the aluminum testing enclosure (Figure 6.8) pressurized with 10.0 psig (1.68 atm) of P-10 gas while conducting neutron-sensitivity testing. The position of the ^{6}Li foil in the one-foil device was the same as the position shown in Figure 6.31. As shown in Figure 6.34, the positions of the ^{6}Li foils in the five-foil device, relative to the sensitive volume, were defined in order to match the simulation environment described in Section 5.3.1. When testing the one-foil device, the operating voltages of the drift electrode, V_{DP}, and anode strips, V_A, were -1212 V and 300 V, respectively. The operating voltages used for testing the five-foil device were a V_{DP} of -1141 V and a V_A of 370 V. Due to the reduction in energy deposition of the five-foil device relative to the one-foil device (predicted from the simulated reaction-product pulse-height spectra shown in Figure 5.12), the V_A for the five-foil measurements was increased to increase the gas-multiplication factor. The operating voltage of the cathode strips, V_C, was maintained at ground potential when testing both devices. The V_{DP} setting for each device was set in order to maintain a reduced electric field strength of approximately 0.3 V cm^{-1} Torr^{-1} [99, 129].

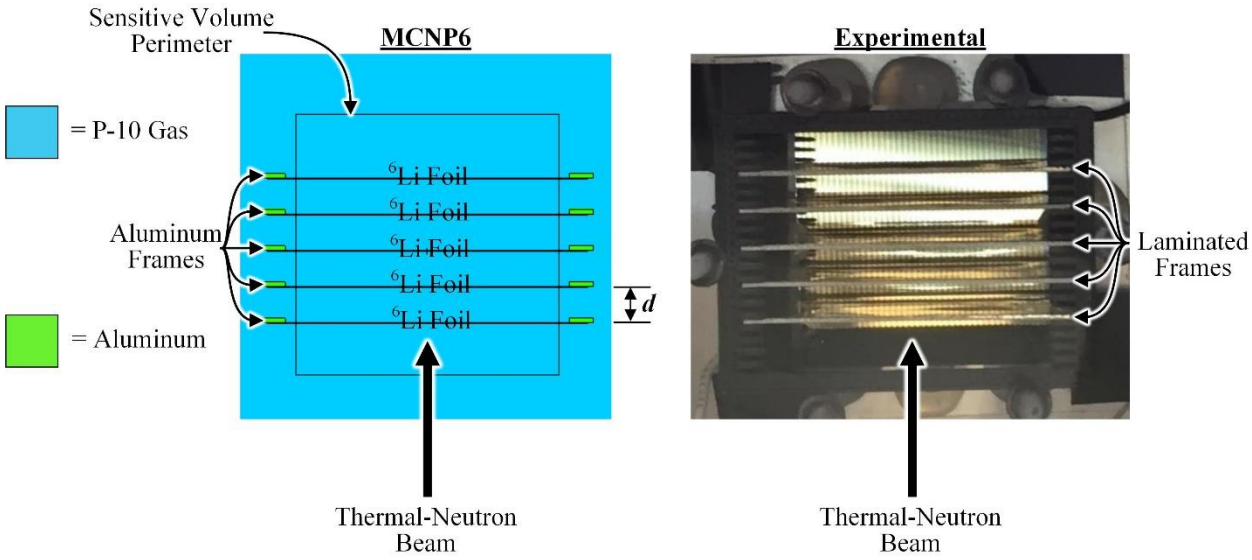

Figure 6.34. Top-down views of the MCNP6 simulation environment (left) and the experimental configuration (right) used for comparing the measured and simulated reaction-product pulse-height spectra and ε_{th} of a five-foil SFMND with a SB33 microstrip electrode.

Reaction-product pulse-height spectrum and ε_{th} measurements were conducted using the diffracted neutron beam of the KSU TRIGA Mk II research reactor. The neutron beam emerging from the diffracted beam port was collimated using a 2.5-mm diameter cadmium collimator. The measurements were performed for eight discrete thermal-neutron beam positions, in 3.18-mm increments, along the span of the ^{6}Li foil(s) between the microstrip and drift electrodes, as illustrated in Figure 6.35. The highest beam position (position 1) was closest to the drift-electrode surface and the lowest beam position (position 8) was closest to the microstrip-electrode surface. The desired beam positions, relative to the position of the ^{6}Li foil(s) within the aluminum testing enclosure, were measured and defined during the assembly of both devices. A laser was used to align the aluminum testing enclosure with the thermal-neutron beam for each beam position. The laser was previously calibrated to be aligned with the thermal-neutron beam. After conducting the reaction-product pulse-height spectrum and ε_{th} measurements, *GRR* measurements were performed for both the one- and five-foil devices using a ^{137}Cs source.

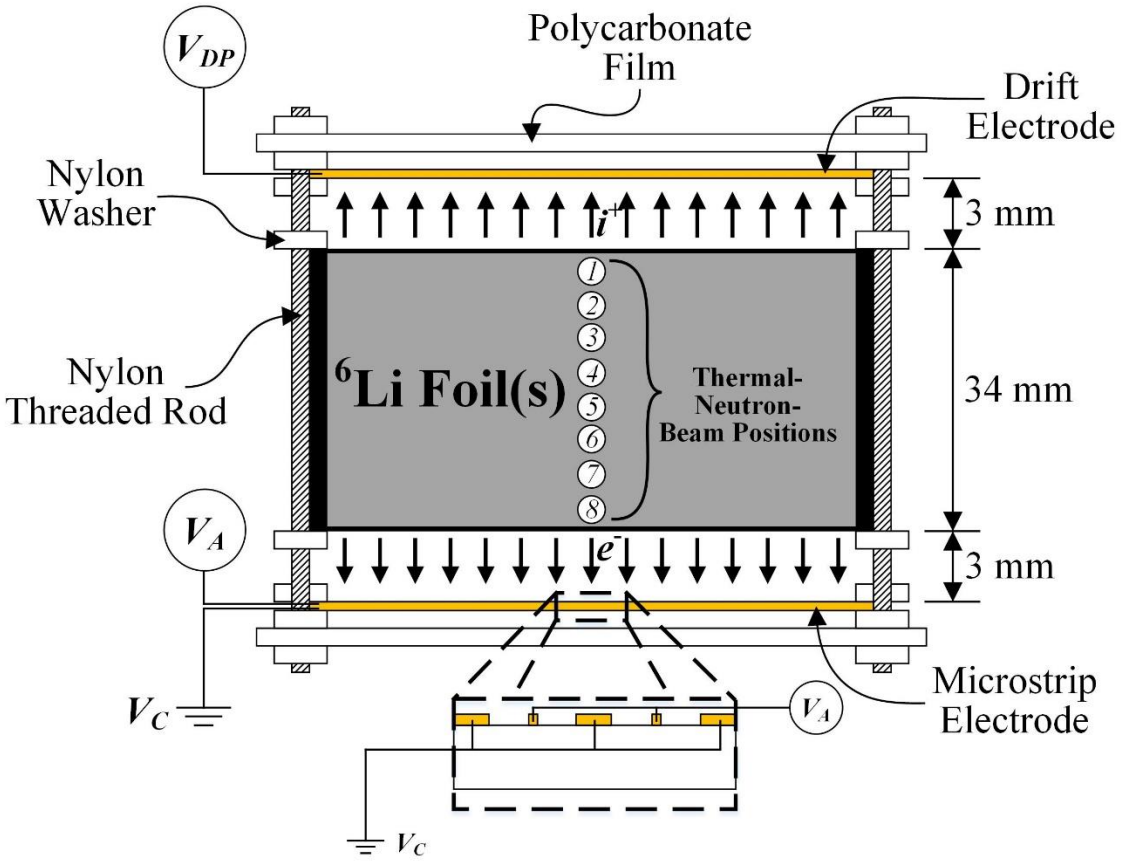

Figure 6.35. Illustration of the testing configuration used for measuring the reaction-product pulse-height spectra and ε_{th} for eight thermal-neutron beam positions.

Shown in Figure 6.36 are the reaction-product pulse-height spectra measured using a one-foil SFMND with a SB33 microstrip electrode for eight discrete thermal-neutron beam positions. As the thermal-neutron beam was positioned further away from the microstrip-electrode surface, a down-shift of spectral features to lower channel numbers occurred. The shift in spectral features is consistent with the drift electric field strength distribution measurements (Section 6.2.6). The down-shift in spectral features resulted in a decrease of ε_{th} as the thermal-neutron beam was positioned further away from the microstrip electrode surface (shown in Figure 6.37 and listed in Table 6.6).

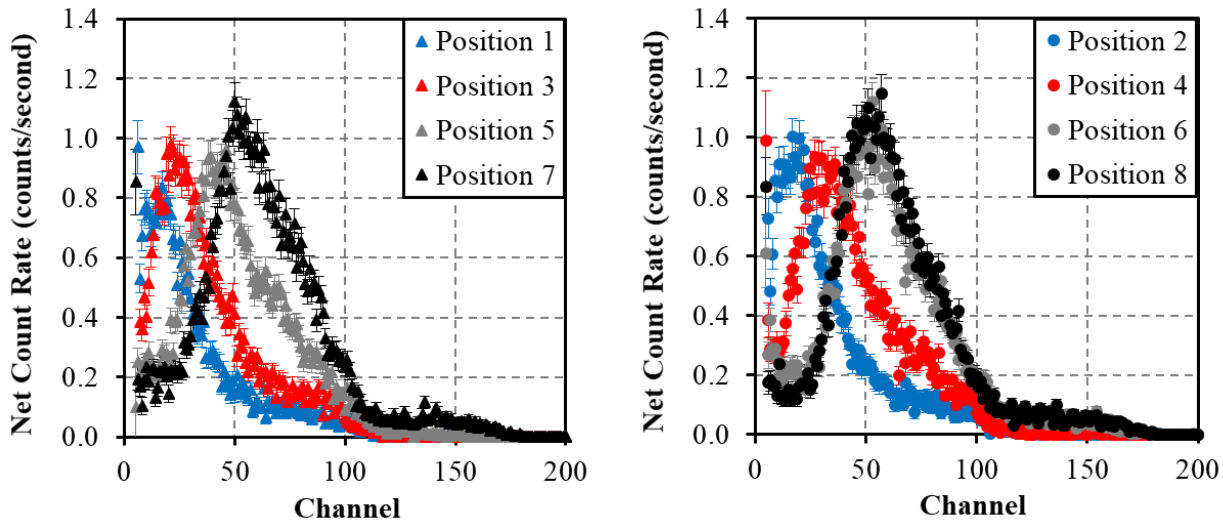

Figure 6.36. Measured reaction-product pulse-height spectra for eight discrete thermal-neutron beam positions incident on a one-foil SFMND with a SB33 microstrip electrode. The measured spectra are plotted on two separate sets of axes to provide clarity for better discernment of the individual reaction-product pulse-height spectra [155].

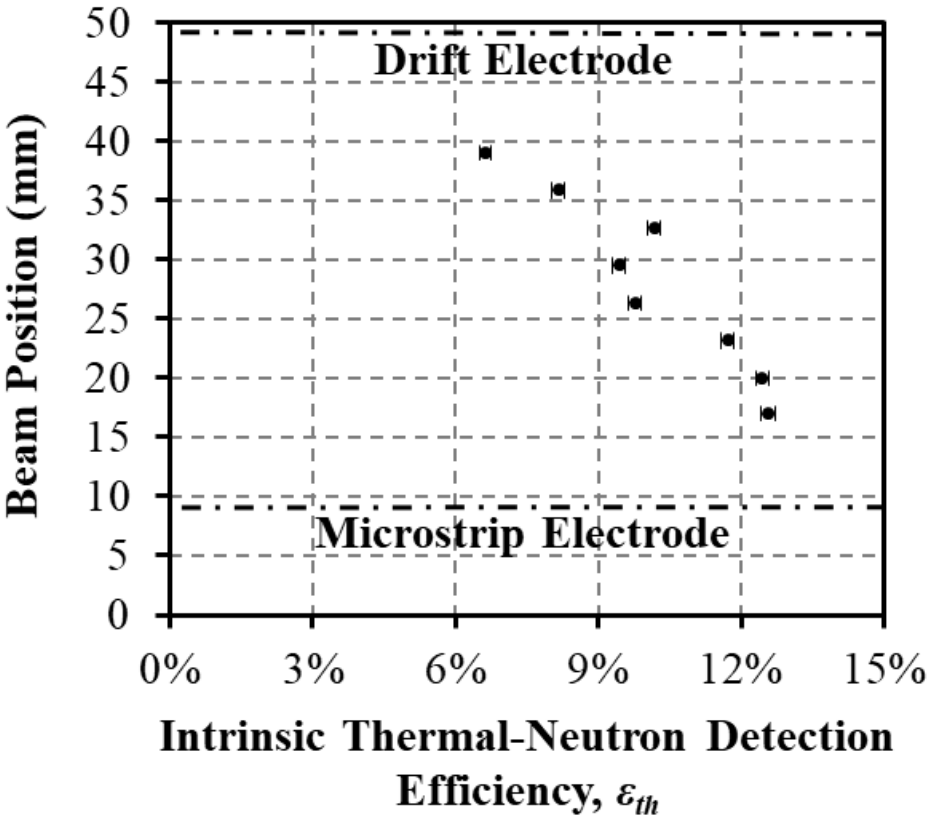

Figure 6.37. Measured ε_{th} as a function of the thermal-neutron beam position for a one-foil ^{6}Li-based SFMND with a SB33 microstrip electrode [155].

Table 6.6. Measured ε_{th} of a one-foil SFMND with a SB33 microstrip electrode. Data for eight discrete thermal-neutron beam positions along the length of the ^{6}Li foil between the microstrip and drift electrodes are tabulated [155].

Position	Beam Height Above Microstrip Surface (mm)	Measured ε_{th}
1	30.6	6.63 ± 0.12%
2	27.4	8.16 ± 0.13%
3	24.2	10.17 ± 0.14%
4	21.0	9.44 ± 0.14%
5	17.9	9.77 ± 0.14%
6	14.7	11.71 ± 0.14%
7	11.5	12.45 ± 0.15%
8	8.5	12.58 ± 0.15%

Using a non-zero LLD setting, a maximum ε_{th} of 12.58 ± 0.15% was measured at position 8, the closest thermal-neutron beam position to the microstrip-electrode surface. The maximum measured ε_{th} for a one-foil ^{6}Li-based SFMND was lower than the expected ε_{th} of 18.36% predicted from *MCNP6* simulations. The lower measured ε_{th} is suspected to be a consequence of combined effects, including a non-uniform electric field strength distribution, electron attachment, and the signal-to-noise ratio of the readout electrode system (arising from the measured SB33 microstrip-electrode capacitance of approximately 60 pF). The non-uniform distribution of pulse-amplitudes previously measured using a collimated ^{241}Am alpha-particle source for a similar electrode setup (Section 6.2.6) is consistent with the non-uniform distribution of measured ε_{th}. Thus, a suspected cause for the non-uniform distribution of measured ε_{th} is a non-uniform electric field strength distribution. A non-uniform electric field strength distribution would result in a distribution of charge-carrier velocities, position dependent between the microstrip and drift electrodes, resulting in a non-uniform distribution of measured pulse amplitudes. A second suspected cause for the non-uniform distribution of measured ε_{th} is attributed to the use of ABS plastic, nylon, and other high-outgassing materials to construct the 3D-printed support device and other components. As previously described in Section 6.2.6, the presence of these materials may have introduced contaminants that promote electron attachment. Such contamination is suspected to have been a cause of the ε_{th} degradation as the thermal-neutron beam was positioned further away from the microstrip electrode surface. The third suspected cause for the non-uniform distribution of measured ε_{th} is attributed to the microstrip-electrode capacitance. A reduction in microstrip-

electrode capacitance should further increase the signal-to-noise ratio, allowing for separation of low-energy neutron events from electronic noise, and therefore further increase the measured ε_{th}.

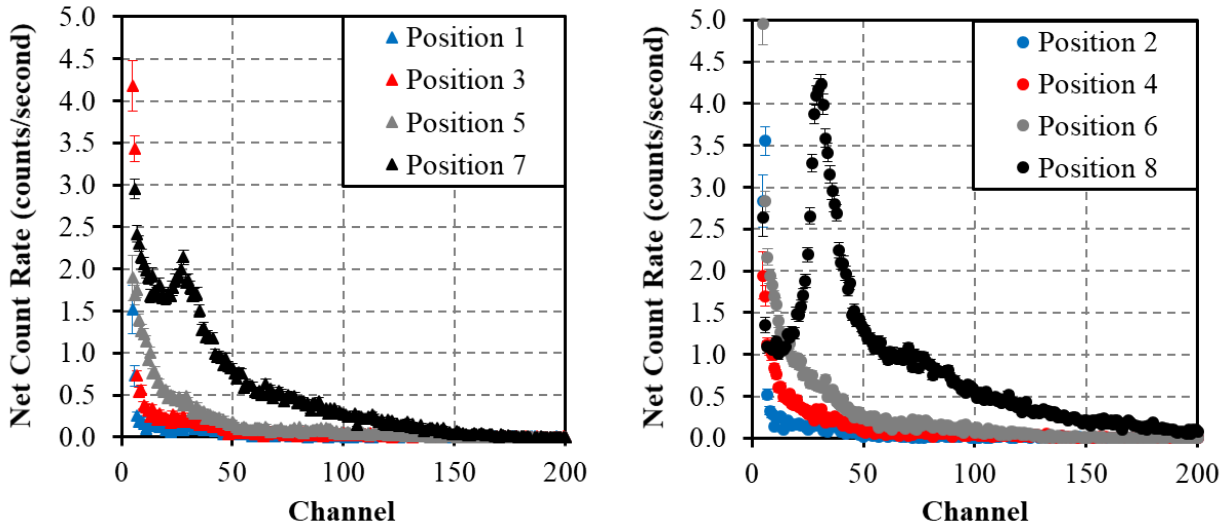

Figure 6.38. Measured reaction-product pulse-height spectra for eight discrete thermal-neutron beam positions incident on a five-foil SFMND with a SB33 microstrip electrode. The measured spectra are plotted on two separate sets of axes to provide clarity for better discernment of the individual reaction-product pulse-height spectra. The spectral features diminished more rapidly compared to the one-foil case (see discussion in text) [155].

Shown in Figure 6.38 are the reaction-product pulse-height spectra as a function of thermal-neutron beam position for the five-foil SFMND with a SB33 microstrip electrode. Similar to the one-foil device (Figure 6.36), a down-shift in spectral features occurred as the thermal-neutron beam was positioned further away from the microstrip-electrode surface. However, the measured ε_{th}, shown in Figure 6.39 and listed in Table 6.7, rapidly decreased as the thermal-neutron beam was positioned further away from the microstrip-electrode surface compared to the distribution of ε_{th} measured using the one-foil device (Figure 6.37 and Table 6.6). Recalling the simulated reaction-product pulse-height spectra shown in Figure 5.12, the spectral features for a five-foil ^{6}Li-based SFMND are most prominent in lower energy bins between 0.3 – 1.0 MeV. In comparison, the spectral features for a one-foil ^{6}Li-based SFMND are most prominent between energies of approximately 1.0 – 2.5 MeV. The more rapid degradation of the measured ε_{th} for the five-foil SFMND compared to the one-foil SFMND is suspected to have occurred due to the lower-energy pulse-height spectral features combined with suspected problems attributed to a non-uniform electric field strength distribution, electron attachment, the signal-to-noise ratio, or any combination thereof. The maximum ε_{th} of 29.75 ± 0.26% was measured at position 8 for a non-

zero LLD setting. The maximum measured ε_{th} was significantly lower than the expected ε_{th} of 54.08% predicted from *MCNP6* simulations.

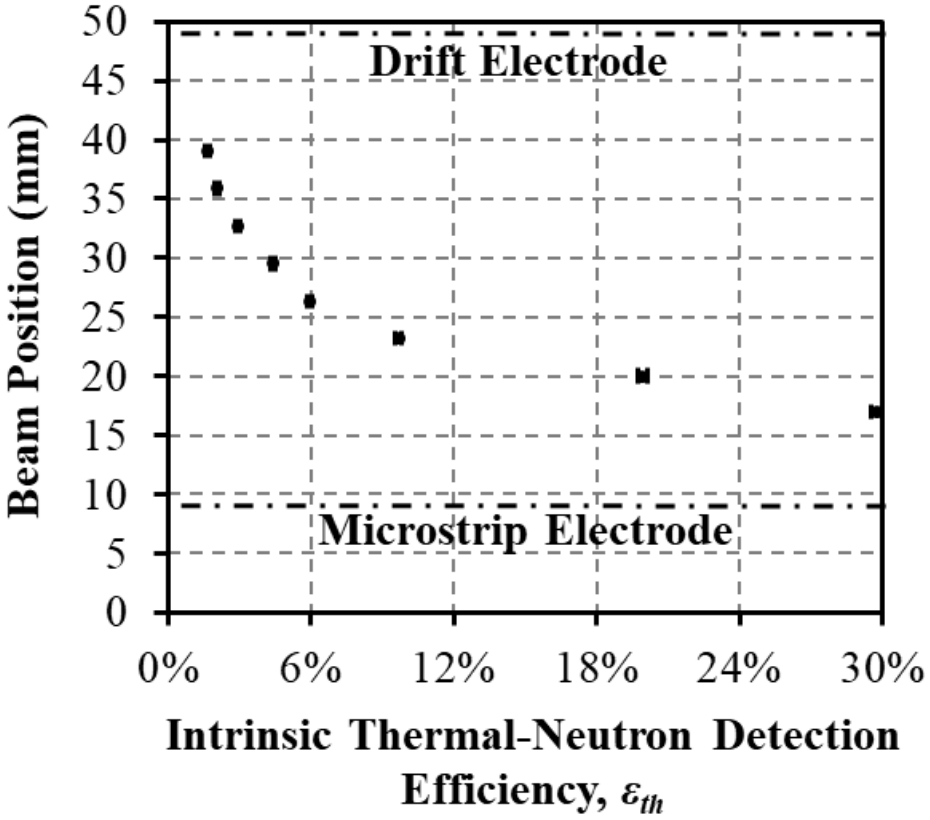

Figure 6.39. Measured ε_{th} as a function of the thermal-neutron beam position for a five-foil ^{6}Li-based SFMND with a SB33 microstrip electrode. The ε_{th} decreased more rapidly as the thermal-neutron beam was positioned further away from the microstrip-electrode surface compared to the one-foil device (Figure 6.37) [155].

Table 6.7. Measured ε_{th} of a SFMND containing five foils with a SB33 microstrip electrode. Data for eight discrete thermal-neutron beam positions along the length of the ^{6}Li foil between the microstrip and drift electrodes are tabulated [155].

Position	Beam Height Above Microstrip Surface (mm)	Measured ε_{th}
1	30.6	1.65 ± 0.09%
2	27.4	2.07 ± 0.09%
3	24.2	2.95 ± 0.10%
4	21.0	4.43 ± 0.10%
5	17.9	5.95 ± 0.11%
6	14.7	9.69 ± 0.11%
7	11.5	19.92 ± 0.19%
8	8.5	29.75 ± 0.26%

The cumulative effects of the non-uniform pulse-amplitude and ε_{th} distributions were studied by conducting isolated ^{252}Cf measurements. The one- and five-foil SFMNDs were separately exposed to a 22-ng ^{252}Cf source and the reaction-product pulse-height spectra were measured for each device. During the measurements, the ^{252}Cf source was surrounded by an ANSI-specified moderator cask [176]. The ^{252}Cf measurements were conducted with the same gas pressure and operating voltage settings as the measurements conducted for the eight discrete thermal-neutron beam positions. For each device, the net count rate measured from the ^{252}Cf source was normalized relative to the net count rate where the most prominent spectral feature was located. Comparisons were performed by summing the reaction-product pulse-height spectra from the eight discrete thermal-neutron beam measurements using the one- (Figure 6.36) and five-foil (Figure 6.38) SFMNDs. The net count rate of the summed reaction-product pulse-height spectra was then normalized relative to the net count rate where the most prominent spectral feature was located. The two sets of data were plotted and compared as shown in Figure 6.40 for the one-foil device. A comparison of the two data sets for the five-foil device is shown in Figure 6.41.

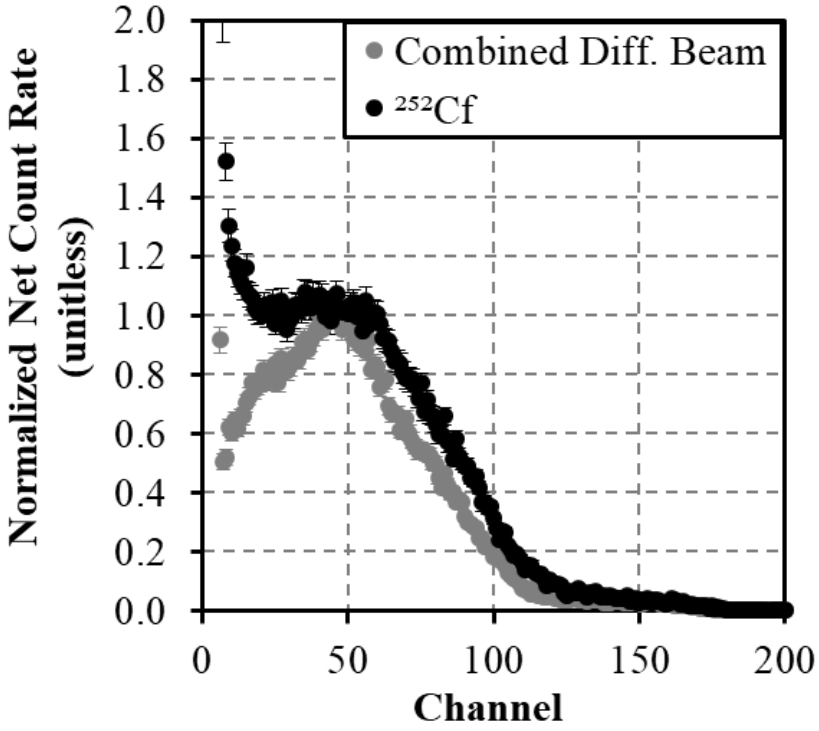

Figure 6.40. Comparison of the normalized summed reaction-product pulse-height spectra measured using the one-foil SFMND (Figure 6.36) relative to the normalized reaction-product pulse-height spectrum measured from a moderated ^{252}Cf neutron source. The net count rates from each spectrum were normalized relative to the net count rate where the most prominent spectral feature was located (approximately at channel 50).

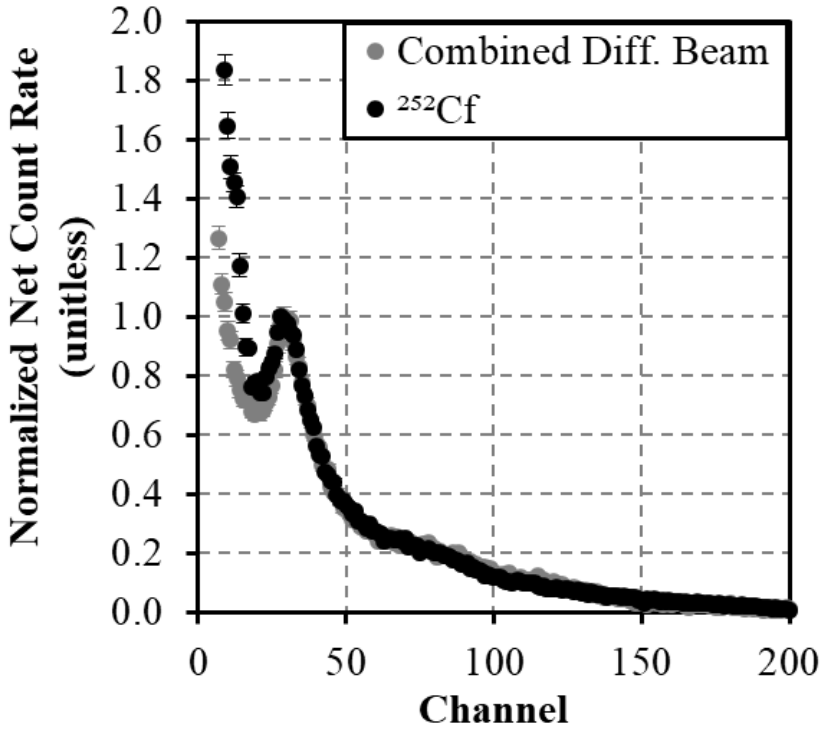

Figure 6.41. Comparison of the normalized summed reaction-product pulse-height spectra measured using the five-foil SFMND (Figure 6.38) relative to the normalized reaction-product pulse-height spectrum measured from a moderated ^{252}Cf neutron source. The net count rates from each spectrum are normalized relative to the net count rate where the most prominent spectral feature is located (approximately at channel 30) [155].

Both data sets shown in Figure 6.40 and Figure 6.41 have similar spectral features. The ^{252}Cf data measured using the one-foil device (Figure 6.40) depicts a higher normalized net count rate in the channels preceding the prominent spectral feature located approximately at channel 50. The ^{252}Cf data measured using the five-foil device (Figure 6.41) also has an elevated normalized net count rate in the lower channels below the prominent spectral feature located approximately at channel 30. For channels above the prominent spectral feature of the one-foil device, the normalized net count rates measured from the ^{252}Cf source are also elevated above that of the summed reaction-product pulse-height spectra from Figure 6.36. The elevated count rates measured from the ^{252}Cf source occurred because the ^{252}Cf measurement includes a nearly uniform distribution of neutron-interaction locations along the length of the foil from the uncollimated ^{252}Cf source and moderator cask. If additional thermal-neutron beam measurements were performed in between the reported beam positions, the spectral features are expected to be closer matched to those measured from the ^{252}Cf measurement.

The *GRR*s of the one- and five-foil SFMNDs with SB33 microstrip electrodes were calculated using Eq. (2.22) and Eq. (2.23) for a ^{137}Cs exposure rate of 50 mR hr^{-1}. The *GRR* measurements were conducted with the same gas pressure and operating voltage settings as the eight discrete thermal-neutron beam position measurements and ^{252}Cf measurements. Shown in Figure 6.42 are the pulse-height spectra measured from the 50 mR hr^{-1} exposure rate of ^{137}Cs relative to the reaction-product pulse-height spectra measured from the moderated ^{252}Cf source. The spectra shown on the left of Figure 6.42 were measured using the one-foil device and the spectra shown on the right of Figure 6.42 were measured using the five-foil device. A comparison of the reaction-product and gamma-ray pulse-height spectra indicates that both devices have low sensitivity to gamma rays relative to the neutron sensitivity of each device. The measured *GRR*s of the one- and five-foil SFMNDs with SB33 microstrip electrodes were 6.46 x 10^{-5} ± 4.32 x 10^{-7} and 7.96 x 10^{-5} ± 4.65 x 10^{-7}, respectively. The difference between the measured *GRR* values and lower values previously reported for Li-foil MWPCs [46, 48] is suspected to be a consequence of the aluminum wall thickness (0.9525 cm) of the sealed test enclosure. The amount of aluminum in the test enclosure, compared to thinner-walled enclosures previously used for fabricating and testing Li-foil MWPCs [46, 48], resulted in an increase in measured ^{137}Cs counts from gamma rays scattering off of the enclosure walls [177]. Therefore, thinner-walled aluminum enclosures (≤ 0.3175 cm) must be used in order to improve the *GRR*.

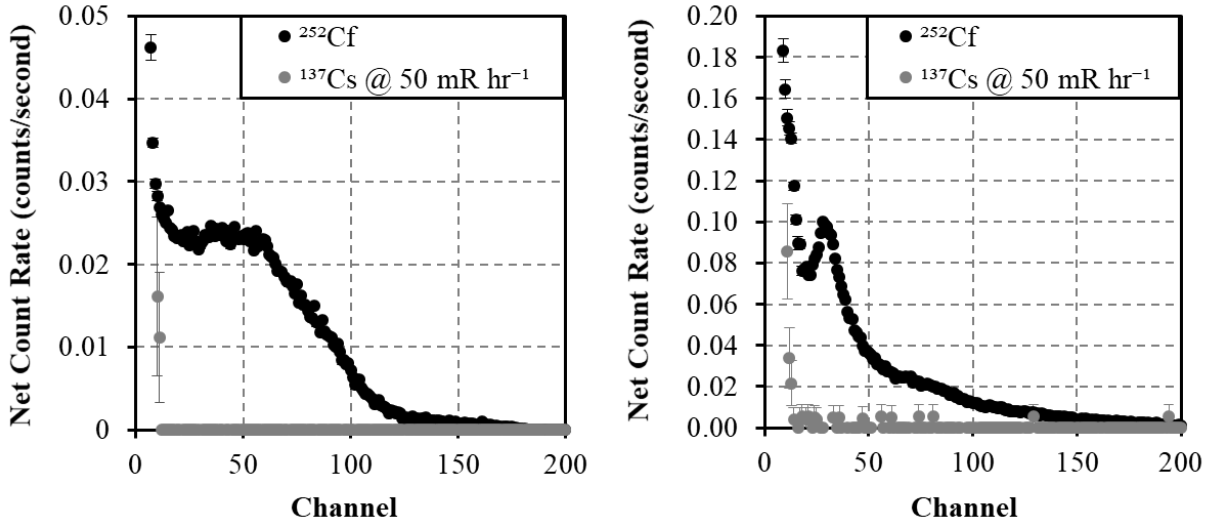

Figure 6.42. The gamma-ray and reaction-product pulse-height spectra measured using the one- (left) and five-foil (right) SFMNDs with a SB33 microstrip electrode. The gamma-ray pulse-height spectra were measured using a 50 mR hr^{-1} ^{137}Cs exposure rate and the reaction-product pulse-height spectra were measured using a moderated ^{252}Cf source.

6.5 Proposed SFMND Improvements

As previously discussed in Section 6.2.6, a non-uniform pulse-height distribution was measured when conducting the drift electric field strength distribution measurements (Figure 6.18). The results from the *COULOMB* simulations (Figure 6.19 and Figure 6.20) suggested that the measured non-uniform pulse-height distribution may have been attributed, in part, to the electric field strength distribution between the microstrip and drift electrodes. In addition to the electric field strength distribution, electron attachment was also suspected to have occurred between the microstrip and drift electrodes due to the use of plastics to fabricate the plastic support structure. When conducting SFMND neutron-sensitivity measurements, the microstrip-electrode capacitance was also suspected to have yielded a poor signal-to-noise ratio, resulting in lower-energy neutron events blending with electronic noise (Figure 6.30). Each of the aforementioned suspected causes for performance deterioration were also suspected to have contributed to the non-uniform distribution of ε_{th} measured using the SFMNDs fabricated with a SB33 microstrip electrode (Figure 6.36 – Figure 6.39). Thus, the following sections discuss proposed improvements to the design of SFMNDs in order to reduce the effect that the electric field strength distribution (Section 6.5.1), electron attachment (Section 6.5.2), and the signal-to-noise ratio (Section 6.5.3) have on the SFMND neutron-detection capabilities.

6.5.1 Implementation of a Frisch Grid

Recalling from Section 6.2.6 the results from the drift electric field profiling measurements (Figure 6.18) and the *COULOMB* electric field strength distribution simulations (Figure 6.19 and Figure 6.20), as well as the SFMND ε_{th} distribution measurements (Figure 6.36 – Figure 6.39) from Section 6.4.2, a non-uniform electric field strength distribution may be occurring between the drift and microstrip electrodes. As previously discussed in Section 6.2.6, the electric field strength distribution should have minimal effect on electron drift. Thus, during the time response of the pulse formation process (defined by the *RC* time constant), electrons should be capable of drifting the full distance between the site of charge-carrier liberation and the collecting electrode. However, because the velocity of the positively-charged ions is dependent on the local electric field strength, the distance displaced by positively-charged ions during the time response of the

pulse formation process will also be dependent on the local electric field strength. Therefore, a non-uniform distribution of pulse amplitudes will occur due to the distribution of distances displaced by positively-charged ions during the time response of the pulse formation process.

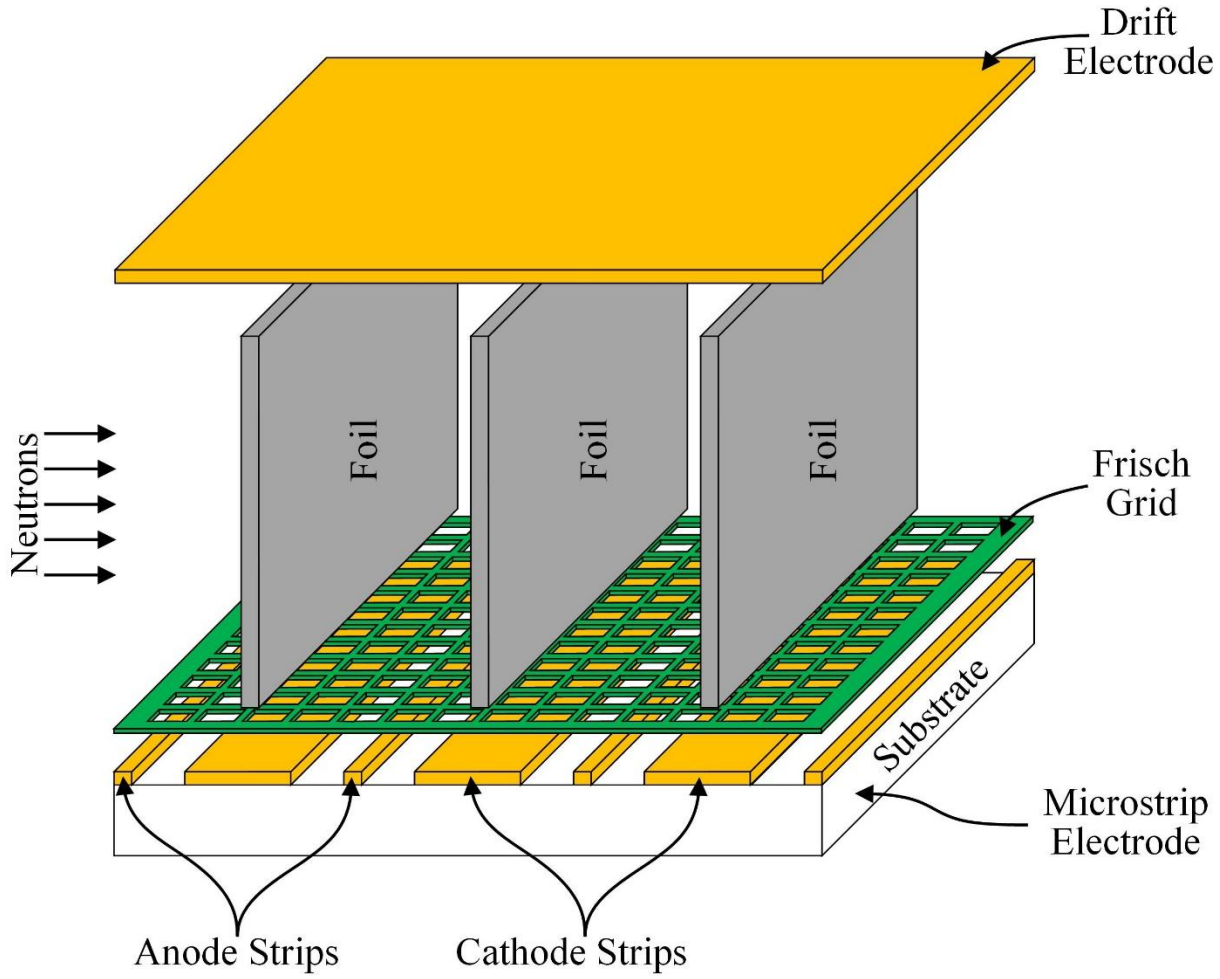

Figure 6.43. Configuration of a SFMND with a Frisch grid depicting the orientation of suspended foils relative to microstrip, drift, and Frisch-grid electrodes.

A method for overcoming the position dependency of the electric field strength distribution is the addition of a Frisch grid between the bottom of the ^{6}Li foil(s) and the microstrip electrode, as illustrated in Figure 6.43. The addition of a Frisch grid would segment the device into a drift region and a detection region, as illustrated in Figure 6.44. The sensitive volume of the device would be contained within the drift region where the ^{6}Li foil(s) are positioned. Recalling the discussion of Frisch grid ionization chambers from Section 3.4.1, charge-carrier motion will occur within both the drift and detection regions. However, only the distance displaced by charge carriers within the detection region contributes to the pulse formation. Because the distance between the

Frisch grid and microstrip electrode would remain constant, the distance displaced by charge carriers within the detection region should be approximately constant, thus improving the uniformity of measured pulse amplitudes.

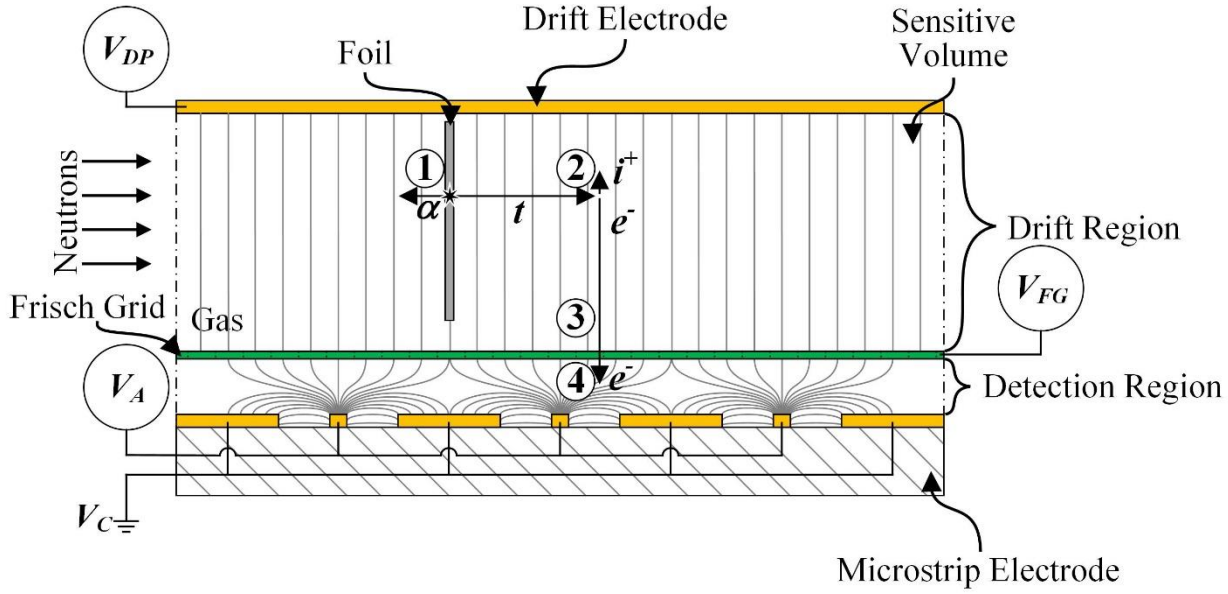

Figure 6.44. Four-step neutron detection process of a ^{6}Li-based SFMND with a Frisch grid.

Due to the segmentation of the device into a drift region and a detection region, a four-step neutron-detection process would occur. The first step of the neutron-detection process remains the same as the first step of the three-step neutron-detection process described in Section 5.2. The second step occurs when charge carriers drift within the drift region under the influence of the electric field formed from the drift electrode, V_{DP}, and the Frisch grid, V_{FG}, operating voltages. The operating voltage condition of $V_{DP} < V_{FG}$ is required to drift electrons towards the Frisch grid and positively-charged ions towards the drift electrode. The third step of the neutron-detection process occurs when the electrons pass through the Frisch grid and enter the detection region. Once the electrons pass through the Frisch grid, the electric field strength increases substantially due to the potential difference between the Frisch grid and the microstrip electrode anode and cathode strips, V_A and V_C, respectively. The operating voltage condition of $V_{FG} < V_C < V_A$ is required. Consequently, the drift velocity of the electrons increases. Eventually, the kinetic energy of the electrons is sufficient to cause impact ionization within the detection region, resulting in Townsend avalanching. Thus, the fourth step of the neutron-detection process occurs within the detection region when Townsend avalanching occurs. Although neutron interactions occur within the drift

region, the amount of current induced on the anode strips is only dependent on the distance displaced by charge carriers within the detection region.

In order to investigate the addition of a Frisch grid between the bottom of the ^{6}Li foils and the microstrip electrode, the scenario was simulated using *COULOMB*. The drift electrode, Frisch grid, and microstrip electrode were oriented parallel to one another. The microstrip and drift electrode geometries used for testing (Section 6.1) were implemented into the simulation environment. Although a gridded electrode is used as a Frisch grid in an experimental setting, the Frisch grid was defined as a planar electrode in the simulation environment. The Frisch grid was positioned 5-mm above the microstrip-electrode surface. The Frisch grid and the drift electrode were separated by a distance of approximately 4 cm. Consequently, the distance separating the microstrip and drift electrodes was approximately 4.5 cm. The anode strips were defined in the simulation environment with an operating voltage of 400 V and the cathode strips were defined at ground potential (0 V). The drift electrode was defined with an operating voltage of -1000 V and the Frisch grid was defined with an operating voltage of -100 V. Ar gas at atmospheric pressure was defined as the dielectric material between the electrodes to provide a close approximation to P-10 gas.

Shown in Figure 6.45 is the *COULOMB* simulation results of the electric field strength as a function of vertical position between the microstrip and drift electrodes. The microstrip electrode, Frisch grid, and drift electrode are located at vertical positions of 0.75 cm, 1.25 cm, and 5.2 cm, respectively. The positions of the microstrip and drift electrodes are indicated by dot-dashed lines (— · —) and the double dashed line (= = =) indicates the position of the Frisch grid. The dashed lines (- - -) indicate the approximate vertical positions of the collimated ^{241}Am alpha-particle source above the Frisch grid (approximately the same vertical positions above the microstrip electrode depicted in Figure 6.18 and listed in Table 6.5). As shown in Figure 6.45, the addition of the Frisch grid results in a uniform drift electric field strength distribution between the drift electrode and Frisch grid where foils would be positioned. The electric field strength increases substantially between the Frisch grid and the microstrip electrode. Near the surface of the microstrip electrode, the strength of the electric field is sufficient to allow electrons to have kinetic energies capable of causing impact ionization. Therefore, the addition of the Frisch grid should improve the uniformity of measured ε_{th} because the device would rely only on the motion of charge carriers drifting within the detection region. Furthermore, the device should still be able to be

operated in proportional mode due to the substantial increase in electric field strength near the surface of the anode that is sufficient for Townsend avalanching.

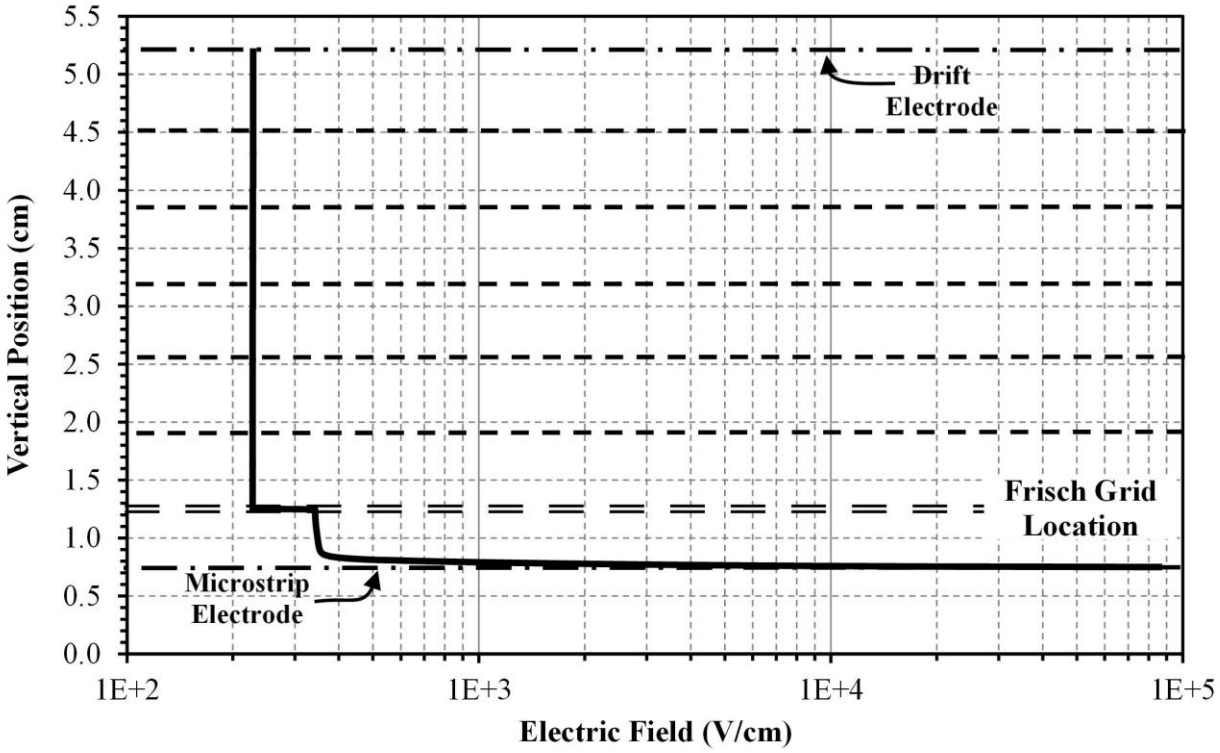

Figure 6.45. COULOMB simulation results for the electric field strength distribution (in logarithmic scale) as a function of vertical distance between the microstrip and drift electrodes with a Frisch grid implemented. The dashed lines provide a frame of reference for the vertical positions of the collimated ^{241}Am alpha-particle source positions defined from Figure 6.18 and Table 6.5.

The application of a wire-mesh Frisch grid may lead to an increase in microphonic sensitivity. A thick gaseous electron multiplier (TGEM) [178] could be used as a Frisch grid instead, thus maintaining the goal of developing a robust device that has minimal microphonic sensitivity. The addition of a Frisch grid requires an additional operating voltage, and in the case of a TGEM may require two additional operating voltages. The required Frisch grid operating voltages could be applied with the application of a voltage divider circuit to either the anode-strip or drift-electrode operating voltage line based on the desired polarity. Although the addition of the Frisch grid is expected to improve the uniformity of measured ε_{th}, electron attachment may still occur between the microstrip and drift electrodes.

6.5.2 Use of Low-Outgassing Materials

Electron attachment is another suspected cause for the non-uniform distributions of measured pulse amplitudes (Section 6.2.6) and ε_{th} (Section 6.4.2). Electron attachment is suspected due to the use of nylon and other high-outgassing materials to construct the plastic support structure (Figure 6.6 and Figure 6.7). Additionally, ABS plastic was used to fabricate the 3D-printed support device (Figure 6.21 and Figure 6.22). As previously discussed in Section 6.2.6, if electron attachment occurred, the population of electrons that arrive at the microstrip electrode would vary as a function of position between the microstrip and drift electrodes.

One proposed solution for studying whether electron attachment is occurring due to the presence of O_2, H_2O, and/or other volatiles outgassed from the high-outgassing materials is to conduct the drift electric field profiling measurements using a continuous-gas-flow configuration of the testing enclosure. The use of a continuous-gas-flow configuration would continuously remove any O_2, H_2O, and other volatiles while performing the measurements and should, therefore, reduce the amount of electron attachment that can occur. The amount of electron attachment occurring between the microstrip and drift electrodes could be assessed by comparing the previously-measured drift electric field profiling results (Section 6.2.6) to the results measured using the continuous-gas-flow configuration.

A second proposed solution is to fabricate the plastic support structure and 3D-printed support device using low-outgassing materials such as PTFE (Polytetrafluoroethylene, more commonly known as Teflon™) or PEEK (Polyether Ether Ketone) [179, 180]. The costs of these low-outgassing materials [181] are an attractive alternative to other, low-outgassing materials such as alumina or quartz that are more expensive due to the additional machining required during fabrication. Regardless of which low-outgassing materials are used, a thorough bake-out procedure of the aluminum enclosure would be necessary prior to testing to ensure that any O_2, H_2O, and other volatiles are removed. The effectiveness of the low-outgassing materials for reducing the probability of electron attachment could be monitored by measuring the O_2 and H_2O contents present within the aluminum testing enclosure during the bake-out procedure and subsequent testing procedures. The O_2 and H_2O content measurements could then be compared for each set of materials used for fabricating the plastic support structure and 3D-printed support device. The amount of electron attachment occurring between the microstrip and drift electrodes could be assessed by repeating the drift electric field profile measurements (Section 6.2.6) for each set of

materials. Like the O_2 and H_2O measurements, the results from the drift electric field profile measurements could be compared to assess the effectiveness of each set of materials used for fabricating the plastic support structure and 3D-printed support device.

6.5.3 Segmentation of Microstrip-Electrode Anode Strips

The capacitance of the microstrip electrode is suspected to have contributed to the non-uniform distributions of measured pulse amplitudes and ε_{th}. The measured pulse amplitudes and ε_{th} are suspected to be affected by the signal-to-noise ratio which is a function of the microstrip-electrode capacitance. Recalling Eq. (3.21), the amplitude of the voltage pulse formed from charge motion within a detector is dependent on the device capacitance. As the capacitance increases, the amplitude of the voltage pulse decreases. Depending on the average amplitude of the electronic noise and the energy range of the spectral features present in the reaction-product pulse-height spectrum, the signal-to-noise ratio may result in lower-energy neutron events blending with electronic noise. If lower-energy neutron events blend with electronic noise, then those events cannot contribute to the measured ε_{th}, thus yielding a lower ε_{th} relative to the predicted value. Therefore, a decrease in the electrode capacitance should increase the amplitude of the voltage pulses. Consequently, an increase in the signal-to-noise ratio should occur, thus providing further separation between neutron-induced events and electronic noise.

Based on the measured capacitances of the three sizes of SB33 microstrip electrodes listed in Table 6.2, one proposed solution for reducing the microstrip-electrode capacitance, and, thus, improve the signal-to-noise ratio, is to reduce the size of the microstrip electrode. As the electrode size decreases, a reduction in the capacitance occurs because fewer anode strips are adjacent to neighboring cathode strips. However, a reduction in ε_{th} occurs when the perimeter of the microstrip electrode does not encompass the width of the foil(s) (based on the simulated scenarios described in Section 5.3.3). Thus, a reduction in the size of the microstrip electrode requires a reduction of the foil and frame size.

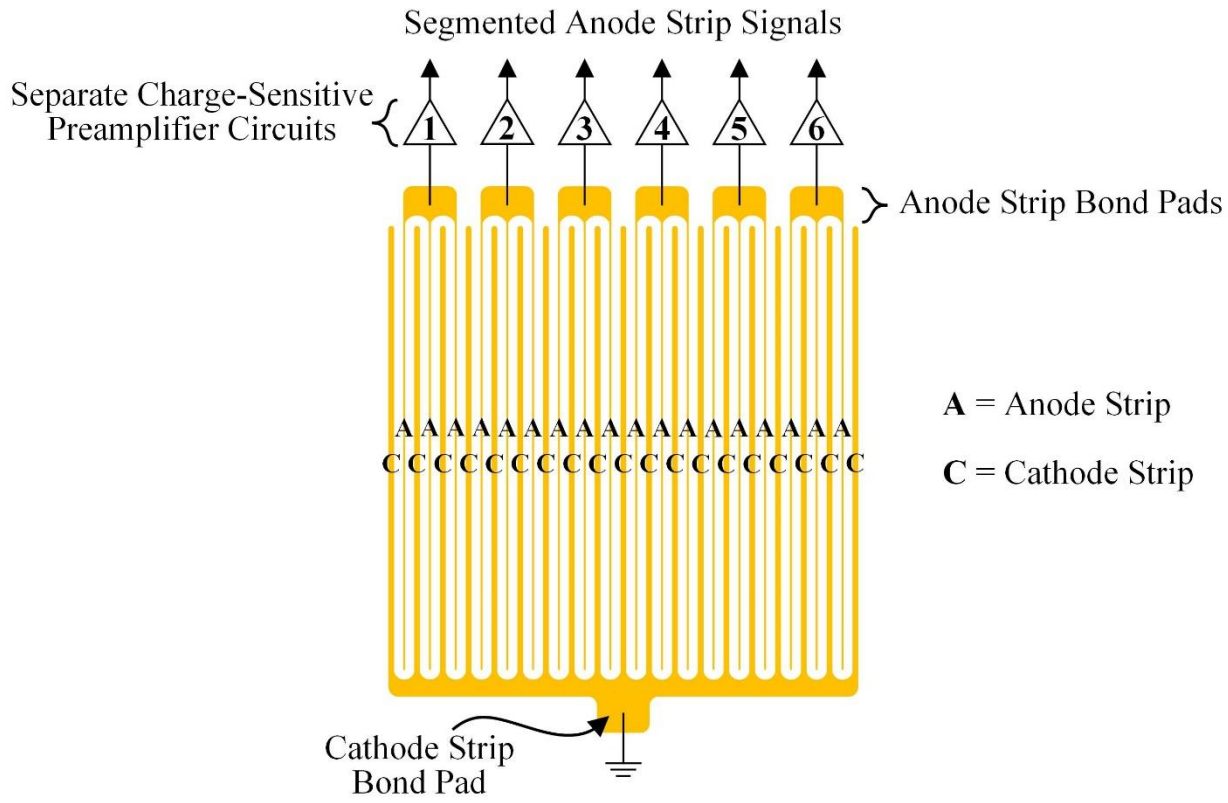

Figure 6.46. Example of a microstrip electrode with segmented anode-strip groups. The signal from each anode-strip group would be measured using a separate charge-sensitive preamplifier circuit.

An alternative solution for improving the signal-to-noise ratio is to segment the anode strips into groups instead of interconnecting all anode strips together (previously discussed in Section 5.1 and illustrated in Figure 5.4). A segmented anode-strip design requires that each segmented group of anode strips be connected to an individual charge-sensitive preamplifier circuit, as illustrated in Figure 6.46. The output signals from the charge-sensitive preamplifiers can then be summed together to allow the device to function strictly as a counter. Alternatively, the signal from each anode-strip group could, instead, be measured independently, providing spatial information regarding the radiation interactions occurring within the sensitive volume.

CHAPTER 7
CONCLUSIONS AND FUTURE WORK

The measure of greatness in a scientific idea is the extent to which it stimulates thought and opens up new lines of research.

Paul A.M. Dirac

Provided in this chapter are concluding remarks and contributions to the science (Section 7.1). The conclusions developed from studying the RVC foam and aluminum honeycomb as thin-film-coating substrates are described. A summary of the design and simulation efforts to study the theoretical capabilities of SFMNDs follows. The microstrip-electrode development is summarized before discussing the measured neutron-detection performance of the SFMNDs. Finally, the chapter concludes with a description of proposed future efforts to further develop thin-film-coated RVC foam and aluminum honeycomb as well as the SFMND as ^{3}He alternative technologies (Section 7.2).

7.1 Concluding Remarks and Contributions to the Science

Prior to the development of the SFMND, $^{10}B_4C$-coated RVC foam and aluminum honeycomb were investigated as multi-layered, thin-film-coated neutron converters. Initially, RVC foams were selected as a thin-film-coating substrate because the material contains a 3D-array of coating surfaces. The structure of RVC foams provides a large amount of surface area within a small form factor for applying thin-film-coatings. The ability for electrons to drift through the bulk of $^{10}B_4C$-coated RVC foams was studied using a parallel-plate ionization chamber with a Frisch grid, a measurement that had never previously been performed. The measurement results indicated that electrons cannot effectively drift through the bulk of 6.35-mm (0.25-in.) thick RVC foam samples with linear pore densities ranging from 5 to 100 PPI.

The results from studying the ability of electrons to traverse the bulk of RVC foam were verified by conducting neutron-sensitivity measurements using a single-anode wire, P-10 continuous-gas-flow proportional counter. The 6.35-mm thick, 4.1275-cm (1.625-in.) diameter 45 PPI RVC foam sample, with a measured $^{10}B_4C$ coating thickness of 1.29 ± 0.47 μm, had a measured ε_{th} of 3.40 ± 0.09%. The measured ε_{th} indicated that the substrate functioned essentially as a thin-film-coated substrate, in which neutron-induced pulses were formed from charge carriers liberated at or near the exterior surfaces of the coated substrate. Thus, the capabilities of RVC foam as a thin-film-coated neutron convertor were characterized, which had never previously been conducted.

$^{10}B_4C$-coated aluminum-honeycomb samples were investigated next because the substrate also contains a large amount of surface area within a small form factor for applying thin-film-coatings. Neutron-sensitivity testing was performed using a single-anode wire, P-10 continuous-gas-flow proportional counter. The 1.27-cm (0.5 in.) thick, 4.1275-cm (1.625 in.) diameter aluminum-honeycomb sample contained 0.15875 cm (0.0625 in.) hexagonal cells. The sample was coated with a $^{10}B_4C$ coating thickness of 4.68 ± 1.25 μm. The measured ε_{th} was 21.45 ± 0.26%, which is the highest measured ε_{th} to date for coated honeycomb media. The measured ε_{th} was slightly lower than the *MCNP6*-simulated value of approximately 24% for the same average $^{10}B_4C$ coating thickness. The deviation between measured and predicted ε_{th} values was suspected to be due to the broad distribution of $^{10}B_4C$ coating thicknesses measured about the sample.

MCNP6-simulations were performed to define the optimal coating thickness of $^{10}B_4C$-coated aluminum honeycomb for commercially-available honeycomb cell sizes of 0.635 cm (0.25 in.), 0.3175 cm (0.125 in.), and 0.15875 cm (0.0625 in.). The ε_{th} was simulated for each $^{10}B_4C$-coating thickness in order to determine the optimal coating thickness for each cell size. The simulated maximum ε_{th}, with a 0 keV LLD setting, was 38.92%, 60.32%, and 71.78%, which corresponded to optimal $^{10}B_4C$-coating thicknesses of 1.6 μm, 1.0 μm, and 0.8 μm for cell sizes of 0.635 cm (0.25 in.), 0.3175 cm (0.125 in.), and 0.15875 cm (0.0625 in.), respectively. The optimal coating thickness increased as the cell size increased due to a decrease in the number of neutron-absorber layers present within the sample.

The azimuthal and polar angular neutron-sensitivity distributions for each honeycomb cell size were then simulated using *MCNP6*. The simulated ε_{th} results of the azimuthal angular neutron-sensitivity distribution study had a 60° periodic behavior. The periodic behavior occurred due to

the change in the number of thin-film-coating layers that neutrons encountered as a function of the angle of neutron incidence. As the total number of thin-film-coating layers present within the sample increased, the azimuthal angular neutron-sensitivity distribution became more uniformly periodic. The results of the polar angular neutron-sensitivity distribution simulations showed a decrease in the probability of neutron absorption within the thin-film-coating layers as the thermal-neutron beam position changed from the 0° and 180° polar angle positions. At the 90° and 270° polar angle positions, the minimum polar angular neutron sensitivity occurred because neutrons were predominantly streaming through the substrate with a low probability of absorption within the vertical thin-film-coating layers lining the honeycomb cells. However, in an experimental setting where consecutive $^{10}B_4C$-coated samples are stacked on top of one another, neutron-streaming effects could be mitigated by rotating and off-setting each honeycomb sample relative to the neighboring samples.

The effects of P-10 gas pressure on the theoretical reaction-product pulse-height spectra and ε_{th} were also simulated using *MCNP6* for each honeycomb cell size. For all cell sizes, the reaction-product pulse-height spectral features shifted into higher energy bins as the P-10 gas pressure was increased. The up-shift in energy range of the spectral features occurred due to an increase in the amount of ionization within the honeycomb cells as the gas pressure was increased. Due to the up-shift in the energy range of the reaction-product pulse-height spectral features as the gas pressure was increased, the reduction in the ε_{th} became less pronounced as the LLD setting was increased.

The angular neutron-sensitivity and P-10 gas pressure simulation studies had never previously been conducted for $^{10}B_4C$-coated aluminum honeycomb. *MCNP6* simulations were also performed to define the optimal coating thickness, study the azimuthal and polar angular neutron-sensitivity, and study the effects of gas pressure on the neutron-detection performance for common thin-film-coating materials of ^{10}B, ^{10}BN, and ^{6}LiF. The *MCNP6* simulations to study the theoretical capabilities of aluminum honeycomb coated with ^{10}B, ^{10}BN, or ^{6}LiF had never previously been conducted. The measured and simulated neutron-sensitivity results indicated that thin-film-coated aluminum honeycomb has the potential to be a viable candidate as a neutron-conversion medium in a ^{3}He alternative technology. However, despite the measured and simulated neutron-sensitivity results of $^{10}B_4C$-coated aluminum honeycomb as a compact, high ε_{th} neutron-conversion medium, applying uniform thin-film coatings still presents a significant challenge. Additionally, like other

thin-film-coated neutron detectors, the strong dependency of ε_{th} on the LLD setting presents a challenge when developing a high ε_{th} with low gamma-ray sensitivity.

The limitations of the $^{10}B_4C$-coated RVC foam and aluminum honeycomb ultimately led to the development of the SFMND. The SFMND represents a new embodiment of a neutron detector for consideration as a potential ^{3}He alternative technology. SFMNDs were designed with the goal of developing a low-cost, robust, and compact ^{3}He alternative technology capable of achieving high ε_{th} with low gamma-ray sensitivity. The SFMND design was inspired by the success of the Li-foil MWPCs. However, SFMNDs were designed and developed as a more compact and robust device, relative to Li-foil MWPCs, by replacing the anode wires of a Li-foil MWPC with a microstrip electrode. Thus, the design of the SFMND combines the mechanical and electrical capabilities of microstrip electrodes with the high ε_{th} capability and low gamma-ray sensitivity of ^{6}Li foils. The replacement of the anode wires with a microstrip electrode eliminates the potential for failure from wire breakage while also reducing microphonic sensitivity.

The SFMNDs design features a microstrip electrode and a drift electrode oriented parallel to one another. Between the electrodes, ^{6}Li foils are oriented perpendicular to the surface of electrodes. Because SFMNDs do not rely on anode wires, more ^{6}Li foils can be positioned in closer proximity to one another, thereby allowing for smaller individual devices to be fabricated, relative to the Li-foil MWPCs. Depending on the thickness and quantity of ^{6}Li foils, SFMNDs are theoretically capable of ε_{th} exceeding 75% while still maintaining low gamma-ray sensitivity. Although cost analysis has not been conducted because SFMNDs are under prototypical investigation, the device cost is expected to be lower relative to ^{3}He proportional counters and other alternatives of similar size based on the materials and labor required to fabricate prototype devices. The compact size of the SFMND allows for the eventual development of modular devices, in which a broad range of instrument sizes and geometries could be configured by interconnecting the modules.

The theoretical neutron-detection capabilities of SFMNDs were studied by conducting *MCNP6* simulations. *MCNP6* simulations were performed to define the optimal ^{6}Li foil thickness as a function of foil quantity, study the effects of gas pressure on the theoretical ε_{th}, and study the effects of the foil width relative to the sensitive volume of the SFMND. The optimal ^{6}Li foil thickness was defined for foil quantities of one, five, ten, and twenty 96%-enriched ^{6}Li foils. Simulated maximum ε_{th} of one, five, ten, and twenty foil devices were 22.16%, 54.43%, 66.80%,

and 75.84%, respectively, which corresponded to ^{6}Li foil thicknesses of 137.5 µm, 85.0 µm, 60.0 µm, and 37.5 µm. Although the optimal simulated ε_{th} for each foil quantity corresponds to a specific foil thickness, simulated ε_{th} for 96%-enriched, 75-µm thick ^{6}Li foils were 18.36%, 54.08%, 65.43%, and 68.36% for foil quantities of one, five, ten, and twenty foils, respectively.

The effects of P-10 gas pressure on the theoretical neutron-detection performance of SFMNDs containing one and five 75-µm thick ^{6}Li foils were studied by simulating the reaction-product pulse-height spectra and ε_{th} as a function of P-10 gas pressure. As the gas pressure was increased, the energy range of the valley preceding the prominent spectral features increased. The increase in energy range of the valley allows for a higher-energy LLD setting to be used without a significant reduction of ε_{th}. However, the charge-carrier velocities are affected by gas pressure, and, therefore, the operating voltage must be adjusted to compensate for the change in gas pressure.

The effects of the foil width relative to the sensitive volume of the SFMND were studied in order to optimize the SFMND geometry. The changes in reaction-product pulse-height spectra and ε_{th} as a function of sensitive volume perimeter for one and five ^{6}Li foils were simulated using *MCNP6*. As the sensitive volume perimeter was increased, the energy range of the spectral features increased. The energy range of the spectral features increased due to an increase in the probability of reaction products depositing more energy within the sensitive volume. An increase in ε_{th} also occurred because more neutron-absorption events occurred within the sensitive volume as the sensitive volume perimeter was increased. The up-shift of the energy range of the spectral features and the increase of ε_{th} occurred in both the one- and five-foil scenarios as the sensitive volume perimeter was increased from 1.27 cm x 1.27 cm to 5.08 cm x 5.08 cm. However, for sensitive volume perimeters exceeding 5.08 cm x 5.08 cm, a majority of the reaction-product energy was already deposited within the sensitive volume. Thus, further increases of the sensitive volume perimeter did not yield a substantial increase in the energy range of the spectral features or $\varepsilon_{th.}$ The gas pressure and sensitive volume simulation studies had never previously been conducted given the novel nature of the SFMND.

Microstrip electrodes were fabricated using metal lift-off photolithography techniques. Three sizes of microstrip electrodes were fabricated, with dimensions of 1.27 cm x 1.27 cm (0.5 in. x 0.5 in.), 2.2225 cm x 2.2225 cm (0.875 in. x 0.875 in.), and 4.1275 cm x 4.1275 cm (1.625 in. x 1.625 in.). The microstrip electrodes were designed with 25-µm wide anode strips and 500-µm wide cathode strips with an anode-to-anode pitch of 1000 µm. Initially, microstrip electrodes

were fabricated using Si wafers that featured a 3-µm thick layer of SiO_2 on both substrate surfaces. A gradual reduction in signal amplitude was observed when conducting electrode characterization and neutron-sensitivity measurements using the Si microstrip electrode. The reduction in signal amplitude was suspected to be due to polarization of the SiO_2 layer, leading to a gradual reduction of the gas gain during the measurements. Therefore, an electrically-stable substrate material was required, which was identified as Schott Borofloat® 33 (SB33). The first-ever microstrip electrodes using SB33 glass as the substrate material were subsequently fabricated.

The Si and SB33 microstrip electrodes were separately characterized by first measuring the capacitance between the interconnected anode and cathode strips. As the size of the microstrip electrodes decreased from 4.1275 cm x 4.1275 cm (1.625 in. x 1.625 in.) to 1.27 cm x 1.27 cm (0.5 in. x 0.5 in.), the measured capacitance of the Si microstrip electrode decreased from approximately 755 pF to 140 pF, respectively. Similarly, the measured capacitance of the SB33 microstrip electrode decreased from 62 pF to 5 pF for electrode sizes of 4.1275 cm x 4.1275 cm (1.625 in. x 1.625 in.) to 1.27 cm x 1.27 cm (0.5 in. x 0.5 in.), respectively. The decrease in capacitance as a function of microstrip electrode size occurred because fewer anode and cathode strips were incorporated within the microstrip electrode as the electrode size decreases. Consequently, fewer anode strips were adjacent to neighboring cathode strips, resulting in a decrease in capacitance. The reduction in capacitance as a function of electrode size indicated that segmentation of anode strips may prove beneficial for further reducing the capacitance of the electrode. The decrease in microstrip-electrode capacitance between the Si and SB33 microstrip electrodes for the same electrode size was suspected to be attributed to the difference between the Si and SB33 dielectric constants and the substrate thicknesses.

The 4.1275 cm x 4.1275 cm (1.625 in. x 1.625 in.) microstrip electrodes were further characterized by defining the counting and gas multiplication curves and measuring the gain stability of each substrate type. The characterization measurements were conducted using a collimated ^{241}Am alpha-particle source. The Si and SB33 microstrip electrodes both exhibited stable counting curve plateaus. The percent change in count rate of the counting curve plateau was 2.5% per 100 V and 4.6% per 100 V for the Si and SB33 microstrip electrodes, respectively. Both electrodes also exhibited an increase in gas multiplication factor as the anode strip operating voltage was increased. The increase of gas multiplication factor with an increase of the anode strip operating voltage indicated that Townsend avalanching occurred, and thus the devices were

operating in proportional mode. Gain stability measurements were conducted over the duration of 24 hours. The relative gain of both microstrip electrodes increased during the first hour of measurements. The initial increase in relative gain was suspected to have occurred until an equilibrium operating condition was reached and was attributed to charging of the substrate surface after initially applying voltage. The SB33 microstrip electrode remained electrically stable for approximately 23 hours after the first hour of operation. However, following the first hour of operation, the relative gain of the Si microstrip electrode began to decrease, which was suspected to be caused by space charge polarization of the SiO_2 surface layer.

The drift electric field strength distribution between the microstrip and drift electrodes was measured using the SB33 microstrip electrode. A collimated ^{241}Am alpha-particle source was positioned at five discrete vertical positions between the microstrip and drift electrodes and the pulse-height spectrum was measured at each source position. The peak channel at each vertical source position was plotted as a function of vertical source position in order to study the drift electric field strength distribution. A non-uniform peak channel distribution, corresponding to a non-uniform pulse amplitude distribution, was measured between the electrodes and was suspected to be due to a non-uniform drift electric field strength distribution between the electrodes. Due to the non-uniform distribution of pulse amplitudes measured between the microstrip and drift electrodes, *COULOMB* simulations were conducted to study the theoretical electric field strength distribution within the device. The *COULOMB* simulation results showed a non-uniform electric field strength distribution. The simulated results had a similar shape to the distribution of measured pulse amplitudes. The similarity in shape between measured and simulated results suggested that a non-uniform electric field strength distribution may have been present within the device when conducting the experimental measurements, resulting in the measurement of a non-uniform distribution of pulse amplitudes. Electron attachment was also suspected to have occurred during the drift electric field profiling measurements due to the use of nylon and other high-outgassing materials that were used to construct the plastic support structure.

The first-ever SFMNDs containing one and five 96%-enriched, 75-μm thick ^{6}Li foils were fabricated using Si microstrip electrodes. Neutron-sensitivity testing was subsequently performed, first by measuring the reaction-product pulse-height spectra from a ^{252}Cf source. The reaction-product pulse-height spectra that were measured were the first spectra ever measured using SFMNDs. The spectral features gradually shifted into lower channels as consecutive one-hour

^{252}Cf measurements were performed, which was eventually attributed to the gain instability of the Si microstrip electrode. ε_{th} measurements were conducted using the one- and five-foil devices, yielding measured ε_{th} of 4.02 ± 0.04% and 14.58 ± 0.11%, respectively. *MCNP6* simulations were performed, yielding simulated ε_{th} of 19.06% and 54.91% for one- and five-foil devices, respectively. The best measured reaction-product pulse-height spectrum appeared similar to the simulated spectrum, however the measured spectral features were down-shifted relative to the simulated spectral features. The measured capacitance of the Si microstrip electrode (approximately 755 pF) was suspected to have yielded a poor signal-to-noise ratio, resulting in lower-energy neutron events blending with electronic noise. The measured capacitance and gain instability of the Si microstrip electrode were suspected to have caused the down-shift in measured spectral features and the difference between measured and simulated ε_{th}.

One- and five-foil SFMNDs using SB33 microstrip electrodes were fabricated using 96%-enriched, 75-μm thick ^{6}Li foils. Based on the drift electric field strength distribution measurements using the SB33 microstrip electrode, neutron-sensitivity measurements were conducted by positioning a thermal-neutron beam at eight discrete locations along the length of the foil between the microstrip and drift electrodes. The reaction-product pulse-height spectrum and ε_{th} were measured for each thermal-neutron beam position. For both one- and five-foil devices, the features of the reaction-product pulse-height spectra shifted into lower channels as the thermal-neutron beam was positioned further away from the microstrip electrode surface. A distribution of ε_{th} was measured and decreased as the thermal-neutron beam was positioned further away from the microstrip-electrode surface. Maximum ε_{th} of 12.58 ± 0.15% and 29.75 ± 0.26% were measured at the closest position to the microstrip electrode for the one- and five-foil SFMNDs, respectively. Simulated ε_{th} for the same measurement scenarios were 18.36% and 54.08% for the one- and five-foil SFMNDs, respectively. The deviation between measured and simulated ε_{th} was suspected to be attributed to the electric field strength distribution between the microstrip and drift electrodes, electron attachment, the microstrip-electrode capacitance, or any combination thereof. The *GRR* of the one- and five-foil SFMNDs was measured to be 6.46 x 10^{-5} ± 4.32 x 10^{-7} and 7.96 x 10^{-5} ± 4.65 x 10^{-7}, respectively, for a ^{137}Cs exposure rate of 50 mR hr^{-1}. The measured *GRR* were higher than those measured previously for Li-foil MWPCs and the deviation was suspected to be attributed to the wall-thickness of 0.9525 cm of the aluminum testing enclosure.

7.2 Future Work

The further development of RVC foam and aluminum honeycomb as thin-film-coated substrates requires addressing the challenges associated with each coating substrate. For RVC foams, in order for the material to be capable of achieving higher ε_{th}, two solutions are proposed. First, several consecutive layers of thin-film-coated RVC foams could be used, but would require collecting electrodes to be positioned on either side of each thin-film-coated RVC foam sample in a similar orientation as the foils relative to the anode wires in a Li-foil MWPC. The second proposed solution is to incorporate macrostructures, such as channels, into the bulk of the sample. The macrostructures would allow charge carriers to be able to drift out of the bulk of the sample. Once in the macrostructure, the charge carriers could then drift toward their respectively-charged electrodes, unimpeded by the RVC foam struts. The feasibility of aluminum honeycomb as a thin-film-coating substrate is dependent on the application of uniform thin-film coatings to all surfaces of the substrate. This concern is also applicable to the RVC foam, regardless of whether macrostructures are incorporated into the bulk of the sample.

Further investigation of the microstrip-electrode performance and optimization of the SFMND are required, based on the measured non-uniform distributions of pulse amplitudes and ε_{th} measured using the one- and five-foil SFMNDs with SB33 microstrip electrodes. The implementation of a Frisch grid between the microstrip electrode and the ^{6}Li foil(s) should produce a uniform drift electric field strength region where the foils are located and should be fabricated and tested. Initially, the Frisch grid could be fabricated in the form of a wire mesh, however, eventually the Frisch grid should be fabricated similar to a TGEM in order to adhere to the goal of fabricating a robust device. The effectiveness of the Frisch grid could be studied by conducting a similar measurement process as was used to study the drift electric field strength distribution using a collimated ^{241}Am alpha-particle source (Section 6.2.6).

Investigation of whether electron attachment is occurring within the SFMND should be conducted by performing the drift electric field profiling measurements (Section 6.2.6) using a continuous-gas-flow configuration of the testing enclosure. Alternatively, the testing fixtures should be built using low-outgassing materials such as PTFE and/or PEEK. The amount of electron attachment occurring for a given set of low-outgassing materials should be studied by conducting a similar measurement process as was used to study the drift electric field strength distribution

using a collimated ^{241}Am alpha-particle source (Section 6.2.6). Additionally, the O_2 and H_2O content should be monitored when conducting these measurements to determine the effectiveness of the low-outgassing materials.

The microstrip-electrode size should be adjusted to encompass the width of the foil(s), based on the simulation results for the effects of the width of the foil(s) relative to the sensitive volume size (Section 5.3.3). However, an increase in the size of the microstrip electrode would also increase the capacitance of the microstrip electrode, thus necessitating the implementation of segmented anode strips. Segmentation of the anode strips would require the development and application of a separate charge-sensitive preamplifier circuit to each group of segmented anode strips. Based on the number of interconnected anode strips, the capacitance can be reduced which should also improve the signal-to-noise ratio. An improvement in the signal-to-noise ratio should further increase the maximum measured ε_{th}.

The neutron-sensitivity measurements using the SFMNDs were conducted using P-10 gas due to the desirable charge-carrier velocities possible in the gas. However, over the course of using the device for a long duration of time without replacing the P-10 gas, the CH_4 component of the P-10 gas will gradually dissociate and potentially react with the ^{6}Li foil(s). Thus, gas type and pressure studies should be performed to identify suitable parameters for long-term counting capabilities. The gas type and pressure studies should be conducted following further optimization of the SFMNDs. As SFMNDs are further optimized, ε_{th} measurements should be conducted using one- and five-foil SFMNDs to track any neutron-detection performance changes. In order to improve the *GRR* capabilities of the SFMND, measurements should be performed using an aluminum testing enclosure with thinner walls. The use of an aluminum testing enclosure with thinner walls should reduce the amount of Compton scattering that can occur within the enclosure walls. Once one- and five-foil SFMNDs have been further optimized, ten- and twenty-foil SFMNDs should also be developed. Eventually, instruments should be investigated by developing an interconnectable modular design. The interconnected instruments could then be deployed in a variety of form factors such as handheld devices, backpacks, radiation portal monitors, etc.

LIST OF PERSONAL PUBLICATIONS (AUGUST 2018)

Refereed Journals

[1] **N.S. Edwards**, B.W. Montag, L.C. Henson, S.L. Bellinger, D.M. Nichols, M.A. Reichenberger, R.G. Fronk, D.S. McGregor, "Neutron Sensitivity of ^{6}Li-Based Suspended Foil Microstrip Neutron Detectors using Schott Borofloat® 33 Microstrip Electrodes," *Rad. Phys. Chem.*, vol. 147, pp. 70 – 76, 2018.

[2] **N.S. Edwards**, J.C. Conley, M.A. Reichenberger, K.A. Nelson, C.N. Tiner, N.J. Hinson, P.B. Ugorowoski, R.G. Fronk, D.S. McGregor, "Characterization of Reticulated Vitreous Carbon Foam using a Frisch-Grid Parallel-Plate Ionization Chamber," *Nucl. Instr. and Meth. A*, vol. 892, pp. 93 – 97, 2018.

[3] **N.S. Edwards**, K.A. Nelson, N.J. Hinson, C.N. Tiner, M.A. Reichenberger, R.G. Fronk, D.S. McGregor, "Neutron Sensitivity of $^{10}B_4C$-Coated Aluminum Honeycomb using a Single-Anode Wire, P-10 Continuous-Gas-Flow Proportional Counter," *Nucl. Instr. and Meth. A*, vol. 898, pp. 85 – 89, 2018.

[4] **N.S. Edwards**, B.W. Montag, L.C. Henson, S.L. Bellinger, D.M. Nichols, M.A. Reichenberger, R.G. Fronk, D.S. McGregor, "Fabrication and Characterization of Schott Borofloat® 33 Microstrip Electrodes," *Rad. Phys. Chem., Submitted*.

[5] B.W. Montag, S.L. Bellinger, **N.S. Edwards**, J. Lage, K.A. Nelson, L.C. Henson, D.S. McGregor, "Recent Progress in the Commercialization of the Li Foil Multi-Wire Proportional Counter Neutron Detectors," *Rad. Phys. Chem., Submitted*.

[6] P. Ghosh, W. Fu, M.J. Harrison, P.K. Doyle, **N.S. Edwards**, J.A. Roberts, D.S. McGregor, "A High-Efficiency, Low-Ĉerenkov Micro-Layered Fast-Neutron Detector for the TREAT Hodoscope," *Nucl. Instr. and Meth. A*, vol. 904, pp. 100 – 106, 2018.

[7] M.A. Reichenberger, R.G. Fronk, J.K. Shultis, J.A. Roberts, **N.S. Edwards**, S.R. Stevenson, C.N. Tiner, D.S. McGregor, "Monte Carlo Simulation of Random, Porous (Foam) Structures for Neutron Detection," *Rad. Phys. Chem.*, vol. 130, pp. 186 – 195, 2017.

[8] B.W. Montag, P.B. Ugorowski, K.A. Nelson, **N.S. Edwards**, D.S. McGregor, "Device Fabrication, Characterization, and Thermal Neutron Detection Response of LiZnP and LiZnAs Semiconductor Devices," *Nucl. Instr. and Meth. A*, vol. 836, pp. 30 – 36, 2016.

[9] B.W. Montag, M.A. Reichenberger, **N.S. Edwards**, P.B. Ugorowski, M. Sunder, J. Weeks, D.S. McGregor, "Static Sublimation Purification Process and Characterization of LiZnAs Semiconductor Material," *J. Cryst. Growth*, vol. 438, pp. 99 – 103, 2016.

[10] B.W. Montag, M.A. Reichenberger, **N. Edwards**, P.B. Ugorowski, M. Sunder, J. Weeks, D.S. McGregor, "Static Sublimation Purification Process and Characterization of LiZnP Semiconductor Material," *J. Cryst. Growth,* vol. 419, pp. 133 – 137, 2015.

[11] K.A. Nelson, **N.S. Edwards**, M.R. Kusner, M.R. Mayhugh, B.W. Montag, A.J. Schmidt, C.D. Wayant, D.S. McGregor, "A Modular Large-Area Lithium Foil Multi-Wire Proportional Counter Neutron Detector," *Rad. Phys. Chem.*, vol. 116, pp. 165 – 169, 2015.

[12] K.A. Nelson, **N.S. Edwards**, N.J. Hinson, C.D. Wayant, D.S. McGregor, "A Suspended Boron Foil Multi-Wire Proportional Counter Neutron Detector," *Nucl. Instr. and Meth. A*, vol. 767, pp. 14 – 18, 2014.

[13] K.A. Nelson, S.L. Bellinger, **N.S. Edwards**, B.W. Montag, A.J. Schmidt, C. Wayant, D.S. McGregor, "Thermal Neutron Response and Theoretical Comparison of LiF Coated Aluminized Mylar," *Nucl. Instr. and Meth. A*, vol. 762, pp. 130 – 134, 2014.

[14] K.A. Nelson, **N. Edwards**, M.J. Harrison, A. Kargar, W.J. McNeil, R.A. Rojeski, D.S. McGregor, "Investigation of CdZnTe and LiNbO3 as Electro-Optic Neutron Detectors," *Nucl. Instr. and Meth. A*, vol. 620, pp. 363 – 367, 2010.

Conference Proceedings

[1] **N.S. Edwards**, B.W. Montag, L.C. Henson, S.L. Bellinger, R.G. Fronk, M.A. Reichenberger, D.S. McGregor, "Lithium Foil Gas-Filled Neutron Detector using Microstrip Electrodes," *Conf. Proc. IEEE Nucl. Sci. Symp.*, Strasbourg, France, Oct. 29 – Nov. 5, 2016, paper N28-30, 3 pages.

[2] **N.S. Edwards**, K.A. Nelson, C.N. Tiner, N.J. Hinson, P.B. Ugorowski, R.G. Fronk, M.A. Reichenberger, D.S. McGregor, "Charge Propagation Through- and Neutron Sensitivity of- Reticulated Vitreous Carbon Foam," *Conf. Proc. IEEE Nucl. Sci. Symp.*, San Diego, CA, Oct. 31 – Nov. 7, 2015, paper N5A3-5, 4 pages.

[3] **N.S. Edwards**, K.A. Nelson, N.J. Hinson, R.G. Fronk, S. Steiner, A. Visentin, R. Nelson, J. Griffin, D.S. McGregor, "Current Status of Aerogel as a Neutron Converting Material," *Conf. Proc. IEEE Nucl. Sci. Symp.*, San Diego, CA, Oct. 31 – Nov. 7, 2015, paper N5A3-4, 4 pages.

[4] **N.S. Edwards**, D.S. McGregor, "Charge Collection Efficiency Mapping of a Frisch Collared BiI_3 Device," *Conf. Proc. IEEE Nucl. Sci. Symp.*, Seattle, WA, Nov. 8 – 15, 2014, paper N11-5, 4 pages.

[5] B.W. Montag, M.A. Reichenberger, **N.S. Edwards**, M. Sunder, P.B. Ugorowski, J. Weeks, D.S. McGregor, "Purification and Crystallinity Results from LiZnAs and LiZnP Semiconductor Materials," *Conf. Proc. IEEE Nucl. Sci. Symp.*, Seattle, WA, Nov. 8 – 15, 2014, paper R07-5, 4 pages.

[6] M.A. Reichenberger, R.G. Fronk, J.K. Shultis, S.R. Stevenson, **N.S. Edwards**, K.A. Nelson, D.S. McGregor, "Monte Carlo Simulation of Energy Deposition by Neutron Reaction Products in Lithiated Foam Using Dynamic Path Generation," *Conf. Proc. IEEE Nucl. Sci. Symp.*, Seattle, WA, Nov. 8 – 15, 2014, paper N04-8, 3 pages.

Patents

[1] D.S. McGregor, **N.S. Edwards**, B.W. Montag, "Micropattern Electrode Neutron Detector," Utility Patent Filed Oct. 27, 2016.

REFERENCES

[1] E. Rutherford, and H. Geiger, "An Electrical Method of Counting the Number of Alpha-Particles from Radio-Active Substances," *Proc. R. Soc. London, A,* vol. 81, no. 546, pp. 141-161, 1908.

[2] D. H. Wilkinson, *Ionization Chambers and Counters*, London: University Press, 1950.

[3] F. N. Flakus, "Detecting and Measuring Ionizing Radiation - a Short History," *IAEA Bulletin,* vol. 23, no. 4, pp. 31-36, 1981.

[4] E. Rutherford, "Bakerian Lecture: Nuclear Constitution of Atoms," *Proc. R. Soc. London, A,* vol. 97, no. 686, pp. 374-400, 1920.

[5] J. Chadwick, "The Existence of a Neutron," *Proc. R. Soc. London, A,* vol. 136, no. 830, pp. 692-708, 1932.

[6] E. Amaldi, O. D'Agostino, E. Fermi *et al.*, "Artificial Radioactivity Produced by Neutron Bombardment - II," *Proc. R. Soc. London, A,* vol. 149, no. 868, pp. 522-558, 1935.

[7] O. R. Frisch, H. von Halban, and J. Koch, "Capture of Slow Neutrons in Light Elements," *Nature,* vol. 140, no. 3551, pp. 895, 1937.

[8] F. N. D. Kurie, "Collisions of Neutrons with Protons," *Phys. Rev.,* vol. 43, no. 8, pp. 672-673, 1933.

[9] W. D. Allen, *Neutron Detection*, New York, NY: Philosophical Library, Inc., 1960.

[10] R. Batchelor, J. S. Eppstein, B. H. Flowers *et al.*, "Slow-Neutron Capture in Helium," *Nature,* vol. 163, pp. 211-212, 1949.

[11] N. Veall, "Small Boron Chambers for Slow Neutron Measurements," *J. Sci. Instrum.,* vol. 24, no. 12, pp. 331, 1947.

[12] E. Segrè, and C. Wiegand, "Boron Trifluoride Neutron Detector for Low Neutron Intensities," *Rev. Sci. Instrum.,* vol. 18, no. 2, pp. 86-89, 1947.

[13] R. Batchelor, "Neutron Energy Measurements with a Helium 3 Filled Proportional Counter," *Proc. Phys. Soc. A,* vol. 65, no. 8, pp. 674, 1952.

[14] R. Batchelor, R. Aves, and T. H. R. Skyrme, "Helium-3 Filled Proportional Counter for Neutron Spectroscopy," *Rev. Sci. Instrum.,* vol. 26, no. 11, pp. 1037-1047, 1955.

[15] K. A. Yamakawa, "A Suggested Slow Neutron Crystal Counter," *Phys. Rev.,* vol. 75, no. 11, pp. 1774-1774, 1949.

[16] R. V. Babcock, R. E. Davis, S. L. Ruby *et al.*, "Coated Semiconductor Is Tiny Neutron Detector," *Nucleonics (U.S.),* vol. 17, no. 4, pp. 116-122, 1959.

[17] R. Stedman, "Scintillator for Thermal Neutrons Using Li^6F and ZnS (Ag)," *Rev. Sci. Instrum.,* vol. 31, no. 10, pp. 1156-1156, 1960.

[18] N. Tsoulfanidis, *Measurement and Detection of Radiation*, 2nd ed., Washington, DC: Taylor & Francis, 1995.

[19] G. F. Knoll, *Radiation Detection and Measurement*, 4th ed., Hoboken, NJ: John Wiley & Sons, Inc., 2010.

[20] R. T. Kouzes, A. T. Lintereur, and E. R. Siciliano, "Progress in Alternative Neutron Detection to Address the Helium-3 Shortage," *Nucl. Instrum. and Meth. A,* vol. 784, pp. 172-175, 2015.

[21] D. S. McGregor, and J. K. Shultis, *Radiation Detection and Measurement: Concepts, Methods, and Devices*: unpublished, expected 2018.

[22] LND Inc., "Neutron Detectors," http://www.lndinc.com/product-category/neutron-detectors/, [February 2, 2018].

[23] GE Energy, "Radiation Detectors and Measurement Products," https://www.gemeasurement.com/radiation-measurement, [February 2, 2018].

[24] Saint-Gobain Crystals, "Helium-3 Proportional Counters," https://www.crystals.saint-gobain.com/products/helium-proportional, [February 2, 2018].

[25] J. L. Lacy, A. Athanasiades, C. S. Martin *et al.*, "Boron-Coated Straw Detectors for Backpack Monitors," *IEEE Trans. Nucl. Sci.,* vol. 60, no. 2, pp. 1111-1117, 2013.

[26] K. A. Nelson, N. S. Edwards, M. R. Kusner *et al.*, "A Modular Large-Area Lithium Foil Multi-Wire Proportional Counter Neutron Detector," *Radiat. Phys. Chem.,* vol. 116, pp. 165-169, 2015.

[27] D. S. McGregor, S. L. Bellinger, R. G. Fronk *et al.*, "Development of Compact High Efficiency Microstructured Semiconductor Neutron Detectors," *Radiat. Phys. Chem.,* vol. 116, pp. 32-37, 2015.

[28] M. A. Reichenberger, D. M. Nichols, S. R. Stevenson *et al.*, "Fabrication and Testing of a 4-Node Micro-Pocket Fission Detector Array for the Kansas State University Triga Mk. II Research Nuclear Reactor," *Nucl. Instrum. and Meth. A,* vol. 862, pp. 8-17, 2017.

[29] C. M. Whitney, L. Soundara-Pandian, E. B. Johnson *et al.*, "Gamma–Neutron Imaging System Utilizing Pulse Shape Discrimination with CLYC," *Nucl. Instrum. and Meth. A,* vol. 784, pp. 346-351, 2015.

[30] K. E. Mesick, D. D. S. Coupland, and L. C. Stonehill, “Pulse-Shape Discrimination and Energy Quenching of Alpha Particles in $Cs_2LiLaBr_6:Ce^{3+}$,” *Nucl. Instrum. and Meth. A*, vol. 841, pp. 139-143, 2017.

[31] LND Inc., "He-3 Detectors," http://www.lndinc.com/product-category/neutron-detectors/he3-detectors/, [February 2, 2018].

[32] Saint-Gobain Crystals, "Gas-Filled Radiation Detectors Helium-3 Proportional Counters," https://www.crystals.saint-gobain.com/sites/imdf.crystals.com/files/documents/proportional-counters-data-sheet_69732.pdf, [February 2, 2018].

[33] GE Energy, "Helium-3 Gas Filled Proportional Detectors," https://www.gemeasurement.com/radiation-measurement/homeland-security-detectors/helium-3-gas-filled-proportional-detectors, [February 2, 2018].

[34] GE Energy, "Reuter Stokes Helium-3 Filled Proportional Counter - RS-P4-0203-201," https://www.gemeasurement.com/sites/gemc.dev/files/reuter_stokes_helium_3_detector_time_of_flight_spectroscopy_and_small_angle_scattering_english.pdf, [February 2, 2018].

[35] GE Energy, "Reuter Stokes Helium-3 Proportional Counter RS-P4-0406-212," https://www.gemeasurement.com/sites/gemc.dev/files/reuter_stokes_helium_3_detector_time-of-flight_spectroscopy_english.pdf, [February 2, 2018].

[36] GE Energy, "Reuter Stokes Helium-3 Filled Proportional Counter - RS-P4-1614-204," https://www.gemeasurement.com/sites/gemc.dev/files/reuter_stokes_helium_3_detector_safeguards_and_spectroscopy_english.pdf, [February 2, 2018].

[37] GE Energy, "Reuter Stokes ^{3}He Neutron Detectors for Homeland Security Radiation Portal Monitors," https://www.gemeasurement.com/sites/gemc.dev/files/reuter_stokes_he-3_neutron_detectors_for_homeland_security_radiation_portal_monitors_english_0.pdf, [February 2, 2018].

[38] International Atomic Energy Agency (IAEA), *Database of Prompt Gamma Rays from Slow Neutron Capture for Elemental Analysis*, Vienna: International Atomic Energy Agency (IAEA), 2007.

[39] N. D'Olympia, P. Chowdhury, C. J. Lister *et al.*, “Pulse-Shape Analysis of CLYC for Thermal Neutrons, Fast Neutrons, and Gamma-Rays,” *Nucl. Instrum. and Meth. A*, vol. 714, pp. 121-127, 2013.

[40] W. M. Higgins, J. Glodo, U. Shirwadkar *et al.*, “Bridgman Growth of Cs_2LiYCl_6:Ce and ^{6}Li-Enriched $Cs_2{}^6LiYCl_6$:Ce Crystals for High Resolution Gamma Ray and Neutron Spectrometers,” *J. Cryst. Growth*, vol. 312, no. 8, pp. 1216-1220, 2010.

[41] J. Glodo, R. Hawrami, and K. S. Shah, “Development of Cs_2LiYCl_6 Scintillator,” *J. Cryst. Growth*, vol. 379, pp. 73-78, 2013.

[42] D. S. McGregor, S. L. Bellinger, and J. K. Shultis, “Present Status of Microstructured Semiconductor Neutron Detectors,” *J. Cryst. Growth,* vol. 379, pp. 99-110, 2013.

[43] R. G. Fronk, “Dual-Side Etched Microstructured Semiconductor Neutron Detectors,” Doctorate, Mechanical and Nuclear Engineering, Kansas State University, 2017.

[44] J. L. Lacy, A. Athanasiades, L. Sun *et al.*, “Boron-Coated Straws as a Replacement for ^{3}He-Based Neutron Detectors,” *Nucl. Instrum. and Meth. A,* vol. 652, no. 1, pp. 359-363, 2011.

[45] J. L. Lacy, A. Athanasiades, C. S. Martin *et al.*, “The Evolution of Neutron Straw Detector Applications in Homeland Security,” *IEEE Trans. Nucl. Sci.,* vol. 60, no. 2, pp. 1140-1146, 2013.

[46] K. A. Nelson, “An Investigation of Aerogels, Foams, and Foils for Multi-Wire Proportional Counter Neutron Detectors,” Doctorate, Mechanical and Nuclear Engineering, Kansas State University, 2013.

[47] K. A. Nelson, N. J. Hinson, M. R. Kusner *et al.*, "Results and Potential Applications of Handheld, Midsized, and Large-Area Low-Cost Li Foil MWPCs," *2014 IEEE Nuclear Science Symposium and Medical Imaging Conference (NSS/MIC)*, paper N25-33, 5 pages, Nov. 8 - 15, 2014.

[48] K. A. Nelson, M. R. Kusner, B. W. Montag *et al.*, “Characterization of a Mid-Sized Li Foil Multi-Wire Proportional Counter Neutron Detector,” *Nucl. Instrum. and Meth. A,* vol. 762, pp. 119-124, 2014.

[49] W. N. Cottingham, and D. A. Greenwood, *An Introduction to Nuclear Physics*, 2nd ed., Cambridge: Cambridge University Press, 2001.

[50] Particle Data Group, J. Beringer, J. F. Arguin *et al.*, “Review of Particle Physics,” *Phys. Rev. D,* vol. 86, no. 010001, pp. 1 - 1526, 2012.

[51] J. K. Shultis, and R. E. Faw, *Fundamentals of Nuclear Science and Engineering*, Boca Raton, FL: CRC Press, 2002.

[52] J. R. Lamarsh, *Introduction to Nuclear Reactor Theory,* LaGrange Park, IL: American Nuclear Society, Inc., 2002.

[53] Oak Ridge National Laboratory (ORNL), "Neutron Sciences | Spallation Neutron Source," https://neutrons.ornl.gov/sns, [November 14, 2017].

[54] J. K. Shultis, and R. E. Faw, *Radiation Shielding*, La Grange Park, IL: American Nuclear Society, Inc., 2000.

[55] E. E. Lewis, *Fundamentals of Nuclear Reactor Physics*, Burlington, MA: Academic Press, 2008.

[56] J. L. Duderstadt, and L. J. Hamilton, *Nuclear Reactor Analysis*, Canada: John Wiley & Sons, 1976.

[57] W. J. Price, *Nuclear Radiation Detection*, New York: McGraw-Hill Book Company, Inc., 1958.

[58] I. Kaplan, *Nuclear Physics*, 2nd ed., Reading, Massachusetts: Addison-Wesley Publishing Company, Inc., 1962.

[59] D. S. McGregor, M. D. Hammig, Y. H. Yang *et al.*, "Design Considerations for Thin Film Coated Semiconductor Thermal Neutron Detectors—I: Basics Regarding Alpha Particle Emitting Neutron Reactive Films," *Nucl. Instrum. and Meth. A*, vol. 500, no. 1–3, pp. 272-308, 2003.

[60] National Nuclear Data Center, "Evaluated Nuclear Data File (ENDF) Retrieval & Plotting," https://www.nndc.bnl.gov/sigma/, [November 14, 2017].

[61] P. Kandlakunta, L. R. Cao, and P. Mulligan, "Measurement of Internal Conversion Electrons from Gd Neutron Capture," *Nucl. Instrum. and Meth. A*, vol. 705, no. Supplement C, pp. 36-41, 2013.

[62] S. Masaoka, T. Nakamura, H. Yamagishi *et al.*, "Optimization of a Micro-Strip Gas Chamber as a Two-Dimensional Neutron Detector Using Gadolinium Converter," *Nucl. Instrum. and Meth. A*, vol. 513, no. 3, pp. 538-549, 2003.

[63] A. Oed, "Detectors for Thermal Neutrons," *Nucl. Instrum. and Meth. A*, vol. 525, no. 1–2, pp. 62-68, 2004.

[64] M. S. Carturan, T. Marchi, E. Fanchini *et al.*, "Scintillator and Solid-State Neutron Detectors and Their Applications," *Eur. Phys. J. Plus*, vol. 129, no. 10, pp. 1-11, 2014.

[65] E. Cazalas, C. Trivelpiece, and I. Jovanovic, "Spatial Resolution and Efficiency of Microchannel Plate Detectors with Neutron Converter Films," *Nucl. Instrum. and Meth. A*, vol. 767, pp. 421-425, 2014.

[66] V. Dangendorf, A. Demian, H. Friedrich *et al.*, "Thermal Neutron Imaging Detectors Combining Novel Composite Foil Convertors and Gaseous Electron Multipiers," *Nucl. Instrum. and Meth. A*, vol. 350, no. 3, pp. 503-510, 1994.

[67] A. G. Vradii, M. I. Krapivin, L. V. Maslova *et al.*, "Possibilities of Recording Thermal Neutrons with Cadmium Telluride Detectors," *Soviet Atomic Energy*, vol. 42, no. 1, pp. 64-66, 1977.

[68] D. S. McGregor, J. T. Lindsay, and R. W. Olsen, "Thermal Neutron Detection with $Cadmium_{1-x}$ $Zinc_x$ Telluride Semiconductor Detectors," *Nucl. Instrum. and Meth. A*, vol. 381, no. 2-3, pp. 498-501, 1996.

[69] D. S. McGregor, R. T. Klann, H. K. Gersch *et al.*, “Thin-Film-Coated Bulk GaAs Detectors for Thermal and Fast Neutron Measurements,” *Nucl. Instrum. and Meth. A*, vol. 466, no. 1, pp. 126-141, 2001.

[70] S. Uno, T. Uchida, M. Sekimoto *et al.*, “Two-Dimensional Neutron Detector with GEM and Its Applications,” *Physics Procedia*, vol. 26, pp. 142-152, 2012.

[71] D. S. McGregor, and J. Kenneth Shultis, “Reporting Detection Efficiency for Semiconductor Neutron Detectors: A Need for a Standard,” *Nucl. Instrum. and Meth. A*, vol. 632, no. 1, pp. 167-174, 2011.

[72] Knolls Atomic Power Laboratory, *Chart of the Nuclides and Isotopes*, 16th ed.: Lockheed Martin Distribution Services, 2002.

[73] Honeywell Performance Materials and Technologies, "Honeywell Boron Trifluoride," 2006.

[74] Ceradyne Inc., "3M ^{10}B Enriched Boron," http://multimedia.3m.com/mws/media/958420O/3m-10b-enriched-boron.pdf, [November 20, 2017].

[75] American Elements, "Boron-10 Carbide Isotope," https://www.americanelements.com/boron-10-carbide-isotope-200443-95-4, [November 20, 2017].

[76] Sigma-Aldrich Inc., "Boron-^{10}B," https://www.sigmaaldrich.com/catalog/product/aldrich/601551?lang=en&region=US, [November 20, 2017].

[77] S. L. Bellinger, “Advanced Microstructured Semiconductor Neutron Detectors: Design, Fabrication, and Performance,” Doctorate, Mechanical and Nuclear Engineering, Kansas State University, 2011.

[78] Sigma-Aldrich Inc., "Lithium-^{6}Li," https://www.sigmaaldrich.com/catalog/product/aldrich/340421?lang=en&region=US, [November 20, 2017].

[79] Albemarle, "Lithium Metal," http://www.albemarle-lithium.com/products/battery-products/lithium-metal/, [November 20, 2017].

[80] E. Brubaker, D. Dibble, W. Mengesha *et al.*, *Thermal Neutron Detection Using Alkali Halide Scintillators with Li-6 and Pulse Shape Discrimination*, SAND2013-8329, Sandia National Laboratories, 2013.

[81] Hamamatsu Photonics K.K., *Photomultiplier Tubes - Basics and Applications*: Hamamatsu Photonics K.K. - Electron Tube Division, 2007.

[82] M. L. Ruch, C. B. Sivels, S. A. Czyz *et al.*, "Comparison between Silicon Photomultipliers and Photomultiplier Tubes for Pulse Shape Discrimination with Stilbene," *2014 IEEE Nuclear Science Symposium and Medical Imaging Conference (NSS/MIC)*, paper N25-11, 3 pages, Nov. 8 - 15, 2014.

[83] S. Piatek, "A Technical Guide to Silicon Photomultipliers (SiPM)," https://www.hamamatsu.com/us/en/community/optical_sensors/articles/technical_guide_to_silicon_photomultipliers_sipm/index.html#, [March 26, 2018].

[84] J. R. Cameron, N. Suntharalingam, and G. N. Kenney, *Thermoluminescent Dosimetry*, Madison, WI: The University of Wisconsin Press, 1968.

[85] B. W. Montag, "Lithiated Ternary Compounds for Neutron Detectors: Material Production and Device Characterization of Lithium Zinc Phosphide and Lithium Zinc Arsenide," Doctorate, Mechanical and Nuclear Engineering, Kansas State University, 2015.

[86] D. S. McGregor, and J. Kenneth Shultis, "Spectral Identification of Thin-Film-Coated and Solid-Form Semiconductor Neutron Detectors," *Nucl. Instrum. and Meth. A*, vol. 517, no. 1–3, pp. 180-188, 2004.

[87] B. B. Rossi, and H. H. Staub, *Ionization Chambers and Counters*, New York: McGraw-Hill Book Company, Inc., 1949.

[88] C. W. Peters, A. L. Snyder, and A. S. Gallia, "BF_3 Counters for Use in Field Instrumentation," *IEEE Trans. Nucl. Sci.*, vol. 13, no. 1, pp. 636-642, 1966.

[89] D. S. McGregor, W. J. McNeil, S. L. Bellinger *et al.*, "Microstructured Semiconductor Neutron Detectors," *Nucl. Instrum. and Meth. A*, vol. 608, no. 1, pp. 125-131, 2009.

[90] T. W. Crane, and M. P. Baker, "Neutron Detectors," in *Passive Nondestructive Assay of Nuclear Materials*, by D. Reilly, N. Ensslin and H. S. Jr., Nuclear Regulatory Commision, NUREG/CR-5550, 1991, pp. 379 - 404.

[91] L. Wilson, A. Duraj, and M. Kusner, "Neutron Detection for Portal Monitors Performance Evaluation," 2011.

[92] J. D. Jackson, *Classical Electrodynamics*, New York, NY: John Wiley & Sons, Inc., 1962.

[93] P. Rice-Evans, *Spark, Streamer, Proportional and Drift Chambers*, London: The Richelieu Press Limited, 1974.

[94] W. R. Smythe, *Static and Dynamic Electricity*, 3rd ed., Bristol: Taylor & Francis, 1989.

[95] R. D. Evans, *The Atomic Nucleus*, New York: McGraw-Hill Book Company, Inc., 1955.

[96] J. F. Ziegler, and J. P. Biersack, SRIM-2013 Code, 2013, http://www.srim.org/.

[97] L. G. Christophorou, *Atomic and Molecular Radiation Physics*: John Wiley & Sons Canada, Limited, 1971.

[98] F. Sauli, *Gaseous Radiation Detectors: Fundamentals and Applications*: Cambridge University Press, 2014.

[99] T. E. Bortner, G. S. Hurst, and W. G. Stone, "Drift Velocities of Electrons in Some Commonly Used Counting Gases," *Rev. Sci. Instrum.*, vol. 28, no. 2, pp. 103-108, 1957.

[100] L. G. H. Huxley, and R. W. Crompton, *The Diffusion and Drift of Electrons in Gases*, New York: Wiley, 1974.

[101] L. B. Loeb, *Basic Processes of Gaseous Electronics*, Berkeley and Los Angeles: University of California Press, 1955.

[102] S. A. Korff, *Electron and Nuclear Counters - Theory and Use*, 2nd ed., New York: D. Van Nostrand Company, Inc., 1955.

[103] O. R. Frisch, *Isotope Analysis of Uranium Samples by Means of Their Alpha-Ray Groups*, British Atomic Energy Report BR-49, 1942.

[104] G. Charpak, R. Bouclier, T. Bressani *et al.*, "The Use of Multiwire Proportional Counters to Select and Localize Charged Particles," *Nucl. Instrum. and Meth.*, vol. 62, no. 3, pp. 262-268, 1968.

[105] A. Oed, "Position-Sensitive Detector with Microstrip Anode for Electron Multiplication with Gases," *Nucl. Instrum. and Meth. A*, vol. 263, no. 2, pp. 351-359, 1988.

[106] W. G. Gong, H. Wieman, J. W. Harris *et al.*, "Microstrip Gas Chambers on Glass and Ceramic Substrates," *IEEE Trans. Nucl. Sci.*, vol. 41, no. 4, pp. 890-897, 1994.

[107] A. Oed, "Properties of Micro-Strip Gas Chambers (MSGC) and Recent Developments," *Nucl. Instrum. and Meth. A*, vol. 367, no. 1–3, pp. 34-40, 1995.

[108] B. Gebauer, C. Schulz, T. Wilpert *et al.*, "Large-Area Low-Pressure Microstrip Gas Chambers for Thermal Neutron Imaging," *Nucl. Instrum. and Meth. A*, vol. 409, no. 1–3, pp. 56-62, 1998.

[109] N. Vellettaz, J. E. Assaf, and A. Oed, "Two-Dimensional Gaseous Microstrip Detector for Thermal Neutrons," *Nucl. Instrum. and Meth. A*, vol. 392, no. 1–3, pp. 73-79, 1997.

[110] N. S. Edwards, K. A. Nelson, N. J. Hinson *et al.*, "Neutron Sensitivity Of $^{10}B_4C$-Coated Aluminum Honeycomb Using a Single-Anode Wire, P-10 Continuous-Gas-Flow Proportional Counter," *Nucl. Instrum. and Meth. A*, vol. 898, pp. 85-89, 2018.

[111] Z. Wang, and C. L. Morris, "Multi-Layer Boron Thin-Film Detectors for Neutrons," *Nucl. Instrum. and Meth. A*, vol. 652, no. 1, pp. 323-325, 2011.

[112] J. Birch, J. C. Buffet, J. Correa *et al.*, "$^{10}B_4C$ Multi-Grid as an Alternative to ^3He for Large Area Neutron Detectors," *IEEE Trans. Nucl. Sci.*, vol. 60, no. 2, pp. 871-878, 2013.

[113] Y. Yang, C. Li, C. Chen *et al.*, "Research of Boron Lined Honey-Comb Neutron Detector Realized with Atomic Layer Deposition," *2013 IEEE Nuclear Science Symposium and Medical Imaging Conference (2013 NSS/MIC)*, paper N7-1, 3 pages, Oct. 27 - Nov. 2, 2013.

[114] Z. Fang, Y. Yang, Y. Li *et al.*, "Research on a Neutron Detector with a Boron-Lined Honeycomb Neutron Converter," *IEEE Trans. Nucl. Sci.*, vol. 64, no. 4, pp. 1048-1055, 2017.

[115] W. M. Hayes, and D. R. Lide, *CRC Handbook of Chemistry and Physics: A Ready-Reference Book of Chemical and Physical Data*, Boca Raton, FL: CRC Press, 2007.

[116] C. Höglund, K. Zeitelhack, P. Kudejova *et al.*, "Stability of $^{10}B_4C$ Thin Films under Neutron Radiation," *Radiat. Phys. Chem.*, vol. 113, pp. 14-19, 2015.

[117] C. Höglund, J. Birch, K. Andersen *et al.*, "B_4C Thin Films for Neutron Detection," *J. Appl. Phys.*, vol. 111, no. 10, pp. 104908, 2012.

[118] F. Piscitelli, "Novel Boron-10-Based Detectors for Neutron Scattering Science," *Eur. Phys. J. Plus*, vol. 130, no. 2, pp. 1-9, 2015.

[119] F. Piscitelli, and P. V. Esch, "Analytical Modeling of Thin Film Neutron Converters and Its Application to Thermal Neutron Gas Detectors," *J. Instrum.*, vol. 8, no. 04, pp. P04020, 2013.

[120] D. S. McGregor, R. T. Klann, H. K. Gersch *et al.*, "New Surface Morphology for Low Stress Thin-Film-Coated Thermal Neutron Detectors," *IEEE Trans. Nucl. Sci.*, vol. 49 I, no. 4, pp. 1999-2004, 2002.

[121] C. M. Lavelle, R. M. Deacon, D. S. Hussey *et al.*, "Characterization of Boron Coated Vitreous Carbon Foam for Neutron Detection," *Nucl. Instrum. and Meth. A*, vol. 729, pp. 346-355, 2013.

[122] C. M. Lavelle, M. Coplan, E. C. Miller *et al.*, "Demonstration of Neutron Detection Utilizing Open Cell Foam and Noble Gas Scintillation," *Appl. Phys. Lett.*, vol. 106, no. 9, pp. 094103, 2015.

[123] M. A. Reichenberger, R. G. Fronk, J. K. Shultis *et al.*, "Monte Carlo Simulation of Energy Deposition by Neutron Reaction Products in Lithiated Foam Using Dynamic Path Generation," *2014 IEEE Nuclear Science Symposium and Medical Imaging Conference (NSS/MIC)*, paper N04-8, 3 pages, Seattle, WA, Nov. 8 -15, 2014.

[124] M. A. Reichenberger, R. G. Fronk, J. K. Shultis *et al.*, "Monte Carlo Simulation of Random, Porous (Foam) Structures for Neutron Detection," *Radiat. Phys. Chem.*, vol. 130, pp. 186-195, 2017.

[125] ERG Aerospace Corporation, "The Basics of Duocel® Foam," http://ergaerospace.com/technical-data/the-basics-of-duocel-foam/, [February 15, 2017].

[126] ERG Aerospace Corporation, "Duocel® Reticulated Vitreous Carbon (RVC) Foam," http://ergaerospace.com/materials/duocel-reticulated-vitreous-carbon-rvc-foam/, [February 15, 2017].

[127] ERG Aerospace Corporation, "Duocel® Foam Properties & Application Guide," http://ergaerospace.com/applications/, [February 15, 2017].

[128] N. S. Edwards, K. A. Nelson, C. N. Tiner *et al.*, "Charge Propagation through- and Neutron Sensitivity of- Reticulated Vitreous Carbon Foam," *2015 IEEE Nuclear Science Symposium and Medical Imaging Conference (NSS/MIC)*, paper N5A3-5, 4 pages, San Diego, CA, Oct. 31 - Nov. 7, 2015.

[129] I.-B. García-Ferreira, J. García-Herrera, and L. Villaseñor, "The Drift Chambers Handbook, Introductory Laboratory Course (Based on, and Adapted from, A H Walenta's Course Notes)," *J. Phys. Conf. Ser.*, vol. 18, no. 1, pp. 346, 2005.

[130] N. S. Edwards, J. C. Conley, M. A. Reichenberger *et al.*, "Characterization of Reticulated Vitreous Carbon Foam Using a Frisch-Grid Parallel-Plate Ionization Chamber," *Nucl. Instrum. and Meth. A*, vol. 892, pp. 93-97, 2018.

[131] Z. Fang, Y. Yang, and Y. Li, "The Research of High Detection Efficiency Boron Lined Detector with a Honeycomb Neutron Converter," *2015 IEEE Nuclear Science Symposium and Medical Imaging Conference (NSS/MIC)*, paper N5A3-3, 4 pages, Oct. 31 - Nov. 7, 2015.

[132] Z. Fang, Y. Yang, Y. Li *et al.*, "Working Gas Selection of the Honeycomb Converter-Based Neutron Detector," *IEEE Trans. Nucl. Sci.*, vol. 64, no. 7, pp. 1683-1688, 2017.

[133] Plascore, "PAMG-XR1 5052 Aluminum Honeycomb," https://www.plascore.com/honeycomb/honeycomb-cores/aluminum/pamg-xr1-5052-aluminum-honeycomb/, [August 31, 2017].

[134] Plascore, "Honeycomb Cores," https://www.plascore.com/download/datasheets/honeycomb_data_sheets/Plascore_Honeycomb_LineCard.pdf, [August 31, 2017].

[135] Alcore, "Commercial Grade Honeycomb," https://www.thegillcorp.com/alcore/datasheets/CGH.pdf, [August 31, 2017].

[136] Cel Components, "Honeycombs and Foams for Sandwich Panels," http://www.honeycombpanels.eu/14/honeycombs-and-foams-for-sandwich-panels, [August 31, 2017].

[137] Core Composites, "Aluminum Honeycomb," http://www.corecomposites.com/products/honeycomb/aluminum-honeycomb.html, [August 31, 2017].

[138] Plascore, "Honeycomb Selector Guide," https://www.plascore.com/download/datasheets/honeycomb_data_sheets/Plascore_Selector.pdf, [August 31, 2017].

[139] K. A. Nelson, S. L. Bellinger, B. W. Montag *et al.*, "Investigation of Aerogel, Saturated Foam, and Foil for Thermal Neutron Detection," *2011 IEEE Nuclear Science Symposium and Medical Imaging Conference (NSS/MIC)*, paper N20-2, pp. 1026-1029, Valencia, Spain, Oct. 23-29, 2011.

[140] K. A. Nelson, S. L. Bellinger, B. W. Montag *et al.*, "Investigation of a Lithium Foil Multi-Wire Proportional Counter for Potential ^{3}He Replacement," *Nucl. Instrum. and Meth. A*, vol. 669, pp. 79-84, 2012.

[141] R. Bouclier, G. Million, L. Ropelewski *et al.*, "Performance of Gas Microstrip Chambers on Glass Substrata with Electronic Conductivity," *Nucl. Instrum. and Meth. A*, vol. 332, no. 1, pp. 100-106, 1993.

[142] J. E. Bateman, J. F. Connolly, R. Stephenson *et al.*, "The Development of Gas Microstrip Detectors for High Energy Physics Applications," *Nucl. Instrum. and Meth. A*, vol. 348, no. 2, pp. 372-377, 1994.

[143] F. Angelini, R. Bellazzini, A. Brez *et al.*, "A Microstrip Gas Avalanche Chamber with Two-Dimensional Readout," *Nucl. Instrum. and Meth. A*, vol. 283, no. 3, pp. 755-761, 1989.

[144] F. Angelini, R. Bellazzini, A. Brez *et al.*, "Operation of MSGCs with Gold Strips Built on Surface-Treated Thin Glasses," *Nucl. Instrum. and Meth. A*, vol. 382, no. 3, pp. 461-469, 1996.

[145] F. Sauli, and A. Sharma, "Micropattern Gaseous Detectors," *Annu. Rev. Nucl. Part. Sci.*, vol. 49, no. 1, pp. 341-388, 1999.

[146] R. Bouclier, M. Capeáns, C. Garabatos *et al.*, "On Some Factors Affecting Discharge Conditions in Micro-Strip Gas Chambers," *Nucl. Instrum. and Meth. A*, vol. 365, no. 1, pp. 65-69, 1995.

[147] A. Oed, P. Convert, M. Berneron *et al.*, "A New Position Sensitive Proportional Counter with Microstrip Anode for Neutron Detection," *Nucl. Instrum. and Meth. A*, vol. 284, no. 1, pp. 223-226, 1989.

[148] J. F. Clergeau, P. Convert, D. Feltin *et al.*, "Operation of Sealed Microstrip Gas Chambers at the ILL," *Nucl. Instrum. and Meth. A*, vol. 471, no. 1–2, pp. 60-68, 2001.

[149] H. Takahashi, P. Siritiprussamee, M. Kai *et al.*, "Development of a Two-Dimensional Multi-Grid-Type Microstrip Gas Chamber for Spallation Neutron Source," *Nucl. Instrum. and Meth. A*, vol. 529, no. 1–3, pp. 348-353, 2004.

[150] K. Fujita, H. Takahashi, P. Siritiprussamee *et al.*, "A High-Resolution Two-Dimensional ^{3}He Neutron MSGC with Pads for Neutron Scattering Experiments," *Nucl. Instrum. and Meth. A*, vol. 580, no. 2, pp. 1027-1030, 2007.

[151] J. E. Bateman, R. M. Dalgliesh, D. M. Duxbury *et al.*, "The Fastgas Detector," *Nucl. Instrum. and Meth. A*, vol. 616, no. 1, pp. 59-64, 2010.

[152] J. E. Bateman, R. Dalgliesh, D. M. Duxbury *et al.*, "The Osmond Detector," *Nucl. Instrum. and Meth. A*, vol. 698, pp. 168-176, 2013.

[153] B. Gebauer, C. Schulz, and T. Wilpert, "Novel Large-Area Thermal Neutron Imaging Detectors Comprising ^{157}Gd/CsI-Convertors and Micro-Strip Gas Detectors with Low-Pressure, Two-Stage Amplification and Delay Line Readout," *Nucl. Instrum. and Meth. A*, vol. 392, no. 1, pp. 68-72, 1997.

[154] N. S. Edwards, B. W. Montag, L. C. Henson *et al.*, "Lithium Foil Gas-Filled Neutron Detector Using Microstrip Electrodes," *2016 IEEE Nuclear Science Symposium and Medical Imaging Conference (NSS/MIC)*, paper N28-30, 3 pages, Oct. 29 - Nov. 5, 2016.

[155] N. S. Edwards, B. W. Montag, L. C. Henson *et al.*, "Neutron Sensitivity of ^{6}Li-Based Suspended Foil Microstrip Neutron Detectors Using Schott Borofloat® 33 Microstrip Electrodes," *Radiat. Phys. Chem.*, vol. 147, pp. 70 - 76, 2018.

[156] S. A. Campbell, *Fabrication Engineering at the Micro and Nanoscale*: OUP USA, 2008.

[157] S. K. Ghandhi, *VLSI Fabrication Principles: Silicon and Gallium Arsenide*: Wiley, 1994.

[158] S. M. Sze, *Semiconductor Devices: Physics and Technology*, 2nd ed., Hoboken, NJ: John Wiley & Sons, Inc., 2002.

[159] MicroChemicals GmbH, "Application Notes," https://www.microchemicals.com/downloads/application_notes.html, [June 14, 2018].

[160] Integrated Micro Materials, "Technical Resources," http://www.imicromaterials.com/technical, [June 14, 2018].

[161] N. S. Edwards, B. W. Montag, L. C. Henson *et al.*, "Fabrication and Characterization of Schott Borofloat® 33 Microstrip Electrodes," *Radiat. Phys. Chem.*, Submitted.

[162] S. M. Sze, *Physics of Semiconductor Devices*, 2nd ed., New York, NY: John Wiley & Sons, Inc., 1981.

[163] H. Bartzsch, D. Glöß, B. Böcher *et al.*, "Properties of SiO_2 and Al_2O_3 Films for Electrical Insulation Applications Deposited by Reactive Pulse Magnetron Sputtering," *Surf. Coat. Tech.*, vol. 174-175, pp. 774-778, 2003.

[164] Schott Technical Glass Solutions GmbH, "Borofloat® 33 - General Information," http://www.schott.com/d/borofloat/b2c50cc4-74a1-4c31-8af3-c7de01877182/1.0/borofloat33_gen_eng_web.pdf, [July 24, 2017].

[165] Schott Technical Glass Solutions GmbH, "Schott Borofloat® 33," https://psec.uchicago.edu/glass/borofloat_33_e.pdf, [April 20, 2018].

[166] Corning, "Properties of Pyrex®, Pyrexplus® and Low Actinic Pyrex Code 7740 Glasses," http://www.quartz.com/pxprop.pdf, [07/24/2017].

[167] Corning Glass Works, "Pyrex Glass Code 7740," 1987.

[168] F. Ortuño-Prados, and C. Budtz-Jørgensen, "The Electron-Conducting Glass Schott S8900 as Substrata for Microstrip Gas Chamber," *Nucl. Instrum. and Meth. A*, vol. 364, no. 2, pp. 287-289, 1995.

[169] Tanner Research Inc., L-Edit Version 16.0, 2013, www.tannereda.com.

[170] SSI Technologies Inc., "Mediagauge™ (Model MGA-9V) Digital Pressure Gage Product Overview," http://www.ssi-sensors.com/pdfs/Pressure%20Sensors/Media%20Guage/PS-AN5_MGA-9V%20PRODUCT%20OVERVIEW.pdf, [April 24, 2018].

[171] Fluke, "8010A/8012A Digital Multimeters Instruction Manual," 1985.

[172] Fluke, "Model 87 & 89 Series IV True RMS Multimeter," 2000.

[173] R. Bouclier, M. Capeáns, C. Garabatos *et al.*, "Results of Wire Chamber Ageing Tests with Ch_4- and DME-Based Gas Mixtures," *Nucl. Instrum. and Meth. A*, vol. 346, no. 1, pp. 114-119, 1994.

[174] Integrated Engineering Software, Coulomb Version 9.0, 2010, http://www.integratedsoft.com/.

[175] SolidWorks Corporation, Solidworks, 2018, https://www.solidworks.com/.

[176] American National Standards Institute, "American National Standard Performance Criteria for Backpack-Based Radiation-Detection Systems Used for Homeland Security," in *ANSI N42.53-2013*, by The Institute of Electrical and Electronics Engineers, Inc., 2013, pp. 1-62.

[177] M. J. Berger, J. H. Hubbell, S. M. Seltzer *et al.*, "XCOM: Photon Cross Section Database (Version 1.5)," in ed., by, 2010.

[178] R. Chechik, A. Breskin, C. Shalem *et al.*, "Thick GEM-Like Hole Multipliers: Properties and Possible Applications," *Nucl. Instrum. and Meth. A*, vol. 535, no. 1, pp. 303-308, 2004.

[179] Boedeker Plastics Inc., "Outgassing of Engineering Plastics in High-Vacuum Applications," http://www.boedeker.com/outgas.htm, [January 31, 2018].

[180] Curbell Plastics Inc., "High Purity Plastics That Limit Contamination and Outgassing," https://www.curbellplastics.com/Research-Solutions/Applications/High-Purity, [January 31, 2018].

[181] McMaster-Carr, "Plastics," https://www.mcmaster.com/#raw-materials/=1bd9v1s, [January 31, 2018].

Appendix A
^{10}B-Coated Aluminum Honeycomb Simulation Results

MCNP6 simulations of ε_{th} were performed to define the optimal ^{10}B coating thickness for commercially-available honeycomb cell sizes of 0.635 cm (0.25 in.), 0.3175 cm (0.125 in.), and 0.15875 cm (0.0625 in.) (Appendix A.1). The azimuthal and polar angular neutron-sensitivities of the substrate for each cell size were also simulated (Appendix A.2). The effects of gas pressure on the ε_{th} as a function of LLD setting were studied to further-optimize the theoretical operating parameters of each cell size (Appendix A.3). For all simulation studies, the height and diameter of the substrate were defined as 1.27 cm (0.5 in.) and 4.1275 cm (1.625 in.), respectively. The wall thickness of the 5052 aluminum between neighboring cells was defined as 130 μm, 75 μm, or 60 μm corresponding to cell sizes of 0.635 cm (0.25 in.), 0.3175 cm (0.125 in.), or 0.15875 cm (0.0625 in.), respectively. The ^{10}B-coating thickness was assumed to be uniform about the interior of each cell. Listed in Table A.1 are the ^{10}B(n, α)^{7}Li reaction-product ranges in ^{10}B, aluminum, and 1 to 5 atm of P-10 gas.

Table A.1. The ranges of ^{10}B(n, α)^{7}Li reaction products in ^{10}B, aluminum honeycomb, and 1 – 5 atm of P-10 gas [96]. The density, ρ, of each material is also listed [96, 115].

Material	**ρ (g cm^{-3})**	**0.840 MeV ^{7}Li (μm)**	**1.015 MeV ^{7}Li (μm)**	**1.470 MeV ^{4}He (μm)**	**1.777 MeV ^{4}He (μm)**
Thin-Film Coating					
^{10}B	2.16	1.83	2.06	3.56	4.41
Substrate					
Aluminum Honeycomb	2.70	2.25	2.59	4.65	5.71
P-10 Gas					
1 atm	0.00156	4210	4690	8040	9900
2 atm	0.00312	2100	2340	4020	4950
3 atm	0.00468	1400	1560	2680	3300
4 atm	0.00624	1050	1170	2010	2470
5 atm	0.00780	842	939	1610	1980

Appendix A.1 Thickness Optimization

The simulation environment shown in Figure 4.29 was used to define the optimal ^{10}B coating thickness for commercially-available honeycomb cell sizes of 0.635 cm (0.25 in.), 0.3175 cm (0.125 in.), and 0.15875 cm (0.0625 in.). The ε_{th} was simulated for ^{10}B coating thicknesses ranging from 0 to 5 µm in 0.1 µm increments in order to determine the optimal coating thickness for each cell size. P-10 gas at a pressure of 2.8 atm was defined as the backfill gas. The center of a 5-mm diameter thermal-neutron beam was positioned at the center of the height of the substrate, normal to the substrate surface. Shown in Figure A.1 are the simulated ε_{th} as a function of ^{10}B coating thickness for honeycomb cell sizes of 0.635 cm (0.25 in.), 0.3175 cm (0.125 in.), and 0.15875 cm (0.0625 in.) with a 0 keV LLD setting. The maximum simulated ε_{th} with corresponding ^{10}B coating thicknesses for each cell size are listed in Table A.2. The number of ^{10}B coating layers corresponding to each cell size are also listed in Table A.2.

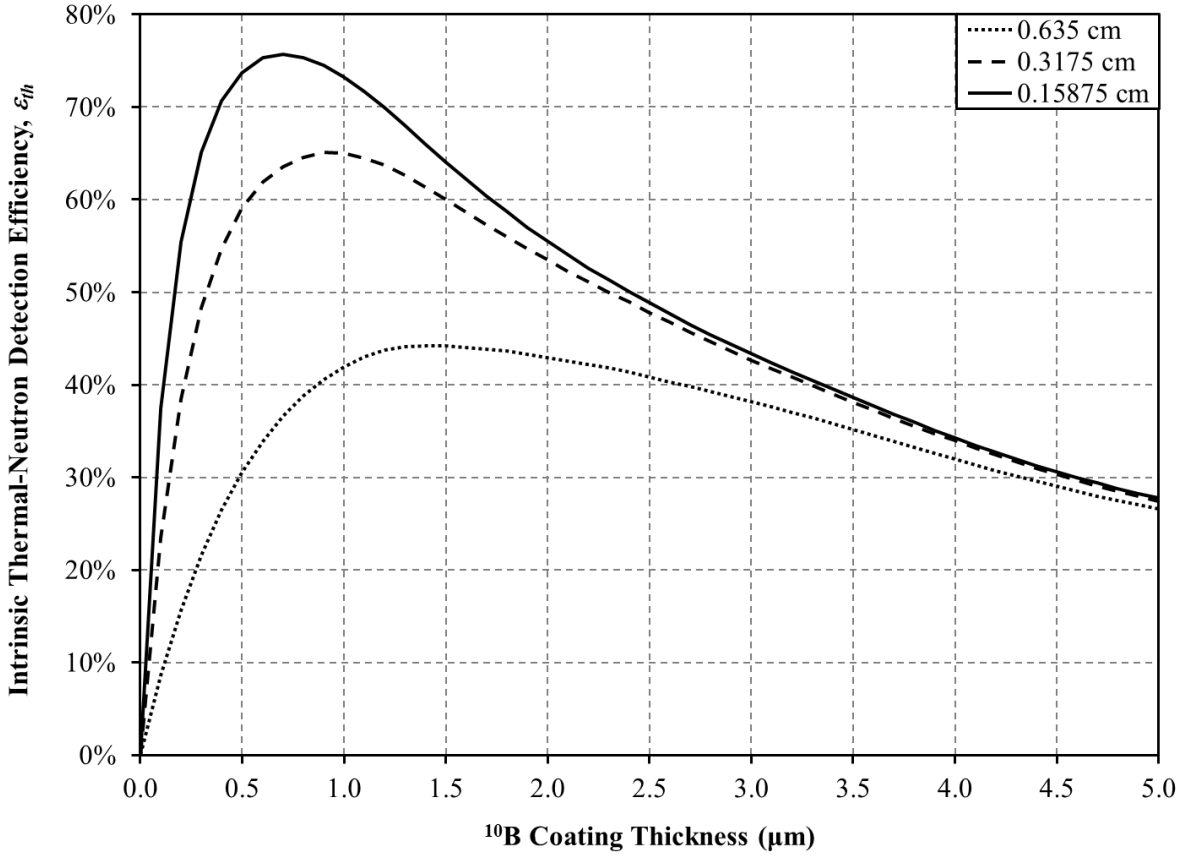

Figure A.1. Simulated ε_{th} as a function of ^{10}B coating thickness with a 0 keV LLD setting. A 1.27-cm (0.5-in.) tall, 4.1275-cm (1.625-in.) diameter aluminum-honeycomb substrate was simulated with cell sizes of 0.635 cm (0.25 in.), 0.3175 cm (0.125 in.), or 0.15875 cm (0.0625 in.).

Table A.2. Simulated maximum ε_{th}, with corresponding ^{10}B coating thickness, of the three honeycomb cell sizes with a 0 keV LLD setting.

Cell Size (cm)	Layers	ε_{th} (%)	Coating Thickness (μm)
0.635	12	44.23	1.4
0.3175	26	65.07	0.9
0.15875	52	75.74	0.7

Shown in Figure A.2 are the simulated reaction-product pulse-height spectra, represented by solid lines and corresponding to the left ordinate with units of "Counts/Source Neutron", of the three cell sizes with the corresponding optimal ^{10}B coating thicknesses (Table A.2). The simulated ε_{th} distributions shown in Figure A.2, represented by dashed lines and corresponding to the right ordinate, depict the ε_{th} as a function of LLD setting for each cell size.

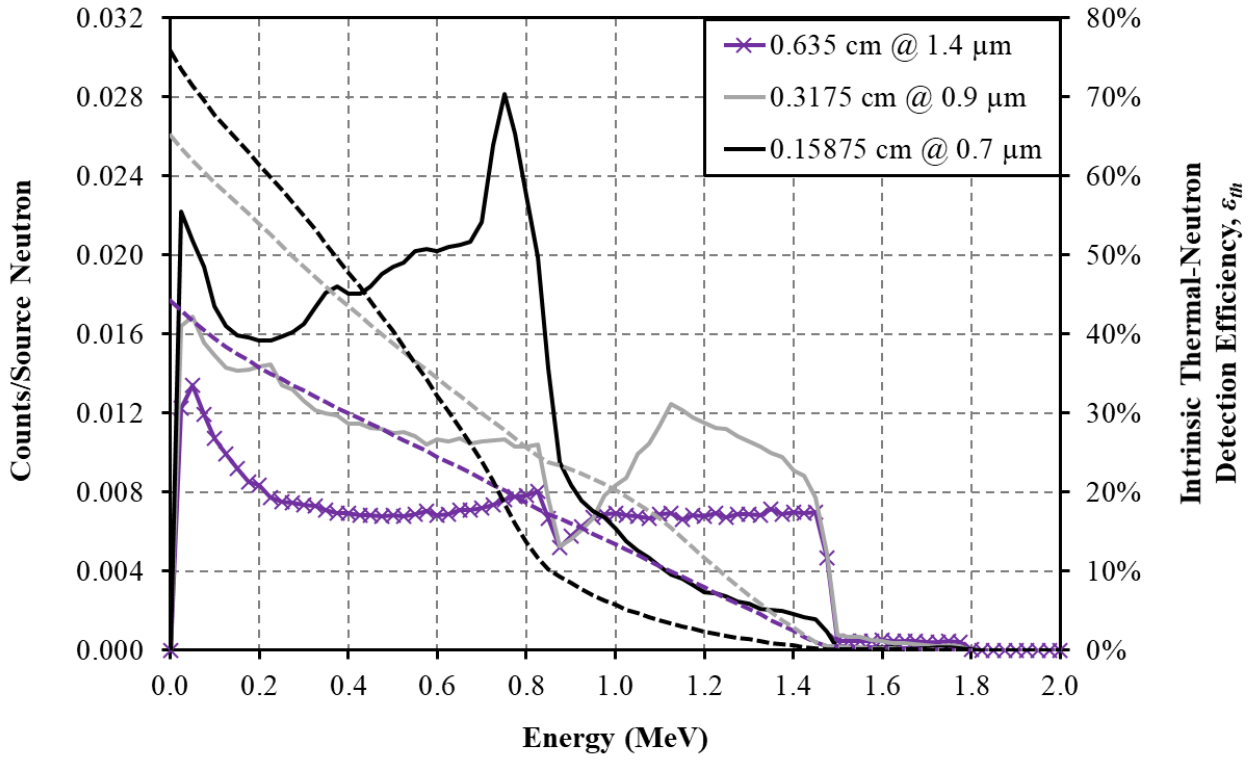

Figure A.2. Simulated reaction-product pulse-height spectra (solid lines corresponding to the left ordinate with units of "Counts/Source Neutron") of the three cell sizes of ^{10}B-coated aluminum honeycomb. The dashed lines correspond to the right ordinate and illustrate the ε_{th} as a function of LLD setting for each cell size. The optimal ^{10}B coating thickness (listed in Table A.2) was defined for each cell size.

Appendix A.2 Angular Neutron Sensitivity

The azimuthal and polar angular neutron-sensitivity distributions were simulated using the simulation environments illustrated in Figure 4.32. The ^{10}B-coating thickness for each cell size was defined from the optimization results shown in Figure A.1 and listed in Table A.2. The incident thermal-neutron beam was adjusted in 15° increments within either the horizontal or vertical source plane and the ε_{th} was simulated at each beam position. For all azimuthal angular neutron-sensitivity simulations, the center of the 5-mm diameter incident thermal-neutron beam was directed toward the center of the sample at the midpoint of the sample height. For all polar angular neutron-sensitivity simulations, the center of the incident thermal-neutron beam was directed toward the center of the sample within the vertical source plane. P-10 gas at a pressure of 2.8 atm was defined as the backfill gas. Shown in Figure A.3 are the simulated azimuthal angular neutron-sensitivity distributions with a 0 keV LLD setting. The azimuthal angles, θ, shown in Figure A.3 directly correspond to the angles illustrated in Figure 4.32. Shown in Figure A.4 are the simulated polar angular neutron-sensitivity distributions with a 0 keV LLD setting. The polar angles, ψ, labeled on the *x*-axis of Figure A.4 directly correspond to the polar angles illustrated in Figure 4.32.

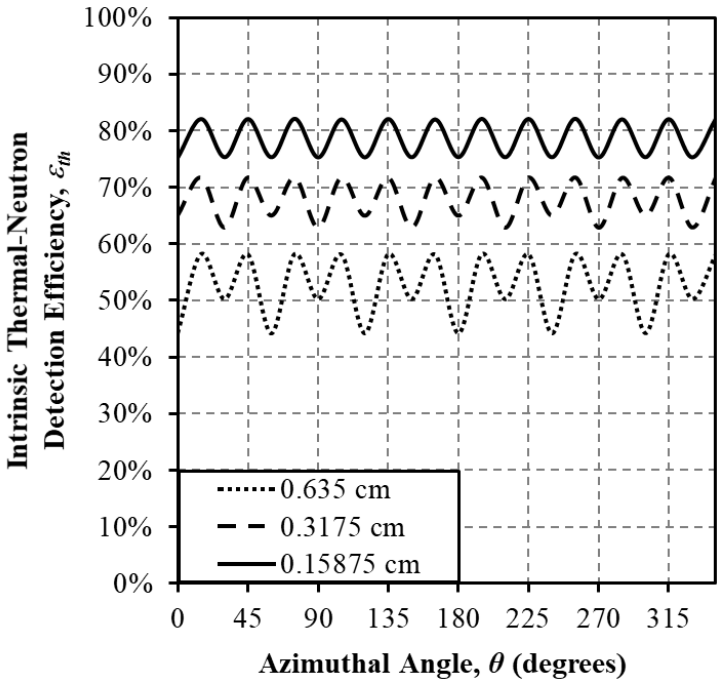

Figure A.3. Simulated azimuthal angular neutron-sensitivity distributions of ^{10}B-coated aluminum-honeycomb substrates with cell sizes of 0.635 cm, 0.3175 cm, or 0.15875 cm and a 0 keV LLD setting.

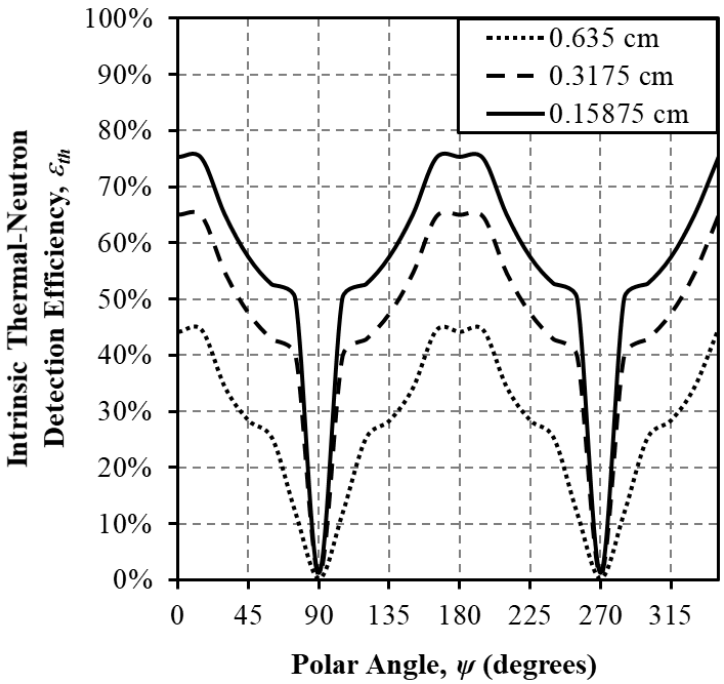

Figure A.4. Simulated polar angular neutron-sensitivity distributions of ^{10}B-coated aluminum-honeycomb substrates with cell sizes of 0.635 cm, 0.3175 cm, or 0.15875 cm and a 0 keV LLD setting.

Appendix A.3 Effects of Gas Pressure

The simulation environment shown in Figure 4.29 was used to simulate the effects of the P-10 gas pressure on the theoretical ε_{th}. The optimized ^{10}B coating thicknesses for each cell size (shown in Figure A.1 and listed in Table A.2) were defined while conducting the P-10 gas pressure simulations. The P-10 gas pressure optimization study was simulated for gas pressures ranging from 1 to 5 atm in increments of 1 atm. The center of a 5-mm diameter thermal-neutron beam was positioned at the center of the height of the substrate, normal to the substrate surface. Shown in Figure A.5 – Figure A.7 are the simulated reaction-product pulse-height spectra, represented by solid lines and corresponding to the left ordinate, with units of "Counts/Source Neutron", for the 0.635-cm, 0.3175-cm, and 0.15875-cm cell sizes, respectively. Also shown in Figure A.5 – Figure A.7 are the simulated ε_{th} as a function of LLD setting, which are represented by dashed lines and correspond to the right ordinate.

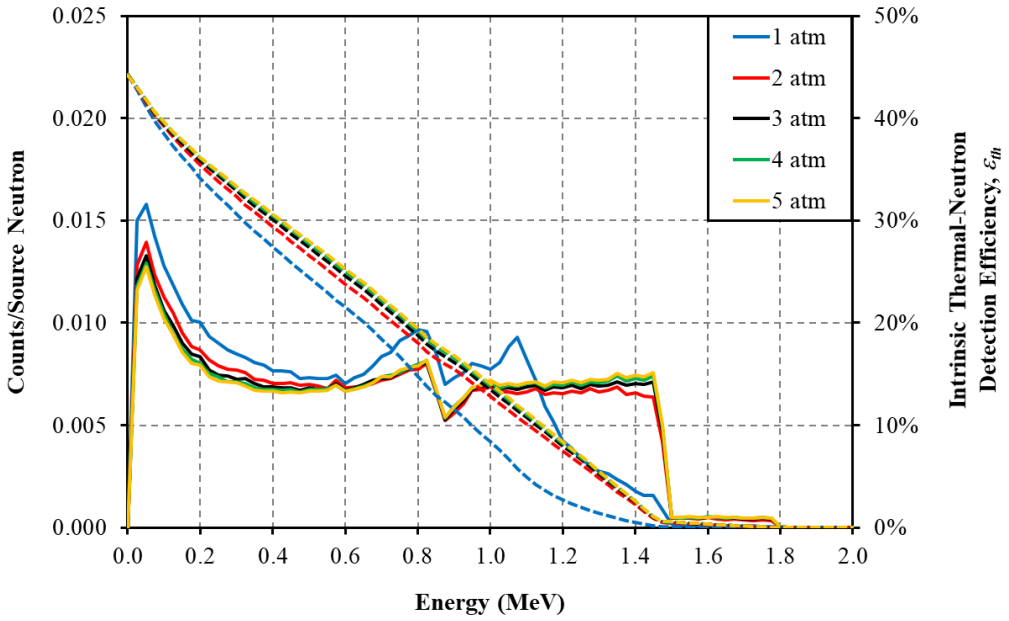

Figure A.5. Simulated reaction-product pulse-height spectra (solid lines corresponding to the left ordinate with units of "Counts/Source Neutron") for a 0.635-cm cell size honeycomb substrate with P-10 gas pressures ranging from 1 to 5 atm. The dashed lines correspond to the right ordinate and illustrate the ε_{th} as a function of LLD setting for each cell size. The honeycomb sample contained hexagonal cells with a cell size of 0.635-cm that were coated with 1.4 µm of ^{10}B.

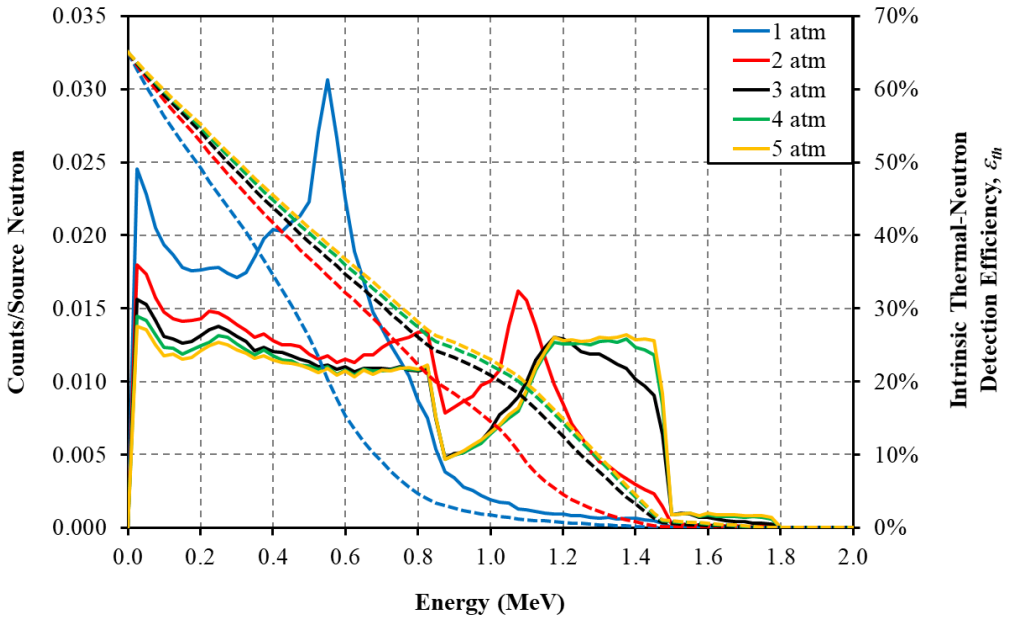

Figure A.6. Simulated reaction-product pulse-height spectra (solid lines corresponding to the left ordinate with units of "Counts/Source Neutron") for a 0.3175-cm cell size honeycomb substrate with P-10 gas pressures ranging from 1 to 5 atm. The dashed lines correspond to the right ordinate and illustrate the ε_{th} as a function of LLD setting for each cell size. The honeycomb sample contained hexagonal cells with a cell size of 0.3175-cm that were coated with 0.9 µm of ^{10}B.

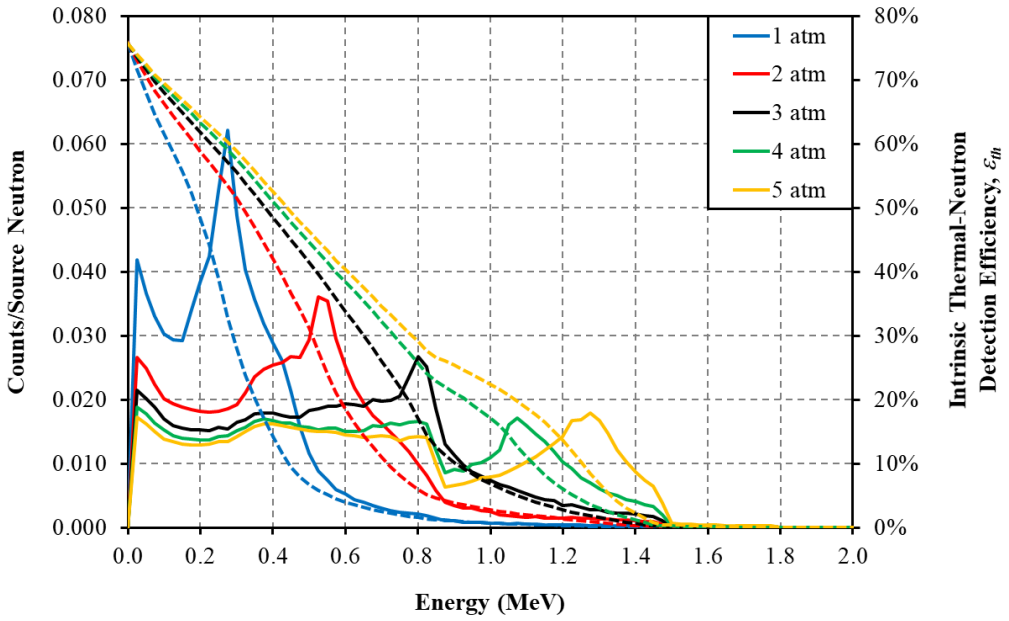

Figure A.7. Simulated reaction-product pulse-height spectra (solid lines corresponding to the left ordinate with units of "Counts/Source Neutron") for a 0.15875-cm cell size honeycomb substrate with P-10 gas pressures ranging from 1 to 5 atm. The dashed lines correspond to the right ordinate and illustrate the ε_{th} as a function of LLD setting for each cell size. The honeycomb sample contained hexagonal cells with a cell size of 0.15875-cm that were coated with 0.7 µm of ^{10}B.

Appendix B
^{10}BN-Coated Aluminum Honeycomb Simulation Results

MCNP6 simulations of ε_{th} were performed to define the optimal ^{10}BN coating thickness for commercially-available honeycomb cell sizes of 0.635 cm (0.25 in.), 0.3175 cm (0.125 in.), and 0.15875 cm (0.0625 in.) (Appendix B.1). The azimuthal and polar angular neutron-sensitivities of the substrate for each cell size were also simulated (Appendix B.2). The effects of gas pressure on the ε_{th} as a function of LLD setting were studied to further-optimize the theoretical operating parameters of each cell size (Appendix B.3). For all simulation studies, the height and diameter of the substrate were defined as 1.27 cm (0.5 in.) and 4.1275 cm (1.625 in.), respectively. The wall thickness of the 5052 aluminum between neighboring cells was defined as 130 μm, 75 μm, or 60 μm corresponding to cell sizes of 0.635 cm (0.25 in.), 0.3175 cm (0.125 in.), or 0.15875 cm (0.0625 in.), respectively. The ^{10}BN-coating thickness was assumed to be uniform about the interior of each cell. Listed in Table B.1 are the ^{10}B(n, α)^{7}Li reaction-product ranges in ^{10}BN, aluminum, and 1 to 5 atm of P-10 gas.

Table B.1. The ranges of ^{10}B(n, α)^{7}Li reaction products in ^{10}BN, aluminum honeycomb, and 1 – 5 atm of P-10 gas [96]. The density, ρ, of each material is also listed [96, 115].

Material	**ρ (g cm^{-3})**	**0.840 MeV ^{7}Li (μm)**	**1.015 MeV ^{7}Li (μm)**	**1.470 MeV ^{4}He (μm)**	**1.777 MeV ^{4}He (μm)**
Thin-Film Coating					
^{10}BN	2.18	2.17	2.44	3.95	4.84
Substrate					
Aluminum Honeycomb	2.70	2.25	2.59	4.65	5.71
P-10 Gas					
1 atm	0.00156	4210	4690	8040	9900
2 atm	0.00312	2100	2340	4020	4950
3 atm	0.00468	1400	1560	2680	3300
4 atm	0.00624	1050	1170	2010	2470
5 atm	0.00780	842	939	1610	1980

Appendix B.1 Thickness Optimization

The simulation environment shown in Figure 4.29 was used to define the optimal ^{10}BN coating thickness for commercially-available honeycomb cell sizes of 0.635 cm (0.25 in.), 0.3175 cm (0.125 in.), and 0.15875 cm (0.0625 in.). The ε_{th} was simulated for ^{10}BN coating thicknesses ranging from 0 to 5 μm in 0.1 μm increments in order to determine the optimal coating thickness for each cell size. P-10 gas at a pressure of 2.8 atm was defined as the backfill gas. The center of a 5-mm diameter thermal-neutron beam was positioned at the center of the height of the substrate, normal to the substrate surface. Shown in Figure B.1 are the simulated ε_{th} as a function of ^{10}BN coating thickness for honeycomb cell sizes of 0.635 cm (0.25 in.), 0.3175 cm (0.125 in.), and 0.15875 cm (0.0625 in.) with a 0 keV LLD setting. The maximum simulated ε_{th} with corresponding ^{10}BN coating thicknesses for each cell size are listed in Table B.2. The number of ^{10}BN coating layers corresponding to each cell size are also listed in Table B.2.

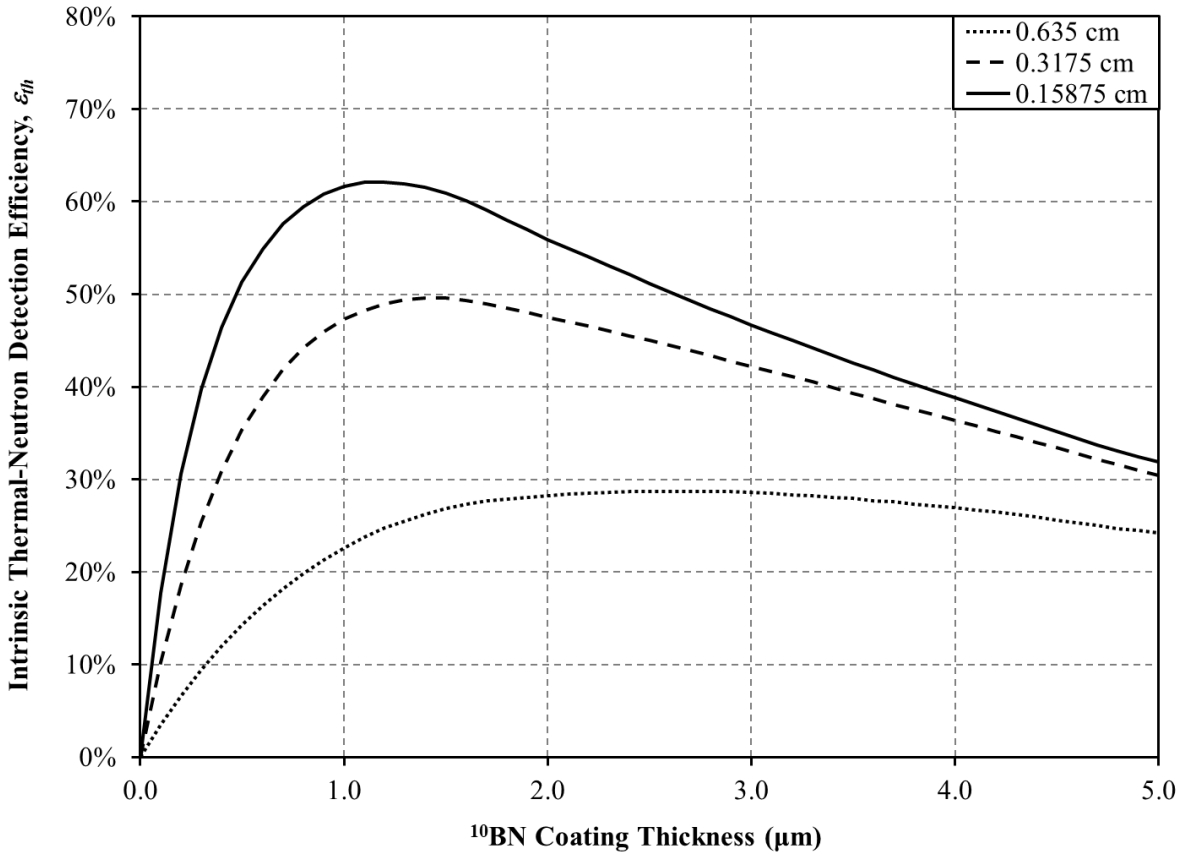

Figure B.1. Simulated ε_{th} as a function of ^{10}BN coating thickness with a 0 keV LLD setting. A 1.27-cm (0.5-in.) tall, 4.1275-cm (1.625-in.) diameter aluminum-honeycomb substrate was simulated with cell sizes of 0.635 cm (0.25 in.), 0.3175 cm (0.125 in.), or 0.15875 cm (0.0625 in.).

Table B.2. Simulated maximum ε_{th}, with corresponding ^{10}BN coating thickness, of the three honeycomb cell sizes with a 0 keV LLD setting.

Cell Size (cm)	Layers	ε_{th} (%)	Coating Thickness (μm)
0.635	12	28.72	2.7
0.3175	26	49.58	1.5
0.15875	52	62.10	1.2

Shown in Figure B.2 are the simulated reaction-product pulse-height spectra, represented by solid lines and corresponding to the left ordinate with units of "Counts/Source Neutron", of the three cell sizes with the corresponding optimal ^{10}BN coating thicknesses (Table B.2). The simulated ε_{th} distributions shown in Figure B.2, represented by dashed lines and corresponding to the right ordinate, depict the ε_{th} as a function of LLD setting for each cell size.

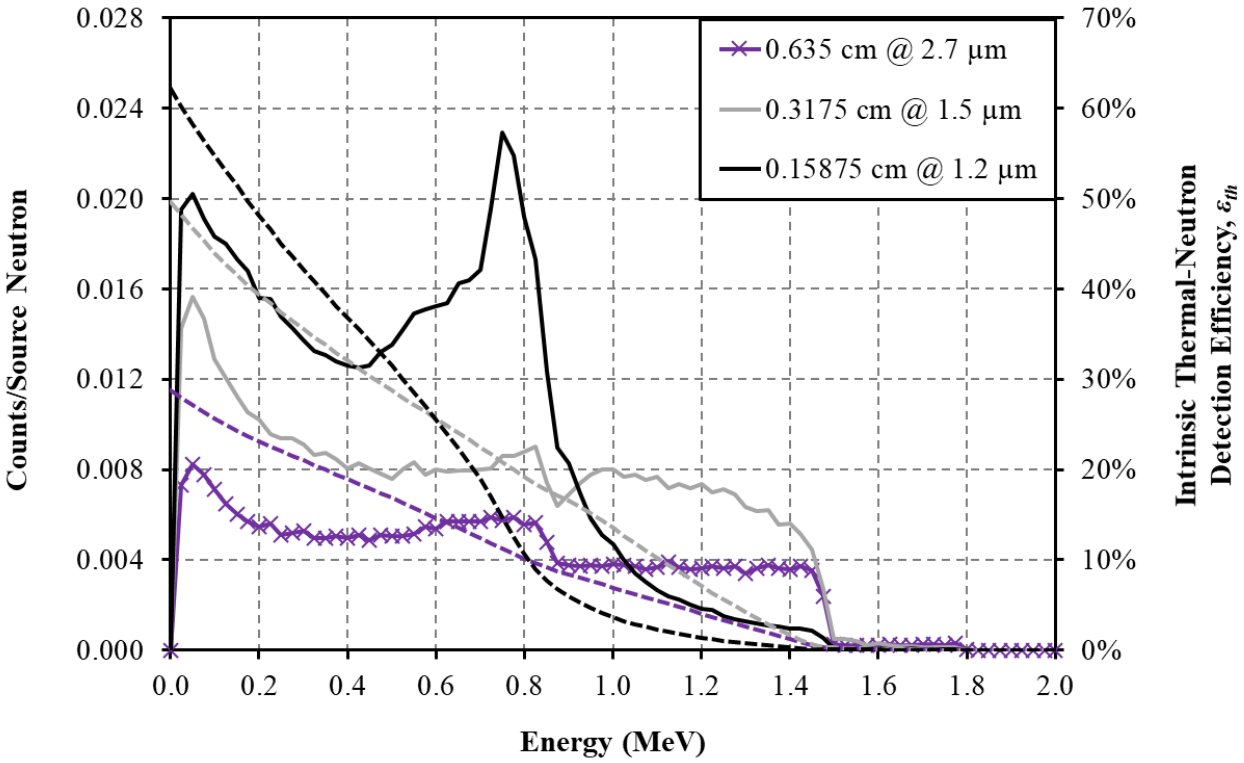

Figure B.2. Simulated reaction-product pulse-height spectra (solid lines corresponding to the left ordinate with units of "Counts/Source Neutron") of the three cell sizes of ^{10}BN-coated aluminum honeycomb. The dashed lines correspond to the right ordinate and illustrate the ε_{th} as a function of LLD setting for each cell size. The optimal ^{10}BN coating thickness (listed in Table B.2) was defined for each cell size.

Appendix B.2 Angular Neutron Sensitivity

The azimuthal and polar angular neutron-sensitivity distributions were simulated using the simulation environments illustrated in Figure 4.32. The ^{10}BN-coating thickness for each cell size was defined from the optimization results shown in Figure B.1 and listed in Table B.2. The incident thermal-neutron beam was adjusted in 15° increments within either the horizontal or vertical source plane and the ε_{th} was simulated at each beam position. For all azimuthal angular neutron-sensitivity simulations, the center of the 5-mm diameter incident thermal-neutron beam was directed toward the center of the sample at the midpoint of the sample height. For all polar angular neutron-sensitivity simulations, the center of the incident thermal-neutron beam was directed toward the center of the sample within the vertical source plane. P-10 gas at a pressure of 2.8 atm was defined as the backfill gas. Shown in Figure B.3 are the simulated azimuthal angular neutron-sensitivity distributions with a 0 keV LLD setting. The azimuthal angles, θ, shown in Figure B.3 directly correspond to the angles illustrated in Figure 4.32. Shown in Figure B.4 are the simulated polar angular neutron-sensitivity distributions with a 0 keV LLD setting. The polar angles, ψ, labeled on the x-axis of Figure B.4 directly correspond to the polar angles illustrated in Figure 4.32.

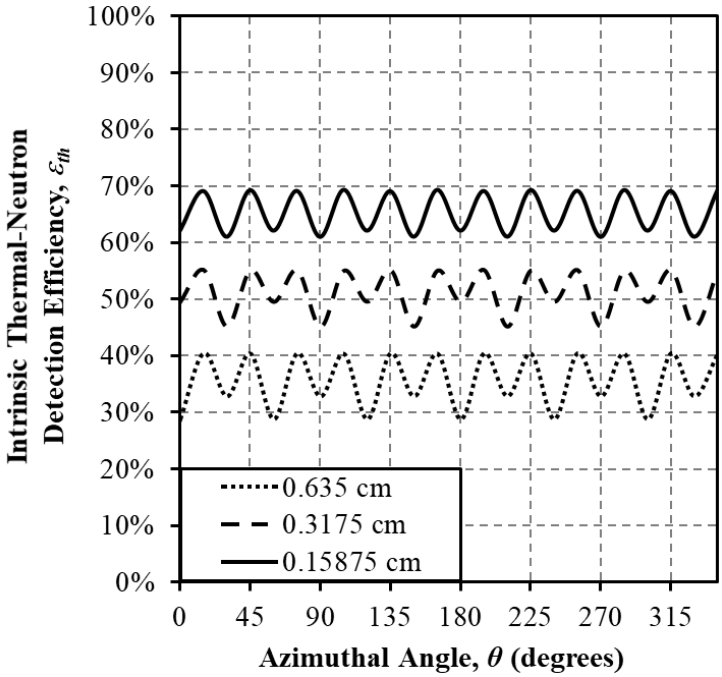

Figure B.3. Simulated azimuthal angular neutron-sensitivity distributions of ^{10}BN-coated aluminum-honeycomb substrates with cell sizes of 0.635 cm, 0.3175 cm, or 0.15875 cm and a 0 keV LLD setting.

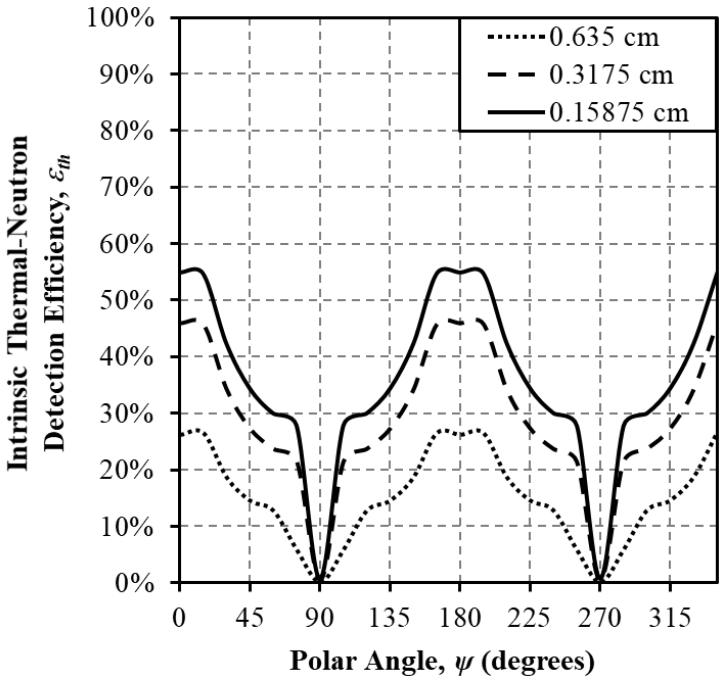

Figure B.4. Simulated polar angular neutron-sensitivity distributions of ^{10}BN-coated aluminum-honeycomb substrates with cell sizes of 0.635 cm, 0.3175 cm, or 0.15875 cm and a 0 keV LLD setting.

Appendix B.3 Effects of Gas Pressure

The simulation environment shown in Figure 4.29 was used to simulate the effects of the P-10 gas pressure on the theoretical ε_{th}. The optimized ^{10}BN coating thicknesses for each cell size (shown in Figure B.1 and listed in Table B.2) were defined while conducting the P-10 gas pressure simulations. The P-10 gas pressure optimization study was simulated for gas pressures ranging from 1 to 5 atm in increments of 1 atm. The center of a 5-mm diameter thermal-neutron beam was positioned at the center of the height of the substrate, normal to the substrate surface. Shown in Figure B.5 – Figure B.7 are the simulated reaction-product pulse-height spectra, represented by solid lines and corresponding to the left ordinate, with units of "Counts/Source Neutron", for the 0.635-cm, 0.3175-cm, and 0.15875-cm cell sizes, respectively. Also shown in Figure B.5 – Figure B.7 are the simulated ε_{th} as a function of LLD setting, which are represented by dashed lines and correspond to the right ordinate.

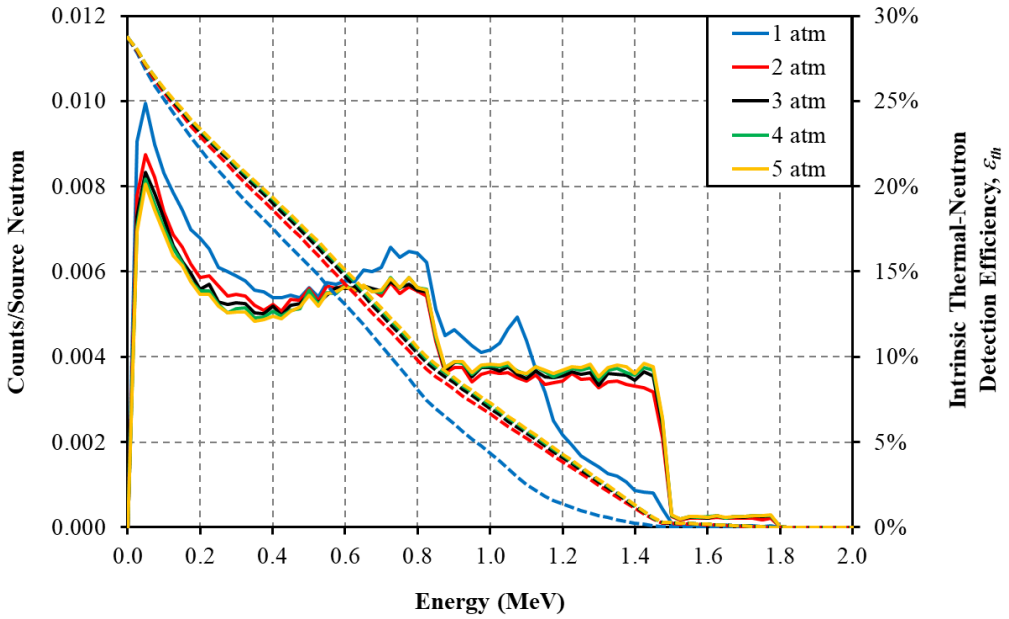

Figure B.5. Simulated reaction-product pulse-height spectra (solid lines corresponding to the left ordinate with units of "Counts/Source Neutron") for a 0.635-cm cell size honeycomb substrate with P-10 gas pressures ranging from 1 to 5 atm. The dashed lines correspond to the right ordinate and illustrate the ε_{th} as a function of LLD setting for each cell size. The honeycomb sample contained hexagonal cells with a cell size of 0.635-cm that were coated with 2.7 µm of ^{10}BN.

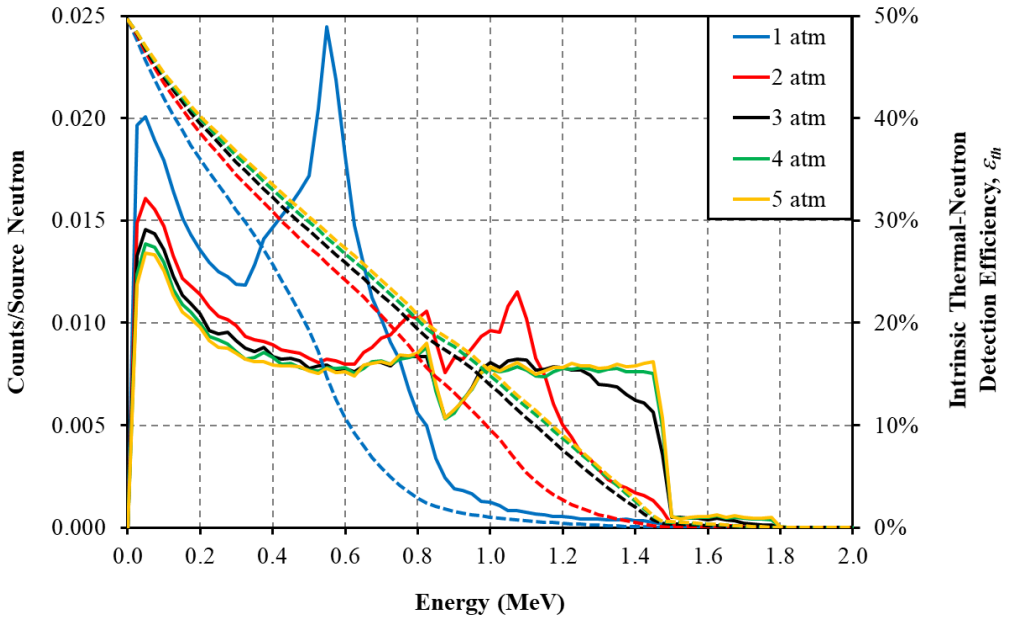

Figure B.6. Simulated reaction-product pulse-height spectra (solid lines corresponding to the left ordinate with units of "Counts/Source Neutron") for a 0.3175-cm cell size honeycomb substrate with P-10 gas pressures ranging from 1 to 5 atm. The dashed lines correspond to the right ordinate and illustrate the ε_{th} as a function of LLD setting for each cell size. The honeycomb sample contained hexagonal cells with a cell size of 0.3175-cm that were coated with 1.5 µm of ^{10}BN.

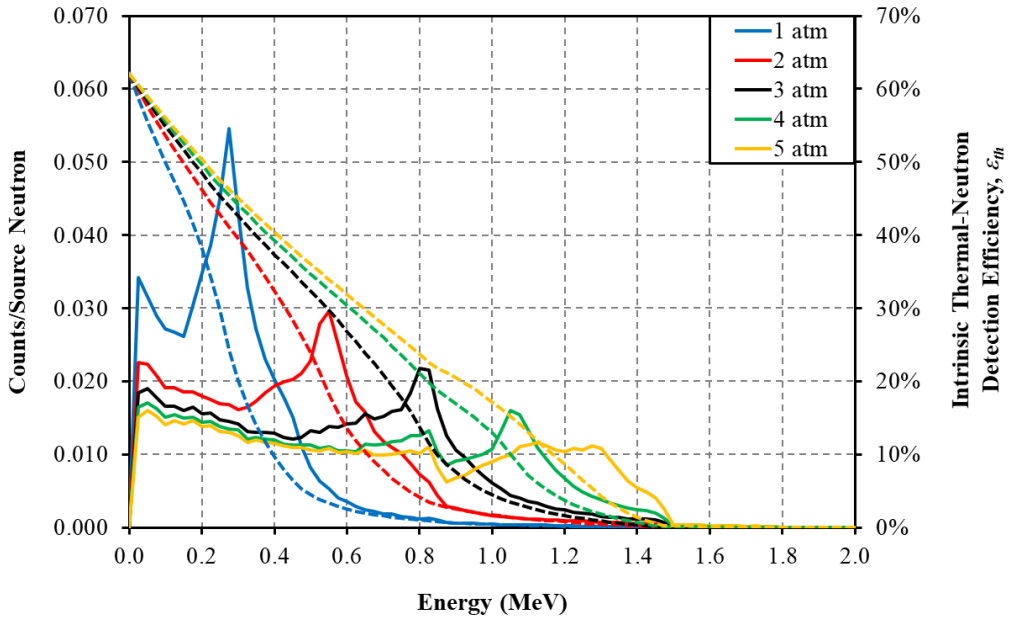

Figure B.7. Simulated reaction-product pulse-height spectra (solid lines corresponding to the left ordinate with units of "Counts/Source Neutron") for a 0.15875-cm cell size honeycomb substrate with P-10 gas pressures ranging from 1 to 5 atm. The dashed lines correspond to the right ordinate and illustrate the ε_{th} as a function of LLD setting for each cell size. The honeycomb sample contained hexagonal cells with a cell size of 0.15875-cm that were coated with 1.2 µm of ^{10}BN.

Appendix C
^{6}LiF-Coated Aluminum Honeycomb Simulation Results

MCNP6 simulations of ε_{th} were performed to define the optimal ^{6}LiF coating thickness for commercially-available honeycomb cell sizes of 0.635 cm (0.25 in.), 0.3175 cm (0.125 in.), and 0.15875 cm (0.0625 in.) (Appendix C.1). The azimuthal and polar angular neutron-sensitivities of the substrate for each cell size were also simulated (Appendix C.2). The effects of gas pressure on the ε_{th} as a function of LLD setting were studied to further-optimize the theoretical operating parameters of each cell size (Appendix C.3). For all simulation studies, the height and diameter of the substrate were defined as 1.27 cm (0.5 in.) and 4.1275 cm (1.625 in.), respectively. The wall thickness of the 5052 aluminum between neighboring cells was defined as 130 μm, 75 μm, or 60 μm corresponding to cell sizes of 0.635 cm (0.25 in.), 0.3175 cm (0.125 in.), or 0.15875 cm (0.0625 in.), respectively. The ^{6}LiF-coating thickness was assumed to be uniform about the interior of each cell. Listed in Table C.1 are the ^{6}Li(n, α)^{3}H reaction-product ranges in ^{6}LiF, aluminum, and 1 to 5 atm of P-10 gas.

Table C.1. The ranges of ^{6}Li(n, α)^{3}H reaction products in ^{6}LiF, aluminum honeycomb, and 1 – 5 atm of P-10 gas [96]. The density, ρ, of each material is also listed [96, 115].

Material	**ρ (g cm^{-3})**	**2.050 MeV ^{4}He (μm)**	**2.730 MeV ^{3}H (μm)**
Thin-Film			
^{6}LiF	2.54	6.05	33.7
Substrate			
Aluminum Honeycomb	2.25	6.72	38.2
P-10 Gas			
1 atm	0.00156	11700	65900
2 atm	0.00312	5860	32900
3 atm	0.00468	3900	21900
4 atm	0.00624	2930	16400
5 atm	0.00780	2340	13100

Appendix C.1 Thickness Optimization

The simulation environment shown in Figure 4.29 was used to define the optimal ^{6}LiF coating thickness for commercially-available honeycomb cell sizes of 0.635 cm (0.25 in.), 0.3175 cm (0.125 in.), and 0.15875 cm (0.0625 in.). The ε_{th} was simulated for ^{6}LiF coating thicknesses ranging from 0 to 20 μm in 0.1 μm increments in order to determine the optimal coating thickness for each cell size. P-10 gas at a pressure of 2.8 atm was defined as the backfill gas. The center of a 5-mm diameter thermal-neutron beam was positioned at the center of the height of the substrate, normal to the substrate surface. Shown in Figure C.1 are the simulated ε_{th} as a function of ^{6}LiF coating thickness for honeycomb cell sizes of 0.635 cm (0.25 in.), 0.3175 cm (0.125 in.), and 0.15875 cm (0.0625 in.) with a 0 keV LLD setting. The maximum simulated ε_{th} with corresponding ^{6}LiF coating thicknesses for each cell size are listed in Table C.2. The number of ^{6}LiF coating layers corresponding to each cell size are also listed in Table C.2.

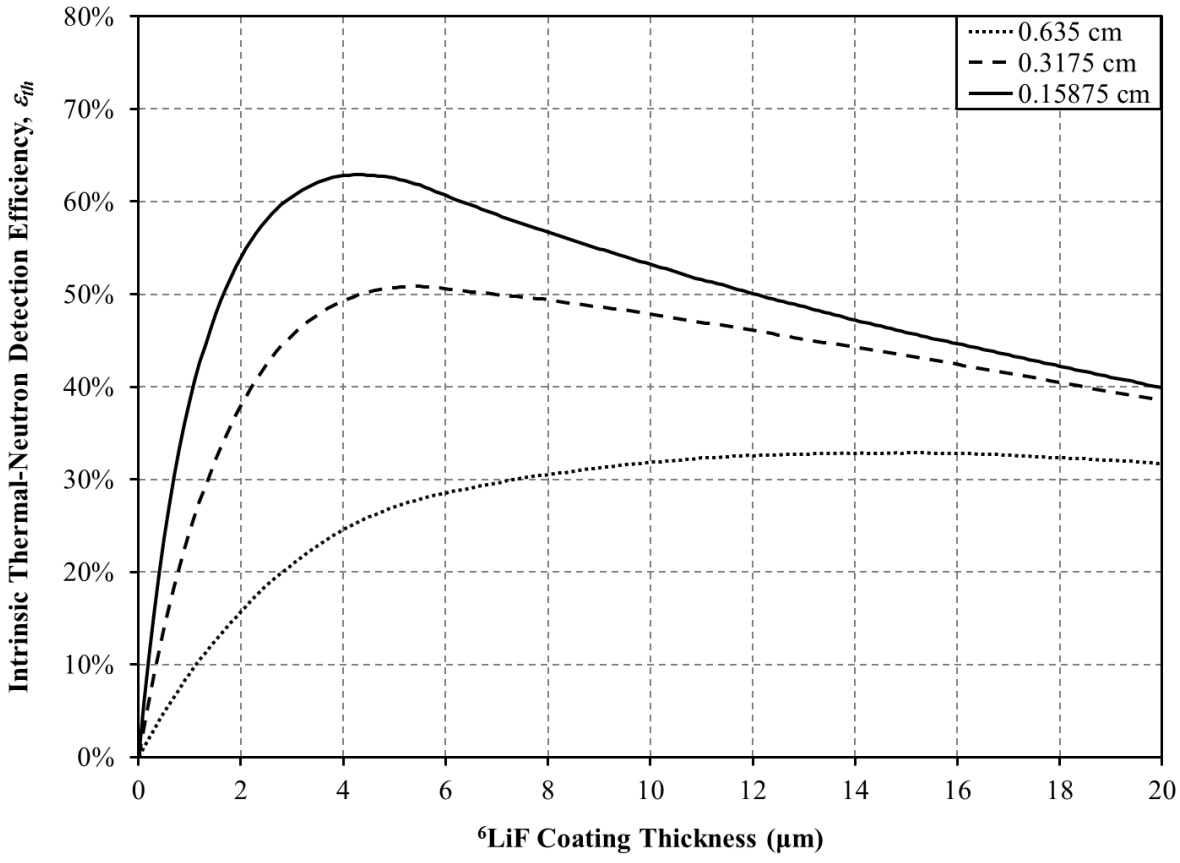

Figure C.1. Simulated ε_{th} as a function of ^{6}LiF coating thickness with a 0 keV LLD setting. A 1.27-cm (0.5-in.) tall, 4.1275-cm (1.625-in.) diameter aluminum-honeycomb substrate was simulated with cell sizes of 0.635 cm (0.25 in.), 0.3175 cm (0.125 in.), or 0.15875 cm (0.0625 in.).

Table C.2. Simulated maximum ε_{th}, with corresponding ^{6}LiF coating thickness, of the three honeycomb cell sizes with a 0 keV LLD setting.

Cell Size (cm)	Layers	ε_{th} (%)	Coating Thickness (μm)
0.635	12	32.87	15.2
0.3175	26	50.82	5.4
0.15875	52	62.89	4.3

Shown in Figure C.2 are the simulated reaction-product pulse-height spectra, represented by solid lines and corresponding to the left ordinate with units of "Counts/Source Neutron", of the three cell sizes with the corresponding optimal ^{6}LiF coating thicknesses (Table C.2). The simulated ε_{th} distributions shown in Figure C.2, represented by dashed lines and corresponding to the right ordinate, depict the ε_{th} as a function of LLD setting for each cell size.

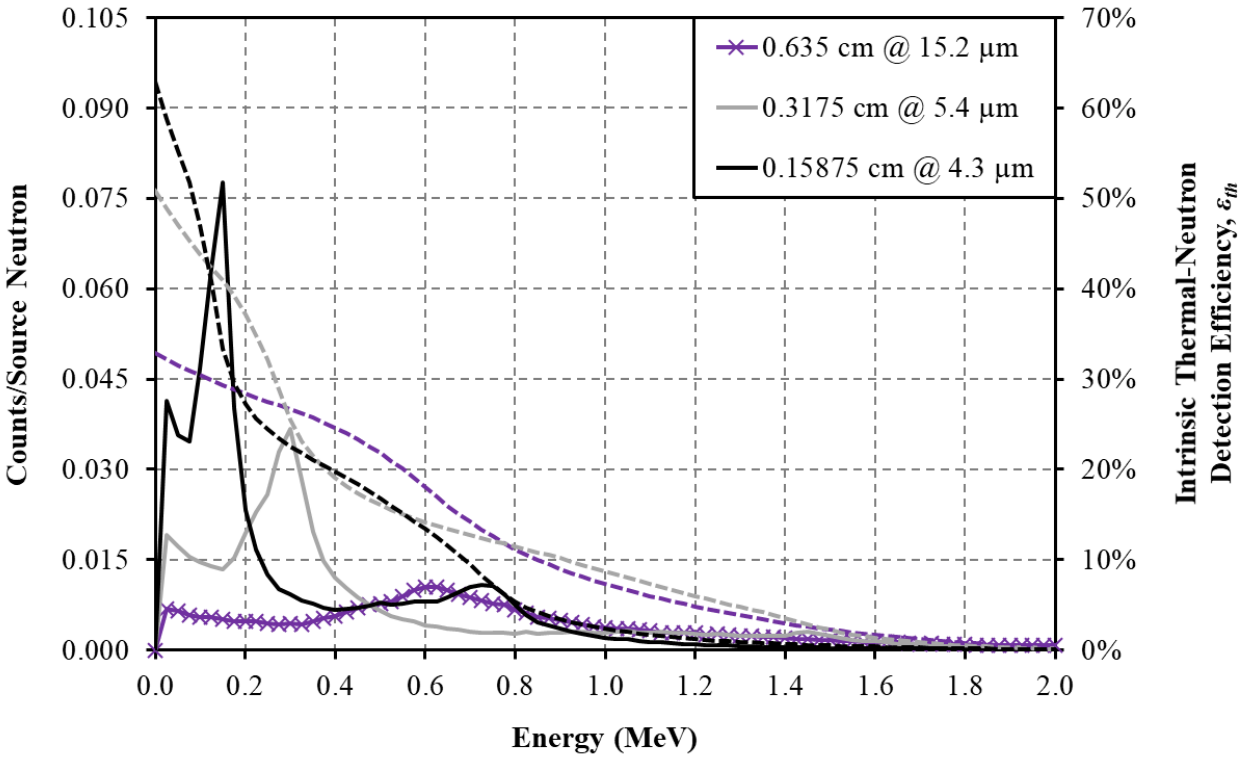

Figure C.2. Simulated reaction-product pulse-height spectra (solid lines corresponding to the left ordinate with units of "Counts/Source Neutron") of the three cell sizes of ^{6}LiF-coated aluminum honeycomb. The dashed lines correspond to the right ordinate and illustrate the ε_{th} as a function of LLD setting for each cell size. The optimal ^{6}LiF coating thickness (listed in Table C.2) was defined for each cell size.

Appendix C.2 Angular Neutron Sensitivity

The azimuthal and polar angular neutron-sensitivity distributions were simulated using the simulation environments illustrated in Figure 4.32. The ^{6}LiF-coating thickness for each cell size was defined from the optimization results shown in Figure C.1 and listed in Table C.2. The incident thermal-neutron beam was adjusted in 15° increments within either the horizontal or vertical source plane and the ε_{th} was simulated at each beam position. For all azimuthal angular neutron-sensitivity simulations, the center of the 5-mm diameter incident thermal-neutron beam was directed toward the center of the sample at the midpoint of the sample height. For all polar angular neutron-sensitivity simulations, the center of the incident thermal-neutron beam was directed toward the center of the sample within the vertical source plane. P-10 gas at a pressure of 2.8 atm was defined as the backfill gas. Shown in Figure C.3 are the simulated azimuthal angular neutron-sensitivity distributions with a 0 keV LLD setting. The azimuthal angles, θ, shown in Figure C.3 directly correspond to the angles illustrated in Figure 4.32. Shown in Figure C.4 are the simulated polar angular neutron-sensitivity distributions with a 0 keV LLD setting. The polar angles, ψ, labeled on the x-axis of Figure C.4 directly correspond to the polar angles illustrated in Figure 4.32.

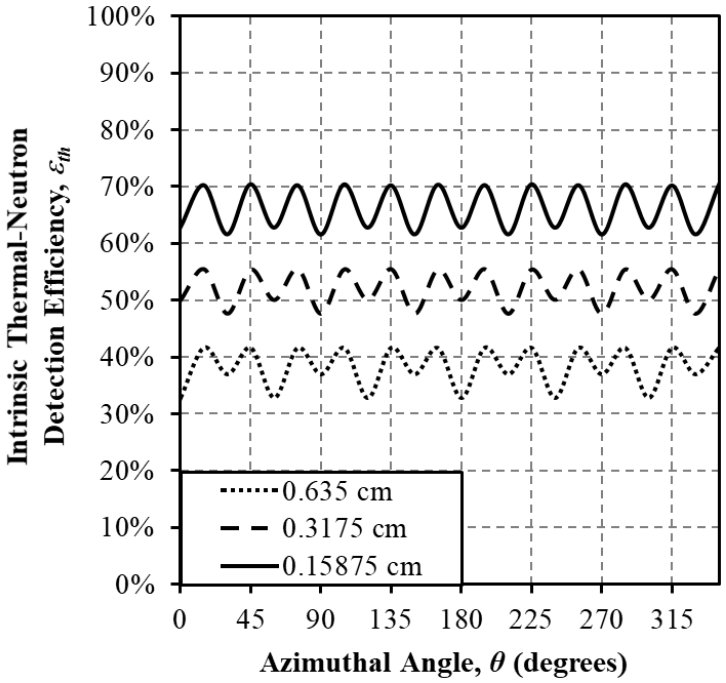

Figure C.3. Simulated azimuthal angular neutron-sensitivity distributions of ^{6}LiF-coated aluminum-honeycomb substrates with cell sizes of 0.635 cm, 0.3175 cm, or 0.15875 cm and a 0 keV LLD setting.

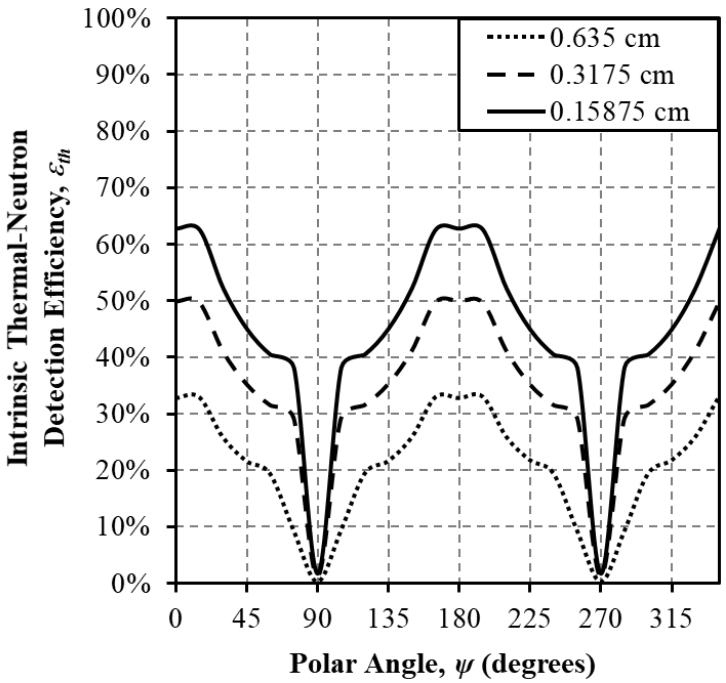

Figure C.4. Simulated polar angular neutron-sensitivity distributions of ^{6}LiF-coated aluminum-honeycomb substrates with cell sizes of 0.635 cm, 0.3175 cm, or 0.15875 cm and a 0 keV LLD setting.

Appendix C.3 Effects of Gas Pressure

The simulation environment shown in Figure 4.29 was used to simulate the effects of the P-10 gas pressure on the theoretical ε_{th}. The optimized ^{6}LiF coating thicknesses for each cell size (shown in Figure C.1 and listed in Table C.2) were defined while conducting the P-10 gas pressure simulations. The P-10 gas pressure optimization study was simulated for gas pressures ranging from 1 to 5 atm in increments of 1 atm. The center of a 5-mm diameter thermal-neutron beam was positioned at the center of the height of the substrate, normal to the substrate surface. Shown in Figure C.5 – Figure C.7 are the simulated reaction-product pulse-height spectra, represented by solid lines and corresponding to the left ordinate, with units of "Counts/Source Neutron", for the 0.635-cm, 0.3175-cm, and 0.15875-cm cell sizes, respectively. Also shown in Figure C.5 – Figure C.7 are the simulated ε_{th} as a function of LLD setting, which are represented by dashed lines and correspond to the right ordinate.

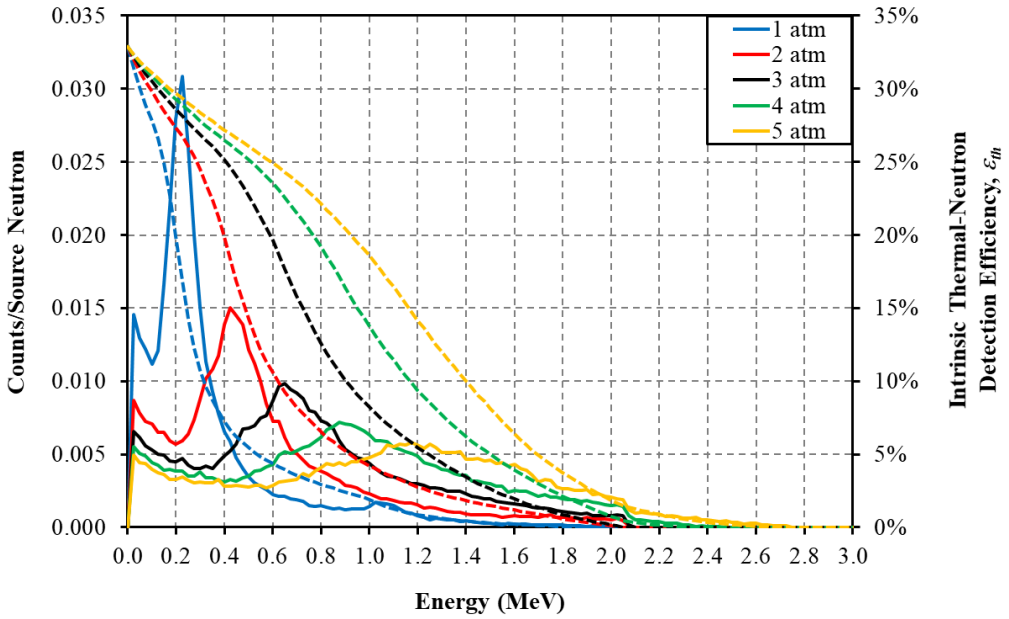

Figure C.5. Simulated reaction-product pulse-height spectra (solid lines corresponding to the left ordinate with units of "Counts/Source Neutron") for a 0.635-cm cell size honeycomb substrate with P-10 gas pressures ranging from 1 to 5 atm. The dashed lines correspond to the right ordinate and illustrate the ε_{th} as a function of LLD setting for each cell size. The honeycomb sample contained hexagonal cells with a cell size of 0.635-cm that were coated with 15.2 µm of ^{6}LiF.

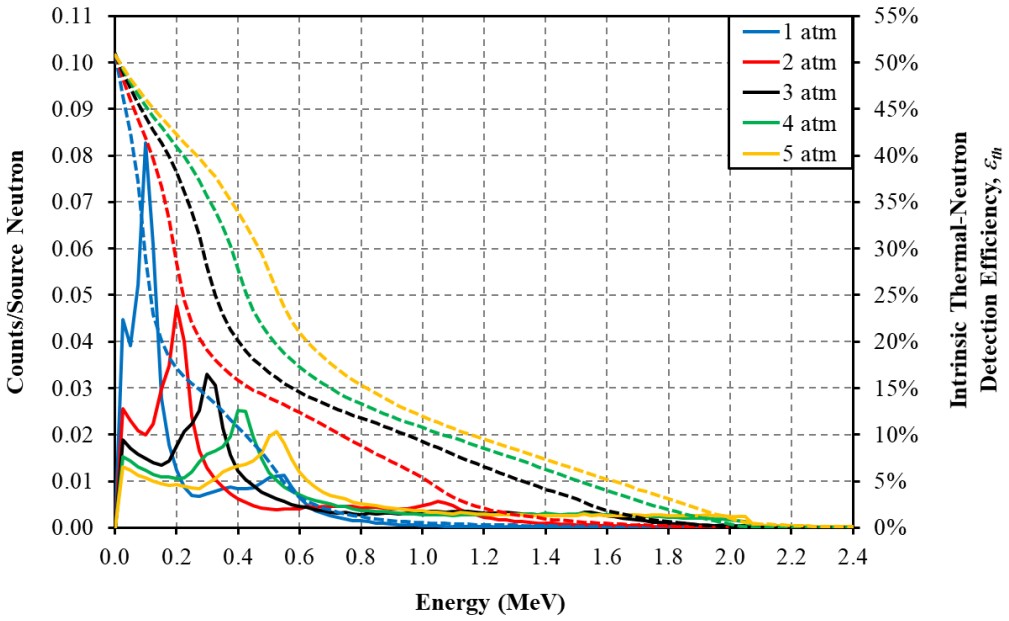

Figure C.6. Simulated reaction-product pulse-height spectra (solid lines corresponding to the left ordinate with units of "Counts/Source Neutron") for a 0.3175-cm cell size honeycomb substrate with P-10 gas pressures ranging from 1 to 5 atm. The dashed lines correspond to the right ordinate and illustrate the ε_{th} as a function of LLD setting for each cell size. The honeycomb sample contained hexagonal cells with a cell size of 0.3175-cm that were coated with 5.4 µm of ^{6}LiF.

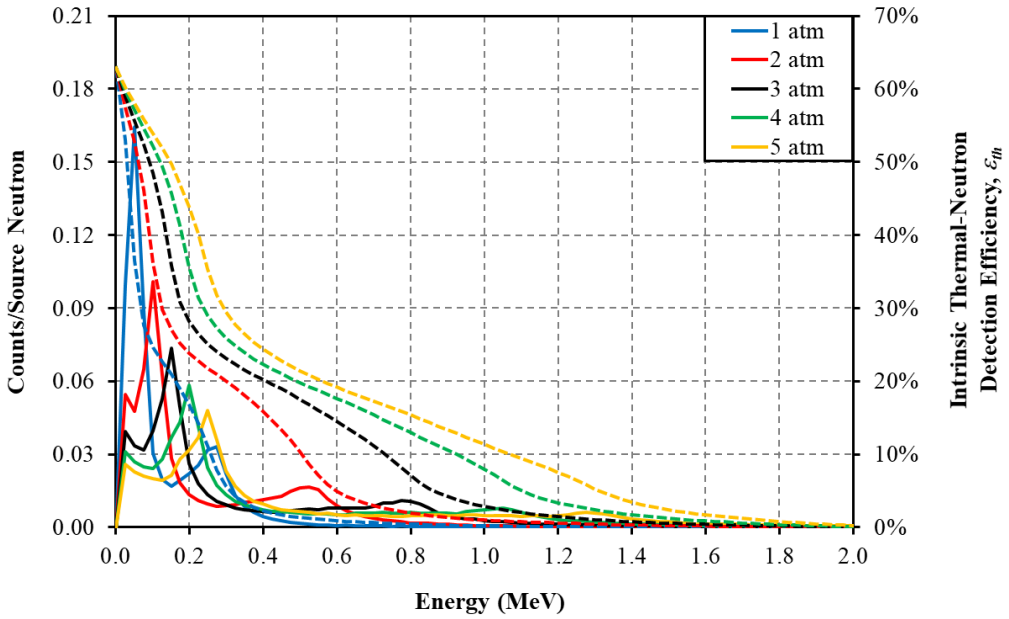

Figure C.7. Simulated reaction-product pulse-height spectra (solid lines corresponding to the left ordinate with units of "Counts/Source Neutron") for a 0.15875-cm cell size honeycomb substrate with P-10 gas pressures ranging from 1 to 5 atm. The dashed lines correspond to the right ordinate and illustrate the ε_{th} as a function of LLD setting for each cell size. The honeycomb sample contained hexagonal cells with a cell size of 0.15875-cm that were coated with 4.3 µm of ^{6}LiF.

Appendix D
Simulated Reaction-Product Pulse-Height Spectra for SFMNDs Containing Ten and Twenty ^{6}Li Foils

Shown in Figure D.1 are the *MCNP6*-simulation results of the reaction-product pulse-height spectra, represented by solid lines and corresponding to the left ordinate with units of "Counts/Source Neutron", for SFMNDs containing ten and twenty 96%-enriched, 75-μm thick ^{6}Li foils. The simulated ε_{th} as a function of LLD setting are represented by dashed lines and correspond to the right ordinate of Figure D.1. The simulation environment described in Sections 5.3 and 5.3.1 (shown in Figure 5.10) was used to simulate the reaction-product pulse-height spectra and ε_{th} distributions. The foil spacing for each foil quantity was defined as listed in Table 5.2. In both of the simulated reaction-product pulse-height spectra, a valley is present that separates the prominent spectral features from low-energy events. As the number of foils increases, the prominent spectral features down-shift in energy range. The down-shift occurs due to a reduction in the distance separating neighboring foils, resulting in a reduction in the amount of reaction-product energy that can be deposited between neighboring foils. The energy range of the valley preceding the prominent spectral features also decreases as the number of foils increases. As a result, when the number of foils increases, the energy range of the LLD setting decreases without a significant reduction of ε_{th}.

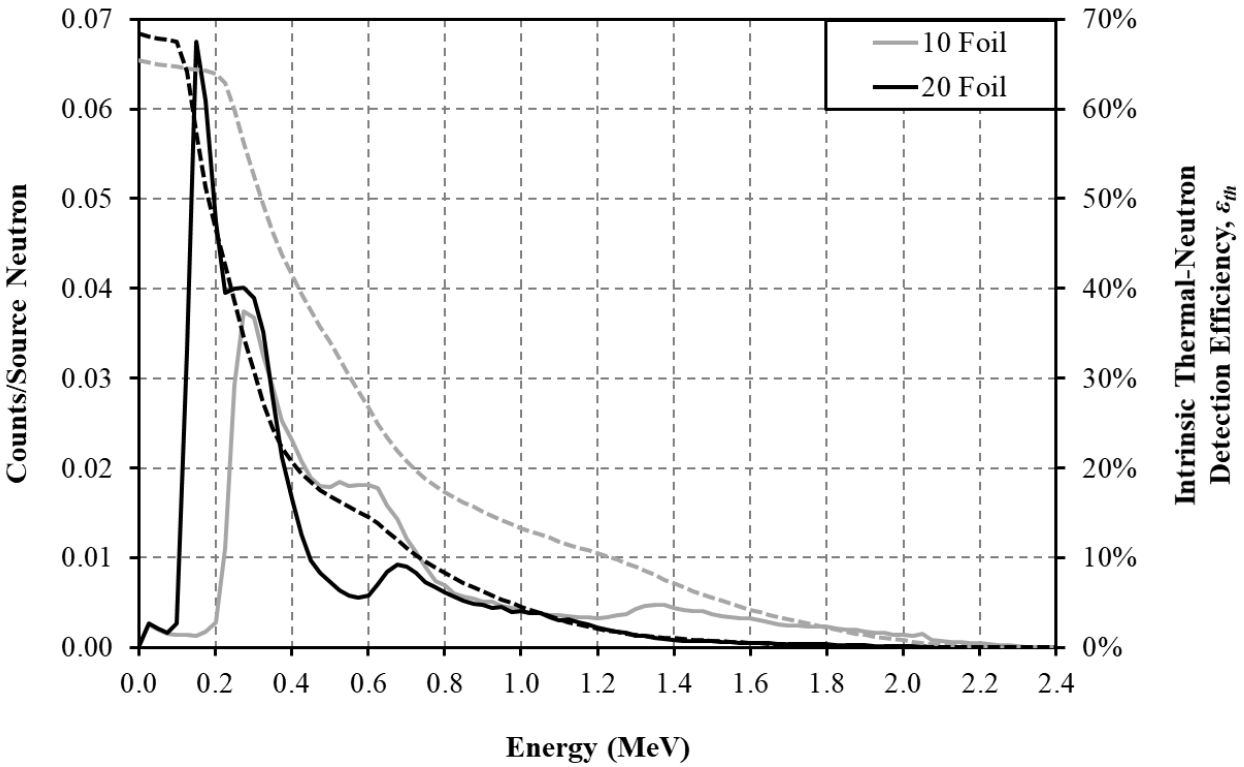

Figure D.1. MCNP6-simulated reaction-product pulse-height spectra (left ordinate with units of "Counts/Source Neutron") for ten (solid gray) and twenty (solid black) 96%-enriched, 75-µm thick ^{6}Li foils contained within 10 psig (1.68 atm) of P-10 proportional gas. The dashed gray and black lines correspond to the right ordinate and illustrate the ε_{th} as a function of LLD setting for ten and twenty ^{6}Li foils, respectively. As the LLD setting is increased, the ε_{th} reduces as a function of the reaction-product spectral features.

Appendix E
EQUIPMENT CONNECTION DIAGRAMS

Shown in Figure E.1 and Figure E.2 are the equipment connection diagrams used for characterizing the microstrip electrodes. The diagram shown in Figure E.1 was used for defining counting and gas-multiplication curves and the diagram shown in Figure E.2 was used for characterization of the gain stability of the microstrip electrodes as well as the drift electric field profiling study. The diagram in Figure E.2 was also used for performing all neutron-sensitivity measurements described in Chapter 6.

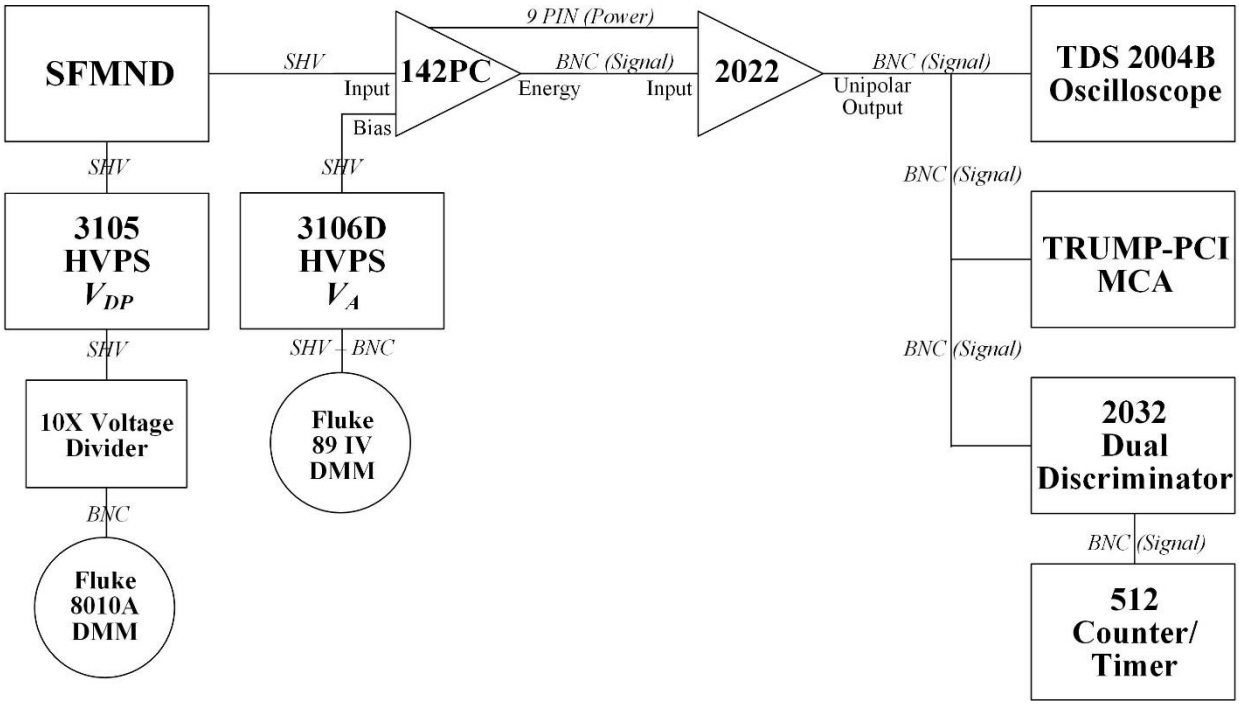

Figure E.1. Equipment connection diagram for defining the counting and gas-multiplication curves of the Si and SB33 microstrip electrodes.

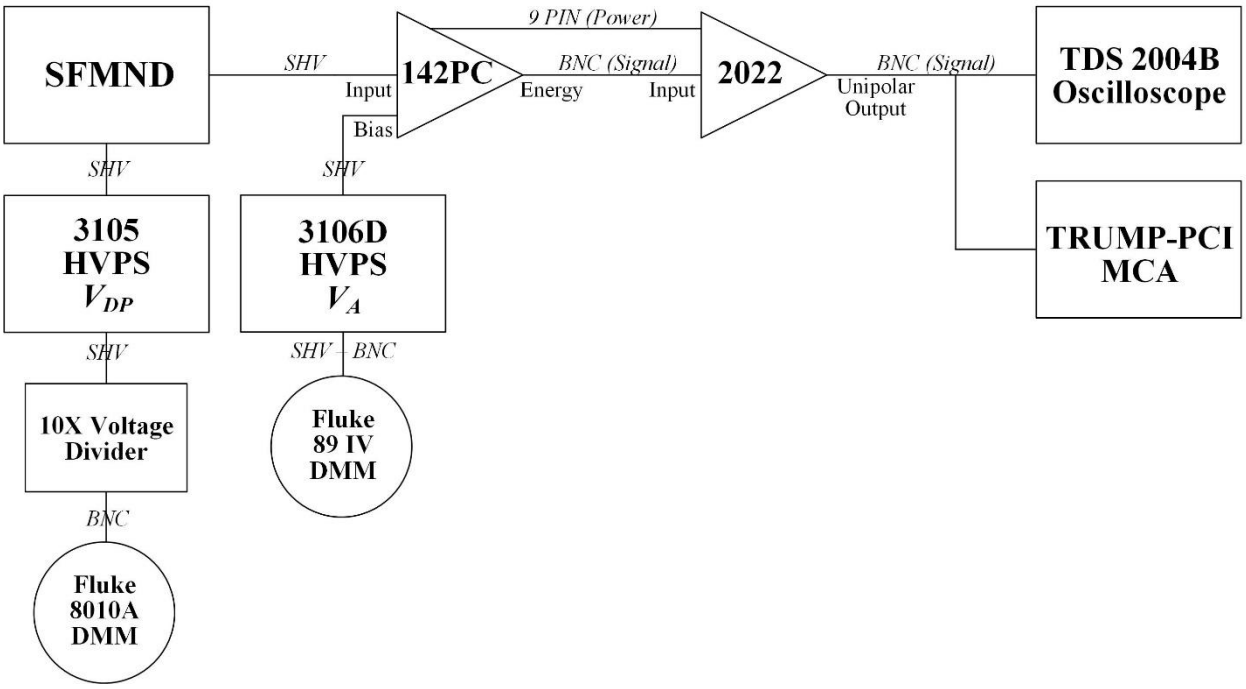

Figure E.2. Equipment connection diagram for conducting characterization of the gain stability of the microstrip electrodes as well as the drift electric field profiling study. This equipment connection diagram was also used for performing all neutron-sensitivity measurements described in Chapter 6.